

**DOCTORAL THESIS**

# Development of Rare-Earth-Free Zinc Silicate as a Novel Deep UV Emitter: Synthesis Strategies and Luminescent Properties

Jallouli Necib

TALLINN UNIVERSITY OF TECHNOLOGY  
DOCTORAL THESIS  
60/2025

# **Development of Rare-Earth-Free Zinc Silicate as a Novel Deep UV Emitter: Synthesis Strategies and Luminescent Properties**

JALLOULI NECIB



TALLINN UNIVERSITY OF TECHNOLOGY

School of Engineering

Department of Mechanical and Industrial Engineering

This dissertation was accepted for the defence of the degree 12/06/2025

**Supervisor:**

Dr. Rocío Estefania Rojas-Hernandez  
School of Engineering  
Tallinn University of Technology  
Tallinn, Estonia

**Co-supervisor:**

Prof. Irina Hussainova  
School of Engineering  
Tallinn University of Technology  
Tallinn, Estonia

**Opponents:**

Dr. Miguel Angel Rodríguez Barbero  
Department of Ceramics  
Institute of Ceramics and Glass  
Madrid, Spain

Prof. Joachim Breternitz  
Department of Chemical Engineering  
FH Münster University of Applied Sciences  
Münster, Germany

**Defence of the thesis:** 11/09/2025, Tallinn

**Declaration:**

Hereby I declare that this doctoral thesis, my original investigation and achievement, submitted for the doctoral degree at Tallinn University of Technology has not been submitted for doctoral or equivalent academic degree.

Jallouli Necib



European Union  
European Regional  
Development Fund



Investing  
in your future

-----  
signature

Copyright: Jallouli Necib, 2025

ISSN 2585-6898 (publication)

ISBN 978-9916-80-339-4 (publication)

ISSN 2585-6901 (PDF)

ISBN 978-9916-80-340-0 (PDF)

TALLINNA TEHNIKAÜLIKOO  
DOKTORITÖÖ  
60/2025

**Haruldaste muldmetallide vaba tsinksilikaadi  
kui uue süva-UV kiirguri arendus:  
sünteesistrateegiad ja luminescents  
omadused**

JALLOULI NECIB





# Contents

List of Publications .....	7
Author's Contribution to the Publications .....	8
Abbreviations .....	9
1 Introduction .....	10
1.1 Background.....	10
1.2 Review of the Literature.....	10
1.2.1 Deep UV and Its Applications .....	10
1.2.2 Conventional Deep UV Sources and Their Challenges .....	11
1.2.3 Alternatives Based on Critical Materials.....	12
1.2.4 Rare Earth Elements: Challenges and Opportunities .....	12
1.2.5 Rare-Earth-Free Wide-Bandgap Materials: A Dual Solution.....	13
1.2.6 Zn <sub>2</sub> SiO <sub>4</sub> as a Promising Alternative .....	13
1.2.6.1 Structural Properties of Zn <sub>2</sub> SiO <sub>4</sub> .....	14
1.2.6.2 Electronic Structure of Zn <sub>2</sub> SiO <sub>4</sub> .....	15
1.2.6.3 Applications of Zn <sub>2</sub> SiO <sub>4</sub> .....	15
1.2.6.4 Zn <sub>2</sub> SiO <sub>4</sub> Synthesis Methods.....	16
1.3 Motivation and Research Problems .....	17
1.4 Research Objectives and Hypotheses .....	18
1.5 Research Tasks and Contributions .....	19
2 Materials and methods .....	21
2.1 Precursors.....	21
2.1.1 Zinc Oxide Source .....	21
2.1.2 Silica Source.....	21
2.1.3 Molten Salt Medium.....	21
2.1.4 Organic Vehicle.....	21
2.2 Processing Routes .....	21
2.2.1 Powders Processing .....	21
2.2.1.1 Solid-State Synthesis.....	21
2.2.1.2 Molten Salt Synthesis .....	22
2.2.1.3 Sol-Gel Synthesis.....	22
2.2.2 Films Processing .....	23
2.2.3 Bulk Processing.....	23
2.3 Characterization Methods.....	24
2.3.1 Thermoanalysis.....	24
2.3.2 Structural and Microstructural Characterization.....	24
2.3.3 Luminescent Characterization .....	24
3 Results and Discussion .....	26
3.1 Zn <sub>2</sub> SiO <sub>4</sub> powders: Synthesis methods, Structural and Microstructural Evolution, and Luminescence Response .....	26
3.1.1 Thermal Analysis.....	26
3.1.2 Phase Evolution and Formation Mechanisms .....	28
3.1.3 Microstructural Evolution.....	31
3.1.4 Evaluation of Luminescence Response Via Different Spectroscopic Techniques .	34
3.1.4.1 XEOL Analysis: Initial Evidence of Deep UV Emission .....	34
3.1.4.2 Room Temperature Cathodoluminescence.....	36

3.1.4.3 Low Temperature Cathodoluminescence .....	38
3.1.4.4 Deep UV Emission Under Synchrotron Excitation .....	40
3.1.4.5 Excitation Mechanisms and Electronic Transitions .....	41
3.1.4.6 Nature and Origin of Deep UV Emission in $\text{Zn}_2\text{SiO}_4$ .....	44
3.2 Innovative Fabrication: Controlled Synthesis of $\text{Zn}_2\text{SiO}_4$ Films via Screen-Printing Assisted by Molten Salt Strategy .....	45
3.2.1 Structural and Interface Dynamics: Phase Transformation and Morphological Evolution .....	45
3.2.2 Luminescence Response: Structural Influences and Emission Mechanisms ....	47
3.2.2.1 Room Temperature Luminescence: XEOL and CL .....	48
3.2.2.2 Low Temperature Luminescence and Excitation Mechanisms .....	48
3.2.3 Correlating Structure and Emission in $\text{Zn}_2\text{SiO}_4$ Films .....	49
3.3 Consolidated $\text{Zn}_2\text{SiO}_4$ : Advancing Densification Through Spark Plasma Sintering ....	49
3.3.1 Phase Evolution and Densification Behaviour .....	50
3.3.2 Microstructural Characteristics of Sintered Ceramics .....	50
3.3.3 Comparative Study of Deep UV Emission in CS and SPS Samples .....	51
4 Conclusions .....	53
5 Future Research .....	55
References .....	56
Acknowledgements .....	64
Abstract .....	65
Lühikokkuvõte .....	67
Appendix .....	69
List of Publications Not Included in This Thesis .....	103
Curriculum vitae .....	105
Elulookirjeldus .....	107

## List of Publications

The PhD thesis is based on the following publications:

- I Necib, J., Hussainova, I., & Rojas-Hernandez, R.E. (2025). Effect of silica precursor on the synthesis of  $\text{Zn}_2\text{SiO}_4$ -based material. *Proceedings of the Estonian Academy of Sciences*, 74(2), 217-221. <https://doi.org/10.3176/proc.2025.2.24>.
- II Necib, J., Feldbach, E., Romet, I., Nagirnyi, V., Hussainova, I., Jüstel, T., & Rojas-Hernandez, R.E. (2025). Elucidating reaction mechanism by molten salt of potential rare-earth-free  $\text{Zn}_2\text{SiO}_4$  UV-B emitter: Insights into morphology and emission features. *Ceramics International*, In Press. <https://doi.org/10.1016/j.ceramint.2025.05.212>.
- III Necib, J., Feldbach, E., Romet, I., Nagirnyi, V., Hussainova, I., & Rojas-Hernandez, R. E. (2025). *Investigation of deep UV emission of rare-earth-free  $\text{Zn}_2\text{SiO}_4$  micropowders: the correlation of structural and luminescence properties*. *Journal of Luminescence*, 280, 121070. <https://doi.org/10.1016/j.jlumin.2025.121070>.

## **Author's Contribution to the Publications**

Contribution to the papers in this thesis are:

- I First and corresponding author. Methodology. Design of experiments. Conducting experiments. Formal analysis. Data analysis. Manuscript preparation.
- II First author. Methodology. Design of experiments. Conducting experiments. Formal analysis. Data analysis. Manuscript preparation.
- III First author. Methodology. Design of experiments. Conducting experiments. Formal analysis. Data analysis. Manuscript preparation.

## Abbreviations

CL	Cathodoluminescence
CS	Conventional Sintering
DFT	Density Functional Theory
DOS	Density of States
DSC	Differential Scanning Calorimetry
DTG	Derivative Thermogravimetry
FE-SEM	Field Emission Scanning Electron Microscope
GGA	Generalized Gradient Approximation
HT-XRD	High-Temperature X-ray Diffraction
JCPDS	Joint Committee on Powder Diffraction Standards
LED	Light-Emitting Diode
LF	Lotgering Factor
LP	Low-Pressure
mBJ	Modified Becke-Johnson
MS	Molten Salt
PL	Photoluminescence
REE	Rare Earth Element
REO	Rare Earth Oxide
SG	Sol-Gel
SPS	Spark Plasma Sintering
SS	Solid-State
TEOS	Tetraethyl Orthosilicate
TGA	Thermogravimetric Analysis
USGS	United States Geological Survey
UV	Ultraviolet
UV-B	Ultraviolet B (280–315 nm)
UV-C	Ultraviolet C (100–280 nm)
UV-LED	Ultraviolet Light-Emitting Diode
XEOL	X-ray-Excited Optical Luminescence
XRD	X-ray Diffraction
YSZ	Yttria-Stabilized Zirconia

# 1 Introduction

## 1.1 Background

Deep ultraviolet (UV) light plays a critical role in applications such as sterilization, phototherapy, and environmental purification (Song et al., 2016). Conventional deep UV light sources, including mercury-based lamps and excimer lamps, have been widely used but face significant limitations. Mercury-based lamps, while efficient, rely on toxic elemental mercury, posing health and environmental risks. Excimer lamps, though mercury-free, suffer from operational instability, low efficiency, and high costs. These challenges have spurred global efforts to phase out mercury-containing devices under the Minamata Convention (United Nations Environment Programme (UNEP), 2013) and to develop more sustainable alternatives.

Currently, rare-earth-based phosphors and gallium-containing semiconductor deep UV light-emitting diodes (UV-LEDs) are the primary alternatives. However, these technologies depend on critical raw materials such as rare earth elements (REEs) and gallium [3], which are subject to supply constraints, geopolitical risks, and environmental concerns. This highlights the critical need for sustainable deep UV light sources that are free of mercury and rare earth elements, and instead rely on abundant, non-toxic components.

To address these challenges, rare-earth-free wide band gap materials have emerged as promising alternatives. Among potential matrices, zinc silicate ( $\text{Zn}_2\text{SiO}_4$ ) is particularly advantageous due to its wide band gap, making it an effective candidate for deep UV emission. Furthermore, the raw materials required for the synthesis of  $\text{Zn}_2\text{SiO}_4$ , such as zinc (or zinc oxide) and silica are not classified as critical raw materials in the latest European Union assessment (European Union, 2024), reflecting a low supply risk.

$\text{Zn}_2\text{SiO}_4$  may therefore represent an interesting target for exploration as a sustainable alternative to conventional and emerging deep UV technologies. While previous studies have demonstrated that doped  $\text{Zn}_2\text{SiO}_4$  exhibits strong visible light emission, research on its undoped deep UV light properties remains limited. This thesis focuses on the synthesis and luminescent properties of undoped  $\text{Zn}_2\text{SiO}_4$ , aiming to develop a sustainable, rare-earth-free, and mercury-free deep UV-emitting material.

## 1.2 Review of the Literature

This section reviews state-of-the-art in deep UV light sources, their applications, challenges, and emerging alternatives. Particular emphasis is placed on  $\text{Zn}_2\text{SiO}_4$  as a sustainable, rare-earth-free, and mercury-free material, as a promising candidate for the next generation of UV technologies. The review covers the structural and electronic properties, applications, and synthesis methods of  $\text{Zn}_2\text{SiO}_4$ , providing a foundation for its development as a deep UV emitter.

### 1.2.1 Deep UV and Its Applications

Deep UV, covering both UV-C (100–280 nm) and UV-B (280–315 nm), plays a crucial role in modern applications. UV-C is particularly significant for its germicidal properties, making it an essential tool for disinfection and sterilization processes (Song et al., 2016). The COVID-19 pandemic highlighted the necessity of efficient, safe, and sustainable disinfection technologies, further driving interest in deep UV sources. UV-B, on the other hand, is utilized in medical treatments such as phototherapy for skin conditions like

psoriasis and vitiligo (Lee et al., 2025), as well as in enhancing vitamin D synthesis (W. Liu et al., 2024), supporting bone health (Guo et al., 2018; W. Liu et al., 2024), and preventing osteoporosis (Ochiai et al., 2021). Beyond healthcare, UV-B-emitting materials hold promise for disinfection and sterilization (X. Lin et al., 2024), serving as eco-friendly alternatives to harmful agricultural chemicals and pesticides (Hidalgo-Sanz et al., 2024), and enabling advanced applications such as bright-field stress sensing (X. Yang et al., 2023).

The widespread use of deep UV light highlights the urgent need for sustainable alternatives, as current technologies rely on toxic or scarce materials that pose environmental and economic challenges.

### 1.2.2 Conventional Deep UV Sources and Their Challenges

Traditional deep UV sources, as illustrated in **Fig. 1**, primarily include mercury-based lamps and excimer lamps. Mercury lamps, particularly low-pressure (LP) variants, have been widely used for over 90 years due to their efficient emission at 254 nm, which aligns with the peak germicidal effectiveness curve (Sharma & Demir, 2022). However, their reliance on toxic elemental mercury has led to significant health and environmental concerns, prompting global restrictions under the Minamata Convention. These lamps also face practical limitations, such as large physical size, long warm-up times, and inefficiency in certain applications (Sharma & Demir, 2022).

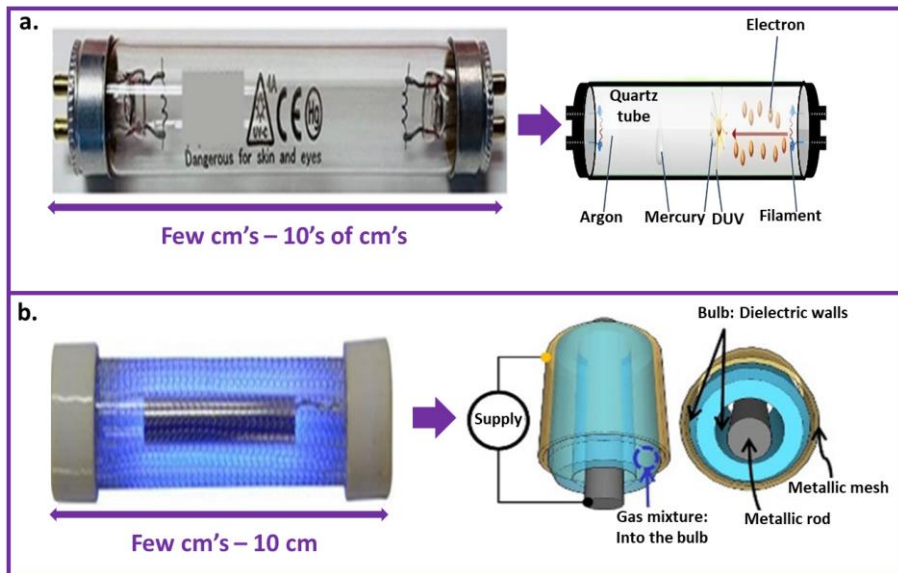


**Fig. 1** Size comparison (on the same scale) and schematics of the following (a) Mercury lamp (Wu et al., 2014) and (b) Excimer lamp (Florez et al., 2012).

Excimer lamps, on the other hand, offer a mercury-free alternative and can emit far-UV-C wavelengths (e.g., 222 nm with Kr-Cl gas mixtures). Their limited penetration depth in human tissue makes them potentially safer for use in occupied spaces. However, excimer lamps exhibit operational instability, low efficiency (~8%), and high costs (Rajkhowa, 2020).

The limitations of both mercury and excimer lamps demonstrate the necessity for new deep UV emitters that combine efficiency, environmental safety, and long-term viability.



1.2.3 Alternatives Based on Critical Materials

In response to these challenges, deep UV-LEDs have emerged as next-generation alternatives, offering mercury-free operation, energy efficiency, and extended operational lifetimes (Muramoto et al., 2014). A comparative analysis of conventional UV lamps and UV-LEDs (**Table 1**) highlights their key advantages and limitations.

**Table1:** Comparison of UV lamps and UV-LEDs features (Muramoto et al., 2014).

Feature	UV Lamps	UV-LEDs
Structure	Bulky	Compact
Power Consumption	High	Low
Standby Time	Long	Short
Heat Generation	High	Low
Environmental Burden	Mercury used	No mercury used
Spectrum	Broad	Narrow

However, deep UV-LEDs rely on gallium (X. Liu et al., 2024, 2025; Z. Zhang et al., 2025; Zhou et al., 2024) which is classified as a critical raw material by the European Commission due to its limited availability and extraction challenges (European Union, 2024). Similarly, rare-earth-based phosphors, such as  $\text{SrAl}_{12}\text{O}_{19}:\text{Ce}$ ,  $\text{Lu}_2\text{SiO}_5:\text{Pr}$ ,  $\text{Ca}_2\text{P}_2\text{O}_7:\text{Pr}$ ,  $\text{CaLa}_4\text{Si}_3\text{O}_{13}:\text{Gd}$ , and  $\text{YPO}_4:\text{Gd}$ , show potential for deep UV emission (Kikuchi et al., 2024; T. Lin et al., 2024; X. Lin et al., 2024; Singh, Bajaj, et al., 2021; Yan et al., 2021) but also face significant limitations.

The next section will delve into rare earth elements and their associated challenges.

1.2.4 Rare Earth Elements: Challenges and Opportunities

Rare earth elements are not only highly used in phosphors but are also essential to high-tech industries due to their unique magnetic, luminescent, and catalytic properties, driving advancements in electronics, renewable energy, and medical technologies (Balaram, 2019). Global production of rare earth oxides (REOs) has tripled since 2015, reaching an estimated 390,000 metric tons per year by 2024 (**Fig.2**) (Mineral Commodity Summaries 2025, 2025).

However, this growth is accompanied by significant geopolitical risks, as REO production is heavily concentrated in a few countries. China dominates the global supply, accounting for 68.81% of production in 2024, while the United States and Burma contribute only 11.47% and 7.9%, respectively (**Fig.2, inset**) (Mineral Commodity Summaries 2025, 2025). This concentration heightens supply chain vulnerabilities, increases price volatility, and reinforces strategic dependencies, posing challenges to global technological and economic stability.

Additionally, the environmental impact of REE extraction and processing raises concerns. Inadequate waste management contributes to soil degradation, freshwater contamination, and marine ecosystem disruption, necessitating stringent regulatory measures to mitigate ecological damage (Ramprasad et al., 2022). To address these challenges, policy initiatives such as the European Critical Raw Materials Act aim to promote alternative materials and reduce reliance on REEs (Guillaume, 2024). This aligns with the goals of this thesis, which seeks to develop sustainable, rare-earth-free materials for deep UV emission.

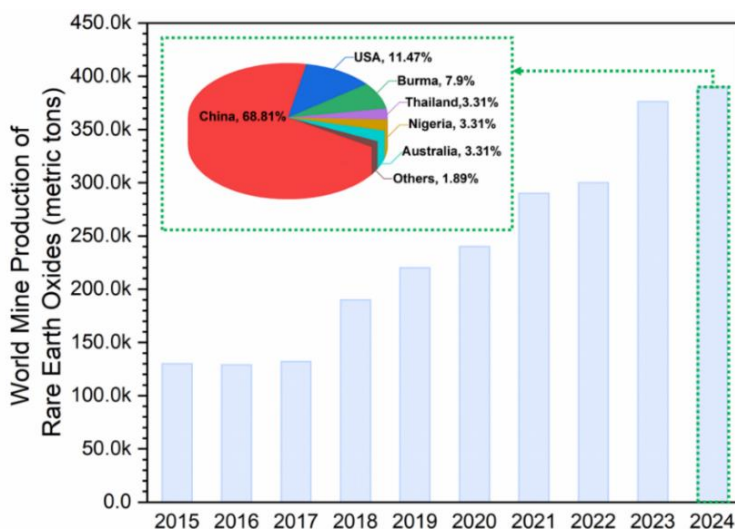


**Fig.2** Mine production of rare earth oxides from 2015 to 2024. The inset pie chart indicates each country's share of REO production in 2024 (data obtained from USGS Mineral Commodity Summaries 2025 (Mineral Commodity Summaries 2025, 2025)).

### 1.2.5 Rare-Earth-Free Wide-Bandgap Materials: A Dual Solution

The transition to mercury-free deep UV technologies presents a sustainability paradox. While deep UV LEDs eliminate toxic mercury, they often rely on critical raw materials such as gallium and REEs. Rare-earth-free wide-bandgap materials offer a dual solution by addressing both mercury toxicity and critical-material supply risks. These materials achieve deep UV luminescence through mechanisms such as host-lattice transitions or defect-mediated processes, thereby eliminating the reliance on REEs. For example,  $\text{ZnAl}_2\text{O}_4$  spinel, with a bandgap of  $\sim 7$  eV (Ishinaga et al., 2015; Kominami. H et al., 2011), has demonstrated UV-C to UV-B emission (Rojas-Hernandez et al., 2022, 2024), while  $\text{K}_2\text{ZrSi}_2\text{O}_7$ , with a bandgap of 5.6 eV, exhibits UV-C emission (Gerdes et al., 2018).

Rare-earth-free wide-bandgap materials align with global sustainability goals by decoupling UV technologies from geopolitically sensitive resources, thus addressing both environmental and supply chain challenges.

### 1.2.6 $\text{Zn}_2\text{SiO}_4$ as a Promising Alternative

Among these materials,  $\text{Zn}_2\text{SiO}_4$  stands out as a strategically significant candidate due to its composition of abundant, non-critical elements. Its inherent abundance, environmental sustainability, and cost-effectiveness position  $\text{Zn}_2\text{SiO}_4$  as a viable alternative to rare-earth-dependent systems. With a wide bandgap of 5.5-6.2 eV (Essalah et al., 2020; Karazhanov et al., 2009; Ramakrishna et al., 2014; Tripathi et al., 2015),  $\text{Zn}_2\text{SiO}_4$  exhibits intrinsic electronic properties suitable for deep UV emission, addressing the dual challenges of mercury toxicity and critical-resource dependency.

Despite this potential, deep UV emission in  $\text{Zn}_2\text{SiO}_4$  remains understudied. Only a handful of studies have reported UV-B emission in  $\text{Zn}_2\text{SiO}_4$  films, nanotubes, and nanocables (Dierre et al., 2010; Feng et al., 2005; Furukawa et al., 2015; C. Li et al., 2010), with proposed mechanisms including radiative recombination within the  $\text{Zn}_2\text{SiO}_4$  lattice (C. Li et al., 2010) or indirect emission (Furukawa et al., 2015). However, these investigations lack rigorous mechanistic analysis, offering limited insight into the origins

of UV emission or strategies for performance optimization. This leaves a significant gap in understanding its full potential as a sustainable deep UV emitter.

Given its promising attributes and the need for further exploration, the following sections will review its structural properties, electronic structure, applications, and synthesis methods, based on the existing literature.

#### 1.2.6.1 Structural Properties of $\text{Zn}_2\text{SiO}_4$

Zinc silicate, first identified in the early 19th century (Takesue et al., 2009), belongs to the phenakite-type mineral family  $\text{Be}_2\text{SiO}_4$  (Bessadok et al., 2024). It exhibits multiple polymorphic forms, with the  $\alpha$ -phase (willemite) being the most thermodynamically stable. The  $\alpha$ -phase crystallizes in a rhombohedral structure (space group R-3) with unit cell parameters:  $a = b = 13.938 \text{ \AA}$ ,  $c = 9.310 \text{ \AA}$  (Masjedi-Arani & Salavati-Niasari, 2016). In willemite, both  $\text{Zn}^{2+}$  and  $\text{Si}^{4+}$  ions adopt tetrahedral coordination, forming isolated  $\text{ZnO}_4$  and  $\text{SiO}_4$  tetrahedra as structural building blocks (R. Dai et al., 2022). These tetrahedra interconnect via corner-sharing oxygen atoms, creating a three-dimensional framework as shown in **Fig. 3**. The metastable  $\beta$ -phase, tentatively assigned to either triclinic or orthorhombic systems, deviates structurally from the  $\alpha$ -phase due to partial octahedral coordination of  $\text{Zn}^{2+}$  ions (Taylor. H. F. W, 1962). This altered geometry disrupts the tetrahedral network, likely contributing to its reduced thermodynamic stability.

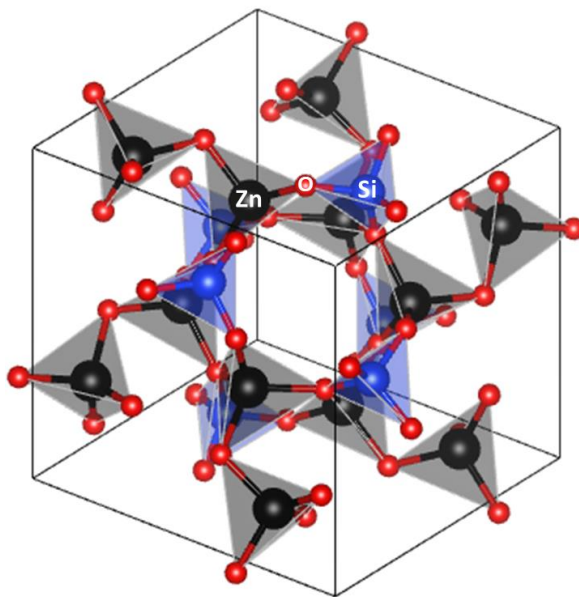


**Fig. 3** Crystal structure of willemite  $\text{Zn}_2\text{SiO}_4$ , visualized using VESTA software.

To date, no precise refinement of the  $\beta$ -phase crystal structure has been reported, reflecting ongoing uncertainty regarding its exact symmetry (triclinic vs. orthorhombic) and atomic positions.

Additional polymorphs form under high-pressure conditions and exhibit distinct crystallographic behaviours, though their structural details remain less explored compared to the  $\alpha$ - and  $\beta$ -phases.

The  $\alpha$ -phase structure is well-characterized by its distinctive tetrahedral framework of  $\text{ZnO}_4$  and  $\text{SiO}_4$  units. Understanding this structural arrangement is crucial for controlling and optimizing the luminescent properties of zinc silicate, particularly for deep UV applications. This structural foundation provides context for examining the electronic properties that govern its optical behaviour.

#### 1.2.6.2 Electronic Structure of $\text{Zn}_2\text{SiO}_4$

Willemite exhibits a direct band gap (R. Dai et al., 2022; Karazhanov et al., 2009). The valence band (VB) is dominated by Zn 3d and O 2p orbitals, while the conduction band (CB) consists of hybridized Zn 4s/4p, Si 3p, and O 2p states (R. Dai et al., 2022). Using Density Functional Theory (DFT) with the Generalized Gradient Approximation (GGA), Dai et al. calculated a band gap of 2.75 eV (R. Dai et al., 2022), as shown in **Fig. 4a**, significantly smaller than experimental values. This underestimation arises because semilocal functionals like GGA fail to properly account for strong on-site electron correlations, particularly in Zn 3d states (Essalah et al., 2020).

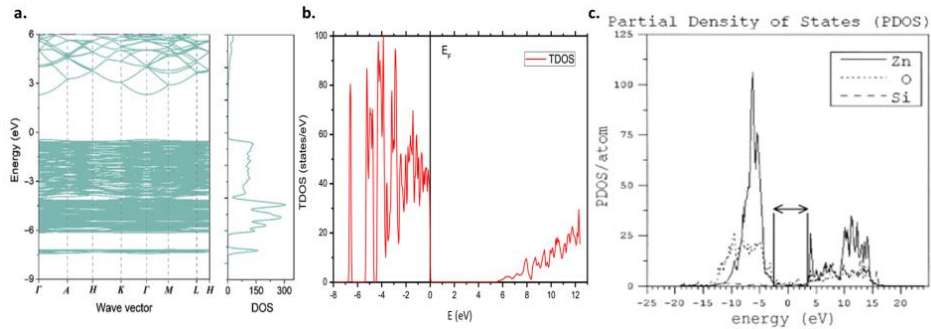


**Fig. 4** Electronic structure of  $\text{Zn}_2\text{SiO}_4$ . (a) Band structure and total DOS calculated with GGA (R. Dai et al., 2022). (b) total DOS calculated with GGA+ mBJ approximation of  $\text{Zn}_2\text{SiO}_4$  (Essalah et al., 2020). Partial DOS near the Fermi energy for a Zn-centered 40-atom cluster. The band gap is marked with an arrow (Chang et al., 1999).

To address this limitation, Essalah et al. employed GGA combined with the modified Becke-Johnson (mBJ) exchange potential, which improves the description of localized d-orbital interactions (Essalah et al., 2020). This approach yields a band gap of 5.54 eV (Essalah et al., 2020), as illustrated in **Fig. 4b**, closely aligning with experimental results. Separately, Chang et al. applied the embedded-cluster Discrete Variational (DV)- $\chi\alpha$  method and reported a band gap of 6 eV (Chang et al., 1999), as shown in **Fig. 4c**.

The agreement between theoretical calculations and experimental measurements validates the wide band gap nature of  $\text{Zn}_2\text{SiO}_4$  (Chang et al., 1999; Essalah et al., 2020; Tripathi et al., 2015), reinforcing its potential for deep UV emission applications.

#### 1.2.6.3 Applications of $\text{Zn}_2\text{SiO}_4$

Given its properties,  $\text{Zn}_2\text{SiO}_4$  demonstrates utility in diverse fields, including UV detectors, gas sensors, toxic ion adsorption, bioimaging, energy storage, and optoelectronic devices (Basavaraj et al., 2015; Bharti et al., 2023; Cheepborisutikul et al., 2025; P. Dai et al., 2015; Effendy et al., 2019; Hsu et al., 2023; Pan et al., 2024; Y. Yang et al., 2010). While  $\text{Zn}_2\text{SiO}_4$  exhibits multifunctionality, research has predominantly focused on its luminescence properties, particularly in manganese-doped  $\text{Zn}_2\text{SiO}_4$ , which is widely studied for its strong green emission resulting from the  $\text{Mn}^{2+}$  d-d transition (Rakov et al.,

2024). In addition to manganese,  $\text{Zn}_2\text{SiO}_4$  serves as a host for various rare earth (Azman et al., 2018; Basavaraj et al., 2015; Bharadwaj et al., 2023; Effendy et al., 2019; Jacob et al., 2019; Jiang et al., 2025; Mbule et al., 2021; Portakal-Uçar, Dogan, et al., 2021; Singh et al., 2024; Sivakumar et al., 2024; Vařák et al., 2023) ( $\text{Eu}^{3+}$ ,  $\text{Er}^{3+}$ ,  $\text{Sm}^{3+}$ ,  $\text{Dy}^{3+}$ ,  $\text{Nd}^{3+}$ ,  $\text{Tm}^{3+}$ ,  $\text{Tb}^{3+}$ ,  $\text{Pr}^{3+}$ , and  $\text{Gd}^{3+}$ ) and transition metal ions (Z. Peng et al., 2008; Sohn et al., 1999; Wahab et al., 2023; Wang et al., 2024) ( $\text{Co}^{2+}$ ,  $\text{Ni}^{2+}$ ,  $\text{Ti}^{4+}$ , and  $\text{Hf}^{4+}$ ), enabling tunable emissions across the ultraviolet, visible, and infrared spectra, as illustrated in **Fig. 5** (Takesue et al., 2009). This adaptability has led to its extensive use in LEDs, displays, and sensors, further highlighting its significance as a phosphor material (Takesue et al., 2009).

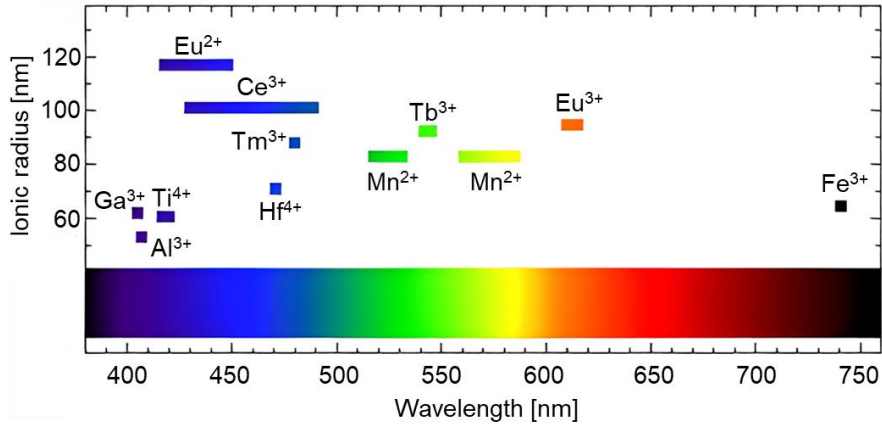


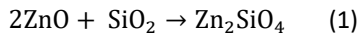
**Fig. 5** Emission peaks and ionic radii of guest ions for  $\alpha$ -phase  $\text{Zn}_2\text{SiO}_4$  host crystals (Takesue et al., 2009).

Despite the substantial research on doped  $\text{Zn}_2\text{SiO}_4$ , studies on its undoped counterpart remain limited. In particular, the emission mechanisms in undoped  $\text{Zn}_2\text{SiO}_4$ , especially in the deep UV range, are not yet fully understood. Addressing this knowledge gap is crucial for evaluating its potential as a sustainable deep UV emitter. Advancing research in this area would support the global transition toward rare-earth-free and mercury-free technologies contributing to the broader development of environmentally sustainable materials.

#### 1.2.6.4 $\text{Zn}_2\text{SiO}_4$ Synthesis Methods

$\text{Zn}_2\text{SiO}_4$  can be synthesized in various forms using different methods, each presenting specific advantages and challenges. Understanding these limitations is crucial for optimizing synthesis strategies for deep UV applications.

The solid-state reaction method remains widely used for  $\text{Zn}_2\text{SiO}_4$  powder synthesis due to its simplicity and scalability (Vien et al., 2019). It forms through the solid-state diffusion of ZnO into  $\text{SiO}_2$ :



However, this approach often requires high temperatures, long reaction times, and often can result in inhomogeneous product with poor control over particle size and morphology, commonly producing agglomerated and irregular particles ranging from 20 to 100  $\mu\text{m}$  in diameter (Rojas-Hernandez, Rubio-Marcos, Enríquez, et al., 2015).

Alternative synthesis routes such as hydrothermal synthesis, gel combustion, spray pyrolysis, combustion synthesis, and sol-gel processing have been developed (Bhatkar et al., 2002; Diana et al., 2024; Portakal-Uçar, Oglakci, et al., 2021; Singh, Prasad, et al., 2021; Sivakumar & Lakshmanan, 2014; Yi et al., 2024). While these methods offer better control over particle characteristics, enabling the formation of more uniform and smaller particles often in the nanometer size range, they also face challenges including complex processing conditions, limited scalability, and potential compositional inhomogeneities.

For thin film fabrication, techniques such as sol-gel-derived spin coating, radio frequency magnetron sputtering, chemical vapor deposition, and vacuum-sealed vapor deposition have been employed (Afandi et al., 2024; Kang et al., 2006; Minho et al., 2022; Park & Kim, 2021). While these methods offer precise thickness control, they typically require complex equipment, high operational costs, and face significant challenges in scaling up for large-area production.

For consolidated  $\text{Zn}_2\text{SiO}_4$  into dense pellets, most reports have utilized conventional sintering methods (F. Liu et al., 2024; Yue et al., 2009), typically employing pressureless sintering. This process involves cold pressing the powder into a disk or pellet shape, followed by a high-temperature sintering step to densify the material. While these approaches offer advantages in simplicity, they require high temperatures and long processing times, leading to challenges in controlling microstructure and consequently, the functional properties. The potential of advanced sintering techniques for  $\text{Zn}_2\text{SiO}_4$  remains largely unexplored.

This thesis explores both established and emerging synthesis methods, including traditional techniques like sol-gel and solid-state reactions, as well as advanced approaches such as molten salt synthesis, screen-printing assisted by molten salt strategy, and spark plasma sintering (SPS). These methods enable precise control over microstructure and phase composition, which are critical for optimizing  $\text{Zn}_2\text{SiO}_4$ 's structural and optical properties, particularly its deep UV emission characteristics.

### 1.3 Motivation and Research Problems

Deep UV light sources are essential for sterilization, phototherapy, and environmental purification. However, current technologies rely on either toxic mercury-based lamps or critical materials like gallium and rare earth elements, which pose environmental, health, and supply chain risks. This highlights the urgent need for a sustainable, scalable, and non-toxic deep UV emitter.  $\text{Zn}_2\text{SiO}_4$ , with its wide bandgap, non-toxic composition, and earth-abundant availability, presents a promising alternative. Despite its potential, several critical challenges remain unaddressed:

- Limited studies exist on UV-B-emitting  $\text{Zn}_2\text{SiO}_4$ , primarily focused on complex nanostructure synthesis (nanotubes, nanocables). The need for precise control over experimental conditions in these approaches hinders practical applications, necessitating the exploration of more straightforward and scalable synthesis methods.
- The influence of material form (particles, films, consolidated materials) and size on UV-B emission remains unexplored. Understanding how morphology and phase composition affect luminescent properties could unlock new strategies for enhancing  $\text{Zn}_2\text{SiO}_4$ 's UV-B emission performance.

- Only one study by (Furukawa et al., 2015) reports  $\text{Zn}_2\text{SiO}_4$  thin films for UV applications, using costly radio frequency magnetron sputtering. There is a need to develop cost-effective, scalable deposition methods as well as a deeper understanding of film-substrate interactions to enable broader practical implementation.
- The development of consolidated  $\text{Zn}_2\text{SiO}_4$ -based deep UV emitters remains largely unexplored. While conventional sintering has been reported, understanding the relationships between consolidation parameters, microstructure, and functional properties requires further investigation, particularly for applications demanding robust bulk materials.
- The origin of UV-B emission in  $\text{Zn}_2\text{SiO}_4$  remains unclear, with existing studies proposing only simplified mechanisms based solely on cathodoluminescence measurements. A comprehensive spectroscopic investigation using multiple techniques is needed to elucidate the underlying emission mechanisms.
- A thorough understanding of the correlations between structural, microstructural, and functional properties is essential for material design. However, an integrated study encompassing all these aspects is currently absent in the scientific literature.

## 1.4 Research Objectives and Hypotheses

The primary aim of this thesis is to establish  $\text{Zn}_2\text{SiO}_4$  as a sustainable, mercury-free, and rare-earth-free deep UV emitter by advancing the fundamental understanding of its deep UV luminescence mechanisms. Through a systematic investigation of diverse synthesis routes, this study seeks to elucidate the relationships between synthesis parameters, structural and microstructural properties, and luminescence response, with the ultimate goal of optimizing  $\text{Zn}_2\text{SiO}_4$ 's performance for practical deep UV applications.

The specific research objectives are as following:

- **RO1:** To explore alternative processing routes for the synthesis of  $\text{Zn}_2\text{SiO}_4$  in powder form. Molten salt and sol-gel techniques have been proposed, both routes are compared to conventional solid-state methods, evaluating their formation mechanisms, phase evolution processes, and ability to stabilize different polymorphs ( $\alpha$  and  $\beta$  phases).
- **RO2:** To establish fundamental correlations between synthesis parameters (precursor reactivity, temperature, processing method) and the resulting structural, morphological, and luminescent properties of  $\text{Zn}_2\text{SiO}_4$  in powder form, focusing on how these relationships can be leveraged to enhance deep UV emission.
- **RO3:** To develop direct synthesis strategies for producing  $\text{Zn}_2\text{SiO}_4$  in form of films suitable for technological applications.
- **RO4:** To consolidate densified ceramics based on  $\text{Zn}_2\text{SiO}_4$  via conventional and advanced techniques such as Spark Plasma Sintering.
- **RO5:** To investigate the underlying nature of the luminescence responsible for deep UV emission in  $\text{Zn}_2\text{SiO}_4$  materials through comprehensive evaluation using multiple luminescence characterization techniques, identifying excitation mechanisms and emission centers.

- **RO6:** To perform a comparative evaluation of conventional versus alternative synthesis approaches for  $\text{Zn}_2\text{SiO}_4$  across different material forms, assessing their influence on phase purity, microstructure, interface characteristics, and deep UV emission properties, with the ultimate goal of establishing  $\text{Zn}_2\text{SiO}_4$  as a viable rare-earth-free alternative for sustainable UV applications.

This thesis tests the following hypotheses:

- **H1:** Undoped  $\text{Zn}_2\text{SiO}_4$  exhibits deep UV emission, demonstrating its potential as a rare-earth-free and mercury-free phosphor.
- **H2:** The deep UV emission in  $\text{Zn}_2\text{SiO}_4$  originates from intrinsic electronic transitions and defect states, both of which can be tuned through synthesis parameters to enhance luminescent properties.
- **H3:** The phase composition, crystallinity, and morphology of  $\text{Zn}_2\text{SiO}_4$  are strongly influenced by precursor type, synthesis temperature, and processing conditions, enabling structural tailoring for optimized functionality.
- **H4:** Applying novel synthesis routes, such as molten salt synthesis, screen-printing, and SPS, to  $\text{Zn}_2\text{SiO}_4$  enables precise control over its structural, microstructural, and optical properties, enhancing its potential as a rare-earth-free deep UV emitter for next-generation applications.

## 1.5 Research Tasks and Contributions

To achieve the research objectives and validate the hypotheses outlined in **Section 1.4**, the following tasks were performed:

- (i) To develop and investigate novel molten salt synthesis as alternative route for  $\text{Zn}_2\text{SiO}_4$  powder, evaluating its influence on phase formation temperature and particle morphology.
- (ii) To synthesize  $\text{Zn}_2\text{SiO}_4$  powders via the sol-gel method and compare its phase evolution with conventional solid-state methods.
- (iii) To study the impact of silica precursor reactivity (crystalline vs. amorphous) on  $\text{Zn}_2\text{SiO}_4$  phase formation, morphology, and luminescent properties via solid-state and molten salt routes, and to evaluate the role of synthesis temperature across all three methods (including sol-gel) on material properties.
- (iv) To establish a screen-printing method assisted by molten salt flux for  $\text{Zn}_2\text{SiO}_4$  films and study the effect of ink formulation and thermal treatment on film structure, morphology, and luminescent properties.
- (v) To synthesize dense  $\text{Zn}_2\text{SiO}_4$  ceramics using both conventional sintering and spark plasma sintering (SPS), comparing their densification behaviour, microstructural development, and luminescence response.
- (vi) To demonstrate  $\text{Zn}_2\text{SiO}_4$  as a rare-earth-free deep UV emitter through investigation of the origin and mechanisms of deep UV emission using comprehensive spectroscopic analysis to identify excitation processes and emission centers.
- (vii) To perform a systematic comparative analysis of all synthesis methods across different material forms, evaluating their effects on structural, microstructural, and luminescent properties.



This work significantly advanced the understanding of  $\text{Zn}_2\text{SiO}_4$ 's deep UV luminescence mechanisms, demonstrating its potential as a rare-earth-free emitter. Three distinct synthesis approaches for powders (solid-state, molten salt, and sol-gel), along with methods for films and consolidated materials, were systematically developed to produce  $\text{Zn}_2\text{SiO}_4$  with tailored properties. The established correlations between processing conditions and material performance enabled optimization of UV-B emission across different material forms. These contributions position  $\text{Zn}_2\text{SiO}_4$  as a viable alternative to rare-earth-based UV emitters, advancing the development of sustainable deep UV technologies.

## 2 Materials and methods

This chapter outlines the materials, synthesis methods, and characterization techniques used in this thesis.

### 2.1 Precursors

#### 2.1.1 Zinc Oxide Source

Two zinc precursors were selected based on the synthesis method. Zinc nitrate hexahydrate ( $\text{Zn}(\text{NO}_3)_2 \cdot 6\text{H}_2\text{O}$ , Lachner, 99%) was used for sol-gel synthesis, while zinc oxide (ZnO, Symrise GmbH, 99.5%,  $d_{50} \approx 400$  nm) was employed for solid-state reactions, molten salt synthesis, screen-printing assisted by molten salt strategy, conventional sintering, and SPS.

#### 2.1.2 Silica Source

Different silicon precursors were used depending on the synthesis method. Tetraethyl orthosilicate (TEOS, VWR, 99%) was used for powder synthesis via the sol-gel method. For solid-state and molten salt synthesis, crystalline silica ( $\text{SiO}_2$ , Alfa Aesar, 99.5%,  $d_{50} \approx 1.21$   $\mu\text{m}$ ) and amorphous silica (Thermo Fisher Scientific, 99.9%,  $d_{50} \approx 500$  nm) were employed. Amorphous silica was also used for bulk ceramics in conventional sintering and SPS. For film fabrication via screen printing, single-side polished quartz single-crystal substrates ( $\text{SiO}_2$  (0001), Biotain Crystal Co.) served as both the substrate and silicon source.

#### 2.1.3 Molten Salt Medium

A eutectic mixture of sodium chloride (NaCl, VWR, 99.5%) and potassium chloride (KCl, VWR, 99.5%) served as the molten salt medium. This mixture was chosen for its low melting point, which facilitates controlled crystal growth, enhances ion diffusion, and lowers reaction temperatures. It was employed in molten salt synthesis for powder preparation and film fabrication via the screen-printing assisted by molten salt strategy.

#### 2.1.4 Organic Vehicle

For film fabrication via screen-printing, an organic-based vehicle was formulated for optimal printability and adhesion. The formulation included  $\alpha$ -terpineol (Thermo Fisher Scientific) as the solvent, ethyl cellulose (Acros Organics) as the binder, 2-(2-butoxyethoxy) ethyl acetate (Alfa Aesar) as the plasticizer, and DuPont™ 8250 as the thinner.

### 2.2 Processing Routes

#### 2.2.1 Powders Processing

##### 2.2.1.1 Solid-State Synthesis

Stoichiometric quantities of ZnO and  $\text{SiO}_2$  powders (crystalline or amorphous) were first mixed using an agate mortar and pestle to achieve initial homogeneity. The mixture was then subjected to planetary ball milling (Model YKM-1) at 250 rpm for 8 h, using yttria-stabilized zirconia (YSZ) balls and zirconia jars under dry conditions. The homogenized powder mixtures were subsequently heat-treated in air at temperatures ranging from 700 to 1300 °C for 2 h. After heat treatment, the products were manually ground and sieved using a 37  $\mu\text{m}$  nylon sieve.

Samples prepared with crystalline silica are designated as crystalline silica-based samples, while those prepared with amorphous silica are referred to as amorphous silica-based samples.

### 2.2.1.2 Molten Salt Synthesis

The molten salt synthesis followed a procedure similar to solid-state synthesis, with the key difference being the addition of a molten salt medium. The medium consisted of a eutectic mixture of NaCl and KCl in a 0.5:0.5 molar ratio, with a salt-to- $\text{Zn}_2\text{SiO}_4$  molar ratio of 3:1. After mixing the stoichiometric amounts of ZnO and  $\text{SiO}_2$  (crystalline or amorphous) with the molten salt medium, the mixture underwent the same homogenization and heat treatment steps as described for solid-state synthesis. A schematic of the molten salt synthesis process is provided in **Fig. 6**.

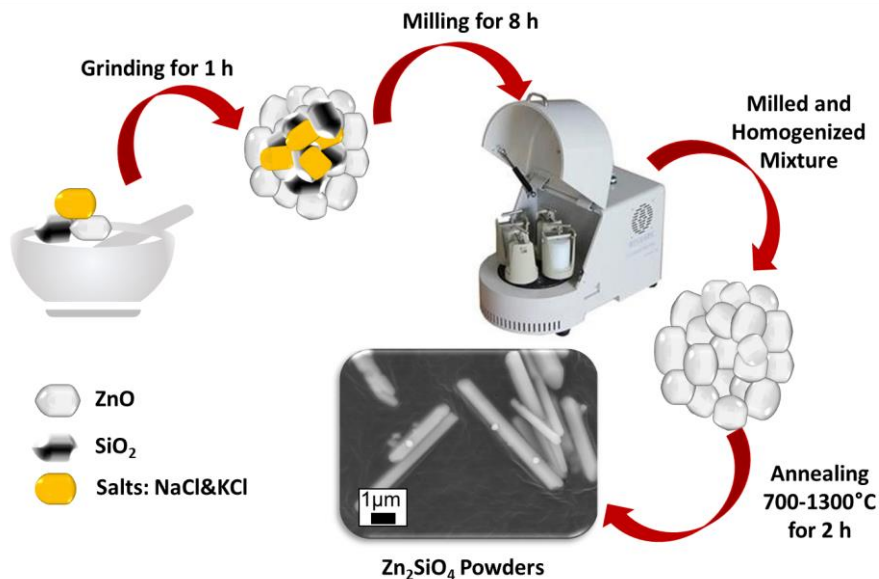


**Fig. 6** Schematic representation of the molten salt synthesis process for  $\text{Zn}_2\text{SiO}_4$ .

### 2.2.1.3 Sol-Gel Synthesis

The sol-gel process involved the partial hydrolysis of TEOS in ethanol and distilled water. Zinc nitrate was dissolved in the pre-hydrolyzed TEOS solution, and the mixture was stirred at room temperature until fully dissolved.

The solution was then heated to 60 °C to accelerate hydrolysis and polycondensation, with nitric acid added as a catalyst. After stirring for an hour, the solution was dried at 85 °C for 24 h to produce a densified powder. The resulting xerogel was heat-treated in air at temperatures ranging from 600 to 1300 °C for 2 h, with a heating rate of 5 °C min<sup>-1</sup>. A schematic of the process is shown in **Fig. 7**.

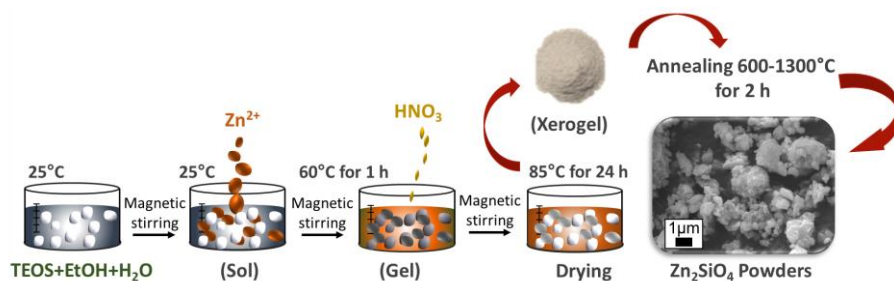


**Fig. 7** Schematic of the sol-gel synthesis process for  $\text{Zn}_2\text{SiO}_4$ .

### 2.2.2 Films Processing

$\text{Zn}_2\text{SiO}_4$  films were synthesized using a screen-printing technique assisted by a molten salt flux. Inks were prepared with varying ZnO concentrations (0.5Zn, 1Zn, 1.5Zn, and 2Zn), incorporating a 0.5NaCl-0.5KCl eutectic mixture (3:1 ratio to ZnO) and an organic vehicle (**Section 2.1.4**). The mixture was homogenized via planetary ball milling for 8 h and further processed in a three-roll mill (Dermamill 100SP Ointment Mill), repeated three times for optimal consistency. The ink was screen-printed onto single-side polished quartz single-crystal substrates and dried using a multi-step procedure. Final thermal treatments were conducted at 1100 and 1200 °C in air for 4 h. A schematic of the process is shown in **Fig. 8**.

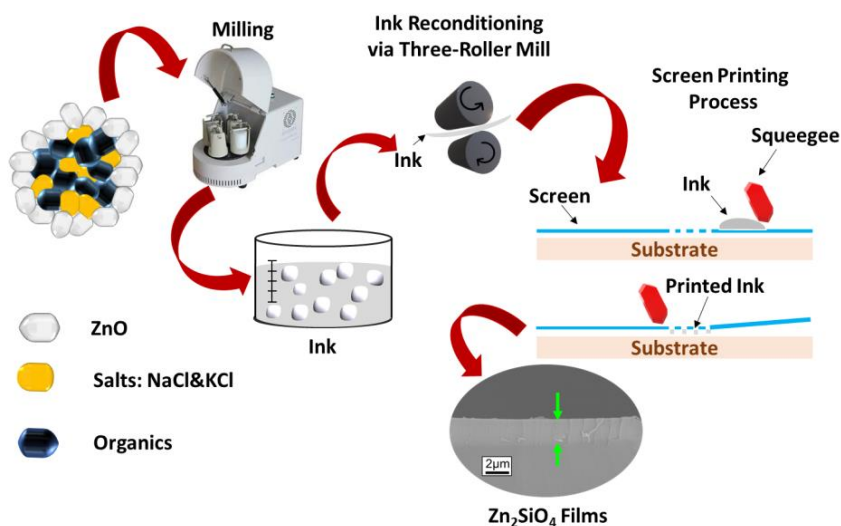


**Fig. 8** Schematic of the screen-printing assisted by molten salt process for  $\text{Zn}_2\text{SiO}_4$  films.

### 2.2.3 Bulk Processing

Bulk  $\text{Zn}_2\text{SiO}_4$  materials were processed through powder synthesis followed by sintering using two distinct methods: conventional sintering (CS) and SPS. For powder synthesis, a mixture of ZnO and amorphous silica was ball-milled in ethanol for 8 h, dried at 60 °C for 10 h, and calcined at 1100 °C for 2 h. The calcined powders were then subjected to an additional 8 h milling session to ensure homogeneity.

For CS, the calcined powders were pressed into disks under approximately 300 MPa for 5 min and sintered at 1300 °C for 4 h to achieve dense ceramics.

For SPS, the powder mixture was pre-shaped into green bodies by pressing at 100 MPa and sintered in a commercial SPS system (Type KCE-FCT HP D 10 BG, FCT Systeme GmbH, Frankenblick, Germany) at 1300 °C under a uniaxial pressure of 75 MPa and a dwell time of 20 min in vacuum conditions.

## **2.3 Characterization Methods**

### **2.3.1 Thermoanalysis**

Thermogravimetric analysis (TGA) and differential scanning calorimetry (DSC) were performed using a Perkin-Elmer DSC-7 calorimeter under an air atmosphere, with a heating rate of 10 °C min<sup>-1</sup> from room temperature to 1200 °C. These techniques were employed to study the thermal stability, decomposition behaviour, and phase transitions of the synthesized materials.

### **2.3.2 Structural and Microstructural Characterization**

The structure, phase composition, and microstructure of the synthesized materials were analyzed using complementary techniques.

X-ray diffraction (XRD) (Rigaku SmartLab SE) with a D/teX Ultra 250 1D detector was employed for phase analysis at room temperature, providing insights into crystallinity and phase purity. For powders prepared by sol-gel synthesis, in-situ high-temperature XRD (HT-XRD) was conducted using an HTK1200N Anton Paar oven chamber to monitor phase evolution under thermal treatment.

Raman spectroscopy was performed using a Horiba LabRAM HR800 system with a 532 nm Nd-YAG laser to identify vibrational modes and confirm phase composition. For films, confocal Raman microscopy was utilized with a WITEC Alpha 300R system, equipped with a 100x objective lens (NA = 0.9) and 0.5 mW laser power, enabling high-resolution spatial mapping of phase transformations and chemical interactions at the film-substrate interface. The system provided a resolution of 200 nm laterally and 500 nm vertically, with spectra processed using Witec Control Plus software.

Microstructural and morphological features were examined using a field emission scanning electron microscope (FE-SEM, Zeiss ULTRA-55), allowing for detailed analysis of particle size, shape, and surface morphology.

### **2.3.3 Luminescent Characterization**

Luminescent properties of rare-earth-free Zn<sub>2</sub>SiO<sub>4</sub> materials were investigated using three complementary techniques: X-ray-excited optical luminescence (XEOL), cathodoluminescence (CL), and synchrotron-excited photoluminescence (PL) (**Fig. 9**).

These techniques were selected to comprehensively characterize the emission properties of the materials, providing insights into their optical behaviour across different excitation energies, penetration depths, and temperature conditions.

XEOL measurements were performed at room temperature using an Edinburgh Instruments FLS980 spectrometer equipped with a Hamamatsu R298P photomultiplier. X-rays were generated using a Neptune 5200 X-ray tube (Oxford Instruments) operating at voltages ranging from 10 to 50 kV. XEOL is particularly useful for studying materials that convert absorbed X-ray energy into light in the optical region (UV to NIR), offering insights into both surface and bulk luminescent properties due to its greater penetration depth compared to other techniques.

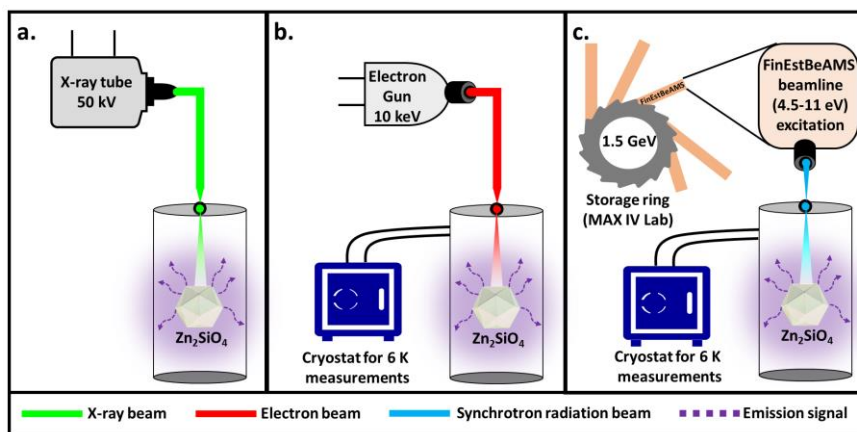


**Fig. 9** Luminescence characterization setups: **(a)** XEOL, **(b)** CL, and **(c)** synchrotron-excited PL under synchrotron radiation excitation.

CL analysis was conducted using an electron gun (Kimball Physics EGG-3101) producing an electron beam with an energy of 10 keV. Emission spectra were recorded through an ARC Spectra Pro 2300i monochromator equipped with a Hamamatsu photon-counting head H8259. Low-temperature measurements were enabled by an ARS closed-cycle helium cryostat. CL provided detailed information on luminescence properties and defect-related emissions under controlled temperature conditions, complementing the XEOL results with its intermediate penetration depth.

Synchrotron-excited PL was conducted at the FinEstBeAMS beamline, MAX IV Lab, Lund, Sweden. This technique allowed for precise control over excitation energy, enabling the study of excitation mechanisms and the origin of observed emission bands. Luminescence was detected using an Andor Shamrock SR-303i spectrometer equipped with a Hamamatsu H8259-01 photon-counting head. To minimize the effects of higher-order incident light,  $\text{MgF}_2$  or fused silica filters were used depending on the excitation energy range. Excitation spectra were normalized to the incident photon flux, and emission spectra were transformed into energy space using the Jacobian transformation procedure.

Together, XEOL, CL, and synchrotron-excited PL provided a comprehensive understanding of the luminescent properties of  $\text{Zn}_2\text{SiO}_4$ , combining insights into emission mechanisms, excitation processes, and depth-dependent behaviour.

### 3 Results and Discussion

The comparative analysis of  $\text{Zn}_2\text{SiO}_4$  synthesis methods reveals distinct strategies for tailoring both structural and luminescent properties. This chapter examines how precursor selection, synthesis conditions, and material form (powders, films, and consolidated specimens) influence phase evolution and deep UV emission characteristics, establishing fundamental correlations for developing rare-earth-free UV phosphors.

This chapter is organized into three sections based on material form:

- $\text{Zn}_2\text{SiO}_4$  powders: Investigating synthesis-dependent properties through solid-state, molten salt, and sol-gel methods.
- $\text{Zn}_2\text{SiO}_4$  films: Developing screen-printing assisted by molten salt strategy for direct film fabrication.
- Consolidated  $\text{Zn}_2\text{SiO}_4$ : Comparing conventional and spark plasma sintering approaches.

Each section provides a detailed examination of phase evolution, structural development, morphological characteristics, and luminescent properties, demonstrating clear correlations between processing conditions and final material performance for each form of  $\text{Zn}_2\text{SiO}_4$ .

#### 3.1 $\text{Zn}_2\text{SiO}_4$ Powders: Synthesis Methods, Structural and Microstructural Evolution, and Luminescence Response

$\text{Zn}_2\text{SiO}_4$  powders were synthesized using solid-state reaction, sol-gel, and molten salt methods, each offering specific advantages. The solid-state method serves as a baseline, highlighting the challenges of high-temperature diffusion. In contrast, the sol-gel process allows for lower-temperature synthesis with fine, homogeneous powders, while molten salt synthesis reduces the reaction onset temperature, enhancing precursor diffusion.

To understand how these different synthesis approaches influence deep UV emission properties, this section presents our findings on  $\text{Zn}_2\text{SiO}_4$  powders in three parts: First, analysis of synthesis-dependent phase evolution and formation mechanisms. Second, examination of the resulting morphological features across different preparation methods. Finally, investigation of luminescent properties through complementary spectroscopic techniques, establishing structure-property relationships crucial for deep UV emission.

##### 3.1.1 Thermal Analysis

Understanding the formation mechanisms of  $\text{Zn}_2\text{SiO}_4$  through different synthesis routes requires detailed analysis of thermal behaviour and precursor reactivity. While conventional solid-state reactions are well-established, requiring temperatures above 800 °C due to limited diffusion between ZnO and  $\text{SiO}_2$  (Synkiewicz-Musialska et al., 2020), alternative routes such as molten salt and sol-gel synthesis may offer distinct transformation mechanisms. Thermal analysis provides crucial insights into these mechanisms, particularly for the previously unexplored molten salt synthesis of undoped  $\text{Zn}_2\text{SiO}_4$ .

The DSC-TG-DTG curves (**Fig. 10**) reveal distinct thermal evolution profiles for the alternative synthesis methods. In molten salt synthesis, the formation of a NaCl-KCl eutectic liquid phase at 662 °C (Rojas-Hernandez et al., 2015) fundamentally transforms the reaction mechanism from solid-state diffusion to liquid-phase-assisted transport.

The samples synthesized using amorphous silica precursor exhibit a higher mass loss (49%) compared to those with crystalline silica (47%) between 25–1053 °C, indicating enhanced reactivity of the amorphous silica in the reaction medium, which directly influences the subsequent phase formation process.

The impact of precursor reactivity on phase evolution is particularly evident in the crystallization behaviour. With amorphous silica, the enhanced reactivity facilitates  $\beta$ - $\text{Zn}_2\text{SiO}_4$  formation at 765 °C before transforming to  $\alpha$ - $\text{Zn}_2\text{SiO}_4$  at 830 °C. In contrast, crystalline silica-based synthesis proceeds directly to  $\alpha$ - $\text{Zn}_2\text{SiO}_4$  formation at 822 °C. This variation in crystallization temperature and phase transformation sequence demonstrates how the precursor's intrinsic nature and corresponding chemical environment fundamentally influence the thermodynamically favourable formation of different polymorphs. The complete salt evaporation is indicated by broad DTG peaks at 1020 °C (amorphous) and 1053 °C (crystalline) (Rojas-Hernandez et al., 2015), reflecting these distinct reaction dynamics.

Sol-gel synthesis reveals complementary aspects of precursor interactions during  $\text{Zn}_2\text{SiO}_4$  formation. The process shows a systematic mass reduction of 48% between 25–600 °C, proceeding through four sequential thermal events: hydration water removal (133 °C), organic decomposition (220 °C), nitrate elimination (302 °C), and ZnO crystallization (395 °C). These sequential decomposition steps create specific chemical conditions for  $\text{Zn}_2\text{SiO}_4$  crystallization at 785 °C, intermediate between the formation temperatures observed in molten salt synthesis.

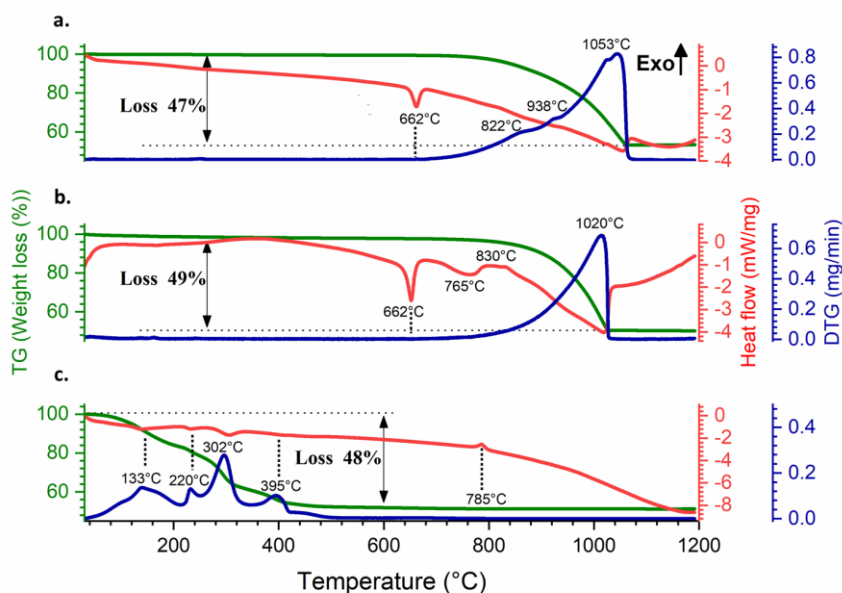


**Fig. 10** Comparative thermal analysis of  $\text{Zn}_2\text{SiO}_4$  formation: molten salt synthesis using (a) crystalline and (b) amorphous silica precursors, and (c) sol-gel route (TGA: green; DSC: red; DTG: blue).

The comparative thermal analysis establishes clear correlations between synthesis method, precursor characteristics, and formation mechanisms. The molten salt synthesis with amorphous silica achieves the lowest formation temperature (765 °C) through enhanced precursor mobility in the liquid phase, while sol-gel processing enables phase formation at intermediate temperatures (785 °C) through sequential precursor



decomposition. Both methods demonstrate enhanced thermal efficiency over conventional solid-state reactions, evidenced by lower formation temperatures and controlled reaction mechanisms. These fundamental differences in thermal behaviour influence the material's structural evolution and phase composition, as will be examined through XRD and Raman analyses in the following sections.

### 3.1.2 Phase Evolution and Formation Mechanisms

Following the thermal analysis findings, complementary XRD and Raman spectroscopy investigations (**Figs. 11-13**) reveal the phase evolution and formation mechanisms in  $\text{Zn}_2\text{SiO}_4$ . These analyses demonstrate how synthesis routes and processing conditions influence phase development across different preparation methods.

In solid-state synthesis (**Fig. 11**), phase evolution is strongly influenced by temperature and precursor reactivity.

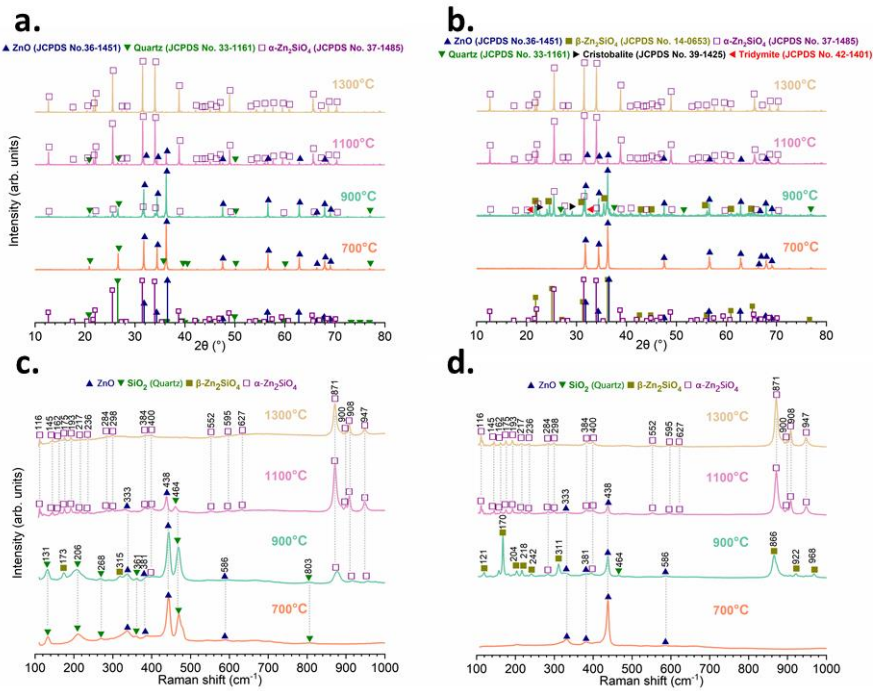


**Fig. 11** Phase composition and structural evolution of  $\text{Zn}_2\text{SiO}_4$  via solid-state synthesis: XRD data using (a) crystalline and (b) amorphous silica, with corresponding Raman spectra (c, d) at different temperatures.

At 700 °C, XRD results reveal primarily unreacted components. The crystalline silica-based samples show quartz reflections (JCPDS No. 33-1161) with the main peak at  $26.64^\circ$  attributed to (101) plane, alongside wurtzite-structured ZnO phase (JCPDS No. 36-1451) with main reflections at  $31.77^\circ$ ,  $34.43^\circ$ , and  $36.24^\circ$  corresponding to (100), (002), and (101) planes, respectively, while amorphous silica-based samples exhibit only ZnO diffraction peaks. Raman spectroscopy confirms this initial state with characteristic ZnO modes ( $E_2^{\text{high}} - E_2^{\text{low}}$  at  $333 \text{ cm}^{-1}$ ,  $A_1(\text{TO})$  at  $381 \text{ cm}^{-1}$ ,  $E_2^{\text{high}}$  at  $438 \text{ cm}^{-1}$ , and  $E_1(\text{LO})$  at  $586 \text{ cm}^{-1}$  (Cuscó et al., 2007)) and additional quartz vibrations at 131, 206, 268, 361, 464, and  $803 \text{ cm}^{-1}$  assigned to the  $E(\text{TO} + \text{LO})$ ,  $A_1$ ,  $E(\text{TO} + \text{LO})$ ,  $A_1$ ,  $E(\text{TO})$ , and  $E(\text{LO})$

modes, respectively, in crystalline samples (Scott & Porto, 1967). By 900 °C, the precursor type critically influences phase transformation. Amorphous silica enables the concurrent formation of rhombohedral  $\alpha$ -Zn<sub>2</sub>SiO<sub>4</sub> (space group R-3, JCPDS No. 37-1485) with main reflections at 25.54°, 31.65°, and 34.12° corresponding to (200), (113), and (410) planes, alongside orthorhombic  $\beta$ -Zn<sub>2</sub>SiO<sub>4</sub> (JCPDS No. 014-0653) with characteristic peaks at 21.88°, 24.89°, and 36.24° attributed to (202), (009), and (023) planes, respectively. The phase identification is further confirmed by Raman spectroscopy, where  $\beta$ -Zn<sub>2</sub>SiO<sub>4</sub> exhibits characteristic vibrational mode at 865, 922, and 965 cm<sup>-1</sup> (Loiko et al., 2018), while  $\alpha$ -Zn<sub>2</sub>SiO<sub>4</sub> shows distinctive peaks at 871 cm<sup>-1</sup> (Si-O( $\nu_1$ ) symmetric stretching), 908 and 948 cm<sup>-1</sup> (Si-O( $\nu_2$ ) asymmetric stretching) (Czaja et al., 2021). In contrast, crystalline silica yields primarily the  $\alpha$ -phase with residual precursors. At higher temperatures (1100-1300°C), both systems lead to the predominant formation of  $\alpha$ -Zn<sub>2</sub>SiO<sub>4</sub>, with more complete transformation in amorphous silica-based samples. More detailed analysis of these structural properties can be found in **paper 1**.

The introduction of a molten salt medium significantly alters Zn<sub>2</sub>SiO<sub>4</sub> formation dynamics. **Fig. 12** shows that at 700 °C, shortly after the NaCl-KCl eutectic melting at 662 °C, both systems exhibit early crystallization of  $\alpha$ - and  $\beta$ -Zn<sub>2</sub>SiO<sub>4</sub> phases, alongside NaCl (JCPDS No. 78-0751) and KCl (JCPDS No. 41-1476). This enhanced reactivity results from the liquid phase-assisted transport of ions, enabling Zn<sub>2</sub>SiO<sub>4</sub> formation at temperatures significantly lower than in solid-state synthesis.

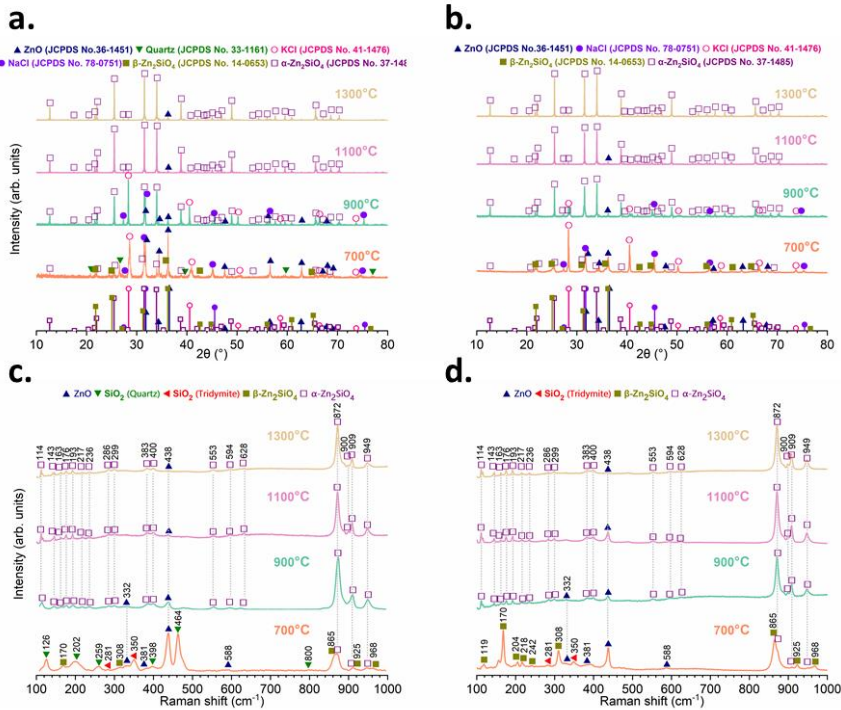


**Fig. 12** Phase composition and structural evolution of Zn<sub>2</sub>SiO<sub>4</sub> via molten salt synthesis: XRD data using (a) crystalline and (b) amorphous silica, with corresponding Raman spectra (c, d) at different temperatures.

The influence of precursor type becomes evident in the phase distribution, with amorphous silica promoting higher  $\beta$ - $\text{Zn}_2\text{SiO}_4$  content, confirmed by XRD reflections and Raman peaks at 865, 922, and 968  $\text{cm}^{-1}$ . In contrast, crystalline silica samples show a more complex phase mixture, including the formation of silica polymorph tridymite for, suggesting phase evolution depending on the initial silica precursor. By 900  $^{\circ}\text{C}$ ,  $\alpha$ - $\text{Zn}_2\text{SiO}_4$  becomes dominant in both systems, with amorphous silica-based samples showing notably reduced ZnO content. The progressive disappearance of salt-related peaks with increasing temperature confirms the transient nature of the molten salt medium. For a more detailed exploration of these findings, refer to **paper 2**.

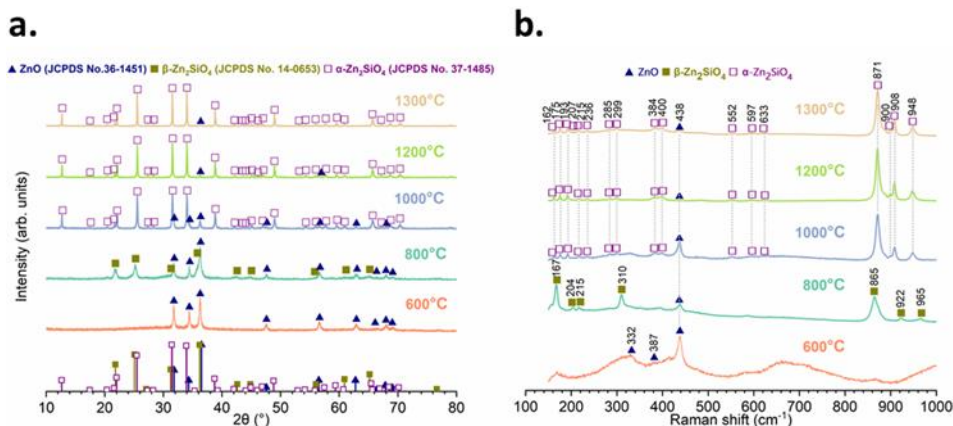


**Fig. 13** Structural and phase evolution of  $\text{Zn}_2\text{SiO}_4$  via sol-gel synthesis: **(a)** XRD data and **(b)** Raman spectra at different temperatures.

Sol-gel processing demonstrates a distinct phase evolution characteristic, as evidenced by complementary XRD and Raman analyses (**Figs. 13**). XRD data (**Fig. 13a**) at 600  $^{\circ}\text{C}$  reveal primarily ZnO reflections with an amorphous background, while corresponding Raman spectra (**Fig. 13b**) confirm this through characteristic ZnO modes at 332, 381, 438 and 588  $\text{cm}^{-1}$ . A significant phase transformation occurs at 800  $^{\circ}\text{C}$  with the emergence of  $\beta$ - $\text{Zn}_2\text{SiO}_4$ , clearly visible in both XRD reflections and corresponding Raman peaks. This preferential formation of the  $\beta$ -phase at intermediate temperatures distinguishes sol-gel synthesis from both solid-state and molten salt routes, suggesting unique nucleation and growth mechanisms enabled by homogeneous precursor distribution.

The progression to higher temperatures, monitored by both techniques, shows systematic evolution toward  $\alpha$ - $\text{Zn}_2\text{SiO}_4$ , with increasing crystallinity and minimal residual ZnO content at 1300  $^{\circ}\text{C}$ . Further details on these structural properties are available in **paper 3**.

The formation mechanisms across these synthesis routes reveal distinct reaction sequences and kinetic processes for  $\text{Zn}_2\text{SiO}_4$  development (**Fig. 14**). In conventional solid-state synthesis, the reaction proceeds through interfacial diffusion between ZnO and  $\text{SiO}_2$  particles, requiring elevated thermal energy owing to diffusion-limited kinetics. The enhanced reactivity of amorphous silica stems from its disordered atomic structure, providing more accessible reaction sites and reduced activation energies for atomic migration. The molten salt medium creates a distinct reaction environment, where the liquid phase facilitates cation transport and reduces activation energies at reactant interface. The eutectic melt functions as both a flux and a reactive medium, enabling

enhanced mass transport and phase formation at reduced temperatures. This mechanism accounts for the early formation of both  $\alpha$ - and  $\beta$ - $\text{Zn}_2\text{SiO}_4$  polymorphs, as the liquid phase increases nucleation sites and facilitates crystallization through improved cationic mobility and interface-driven growth.

## Formation mechanism schematic

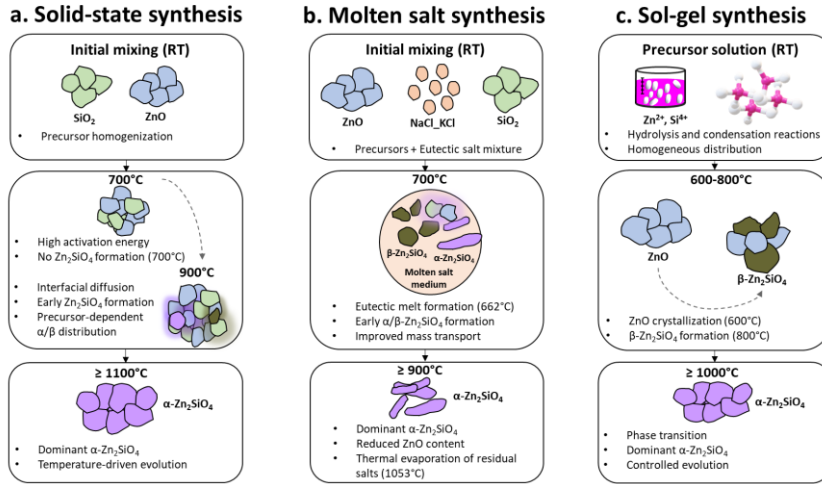


**Fig. 14** Comparative illustration of formation mechanisms for different synthesis routes: **(a)** solid-state synthesis, **(b)** molten salt synthesis, and **(c)** sol-gel synthesis.

Sol-gel processing operates through hydrolysis and condensation reactions, resulting in the dispersion of the precursors within the sol and ensuring intimate contact and uniform composition throughout the gel network. The use of metal alkoxides as precursors promotes the formation  $\beta\text{-Zn}_2\text{SiO}_4$  at comparatively low temperatures, with subsequent transformation to thermodynamically stable  $\alpha$ -phase upon further heating. This systematic phase evolution demonstrates the advantages of solution-based synthesis for achieving controlled crystallization and phase selectivity.

These distinct formation mechanisms directly influence not only phase development but also particle morphology and surface characteristics. The following section examines how these synthesis-dependent processes are reflected in the morphological evolution of  $\text{Zn}_2\text{SiO}_4$ , providing further insights into structure-property relationships that are crucial for its development as a deep UV phosphor.

### 3.1.3 Microstructural Evolution

Microstructural investigations by SEM of  $\text{Zn}_2\text{SiO}_4$  synthesized via different routes reveal how reaction mechanisms fundamentally influence particle development and morphological evolution, providing valuable insights for optimizing structural and microstructural features relevant to deep UV emission applications.

In solid-state synthesis, restricted particle mobility and slow diffusion-controlled reaction kinetics limit the rate of phase formation and yield distinct morphological transformations. **Fig. 15** illustrates the temperature-dependent evolution of particle characteristics. At 700 °C, crystalline silica-based samples exhibit a heterogeneous distribution of smaller  $\text{ZnO}$  and larger  $\text{SiO}_2$  particles, reflecting restricted diffusion between precursors. The onset of  $\text{Zn}_2\text{SiO}_4$  formation at 900°C results in the appearance

of smaller, spherical particles alongside the original precursor morphologies. At 1100 °C, sub-micron  $\alpha$ - $\text{Zn}_2\text{SiO}_4$  particles ( $\leq 800$  nm) adopt a rounded morphology and display a pronounced agglomeration. Further heating to 1300 °C, the particles develop irregular shapes with sharp edges and increase in size, reaching up to 2  $\mu\text{m}$  in diameter. In contrast, synthesis using amorphous silica as precursor exhibits enhanced reactivity and follows a different morphological evolution, owing to the initially uniform spherical morphology of the precursor ( $d \approx 500$  nm). This promotes the early emergence of homogeneous  $\text{Zn}_2\text{SiO}_4$  material at 900 °C, characterized by spherical, discrete and well-dispersed particles. As the temperature increases, these particles tend to aggregate, driven by the thermodynamic tendency to minimize surface free energy, and grow to diameters around 1  $\mu\text{m}$  at 1100 °C. At 1300 °C, significant sintering occurs, leading to interconnected structures with evident necking between particles, particularly in amorphous silica-based samples.

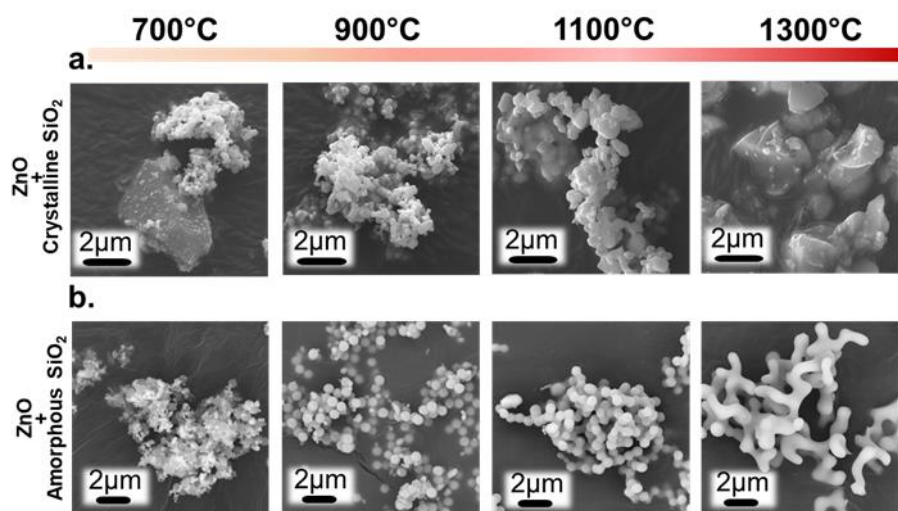


**Fig. 15** Microstructural analysis via low-resolution SEM micrographs of solid-state synthesized  $\text{Zn}_2\text{SiO}_4$ : Morphological evolution using (a) crystalline and (b) amorphous silica (700–1300 °C).

The incorporation of a molten salt medium induces a unique morphological evolution, primarily by improving mass transport and enabling more frequent interactions between  $\text{Zn}^{2+}$  and  $\text{Si}^{4+}$  cations within the liquid phase. As shown in **Fig. 16**, the formation of distinctive rod-like structures occurs following eutectic melting at 662 °C. The dimensions of these rod-like particles exhibit clear precursor dependence: crystalline silica produces structures with lengths of 1.52–10  $\mu\text{m}$  and diameters of 0.37–1.31  $\mu\text{m}$ , while amorphous silica yields more uniform rods (0.72–8.33  $\mu\text{m}$  length, 0.31–0.91  $\mu\text{m}$  diameter). Control experiments with individual components in the molten salt medium elucidate the formation mechanism: ZnO independently develops rod-like features (**Fig. 16f**), while silica shows primarily particle growth (**Fig. 16g**), establishing ZnO's role as a structural template. The schematic in **Fig. 16h** illustrates how the liquid phase facilitates directional growth through enhanced cation diffusion. Notably, amorphous silica-based samples retain their rod-like morphology at elevated temperatures, correlating with their enhanced phase purity observed in XRD analysis.



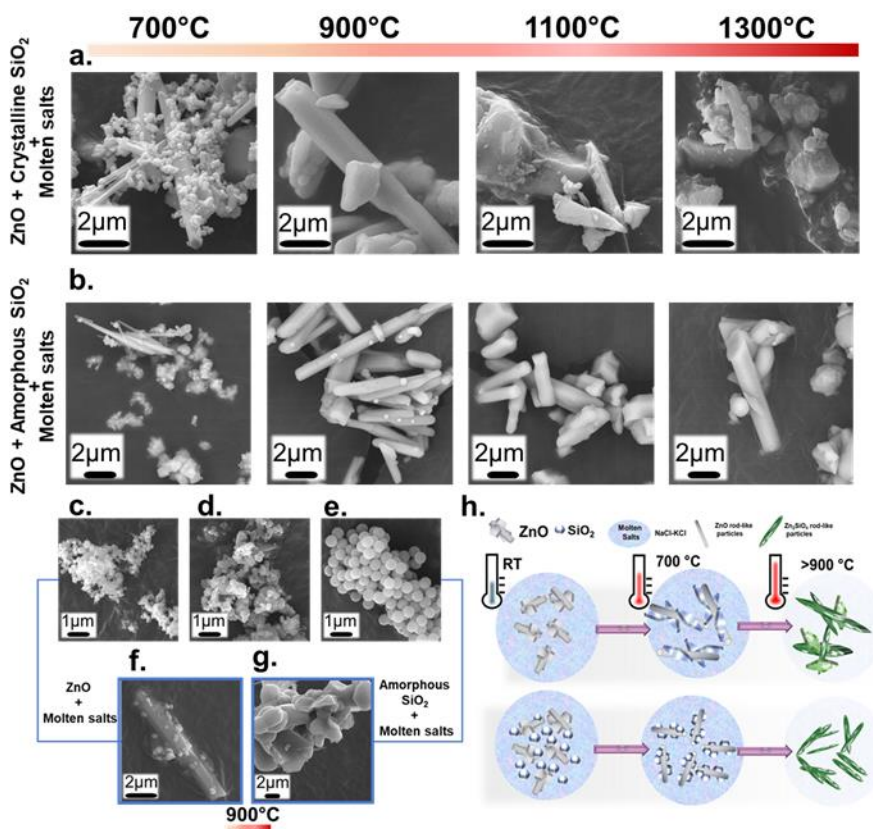


**Fig. 16** Low-resolution microstructural analysis by FE-SEM of molten salt synthesized  $\text{Zn}_2\text{SiO}_4$ : Morphological evolution using (a) crystalline and (b) amorphous silica (700–1300 °C); characterization of precursors: (c) ZnO, (d) crystalline silica, (e) amorphous silica; effect of molten salt treatment at 900 °C on (f) ZnO and (g) amorphous silica; (h) schematic representation of rod formation mechanism.

Sol-gel synthesis demonstrates distinct particle evolution characteristics. **Fig. 17** reveals the temperature-dependent growth: at lower temperatures (600–800 °C), small spherical particles with relatively smooth surfaces form, corresponding to initial ZnO crystallization within an amorphous matrix. The emergence of  $\beta\text{-Zn}_2\text{SiO}_4$  at 800 °C coincides with more defined particle shapes.

As temperature increases, controlled and uniform particle growth occurs, contrasting with the rod-like structures observed in molten salt synthesis and the precursor-dependent features of solid-state reaction. The controlled evolution results from the initial homogeneous reaction between TEOS and metal nitrate precursors, which facilitates the uniform distribution of constituent elements in solution during sol-gel preparation.

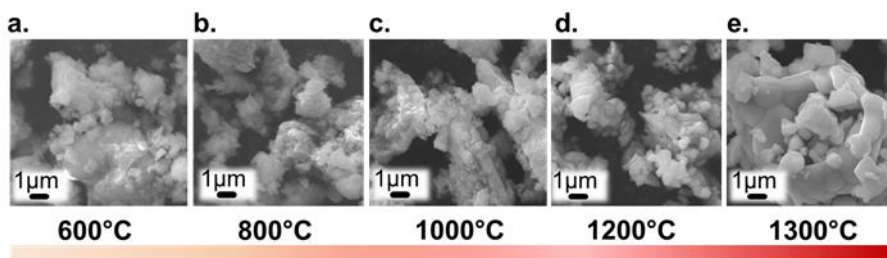


**Fig. 17** Morphological assessment by SEM of sol-gel synthesized  $\text{Zn}_2\text{SiO}_4$ : Growth particle evolution from 600 °C to 1300 °C.

These distinctive morphological developments reflect the specific reaction mechanisms identified through structural analysis: diffusion-controlled growth in solid-state synthesis, template-directed development in molten salt processing, and uniform reaction evolution in sol-gel route. Understanding how these structural and morphological features influence  $\text{Zn}_2\text{SiO}_4$ 's luminescence response is crucial for optimizing its performance as a deep UV emitter.

### 3.1.4 Evaluation of Luminescence Response Via Different Spectroscopic Techniques

The development of sustainable deep UV emitters requires thorough understanding of their luminescence mechanisms. Previous studies of UV-B emission in  $\text{Zn}_2\text{SiO}_4$  have relied primarily on single-technique approaches, limiting mechanistic insights and leaving fundamental questions about emission origins unanswered.

To address this critical gap, a multi-technique spectroscopic approach was applied, combining X-ray excited optical luminescence, cathodoluminescence, and synchrotron-excited photoluminescence. Each technique offers complementary information: XEOL probes bulk luminescent properties through deep X-ray penetration, CL offers surface-sensitive analysis under controlled thermal conditions, and synchrotron-excited PL enables precise investigation of electronic transitions through selective excitation.

This comprehensive methodology directly addresses the research objective of elucidating the underlying nature of deep UV emission in  $\text{Zn}_2\text{SiO}_4$  and reveals correlations between synthesis parameters and luminescent properties. In addition, the findings provide a foundation for understanding deep UV emission mechanisms, essential for the practical development of  $\text{Zn}_2\text{SiO}_4$  in film and consolidated material forms.

#### 3.1.4.1 XEOL Analysis: Initial Evidence of Deep UV Emission

Initial investigation of  $\text{Zn}_2\text{SiO}_4$ 's luminescent properties was conducted through XEOL measurements, providing the first evidence of deep UV emission capability in this material.

**Fig. 18** presents the XEOL spectra recorded at room temperature, illustrating the evolution of luminescent centers during phase formation for each synthesis route.

For solid-state synthesis with crystalline silica (**Fig. 18a**), initial spectra at 700 °C show ZnO-dominated emission with a characteristic near-band-edge transition at 3.19 eV (388 nm) (Baratto et al., 2013), reflecting the predominant presence of unreacted precursors. As temperature increases to 900 °C, multiple emissions emerge:  $\text{Mn}^{2+}$  emission at 2.38 eV (521 nm) from  $^4\text{T}_1 \rightarrow ^6\text{A}_1$  transitions (Rakov et al., 2024) correlates with the initial formation of  $\alpha\text{-Zn}_2\text{SiO}_4$ . This  $\text{Mn}^{2+}$  emission, arising from trace impurities

in the starting materials, appears consistently across all synthesis methods, reflecting the well-known sensitivity of the  $\text{Zn}_2\text{SiO}_4$  structure to Mn incorporation, as demonstrated in commercial green phosphors.

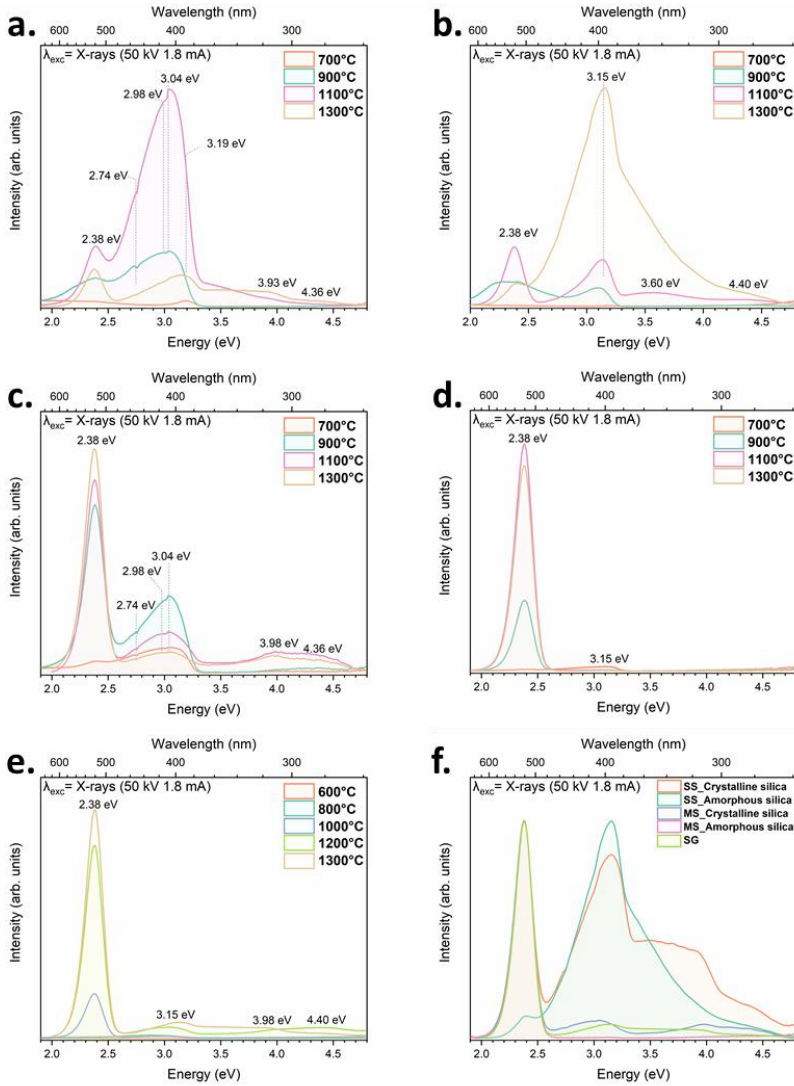


**Fig. 18:** Room temperature XEOL spectra of  $\text{Zn}_2\text{SiO}_4$  synthesized via: solid-state using (a) crystalline and (b) amorphous silica, molten salt using (c) crystalline and (d) amorphous silica, and (e) sol-gel at different temperatures. (f) Normalized spectra comparison of all synthesis routes at 1300 °C.

Additional features include zinc-related defect emissions at 2.74 eV (452 nm) and 2.98 eV (416 nm) (Ahn et al., 2009; Kaur et al., 2018), and silica defect bands at 3.04 eV (408 nm) (Nishikawa et al., 1992). Most significantly, the appearance of weak deep UV transitions at 3.93 eV (315 nm) and 4.36 eV (284 nm) at 1100°C correlates with the dominance of  $\alpha$ - $\text{Zn}_2\text{SiO}_4$  phase identified through XRD and Raman analyses.

Amorphous silica-based samples (Fig. 18b) demonstrate distinctly different behaviour. At 1100 °C, these samples show stronger  $\text{Mn}^{2+}$  emission and a characteristic



band at 3.60 eV (344 nm) from non-bridging oxygen hole centers (He et al., 2003), evolving into a broad emission profile (2.1-4.7 eV) at 1300°C. This enhanced emission development aligns with the improved phase formation kinetics observed with amorphous precursors.

The influence of synthesis method on emission characteristics becomes evident in molten salt and sol-gel routes. Molten salt synthesis (**Fig. 18c,d**) shows accelerated  $\text{Zn}_2\text{SiO}_4$  formation through early  $\text{Mn}^{2+}$  emission at 700 °C, with UV-B emissions (3.93 eV (315 nm) and 4.36 eV (284 nm)) emerging at elevated temperatures alongside typical defect-related features. Sol-gel derived samples (**Fig. 18e**) demonstrate systematic evolution from ZnO-dominated transitions to well-crystallized  $\alpha\text{-Zn}_2\text{SiO}_4$  emission features at higher temperatures.

The normalized spectra comparison at 1300 °C (**Fig. 18f**) reveals synthesis-dependent variations in emission characteristics across all preparation methods. While  $\text{Mn}^{2+}$  emission dominates the room temperature spectra, the consistent observation of weak but distinct deep UV bands across all synthesis routes establishes the fundamental capability of  $\text{Zn}_2\text{SiO}_4$  as a deep UV emitter. These room temperature measurements, however, are influenced by thermal quenching effects, necessitating low-temperature studies to reveal intrinsic emission features.

To gain deeper insights into the emission mechanisms, cathodoluminescence spectroscopy was performed at both room temperature and cryogenic conditions (6 K). This dual-temperature approach, coupled with CL's surface sensitivity, reveals critical aspects of the luminescence response.

#### **3.1.4.2 Room Temperature Cathodoluminescence**

Following the identification of UV-B emission potential through XEOL, selected samples were investigated using cathodoluminescence spectroscopy. Room temperature CL spectra, presented in **Fig. 19**, reveal how synthesis methods fundamentally influence the formation and distribution of emission centers in  $\text{Zn}_2\text{SiO}_4$ .

For solid-state synthesis with crystalline silica, **Fig. 19a** demonstrates the evolution from a dominant emission at 3.11 eV (399 nm) at 1100°C to a broader, shifted band at 3.20 eV (388 nm) at 1300 °C. This spectral evolution reflects the diffusion-limited nature of solid-state reactions, where incomplete phase transformation and structural heterogeneities contribute to emission broadening. The emission spectra of amorphous silica-based samples, displayed in **Fig. 19b**, reveal a more complex electronic structure, with multiple emission bands at 1100 °C including UV-B features, evolving into a broad band centered at 3.15 eV (394 nm) at 1300 °C.

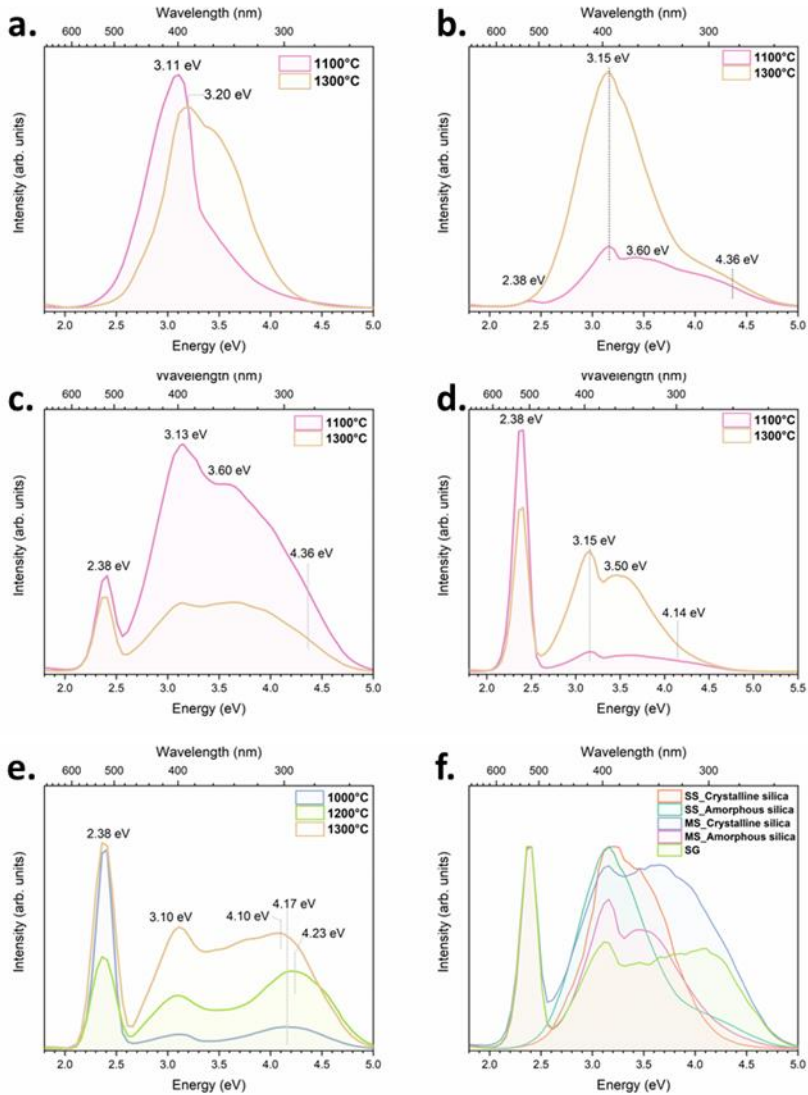


**Fig. 19:** Room temperature CL spectra of  $\text{Zn}_2\text{SiO}_4$  synthesized via: solid-state using (a) crystalline and (b) amorphous silica, molten salt using (c) crystalline and (d) amorphous silica, and (e) sol-gel at different temperatures. (f) Normalized spectra comparison of all synthesis routes at 1300 °C.

The molten salt synthesis, shown in **Fig. 19c** and **19d**, demonstrates distinct emission behaviour based on precursor type. Crystalline silica samples show broad emission features with UV-B contribution, while amorphous silica samples exhibit predominantly  $\text{Mn}^{2+}$  emission with temperature-dependent modifications in emission center distribution.

Sol-gel derived samples display systematic emission behaviour, as shown in **Fig. 19e**. Three main features evolve with temperature:  $\text{Mn}^{2+}$  emission, ZnO-related emission at 3.10 eV (400 nm), and a UV-B band. The UV-B band systematically shifts from 4.17 eV (297 nm) to 4.23 eV (293 nm) to 4.10 eV (302 nm), correlating with the transformation from an initial ZnO-dominated structure to well-crystallized  $\alpha\text{-Zn}_2\text{SiO}_4$ . Significantly,

at 1200 °C, the comparable intensities of  $\text{Mn}^{2+}$  and UV-B emissions suggest an optimal condition for UV-B emission center formation.

The comparative spectra at 1300 °C, presented in **Fig. 19f**, reveal crucial insights into UV-B emission across synthesis methods. The varying spectral distributions and relative intensities of the deep UV bands demonstrate synthesis-dependent emission characteristics, with sol-gel samples showing more resolved UV-B features compared to solid-state and molten salt syntheses.

While room temperature measurements establish the presence of UV-B emission across all synthesis routes, thermal quenching effects may mask intrinsic features. To reveal these fundamental characteristics, low-temperature measurements were performed.

#### 3.1.4.3 Low Temperature Cathodoluminescence

Cathodoluminescence spectra recorded at 6K, presented in **Fig. 20**, reveal remarkably distinct emission profiles for each synthesis route.

Samples prepared with crystalline silica via solid-state synthesis, shown in **Fig. 20a**, exhibit multiple well-resolved emissions at 1100 °C: a weak  $\text{Mn}^{2+}$  band at 2.38 eV (521 nm), silica defect-related transitions at 3.04 eV (408 nm) and 3.60 eV (344 nm), ZnO-related features at 3.22 eV (385 nm) and a sharp peak at 3.31 eV (375 nm) corresponding to excitons bound to neutral donors ( $\text{D}^0\text{X}$ ) in ZnO (Dumcenco et al., 2012), and a prominent UV-B emission at 4.25 eV (292 nm). The 1300 °C treatment leads to broader, less intense features, suggesting thermal modification of these emission centers.

In contrast, amorphous silica-derived samples shown in **Fig. 20b** display a remarkably different emission profile dominated by an intense, well-defined UV-B band at 4.31 eV (288 nm) at 1100 °C, with minimal contribution from other emission centers. The UV-B emission intensity notably decreases at 1300 °C while maintaining its spectral position. This spectral purity correlates with the enhanced phase homogeneity and uniform microstructure achieved through amorphous precursor reactivity.

The molten salt synthesis route demonstrates distinct temperature-dependent behaviour (**Fig. 20c,d**). Crystalline silica-based samples show strong UV-B emission at 4.25 eV (292 nm) at 1100 °C, with significant intensity decrease at 1300 °C, while amorphous silica samples exhibit a blue-shifted UV-B band at 4.31 eV (288 nm) with enhanced intensity retention at elevated temperatures. This behaviour correlates with the uniform rod morphology and improved phase purity previously observed.

Sol-gel derived samples, shown in **Fig. 20e**, demonstrate a remarkable temperature dependence of emission features. The UV-B emission at 4.31 eV (288 nm) shows maximum intensity at 1200°C, alongside  $\text{Mn}^{2+}$  emission at 2.38 eV (521 nm) and ZnO-related emission at 3.16 eV (392 nm). The UV-B emission intensity at 1000 °C and 1300 °C is notably lower but maintains a similar spectral position, suggesting that 1200 °C provides optimal conditions for the formation of deep UV emission centers.

The comparative low-temperature spectra at 1300 °C (**Fig. 20f**) highlight fundamental differences in UV-B emission across synthesis routes. Solid-state synthesis with crystalline silica shows the most complex spectral structure, reflecting multiple radiative processes arising from heterogeneous phase development. In contrast, amorphous silica-based samples from both solid-state and molten salt routes exhibit more resolved UV-B profiles, indicating enhanced emission efficiency. Sol-gel samples achieve a balance between spectral purity and emission intensity, demonstrating the advantages of controlled structural evolution.

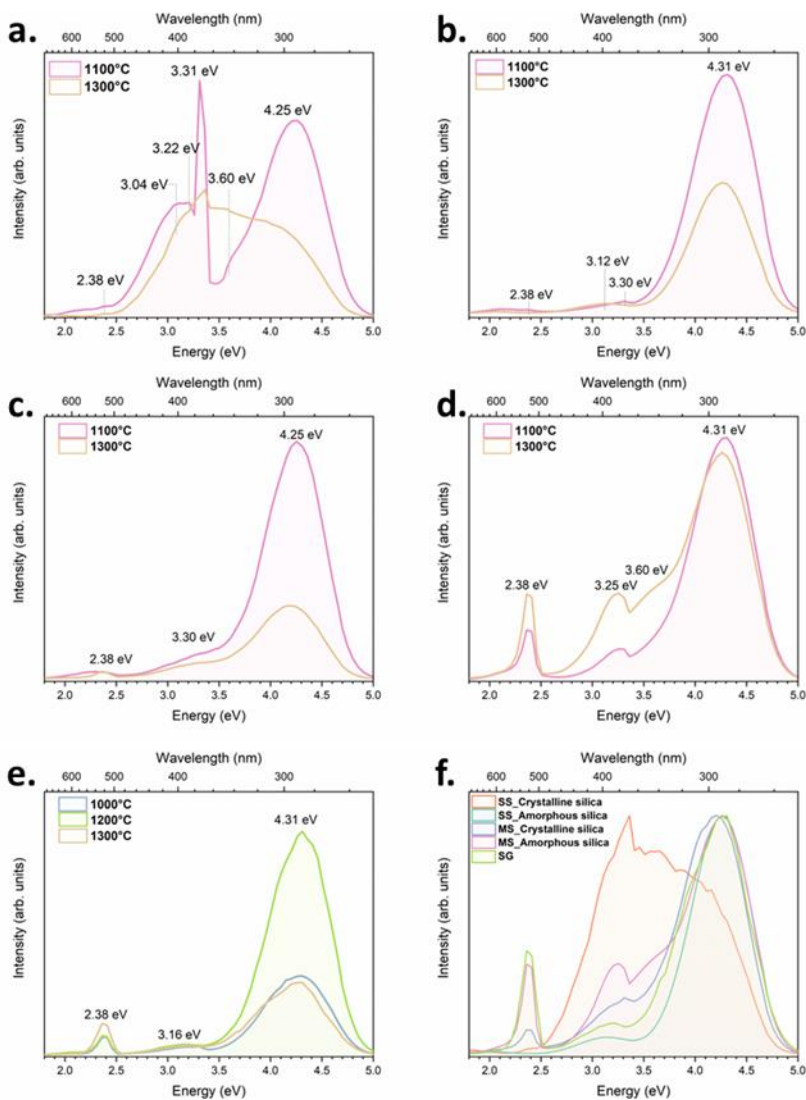


**Fig. 20:** CL spectra at 6 K of  $\text{Zn}_2\text{SiO}_4$  synthesized via: solid-state using (a) crystalline and (b) amorphous silica, molten salt using (c) crystalline and (d) amorphous silica, and (e) sol-gel at different temperatures. (f) Normalized spectra comparison of all synthesis routes at 1300 °C.

A significant finding emerges from these low-temperature investigations: the most intense UV-B emission occurs at intermediate processing temperatures (1100 °C for solid-state and molten salt synthesis, 1200 °C for sol-gel processing). These optimal temperatures do not correspond to conditions yielding maximum phase purity in  $\text{Zn}_2\text{SiO}_4$ .

The concurrent presence of ZnO-related emissions (3.16–3.31 eV) suggests that UV-B emission characteristics are influenced by the complex interplay between phase composition and structural features.

Having established the temperature dependence of UV-B emission through CL studies, precise investigation of the underlying electronic transitions requires selective excitation

capabilities. Synchrotron-excited photoluminescence measurements enable systematic probing of specific electronic states, offering detailed insights into the fundamental mechanisms of UV-B emission.

#### 3.1.4.4 Deep UV Emission Under Synchrotron Excitation

Building on the temperature-dependent behaviour revealed by CL measurements, synchrotron-excited PL studies at 6 K provide deeper insights into the electronic transitions responsible for UV-B emission.

**Fig. 21** presents the emission spectra under selective excitation at 6 eV (207 nm), chosen to probe transitions near the fundamental absorption edge of  $\text{Zn}_2\text{SiO}_4$  (Chang et al., 1999).

The synthesis method significantly influences the emission characteristics. Solid-state synthesis with crystalline silica (**Fig. 21a**) shows a dominant deep UV band at 4.45 eV (279 nm) alongside residual ZnO-related features (3.15-3.31 eV), reflecting complex phase evolution. In contrast, amorphous silica-based samples (**Fig. 21b**) achieve well-resolved UV-B emission at 4.43 eV (280 nm), correlating with improved phase homogeneity.

Molten salt synthesis reveals the impact of liquid-phase transport on electronic transitions (**Fig. 21c,d**). Enhanced cationic mobility in crystalline silica samples enables UV-B emission at 4.39 eV (282 nm) with minimal secondary contributions. Amorphous silica samples exhibit highly resolved emission at 4.43 eV (280 nm), benefiting from the combination of reactive precursor and liquid-phase transport.

Sol-gel derived samples (**Fig. 21e**) display systematic emission behaviour with a well-defined UV-B band at 4.37 eV (284 nm). The emission intensity reaches its maximum at 1200 °C, then decreases significantly at 1300 °C and shows a notably weaker emission at 1000 °C, indicating a narrow processing window for optimal UV-B emission. The evolution of spectral features correlates with the temperature-dependent morphological development observed in microstructural analyses.

The normalized emission spectra comparison at 1300 °C (**Fig. 21f**) reveals systematic variations in UV-B emission energy (4.37–4.45 eV) across synthesis methods, suggesting that processing conditions fundamentally influence the final electronic structure of  $\text{Zn}_2\text{SiO}_4$ . While all methods demonstrate UV-B as the dominant emission, confirming its intrinsic nature, the spectral resolution vary significantly with both synthesis route and precursor type.

While the emission spectra under 6 eV (207 nm) excitation suggest the intrinsic nature of UV-B emission in  $\text{Zn}_2\text{SiO}_4$ , understanding the complete excitation mechanism is crucial for elucidating the emission process.

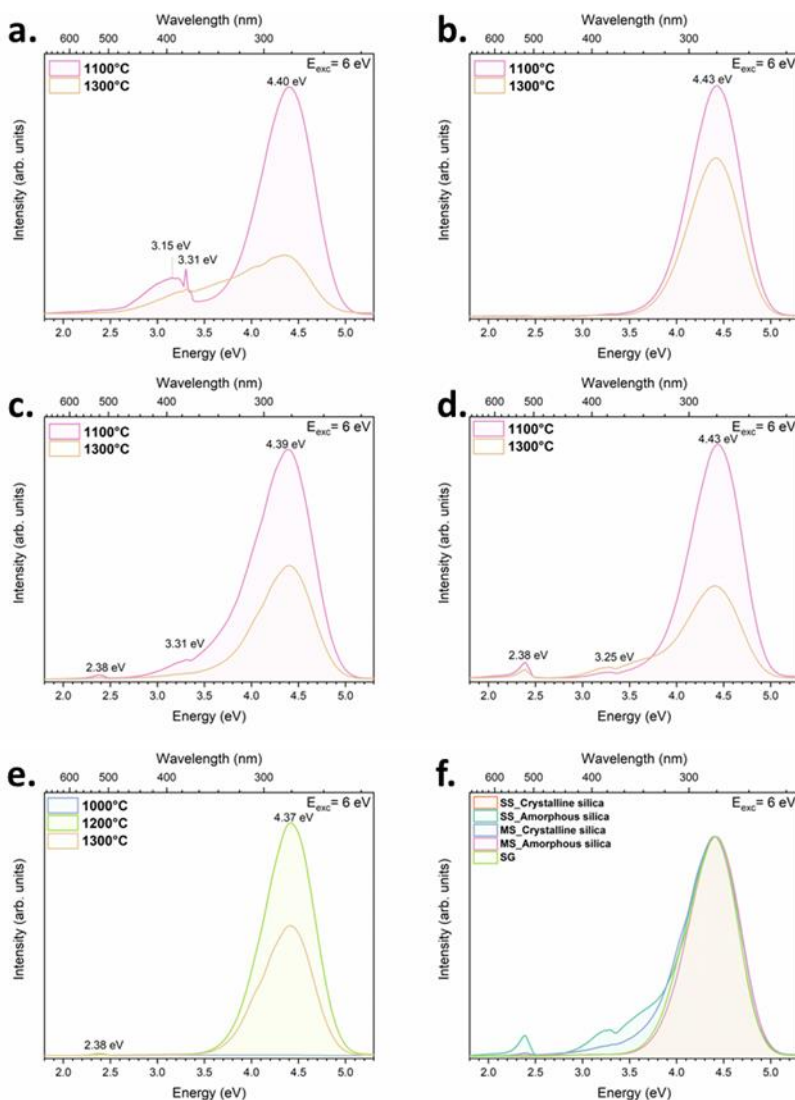


**Fig. 21:** PL spectra under synchrotron excitation at 6 K of  $\text{Zn}_2\text{SiO}_4$  synthesized via: solid-state using (a) crystalline and (b) amorphous silica, molten salt using (c) crystalline and (d) amorphous silica, and (e) sol-gel at different temperatures. (f) Normalized spectra comparison of all synthesis routes at 1300 °C.

### 3.1.4.5 Excitation Mechanisms and Electronic Transitions

The excitation spectra recorded at 6 K for the UV-B emission, presented in Fig. 22, provide fundamental insights into the absorption processes and energy transfer mechanisms in  $\text{Zn}_2\text{SiO}_4$ .

Three characteristic excitation regions are identified: the onset at approximately 6 eV (207 nm) corresponds to the  $\text{Zn}_2\text{SiO}_4$  bandgap, as predicted by partial densities of states (PDOS) calculations (Chang et al., 1999). Features at 7.31 eV (170 nm) and 7.22 eV (172 nm) are attributed to excitation of  $[\text{SiO}_4]^{4-}$  tetrahedral clusters (Hao & Wang, 2007; Kortov et al., 2017; Mishra et al., 1991), while the band at 10.44 eV (119 nm) corresponds to

[ZnO<sub>4</sub>]<sup>6-</sup> cluster excitation (Hao & Wang, 2007; Kortov et al., 2017; Mishra et al., 1991; S. Zhang et al., 2012), both assignments supported by first-principles calculations of the electronic band structure.

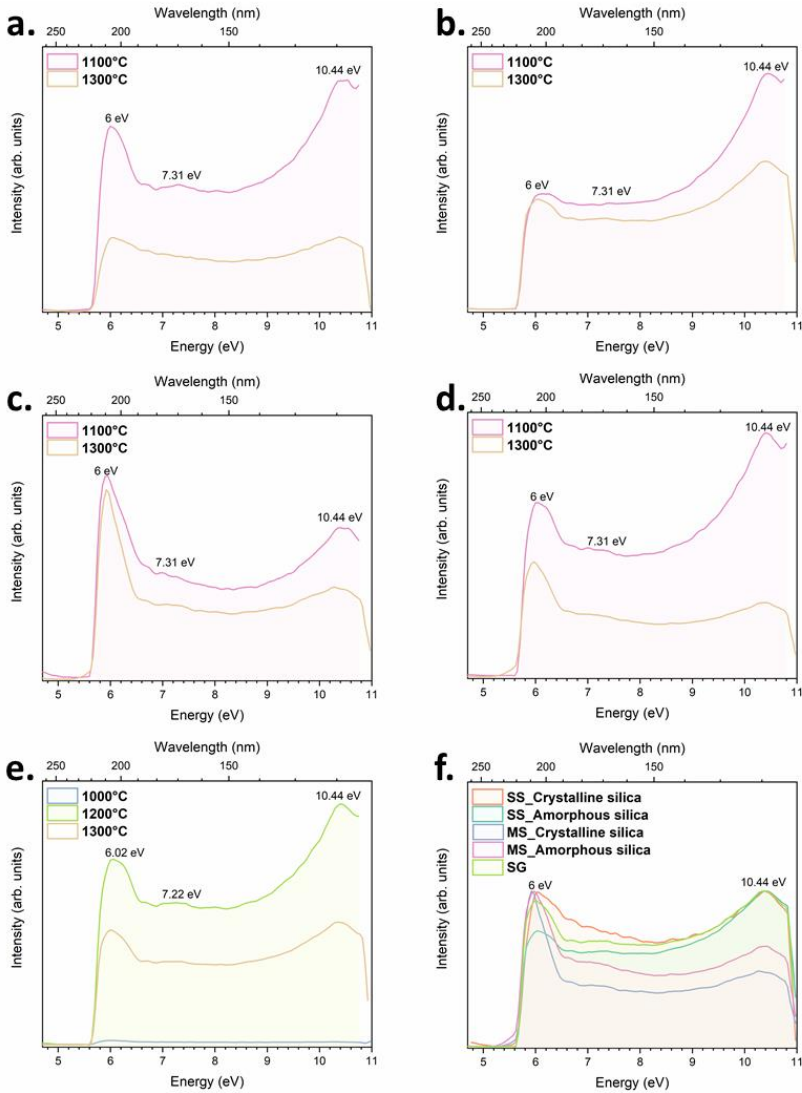


**Fig. 22:** Excitation spectra monitored at UV-B emission at 6 K of Zn<sub>2</sub>SiO<sub>4</sub> synthesized via: solid-state using (a) crystalline and (b) amorphous silica, molten salt using (c) crystalline and (d) amorphous silica, and (e) sol-gel at different temperatures. (f) Normalized spectra comparison of all synthesis routes at 1300 °C.

For solid-state synthesis with crystalline silica (Fig. 22a), these three excitation regions show strong temperature dependence, with features maximizing at 1100 °C before decreasing at 1300 °C. Amorphous silica-based samples (Fig. 22b) demonstrate similar excitation bands but with notably better preservation of features at high temperatures, reflecting the enhanced structural stability achieved through more reactive precursors.

The stronger intensity of the 10.44 eV (119 nm) band in amorphous silica-based samples correlates with their well-resolved UV-B emission profiles.

Molten salt synthesis reveals the influence of liquid-phase transport on excitation features. Crystalline silica-based samples (**Fig. 22c**) show modified  $[\text{ZnO}_4]^{6-}$  cluster excitation intensity distribution compared to solid-state synthesis. Amorphous silica-based samples (**Fig. 22d**) achieve significantly enhanced excitation intensity through the combined effects of precursor reactivity and efficient cation transport, as evidenced by accelerated phase formation and distinct morphological development.

Sol-gel derived samples (**Fig. 22e**) reveal distinct temperature-dependent evolution of excitation features. The excitation spectra show three characteristic regions: the bandgap absorption at 6.02 eV (206 nm),  $[\text{SiO}_4]^{4-}$  excitation at 7.22 eV (172 nm) (slightly shifted from 7.31 eV (170 nm) observed in other synthesis routes), and  $[\text{ZnO}_4]^{6-}$  cluster excitation at 10.44 eV (119 nm). The intensity of these features reaches its maximum at 1200 °C and decreases significantly at both 1000 °C and 1300 °C, demonstrating a narrow temperature window for optimal excitation efficiency. This temperature dependence correlates with the evolution of UV-B emission observed in both CL and PL measurements.

The normalized excitation spectra comparison at 1300 °C (**Fig. 22f**) reveals synthesis-dependent variations in electronic structure across preparation methods. While all samples show the characteristic three-region excitation profile, their relative intensities vary significantly with synthesis route and precursor type. Amorphous silica consistently enables stronger  $[\text{ZnO}_4]^{6-}$  excitation, while sol-gel processing achieves the most uniform feature distribution.

A systematic comparison of synthesis-dependent properties, derived from multiple characterization techniques, is presented in **Table 2**, encompassing phase evolution, morphological development, and luminescence characteristics.

**Table 2:** Synthesis-dependent characteristics of  $\text{Zn}_2\text{SiO}_4$ .

Parameter	Solid-state (crystalline $\text{SiO}_2$ )	Solid-state (amorphous $\text{SiO}_2$ )	Molten salt (crystalline $\text{SiO}_2$ )	Molten salt (amorphous $\text{SiO}_2$ )	Sol-Gel
<b>Phase evolution</b>	700 °C: ZnO+quartz 900 °C: early $\alpha$ > 1100 °C: dominant $\alpha$	700 °C: ZnO 900 °C: early $\alpha+\beta$ >1100 °C: dominant $\alpha$	700 °C: early $\alpha+\beta$ >900 °C: dominant $\alpha$	700 °C: early $\alpha+\beta$ >900 °C: dominant $\alpha$	600 °C: ZnO 800 °C: $\beta$ >1000 °C: dominant $\alpha$
<b>Morphology</b>	700 °C: heterogeneous 900–1100 °C: spherical 1300 °C: sintered	700 °C: heterogeneous 900–1100 °C: spherical 1300 °C: interconnected	700–1100 °C: non-uniform rods 1300 °C: irregular	Uniform rods	600–800 °C: aggregates 1000–1300 °C: gradual growth
<b>RT UV-B resolution</b>	Broad overlap	Shoulder	Shoulder	Shoulder	Most resolved
<b>UV-B energy</b>	4.45 eV	4.43 eV	4.39 eV	4.43 eV	4.37 eV
<b>Optimal T for UV-B</b>	1100 °C	1100 °C	1100 °C	1100 °C	1200 °C
<b><math>[\text{ZnO}_4]^{6-}</math> excitation</b>	Strong	Strong	Moderate	Strong	Strong



The comparative analysis establishes clear correlations between synthesis conditions and material properties, demonstrating the critical influence of precursor selection and processing temperature on both structural and microstructural development, as well as UV-B emission characteristics. These established relationships, combined with comprehensive spectroscopic investigations, provide the foundation for elucidating the fundamental nature of deep UV emission in  $\text{Zn}_2\text{SiO}_4$ .

#### **3.1.4.6 Nature and Origin of Deep UV Emission in $\text{Zn}_2\text{SiO}_4$**

The fundamental nature of UV-B emission in  $\text{Zn}_2\text{SiO}_4$  is established through multiple spectroscopic observations. The excitation onset at 6 eV (207 nm), corresponding to the material's bandgap, indicates direct excitation of the host lattice. This intrinsic character is evidenced by the systematic occurrence of UV-B emission across all synthesis methods, with its enhancement at low temperature where thermal effects are minimized. The characteristic spectral features suggest that the luminescence originates from host excitons, which can exist in the lattice either as self-trapped states or become modified through interaction with structural defects, notably oxygen vacancies, a common phenomenon in wide bandgap oxide materials.

The synchrotron spectroscopy results reveal crucial excitation mechanisms, particularly the strong correlation between  $[\text{ZnO}_4]^{6-}$  cluster excitation at 10.44 eV (119 nm) and UV-B emission efficiency. The systematic variations in excitation band intensities with synthesis conditions reflect modifications in the local environment of emission centers, supporting their host-related nature rather than impurity-related transitions.

The synthesis-dependent emission energies (4.37–4.45 eV) and varying excitation efficiencies can be understood through the different structural development processes.

Notably, amorphous silica-based synthesis achieves enhanced performance through improved phase formation kinetics and structural uniformity, as evidenced by stronger  $[\text{ZnO}_4]^{6-}$  excitation and more stable UV-B emission.

The spectroscopic observations suggest a possible mechanism for deep UV emission in  $\text{Zn}_2\text{SiO}_4$ :

1. Initial excitation creates host excitons following bandgap absorption at 6 eV.
2. These excitons can become self-trapped in the lattice or interact with structural defects, particularly oxygen vacancies.
3. The strong correlation with  $[\text{ZnO}_4]^{6-}$  excitation suggests these tetrahedral units play a key role in localizing the excited states.
4. Radiative recombination of these localized excitons results in deep UV emission, with energies modulated by the local structural environment (4.37–4.45 eV).

However, confirmation of this proposed mechanism would require additional spectroscopic and structural investigations to fully elucidate the detailed energy transfer processes and the role of local environments in the emission mechanism.

These findings have significant implications for the development of  $\text{Zn}_2\text{SiO}_4$  as a sustainable deep UV emitter. The identification of host excitons as the source of UV-B emission, rather than impurity or defect-related transitions, establishes  $\text{Zn}_2\text{SiO}_4$  as an intrinsic UV-B phosphor. This characteristic is particularly valuable as it eliminates the need for rare-earth dopants or other critical materials typically required for deep UV emission.

The understanding that emission properties can be modulated through synthesis conditions provides clear strategies for material optimization. The correlation between structural development and emission efficiency suggests that synthesis methods promoting uniform phase formation and controlled structural evolution, such as those

achieved through amorphous precursors or solution-based processing, offer advantages for enhancing UV-B emission. Moreover, the identification of optimal processing temperatures for each synthesis method establishes practical guidelines for material preparation.

Building on these fundamental insights from powder studies, the next section examines the translation of these principles to film fabrication.

### **3.2 Innovative Fabrication: Controlled Synthesis of $\text{Zn}_2\text{SiO}_4$ Films via Screen-Printing Assisted by Molten Salt Strategy**

While powder studies established the potential of  $\text{Zn}_2\text{SiO}_4$  as a deep UV emitter, practical technological applications require film architectures with precise structural control.

Conventional film deposition methods, such as RF magnetron sputtering, face limitations in complexity, energy consumption, and scalability (Furukawa et al., 2015). Moreover, these techniques often yield inconsistent UV emission results (K.-C. Peng et al., 2013), underscoring the need for more reliable and practical fabrication approaches.

This study introduces an innovative strategy that combines screen printing assisted by molten salt strategy. Screen printing offers inherent advantages as a solution-based technique, enabling straightforward fabrication under ambient conditions (Kuo et al., 2016; Rojas-Hernandez et al., 2020; Yao et al., 2016). The integration of molten salt media, previously demonstrated in powder synthesis, enhances mass transport and controls crystallization, addressing key challenges in film fabrication.

#### **3.2.1 Structural and Interface Dynamics: Phase Transformation and Morphological Evolution**

The synthesis strategy systematically investigated composition-temperature relationships using four ZnO concentrations (0.5-2Zn) relative to stoichiometric  $\text{Zn}_2\text{SiO}_4$ , processed at 1100 °C and 1200 °C. XRD analysis, as shown in **Fig. 23a** and **Fig. 23b**, demonstrated efficient  $\text{Zn}_2\text{SiO}_4$  crystallization across all compositions, with trace ZnO detected only in zinc-rich samples. This confirms the effectiveness of the molten salt medium in promoting phase formation in films.

A distinctive feature of the films was the pronounced preferential orientation along the (300) crystallographic plane. This texturing, quantified through Lotgering factor analysis (Lotgering, 1959) (**Figs. 23c** and **23d**), showed strong dependence on both composition and processing temperature. At 1100 °C, LF values demonstrated remarkable optimization: 0.47 (0.5Zn), 0.94 (1Zn), 0.83 (1.5Zn), and 0.29 (2Zn). The exceptional texturing in 1Zn samples suggests optimal epitaxial matching between the growing film and substrate surface.

Processing at 1200 °C produced a distinct evolution pattern, with LF values converging across compositions (0.76–0.64). This behaviour suggests a transition from interface-controlled growth at 1100 °C to bulk diffusion-dominated processes at higher temperatures, where enhanced atomic mobility reduces the influence of local composition variations.

Depth-resolved Raman spectroscopy identified three distinct phases:  $\text{Zn}_2\text{SiO}_4$ , cristobalite, and the quartz substrate.

The interface structure showed systematic evolution with both composition and temperature, as illustrated in **Figs. 24a-d** and **25a-d**, enabling precise control over film properties.

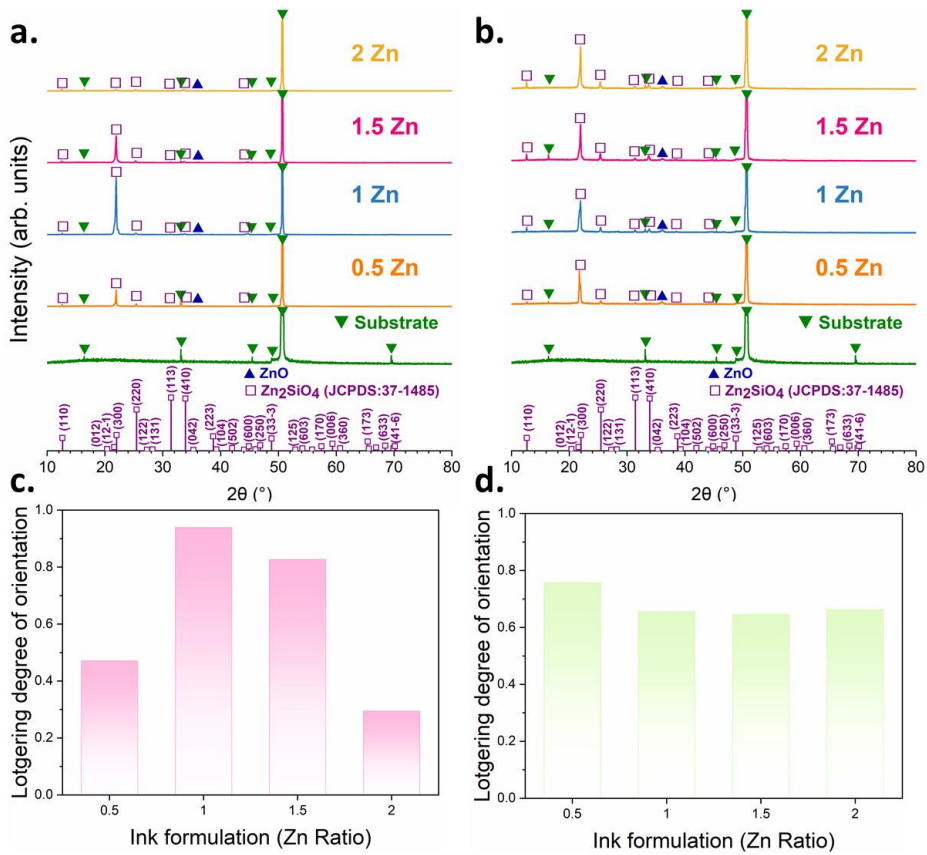


**Fig. 23:** Structural and phase evolution of  $\text{Zn}_2\text{SiO}_4$  films for different ZnO concentrations (0.5Zn, 1Zn, 1.5Zn, and 2Zn) processed at 1100°C (a,c) and 1200°C (b,d): XRD data (a,b) and Lotgering factor analysis (c,d).

At 1100 °C, the interface evolution demonstrated a complex interplay between salt-mediated phase transformation and direct  $\text{Zn}_2\text{SiO}_4$  formation. The emergence of cristobalite in 1Zn films and its development into a continuous interlayer in 1.5Zn samples reflects the increasing effectiveness of the salt-mediated transformation (W. Li et al., 2021).

This transformation is facilitated by the alkali ions in the molten salt, which weaken Si-O bonds in the quartz, promoting the reorganization of  $\text{SiO}_4$  tetrahedra necessary for cristobalite formation (W. Li et al., 2021).

SEM analysis revealed systematic evolution of surface morphology correlating with these interface dynamics. **Figs. 24e-l** and **25e-l** show distinct morphological regimes, with 1Zn films at 1100 °C displaying well-defined prismatic structures corresponding to maximum texturing (LF = 0.94). The 1.5Zn films exhibited a transition to ovoid-prismatic morphologies, indicating the onset of competing growth mechanisms.

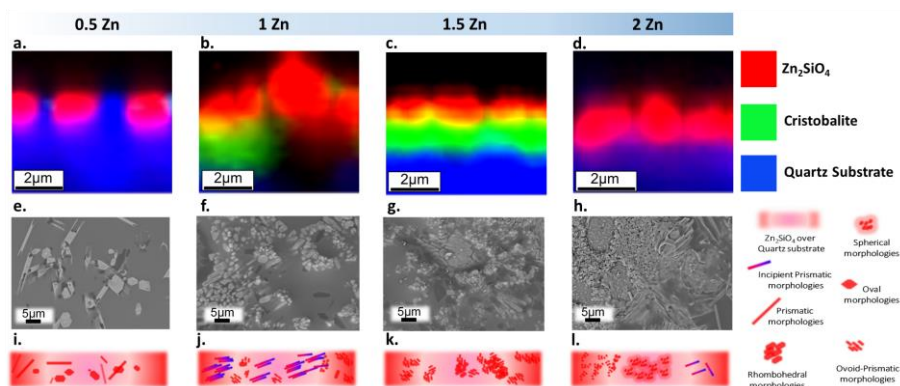


**Fig. 24:** Interface and microstructural characterization of  $\text{Zn}_2\text{SiO}_4$  films with varying  $\text{ZnO}$  concentrations (0.5Zn, 1Zn, 1.5Zn, and 2Zn) processed at 1100 °C: (a-d) Raman depth-resolved images showing phase distribution, (e-h) SEM micrographs of film surface morphology, and (i-l) schematic representations of morphological evolution at different compositions.

At 1200 °C, the presence of cristobalite across all compositions indicates enhanced alkali cation diffusion and accelerated quartz transformation, independent of zinc content. These observations highlight the critical role of the molten salt in mediating both atomic transport and crystal growth processes.

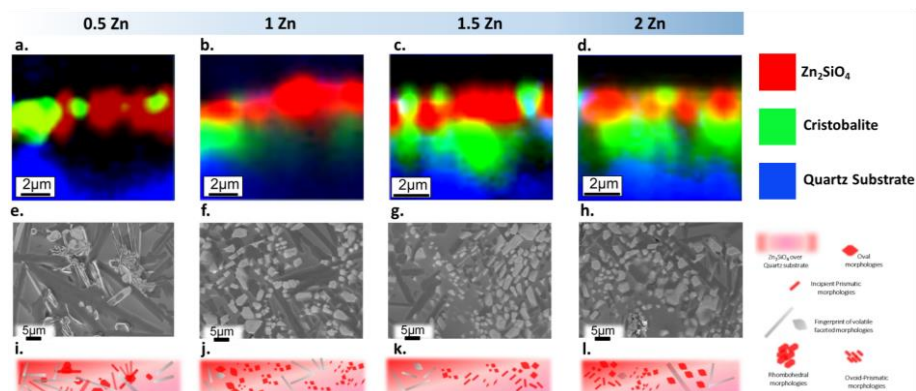


**Fig. 25:** Interface and microstructural characterization of  $\text{Zn}_2\text{SiO}_4$  films with varying  $\text{ZnO}$  concentrations (0.5Zn, 1Zn, 1.5Zn, and 2Zn) processed at 1200 °C: (a-d) Raman depth-resolved images showing phase distribution, (e-h) SEM micrographs of film surface morphology, and (i-l) schematic representations of morphological evolution at different compositions.

### 3.2.2 Luminescence Response: Structural Influences and Emission Mechanisms

The luminescent properties of  $\text{Zn}_2\text{SiO}_4$  films were investigated using complementary spectroscopic techniques, providing insights into the emission mechanisms and their relationship to structural characteristics.

This analysis builds on the foundational understanding of  $\text{Zn}_2\text{SiO}_4$ 's deep UV emission established in powder form, while highlighting the unique aspects of film form.

### 3.2.2.1 Room Temperature Luminescence: XEOL and CL

**Figs. 26a and 26b** present the room temperature XEOL spectra for  $\text{Zn}_2\text{SiO}_4$  films synthesized at 1100 °C and 1200 °C, respectively, with varying ZnO concentrations.

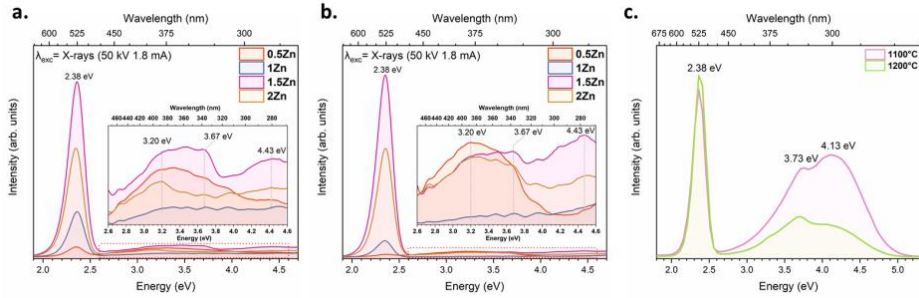


**Fig. 26:** Room temperature luminescence of  $\text{Zn}_2\text{SiO}_4$  films: XEOL spectra for different ZnO concentrations (0.5Zn, 1Zn, 1.5Zn, 2Zn) processed at (a) 1100 °C, (b) 1200 °C, (c) CL spectra for 1.5Zn films at 1100 °C and 1200 °C.

The spectra reveal multiple emission features, with a dominant band centered at 2.38 eV (521 nm), characteristic of  $\text{Mn}^{2+}$  transitions, similar to the behaviour observed in powders. A weak but distinct deep UV emission at 4.43 eV (280 nm) is observed, with the highest intensity in the 1.5Zn films. This suggests that the processing conditions and resulting structural characteristics, such as crystallographic texturing, play a role in enhancing deep UV emission.

For the CL analysis, shown in **Fig. 26c**, we focused on films with 1.5Zn concentration processed at both 1100 °C and 1200 °C, as this composition exhibited the most promising deep UV emission characteristics in the XEOL study. The CL spectra further highlight the influence of processing conditions on emission properties. Films processed at 1100 °C exhibit enhanced deep UV emission compared to those at 1200 °C, correlating with higher crystallographic ordering and the presence of a continuous cristobalite interlayer. These structural characteristics provide an optimized environment for radiative recombination, similar to the enhanced emission observed in powders with optimal phase purity and morphology.

### 3.2.2.2 Low Temperature Luminescence and Excitation Mechanisms

**Figs. 27a and 27b** present the 6 K CL and synchrotron-excited PL emission spectra of films with 1.5Zn concentration processed at both 1100 °C and 1200 °C. The selection of the 1.5Zn films for low-temperature analysis was based on their superior deep UV emission performance observed in room temperature studies.

At low temperatures, the emission spectrum transforms to display a dominant peak at 4.28 eV (290 nm), with significantly suppressed  $\text{Mn}^{2+}$  emission. The enhanced deep UV emission in the 1100 °C films suggests that the structural characteristics achieved at this temperature provide favourable conditions for radiative recombination, paralleling the temperature-dependent behaviour observed in powders.

**Fig. 27c** illustrates the PL excitation spectra, monitored at the deep UV emission energy of 4.43 eV (280 nm). The spectra reveal two primary excitation channels: bandgap excitation at 6 eV (207 nm) and electronic transitions within  $[\text{ZnO}_4]^{6-}$  tetrahedral clusters at 10.44 eV (119 nm).

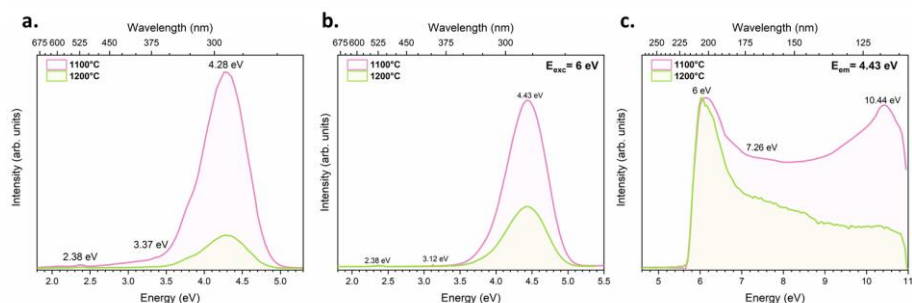


**Fig. 27:** Low-temperature luminescence of  $\text{Zn}_2\text{SiO}_4$  films with 1.5Zn concentration processed at 1100 °C and 1200 °C: (a) CL spectra, (b) Synchrotron-excited emission spectra under 6 eV excitation, (c) Excitation spectra monitored at 4.43 eV.

These excitation features were also identified in powder studies, confirming the intrinsic nature of deep UV emission in  $\text{Zn}_2\text{SiO}_4$ . The enhanced intensity of the high-energy excitation band in the 1100 °C films suggests that ordered crystal growth promotes effective energy transfer through the tetrahedral network.

### 3.2.3 Correlating Structure and Emission in $\text{Zn}_2\text{SiO}_4$ Films

The investigation of  $\text{Zn}_2\text{SiO}_4$  films reveals key correlations between processing conditions, structural development, and deep UV emission characteristics. The screen-printing assisted by molten salt strategy enables precise control over crystallographic texturing, interface quality, and processing temperature effects, directly influencing emission properties.

Optimal conditions (1.5Zn composition, 1100 °C processing) produce films combining high crystallographic ordering, well-defined interfaces, and enhanced UV emission. These relationships provide practical guidelines for developing  $\text{Zn}_2\text{SiO}_4$ -based UV emitting devices while maintaining the advantages of rare-earth-free composition.

In summary, the luminescence analysis demonstrates that the screen-printing assisted by molten salt strategy effectively controls structural, microstructural, and optical properties, influencing deep UV emission characteristics. The findings underscore the importance of crystallographic texturing and processing conditions in optimizing luminescent performance, providing a robust foundation for developing  $\text{Zn}_2\text{SiO}_4$ -based UV emitting devices. This work extends the potential of  $\text{Zn}_2\text{SiO}_4$  as a sustainable UV emitter from powder form to practical device applications, reinforcing insights from powder studies and establishing a framework for next-generation UV technologies.

The next section explores consolidation techniques for bulk ceramic forms, addressing a new range of potential applications through advanced sintering methods.

## 3.3 Consolidated $\text{Zn}_2\text{SiO}_4$ : Advancing Densification Through Spark Plasma Sintering

Building upon the insights gained from powder and film studies, this section explores the development of densified  $\text{Zn}_2\text{SiO}_4$  ceramics through advanced consolidation techniques. While previous sections demonstrated successful UV-B emission in powder and film forms, consolidation allows shaping into defined geometries for functional applications. This investigation introduces spark plasma sintering as a novel approach for  $\text{Zn}_2\text{SiO}_4$

densification, comparing its performance with conventional sintering methods to establish fundamental correlations between processing conditions, microstructural evolution, and deep UV emission characteristics.

### 3.3.1 Phase Evolution and Densification Behaviour

The processing temperature of 1300 °C was selected based on powder studies, which demonstrated that complete  $\alpha$ -phase formation and optimal structural stability are achieved at this temperature. XRD results presented in **Fig. 28a-b** confirm the successful formation of  $\alpha$ - $\text{Zn}_2\text{SiO}_4$  (JCPDS No. 37-1485) as the primary phase in both CS and SPS samples processed at 1300 °C.

The comparative analysis highlights significant differences between the two methods: SPS-processed samples shown in **Fig. 28b** display notably sharper and more intense reflections compared to CS samples in **Fig. 28a**, indicating enhanced crystallization kinetics under the combined influence of pressure and pulsed current heating. While both techniques produce minor residual ZnO, identifiable through characteristic reflections marked in the diffractograms, the SPS approach yields reduced secondary phase content, suggesting more complete phase transformation.

The consolidation behaviour differs markedly between the two sintering methods. Archimedes-based density measurements show that the CS sample reaches approximately 91% relative density, whereas SPS achieves 98%, approaching near-full densification. According to Chaim (Chaim, 2007), this improvement stems from the synergistic effects of the SPS process, including pressure-induced particle rearrangement, enhanced grain boundary diffusion, and current-assisted mass transport.

### 3.3.2 Microstructural Characteristics of Sintered Ceramics

Microstructural characterization by SEM reveals that grain growth and porosity in  $\text{Zn}_2\text{SiO}_4$  ceramics are governed by distinct thermodynamic and kinetic mechanisms, depending on the sintering route employed.

The polished and thermal etched surface of the CS sample, shown in **Fig. 28c** displays well-defined grain boundaries and triple junctions.

ZnO secondary phase is evident at grain boundary triple points, indicating non-equilibrium conditions during the conventional sintering. Intergranular porosity is primarily observed at triple junctions, localized near 120° angles, which is consistent with the minimization at local interfacial energy. The microstructure exhibits a heterogeneous grain size distribution, with grains ranging from 400 nm to 1  $\mu\text{m}$ . These features result from the extended sintering duration of 4h, which permits partially uncontrolled grain growth while achieving nearly full densification (91% of the theoretical density).

In contrast, the SPS-consolidated sample shown in **Fig. 28d** presents a uniform microstructure with well-defined grain boundaries and minimal porosity, attributed to localized Joule heating and pulsed current effects during sintering. Some intragranular porosity is observed, which could be related to close porosity from trapped gases or from differences in the thermal expansion coefficients of the constituent phases during the SPS process. Residual ZnO appears as smaller and more isolated inclusions, visible as bright contrast regions in the micrograph. The homogeneous grain distribution stems from the significantly shorter processing duration (20 min), which effectively suppresses excessive grain growth while maintaining effective densification. This optimization of the microstructure directly influences the material's luminescent response.



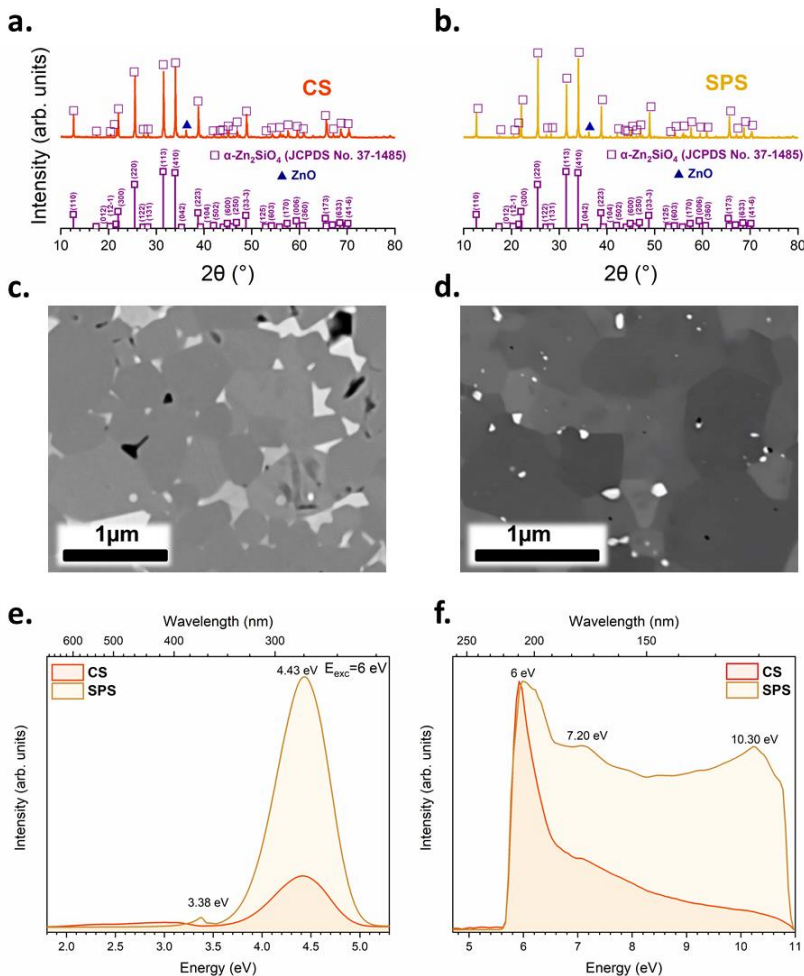


**Fig. 28:**  $\text{Zn}_2\text{SiO}_4$  Structural and luminescence characterization of  $\text{Zn}_2\text{SiO}_4$  ceramics processed by CS and SPS: XRD data for (a) CS and (b) SPS  $\text{Zn}_2\text{SiO}_4$  based material; SEM micrographs showing microstructural features of (c) CS and (d) SPS  $\text{Zn}_2\text{SiO}_4$  based material; low-temperature (6 K) synchrotron-excited (e) emission spectra under 6 eV excitation and (f) excitation spectra monitored at 4.43 eV.

### 3.3.3 Comparative Study of Deep UV Emission in CS and SPS Samples

Low-temperature (6 K) synchrotron-excited photoluminescence measurements provide detailed insight into the emission characteristics. The emission spectra shown in **Fig. 28e** reveal UV-B emission centered at 4.43 eV (280 nm) in both samples, maintaining the characteristic emission energy observed in powder and film forms.

Notably, the SPS  $\text{Zn}_2\text{SiO}_4$  based material demonstrates approximately threefold higher emission intensity compared to its CS counterpart, correlating with its improved crystallinity.

Excitation spectra monitored at 4.43 eV (280 nm) presented in **Fig. 28f** demonstrate enhanced absorption across all characteristic regions in the SPS sample compared to the CS counterpart. The spectra reveal three distinct excitation bands previously identified in powder and film forms: bandgap excitation at 6 eV (207 nm),  $[\text{SiO}_4]^{4-}$  tetrahedral



transitions at 7.20 eV (172 nm), and  $[\text{ZnO}_4]^{6-}$  cluster-related absorption at 10.30 eV (120 nm). Most significantly, the  $[\text{ZnO}_4]^{6-}$  cluster-related excitation band shows pronounced enhancement in the SPS  $\text{Zn}_2\text{SiO}_4$  based material, reinforcing the critical role of these tetrahedral units in deep UV emission mechanisms.

The successful application of SPS for  $\text{Zn}_2\text{SiO}_4$  consolidation, demonstrated here for the first time, achieves near-theoretical density (98%) with enhanced UV-B emission intensity. The threefold improvement in emission compared to conventional sintering, combined with significantly reduced processing time (20 min vs. 4h), establishes SPS as an efficient approach for fabricating high-performance UV-emitting ceramics. The optimized microstructure and enhanced  $[\text{ZnO}_4]^{6-}$  cluster excitation in SPS-processed samples demonstrate the advantages of rapid densification under controlled pressure and temperature conditions.

The systematic investigation of  $\text{Zn}_2\text{SiO}_4$  across multiple material forms has established clear relationships between synthesis approaches, structural development, and deep UV emission properties. The complementary nature of the various characterization techniques revealed how processing conditions fundamentally control material performance through their influence on phase formation, microstructural evolution, and emission center development. Notably, the successful demonstration of UV-B emission in powders, films, and consolidated ceramics, combined with the elucidation of the underlying emission mechanisms, validates the potential of  $\text{Zn}_2\text{SiO}_4$  as a sustainable alternative to current deep UV technologies.

The key processing-structure-property relationships identified in this work provide a robust foundation for future development of rare-earth-free UV emitting materials. These findings demonstrate that careful control of synthesis conditions can enable the development of environmentally sustainable materials that maintain high performance while eliminating dependence on critical raw materials.

## 4 Conclusions

A novel rare-earth-free and mercury-free deep UV emitter based on  $\text{Zn}_2\text{SiO}_4$  has been developed by systematically investigating synthesis-property relationships. A comprehensive experimental approach combining multiple synthesis routes, enabled the formation of  $\text{Zn}_2\text{SiO}_4$  in various forms (powders, films, and bulk ceramics). Detailed structural and spectroscopic characterization established the fundamental mechanisms of deep UV emission, and processing conditions were optimized for enhanced luminescent performance.

This comprehensive experimental approach across multiple material forms demonstrates the following findings:

- (i) Alternative routes of molten salt and sol-gel were successfully developed for the synthesis of  $\text{Zn}_2\text{SiO}_4$  powders. Molten salt synthesis resulted in the formation of rod-shaped particle morphology at temperatures below 700 °C, demonstrating accelerated phase formation due to improved mass transfer via liquid-phase mediation. Sol-gel processing facilitated the controlled evolution of both  $\alpha$ - and  $\beta$ - $\text{Zn}_2\text{SiO}_4$  polymorphs with optimal UV-B emission at 1200 °C. For comparison, the solid-state reaction served as a starting point for assessing structural and optical properties.
- (ii) Clear correlations were established between the synthesis parameters and the properties of the material synthesized in powder form. Amorphous silica precursors consistently produced materials with a higher phase purity and improved UV-B emission properties as compared to the crystalline counterparts across molten salt and solid-state synthesis methods. Optimal processing temperatures of 1100–1200 °C were identified to yield maximum UV-B emission intensity, with enhanced  $[\text{ZnO}_4]^{6-}$  excitation consistently correlates with improved emission efficiency.
- (iii) A novel screen-printing method assisted by molten salt was developed as a direct synthesis route to obtain  $\text{Zn}_2\text{SiO}_4$  in film form, achieving highly textured films (Lotgering factor up to 0.94) with peak UV-B emission at 1.5Zn composition processed at 1100 °C.
- (iv) For bulk ceramics, spark plasma sintering made it possible to achieve a density close to theoretical density (98%) with a threefold increase in emission intensity compared to conventional sintering.
- (v) The fundamental nature of deep UV emission in  $\text{Zn}_2\text{SiO}_4$  was elucidated through a comprehensive spectroscopic analysis. Intrinsic deep UV emission was demonstrated for the first time, with characteristic emission energies between 4.37–4.45 eV (280–284 nm). The emission originates from host excitons interacting with  $[\text{ZnO}_4]^{6-}$  tetrahedral units, supported by the identification of three distinct excitation mechanisms: bandgap absorption,  $[\text{SiO}_4]^{4-}$  tetrahedral transitions, and  $[\text{ZnO}_4]^{6-}$  cluster excitation.
- (vi) Systematic comparison across different material forms demonstrated unique advantages of structural and luminescent properties for specific applications. Sol-gel derived powders exhibited the most resolved UV-B emission at room temperature, molten salt synthesis produced the superior phase purity and controlled morphology, screen-printing assisted by molten salt strategy enabled the oriented growth with an enhanced interface quality, and spark plasma sintering achieved optimized microstructure in bulk ceramics.

These findings establish  $\text{Zn}_2\text{SiO}_4$  as a viable rare-earth-free alternative for deep UV applications, with each material form offering specific advantages for different technological requirements.

## 5 Future Research

This thesis establishes  $\text{Zn}_2\text{SiO}_4$  as a promising rare-earth-free deep UV emitter and demonstrates multiple synthesis strategies for producing materials in various forms. To advance the practical implementation and deepen the scientific understanding of these sustainable deep UV technologies, several research directions merit further exploration:

- (i) Defect state characterization through electron paramagnetic resonance (EPR) spectroscopy could elucidate the specific contributions of oxygen vacancies and other defects to the observed deep UV emission mechanisms, enabling precise defect engineering for optimized performance.
- (ii) Quantitative photoluminescence quantum yield determination through collaboration with specialized vacuum ultraviolet facilities capable of 207 nm excitation would provide absolute emission efficiency measurements across different synthesis routes and processing conditions.
- (iii) Transparent ceramic development via optimized consolidation parameters and advanced sintering techniques would minimize optical losses through light scattering reduction, enabling high-performance bulk optical components for deep UV applications.
- (iv) Strategic incorporation of dopants into the proven deep UV-emitting  $\text{Zn}_2\text{SiO}_4$  host could achieve simultaneous deep UV and visible emissions, expanding functionality for multifunctional applications.

## References

- Afandi, M. M., Park, H., Lee, S., & Kim, J. (2024). Yellow electroluminescence from metastable zinc silicate in an electrolyte-assisted silicon semiconductor structure. *Journal of Luminescence*, 275, 120794. <https://doi.org/10.1016/j.jlumin.2024.120794>
- Ahn, C. H., Kim, Y. Y., Kim, D. C., Mohanta, S. K., & Cho, H. K. (2009). A comparative analysis of deep level emission in ZnO layers deposited by various methods. *Journal of Applied Physics*, 105(1). <https://doi.org/10.1063/1.3054175>
- Azman, A. Z. K., Matori, K. A., Ab Aziz, S. H., Zaid, M. H. M., Wahab, S. A. A., & Khaidir, R. E. M. (2018). Comprehensive study on structural and optical properties of Tm<sub>2</sub>O<sub>3</sub> doped zinc silicate based glass–ceramics. *Journal of Materials Science: Materials in Electronics*, 29(23), 19861–19866. <https://doi.org/10.1007/s10854-018-0115-9>
- Balaram, V. (2019). Rare earth elements: A review of applications, occurrence, exploration, analysis, recycling, and environmental impact. *Geoscience Frontiers*, 10(4), 1285–1303. <https://doi.org/10.1016/j.gsf.2018.12.005>
- Baratto, C., Comini, E., Ferroni, M., Faglia, G., & Sberveglieri, G. (2013). Plasma-induced enhancement of UV photoluminescence in ZnO nanowires. *CrystEngComm*, 15(39), 7981. <https://doi.org/10.1039/c3ce41055b>
- Basavaraj, R. B., Nagabhushana, H., Daruka Prasad, B., Sharma, S. C., Prashantha, S. C., & Nagabhushana, B. M. (2015). A single host white light emitting Zn<sub>2</sub>SiO<sub>4</sub>:Re<sup>3+</sup> (Eu, Dy, Sm) phosphor for LED applications. *Optik - International Journal for Light and Electron Optics*, 126(19), 1745–1756. <https://doi.org/10.1016/j.ijleo.2014.07.149>
- Bessadok, M. N., Bouri, A., Ananias, D., Mrabet, S., Vázquez-Vázquez, C., & El Mir, L. (2024). Physical properties of a Eu<sup>3+</sup>-doped Zn<sub>2</sub>SiO<sub>4</sub> phosphor ceramic material with enhanced thermal sensitivity at low temperatures. *RSC Advances*, 14(53), 39598–39608. <https://doi.org/10.1039/D4RA07535H>
- Bharadwaj, M., Rai, S., & Gaur, A. (2023). Structural and morphological characterizations of ex-situ sol-gel derived luminescent Nd<sup>3+</sup>-Yb<sup>3+</sup> ion co-doped zinc-silicate dense glass-ceramic. *Journal of Non-Crystalline Solids*, 619, 122552. <https://doi.org/10.1016/j.jnoncrysol.2023.122552>
- Bharti, D. K., Verma, R., Rani, S., Agarwal, D., Mehra, S., Gangwar, A. K., Gupta, B. K., Singh, N., & Srivastava, A. K. (2023). Synthesis and Characterization of Highly Crystalline Bi-Functional Mn-Doped Zn<sub>2</sub>SiO<sub>4</sub> Nanostructures by Low-Cost Sol–Gel Process. *Nanomaterials*, 13(3), 538. <https://doi.org/10.3390/nano13030538>
- Bhatkar, V. B., Omanwar, S. K., & Moharil, S. V. (2002). Combustion Synthesis of the Zn<sub>2</sub>SiO<sub>4</sub>:Mn Phosphor. *Physica Status Solidi (a)*, 191(1), 272–276. [https://doi.org/10.1002/1521-396X\(200205\)191:1<272::AID-PSSA272>3.0.CO;2-R](https://doi.org/10.1002/1521-396X(200205)191:1<272::AID-PSSA272>3.0.CO;2-R)
- Chaim, R. (2007). Densification mechanisms in spark plasma sintering of nanocrystalline ceramics. *Materials Science and Engineering: A*, 443(1–2), 25–32. <https://doi.org/10.1016/j.msea.2006.07.092>
- Chang, H. J., Park, H. D., Sohn, K. S., & Lee, J. D. (1999). Electronic structure of Zn<sub>2</sub>SiO<sub>4</sub> and Zn<sub>2</sub>SiO<sub>4</sub>:Mn. *Journal of the Korean Physical Society*, 34, 545–548.
- Cheepborisutikul, S. J., Kessaratikoon, T., D’Elia, V., & Ogawa, M. (2025). Precisely Designed Synthesis of Hollow Zn<sub>2</sub>SiO<sub>4</sub> Particles from ZnO/SiO<sub>2</sub> Core/Shell Particles with Varied Silica Thicknesses. *Crystal Growth & Design*, 25(5), 1386–1393. <https://doi.org/10.1021/acs.cgd.4c01320>

- Cuscó, R., Alarcón-Lladó, E., Ibáñez, J., Artús, L., Jiménez, J., Wang, B., & Callahan, M. J. (2007). Temperature dependence of Raman scattering in ZnO. *Physical Review B*, 75(16), 165202. <https://doi.org/10.1103/PhysRevB.75.165202>
- Czaja, M., Lisiecki, R., Juroszek, R., & Krzykowski, T. (2021). Luminescence Properties of Tetrahedral Coordinated Mn<sup>2+</sup>; Genthelvite and Willemite Examples. *Minerals*, 11(11), 1215. <https://doi.org/10.3390/min11111215>
- Dai, P., Xu, Z., Yu, X., Wang, Y., Zhang, L., Li, G., Sun, Z., Liu, X., & Wu, M. (2015). Mesoporous hollow Zn<sub>2</sub>SiO<sub>4</sub>:Mn<sup>2+</sup> nanospheres: The study of photoluminescence and adsorption properties. *Materials Research Bulletin*, 61, 76–82. <https://doi.org/10.1016/j.materresbull.2014.10.002>
- Dai, R., Cheng, R., Wang, J., Zhang, C., Li, C., Wang, H., Wang, X., & Zhou, Y. (2022). Tunnel-structured willemite Zn<sub>2</sub>SiO<sub>4</sub>: Electronic structure, elastic, and thermal properties. *Journal of Advanced Ceramics*, 11(8), 1249–1262. <https://doi.org/10.1007/s40145-022-0607-1>
- Diana, P., Sebastian, S., Sivaganesh, D., Manthrammel, M. A., Kumar, A., & Shkir, M. (2024). Hydrothermal synthesis of cerium-doped Zn<sub>2</sub>SiO<sub>4</sub> phosphor for futuristic lighting applications. *Journal of Solid-State Chemistry*, 329, 124441. <https://doi.org/10.1016/j.jssc.2023.124441>
- Dierre, B., Yuan, X., & Sekiguchi, T. (2010). Low-energy cathodoluminescence microscopy for the characterization of nanostructures. *Science and Technology of Advanced Materials*, 11(4), 043001. <https://doi.org/10.1088/1468-6996/11/4/043001>
- Dumcenco, D. O., Huang, Y. S., Kuo, D. H., & Tiong, K. K. (2012). Photoluminescence characterization of vertically aligned ZnO microrods. *Journal of Luminescence*, 132(8), 1890–1895. <https://doi.org/10.1016/j.jlumin.2012.02.037>
- Effendy, N., Aziz, S. H. A., Kamari, H. M., Matori, K. A., & Zaid, M. H. M. (2019). Enhanced green photoluminescence of erbium doped Zn<sub>2</sub>SiO<sub>4</sub> glass-ceramics as phosphor in optoelectronic devices. *Journal of Alloys and Compounds*, 783, 441–447. <https://doi.org/10.1016/j.jallcom.2018.12.362>
- Essalah, G., Kadim, G., Jabar, A., Masrour, R., Ellouze, M., Guermazi, H., & Guermazi, S. (2020). Structural, optical, photoluminescence properties and Ab initio calculations of new Zn<sub>2</sub>SiO<sub>4</sub>/ZnO composite for white light emitting diodes. *Ceramics International*, 46(8), 12656–12664. <https://doi.org/10.1016/j.ceramint.2020.02.031>
- European Union. (2024). Critical raw materials Act. Regulation (EU) 2024/1252 of the European Parliament and of the Council of 11 April 2024 establishing a framework for ensuring a secure and sustainable supply of critical raw materials and amending. In *Regulations (EU) No 168/2013, (EU) 2018/858, (EU) 2018/1724 and (EU) 2019/1020 Text with EEA relevance*.
- Feng, X., Yuan, X., Sekiguchi, T., Lin, W., & Kang, J. (2005). Aligned Zn– Zn<sub>2</sub>SiO<sub>4</sub> Core–Shell Nanocables with Homogenously Intense Ultraviolet Emission at 300 nm. *The Journal of Physical Chemistry B*, 109(33), 15786–15790. <https://doi.org/10.1021/jp0514980>
- Florez, D., Diez, R., Hay, K., & Piquet, H. (2012). DBD excimer lamp power supply with fully controlled operating conditions. *2012 13th International Conference on Optimization of Electrical and Electronic Equipment (OPTIM)*, 1346–1352. <https://doi.org/10.1109/OPTIM.2012.6231836>
- Furukawa, T., Kanamori, S., Fukuta, M., Nawa, Y., Kominami, H., Nakanishi, Y., Sugita, A., Inami, W., & Kawata, Y. (2015). Fabrication of bright and thin Zn<sub>2</sub>SiO<sub>4</sub> luminescent film for electron beam excitation-assisted optical microscope. *Optics Express*, 23(14), 18630. <https://doi.org/10.1364/OE.23.018630>

- Gerdes, R., Enseling, D., Haase, M., & Jüstel, T. (2018). UV C luminescence of a modified zirconium silicate framework upon cathode ray and VUV excitation. *Journal of Luminescence*, 198, 410–417. <https://doi.org/10.1016/j.jlumin.2018.02.071>
- Guillaume, R. (2024). *Implementing the EU Critical Raw Materials Act*.
- Guo, R., Du, Y., Zhang, S., Liu, H., & Fu, Y. (2018). The effects of ultraviolet supplementation to the artificial lighting on rats' bone metabolism, bone mineral density, and skin. *Journal of Photochemistry and Photobiology B: Biology*, 188, 12–18. <https://doi.org/10.1016/j.jphotobiol.2018.08.020>
- Hao, Y., & Wang, Y. (2007). Luminescent properties of  $\text{Zn}_2\text{SiO}_4\text{:Mn}^{2+}$  phosphor under UV, VUV and CR excitation. *Journal of Luminescence*, 122–123, 1006–1008. <https://doi.org/10.1016/j.jlumin.2006.01.352>
- He, H., Wang, Y., & Zou, Y. (2003). Photoluminescence property of  $\text{ZnO-SiO}_2$  composites synthesized by sol-gel method. *Journal of Physics D: Applied Physics*, 36(23), 2972–2975. <https://doi.org/10.1088/0022-3727/36/23/017>
- Hidalgo-Sanz, R., Del-Castillo-Alonso, M.-Á., Sanz, S., Olarte, C., Martínez-Abaigar, J., & Núñez-Olivera, E. (2024). The Two Mycological Sides of Ultraviolet-B Radiation: Harmless for Mushroom Mycelia, Harmful for Mycopathogenic Mould Spores. *Agriculture*, 14(5), 681. <https://doi.org/10.3390/agriculture14050681>
- Hsu, C.-H., Liu, C.-E., Lai, L.-Y., Kuo, M.-T., He, J.-R., & Lin, H.-P. (2023). Synthesis of Mesoporous  $\text{Eu}^{3+}$ -Doped Zinc/Silicate Phosphors for Highly Selective and Sensitive Detection of Sulfide Ions. *ACS Omega*, 8(46), 44229–44237. <https://doi.org/10.1021/acsomega.3c06823>
- Ishinaga, T., Iguchi, T., Kominami, H., Hara, K., Kitaura, M., & Ohnishi, A. (2015). Luminescent property and mechanism of  $\text{ZnAl}_2\text{O}_4$  ultraviolet emitting phosphor. *Physica Status Solidi c*, 12(6), 797–800. <https://doi.org/10.1002/pssc.201400317>
- Jacob, S., Nagabhushana, B. M., & Chikkahanumantharayappa. (2019). Tb and Li doped Zinc Silicate green nanophosphors synthesized by solution combustion method. *Nano-Structures & Nano-Objects*, 19, 100363. <https://doi.org/10.1016/j.nanoso.2019.100363>
- Jiang, T., Yang, W., Deng, W., Yu, Z., & Wen, W. (2025). Improvement of microstructure and dielectric properties of  $\text{Zn}_{1.8}\text{SiO}_{3.8}$  ceramics by doping with rare earth elements (La, Pr, Nd, Sm). *Journal of Alloys and Compounds*, 1010, 177679. <https://doi.org/10.1016/j.jallcom.2024.177679>
- Kang, Z. T., Liu, Y., Wagner, B. K., Gilstrap, R., Liu, M., & Summers, C. J. (2006). Luminescence properties of  $\text{Mn}^{2+}$  doped  $\text{Zn}_2\text{SiO}_4$  phosphor films synthesized by combustion CVD. *Journal of Luminescence*, 121(2), 595–600. <https://doi.org/10.1016/j.jlumin.2005.12.066>
- Karazhanov, S. Zh., Ravindran, P., Fjellvåg, H., & Svensson, B. G. (2009). Electronic structure and optical properties of  $\text{ZnSiO}_3$  and  $\text{Zn}_2\text{SiO}_4$ . *Journal of Applied Physics*, 106(12). <https://doi.org/10.1063/1.3268445>
- Kaur, N., Lee, Y., Kim, D. Y., & Lee, S. (2018). Optical bandgap tuning in nanocrystalline  $\text{ZnO:Y}$  films via forming defect-induced localized bands. *Materials & Design*, 148, 30–38. <https://doi.org/10.1016/j.matdes.2018.03.042>
- Kikuchi, Y., Matsuyama, S., Kawamura, S., Fujishiro, F., Miwa, M., & Toyama, S. (2024). Experimental investigation on UV light output of  $\text{YPO}_4\text{:Gd}$  particles for ion beam induced fluorescence microscopy. *Nuclear Instruments and Methods in Physics Research Section B: Beam Interactions with Materials and Atoms*, 557, 165518. <https://doi.org/10.1016/j.nimb.2024.165518>

- Kominami, H., Iguchi, T., Nakanishi, Y., & Hara, K. (2011). Ultra-Violet Emission of Aluminates Phosphors Prepared by Solid Phase Synthesis. *J. Adv. Res. Phys*, 2, 3–5.
- Kortov, V. S., Sergeeva, K. A., Pustovarov, V. A., & Rempel, A. A. (2017). Photoluminescence of nanostructured  $\text{Zn}_2\text{SiO}_4\text{:Mn}^{2+}$  ceramics under UV and VUV excitation. *Journal of Surface Investigation: X-Ray, Synchrotron and Neutron Techniques*, 11(4), 727–731. <https://doi.org/10.1134/S1027451017040097>
- Kuo, H.-P., Tsai, H.-A., Huang, A.-N., & Pan, W.-C. (2016). CIGS absorber preparation by non-vacuum particle-based screen printing and RTA densification. *Applied Energy*, 164, 1003–1011. <https://doi.org/10.1016/j.apenergy.2015.04.002>
- Lee, J.-K., Bhat, A. A., Watanabe, S., Rao, T. K. G., & Singh, V. (2025). Unveiling the photoluminescence and electron paramagnetic resonance of  $\text{Gd}^{3+}$ -Doped  $\text{CaYAl}_3\text{O}_7$  phosphor emitting narrowband ultraviolet B radiation. *Ceramics International*, 51(8), 10415–10422. <https://doi.org/10.1016/j.ceramint.2024.12.474>
- Li, C., Bando, Y., Dierre, B., Sekiguchi, T., Huang, Y., Lin, J., & Golberg, D. (2010). Effect of Size-Dependent Thermal Instability on Synthesis of  $\text{Zn}_2\text{SiO}_4\text{-SiO}_x$  Core–Shell Nanotube Arrays and Their Cathodoluminescence Properties. *Nanoscale Research Letters*, 5(4), 773–780. <https://doi.org/10.1007/s11671-010-9556-7>
- Lin, T., Fu, X., Liu, Z., Chen, N., Zhang, J., Liu, R., Meng, W., & Zhang, H. (2024). X-ray induced long afterglow luminescence from UVC to red region in  $\text{Ca}_2\text{P}_2\text{O}_7\text{:Pr}^{3+}$ . *Journal of Rare Earths*. <https://doi.org/10.1016/j.jre.2024.08.012>
- Lin, X., Li, C., Xu, S., Wang, J., Yang, H., Qu, Y., Chen, Q., Li, Z., Su, M., Liu, G., Liu, H., Yang, J., Lv, Y., Li, Y., & Wu, H. (2024). Smart windows based on ultraviolet-B persistent luminescence phosphors for bacterial inhibition and food preservation. *Food Chemistry*, 448, 139142. <https://doi.org/10.1016/j.foodchem.2024.139142>
- Liu, F., Guo, X., Ding, X., Que, T., Wang, H., Xu, J., Miao, H., & Zhou, H. (2024). Effect of  $\text{Mn}^{2+}$  substitution on phase composition, microstructure, and microwave dielectric properties of  $\text{Zn}_{1.8}\text{SiO}_{3.8}$  ceramics. *Journal of Materials Science: Materials in Electronics*, 35(36), 2252. <https://doi.org/10.1007/s10854-024-13909-2>
- Liu, W., Wang, Y., Qiu, H., Chen, D., Wu, S., Ji, Q., Chang, B., Li, Y., Zhao, H., Tan, Y., & Gu, Y. (2024). Long-term ultraviolet B irradiation at 297 nm with light-emitting diode improves bone health via vitamin D regulation. *Biomedical Optics Express*, 15(7), 4081. <https://doi.org/10.1364/BOE.520348>
- Liu, X., Lv, Z., Liao, Z., Sun, Y., Zhang, Z., Sun, K., Zhou, Q., Tang, B., Geng, H., Qi, S., & Zhou, S. (2024). Highly efficient AlGaIn-based deep-ultraviolet light-emitting diodes: from bandgap engineering to device craft. *Microsystems & Nanoengineering*, 10(1), 110. <https://doi.org/10.1038/s41378-024-00737-x>
- Liu, X., Song, J., Lv, Z., Liao, Z., Geng, H., Zhang, Z., Jiang, J., Tang, B., Qi, S., Liu, S., & Zhou, S. (2025). Doping Engineering Strategy for Boosting the Performance of AlGaIn-Based Deep-Ultraviolet Light-Emitting Diodes. *Crystal Growth & Design*, 25(6), 1833–1841. <https://doi.org/10.1021/acs.cgd.4c01612>
- Li, W., Xu, C., Xie, A., Chen, K., Yang, Y., Liu, L., & Zhu, S. (2021). Microstructure Study of Phase Transformation of Quartz in Potassium Silicate Glass at 900 °C and 1000 °C. *Crystals*, 11(12), 1481. <https://doi.org/10.3390/cryst11121481>
- Loiko, P., Dymshits, O., Volokitina, A., Alekseeva, I., Shemchuk, D., Tsenter, M., Bachina, A., Khubetsov, A., Vilejshikova, E., Petrov, P., Baranov, A., & Zhilin, A. (2018). Structural transformations and optical properties of glass-ceramics based on  $\text{ZnO}$ ,  $\beta$ - and  $\alpha$ - $\text{Zn}_2\text{SiO}_4$  nanocrystals and doped with  $\text{Er}_2\text{O}_3$  and  $\text{Yb}_2\text{O}_3$ : Part I. The role of heat-treatment. *Journal of Luminescence*, 202, 47–56. <https://doi.org/10.1016/j.jlumin.2018.05.010>



- Lotgering, F. K. (1959). Topotactical reactions with ferrimagnetic oxides having hexagonal crystal structures—I. *Journal of Inorganic and Nuclear Chemistry*, 9(2), 113–123. [https://doi.org/10.1016/0022-1902\(59\)80070-1](https://doi.org/10.1016/0022-1902(59)80070-1)
- Masjedi-Arani, M., & Salavati-Niasari, M. (2016). A simple sonochemical approach for synthesis and characterization of  $\text{Zn}_2\text{SiO}_4$  nanostructures. *Ultrasonics Sonochemistry*, 29, 226–235. <https://doi.org/10.1016/j.ultsonch.2015.09.020>
- Mbule, P., Mlotswa, D., Mothudi, B., & Dhlamini, M. (2021). Photoluminescence and thermoluminescence analysis of  $\text{Zn}_2\text{SiO}_4:\text{Dy}^{3+}$  nanophosphor. *Journal of Luminescence*, 235, 118060. <https://doi.org/10.1016/j.jlumin.2021.118060>
- Mineral commodity summaries 2025. (2025). <https://doi.org/10.3133/mcs2025>
- Minho, I., Kim, J., Park, K., & Sok, J. (2022). Resistive Switching Effects of Zinc Silicate for Nonvolatile Memory Applications. *Journal of the Korean Institute of Electrical and Electronic Material Engineers*, 35(4), 348–352.
- Mishra, K. C., Johnson, K. H., DeBoer, B. G., Berkowitz, J. K., Olsen, J., & Dale, E. A. (1991). First principles investigation of electronic structure and associated properties of zinc orthosilicate phosphors. *Journal of Luminescence*, 47(5), 197–206. [https://doi.org/10.1016/0022-2313\(91\)90012-K](https://doi.org/10.1016/0022-2313(91)90012-K)
- Muramoto, Y., Kimura, M., & Nouda, S. (2014). Development and future of ultraviolet light-emitting diodes: UV-LED will replace the UV lamp. *Semiconductor Science and Technology*, 29(8), 084004. <https://doi.org/10.1088/0268-1242/29/8/084004>
- Nishikawa, H., Shiroyama, T., Nakamura, R., Ohki, Y., Nagasawa, K., & Hama, Y. (1992). Photoluminescence from defect centers in high-purity silica glasses observed under 7.9-eV excitation. *Physical Review B*, 45(2), 586–591. <https://doi.org/10.1103/PhysRevB.45.586>
- Ochiai, S., Nishida, Y., Higuchi, Y., Morita, D., Makida, K., Seki, T., Ikuta, K., & Imagama, S. (2021). Short-range UV-LED irradiation in postmenopausal osteoporosis using ovariectomized mice. *Scientific Reports*, 11(1), 7875. <https://doi.org/10.1038/s41598-021-86730-0>
- Pan, Y., Han, X., Jiang, Z., Hong, X., Chen, J., Sui, Z., Tian, Q., & Zhou, B. (2024). Stable lithium storage of hierarchical  $\text{Zn}_2\text{SiO}_4/\text{C}$  micro-/nanospheres enabled by in-situ introduction of an endogenous  $\text{Zn}_4\text{Si}_2\text{O}_7(\text{OH})_2$ . *Journal of Alloys and Compounds*, 1000, 175136. <https://doi.org/10.1016/j.jallcom.2024.175136>
- Park, J., & Kim, J. (2021). Single-crystalline  $\text{Zn}_2\text{SiO}_4:\text{Mn}^{2+}$  luminescent film on amorphous quartz glass. *Journal of Alloys and Compounds*, 855, 157343. <https://doi.org/10.1016/j.jallcom.2020.157343>
- Peng, K.-C., Kao, H.-C., Liu, S.-J., Tsai, K.-L., & Lin, J.-C. (2013). Annealing Effect on the Microstructure and Optical Characterization of  $\text{Zn}_2\text{SiO}_4$  Thin Film Sputtered on Quartz Glass. *Japanese Journal of Applied Physics*, 52(11S), 11NB04. <https://doi.org/10.7567/JJAP.52.11NB04>
- Peng, Z., Luo, C., Yu, J., Xu, Z., Lu, X., & Zhang, G. (2008). Preparation and characterization of an  $\text{Hf}^{4+}$ -doped zinc silicate long-lasting phosphorescent material. *Materials Letters*, 62(3), 487–490. <https://doi.org/10.1016/j.matlet.2007.05.087>
- Portakal-Uçar, Z. G., Dogan, T., Akça, S., Kaynar, Ü. H., & Topaksu, M. (2021). Effect of  $\text{Sm}^{3+}$  and  $\text{Mn}^{2+}$  incorporation on the structure and luminescence characteristics of  $\text{Zn}_2\text{SiO}_4$  phosphor. *Radiation Physics and Chemistry*, 181, 109329. <https://doi.org/10.1016/j.radphyschem.2020.109329>

- Portakal-Uçar, Z. G., Oglakci, M., Yüksel, M., Ayvaci, M., & Can, N. (2021). Structural and luminescence characterization of Ce<sup>3+</sup> and Mn<sup>2+</sup> co-activated zinc silicate nanocrystal obtained by gel combustion synthesis. *Materials Research Bulletin*, 133, 111025. <https://doi.org/10.1016/j.materresbull.2020.111025>
- Rajkhowa, S. (2020). Heat, solar pasteurization, and ultraviolet radiation treatment for removal of waterborne pathogens. In *Waterborne Pathogens* (pp. 169–187). Elsevier. <https://doi.org/10.1016/B978-0-12-818783-8.00009-8>
- Rakov, N., Matias, F., Xing, Y., & Maciel, G. S. (2024). Mn<sup>2+</sup> doped Zn<sub>2</sub>SiO<sub>4</sub> phosphors: A threefold-mode sensing approach for optical thermometry in the visible region at 525 nm. *Optical Materials*, X, 24, 100359. <https://doi.org/10.1016/j.omx.2024.100359>
- Ramakrishna, P. V., Murthy, D. B. R. K., Sastry, D. L., & Samatha, K. (2014). Synthesis, structural and luminescence properties of Mn doped ZnO/Zn<sub>2</sub>SiO<sub>4</sub> composite microphosphor. *Spectrochimica Acta Part A: Molecular and Biomolecular Spectroscopy*, 129, 274–279. <https://doi.org/10.1016/j.saa.2014.03.081>
- Ramprasad, C., Gwenzi, W., Chaukura, N., Izyan Wan Azelee, N., Upamali Rajapaksha, A., Naushad, M., & Rangabhashiyam, S. (2022). Strategies and options for the sustainable recovery of rare earth elements from electrical and electronic waste. *Chemical Engineering Journal*, 442, 135992. <https://doi.org/10.1016/j.cej.2022.135992>
- Rojas-Hernandez, R. E., Rubio-Marcos, F., Enríquez, E., De La Rubia, M. A., & Fernandez, J. F. (2015). A low-energy milling approach to reduce particle size maintains the luminescence of strontium aluminates. *RSC Advances*, 5(53), 42559–42567. <https://doi.org/10.1039/C5RA04878H>
- Rojas-Hernandez, R. E., Rubio-Marcos, F., Gonçalves, R. H., Rodriguez, M. Á., Véron, E., Allix, M., Bessada, C., & Fernandez, J. F. (2015). Original Synthetic Route to Obtain a SrAl<sub>2</sub>O<sub>4</sub> Phosphor by the Molten Salt Method: Insights into the Reaction Mechanism and Enhancement of the Persistent Luminescence. *Inorganic Chemistry*, 54(20), 9896–9907. <https://doi.org/10.1021/acs.inorgchem.5b01656>
- Rojas-Hernandez, R. E., Rubio-Marcos, F., Romet, I., del Campo, A., Gorni, G., Hussainova, I., Fernandez, J. F., & Nagirnyi, V. (2022). Deep-Ultraviolet Emitter: Rare-Earth-Free ZnAl<sub>2</sub>O<sub>4</sub> Nanofibers via a Simple Wet Chemical Route. *Inorganic Chemistry*, 61(30), 11886–11896. <https://doi.org/10.1021/acs.inorgchem.2c01646>
- Rojas-Hernandez, R. E., Rubio-Marcos, F., Romet, I., Feldbach, E., Buryi, M., John, D., Ivanov, R., Hussainova, I., Fernandez, J. F., & Nagirnyi, V. (2024). On the potential of Transparent Rare-Earth-Free ZnAl<sub>2</sub>O<sub>4</sub> Ceramics targeted at the UV-C to UV-B emission. *Applied Materials Today*, 38, 102230. <https://doi.org/10.1016/j.apmt.2024.102230>
- Rojas-Hernandez, R. E., Rubio-Marcos, F., Serrano, A., Hussainova, I., & Fernandez, J. F. (2020). Boosting phosphorescence efficiency by crystal anisotropy in SrAl<sub>2</sub>O<sub>4</sub>:Eu, Dy textured ceramic layers. *Journal of the European Ceramic Society*, 40(4), 1677–1683. <https://doi.org/10.1016/j.jeurceramsoc.2019.11.019>
- Scott, J. F., & Porto, S. P. S. (1967). Longitudinal and Transverse Optical Lattice Vibrations in Quartz. *Physical Review*, 161(3), 903–910. <https://doi.org/10.1103/PhysRev.161.903>
- Sharma, V. K., & Demir, H. V. (2022). Bright Future of Deep-Ultraviolet Photonics: Emerging UVC Chip-Scale Light-Source Technology Platforms, Benchmarking, Challenges, and Outlook for UV Disinfection. *ACS Photonics*, 9(5), 1513–1521. <https://doi.org/10.1021/acsphotonics.2c00041>

- Singh, V., Bajaj, R., Kaur, S., Rao, A. S., & Singh, N. (2021). UVB emission from sol-gel derived Gd<sup>3+</sup>-doped CaLa<sub>4</sub>Si<sub>3</sub>O<sub>13</sub> phosphor. *Optik*, 242, 167275. <https://doi.org/10.1016/j.ijleo.2021.167275>
- Singh, V., Bhatia, K., Rao, A. S., & Joo, J. B. (2024). Trivalent Gd incorporated Zn<sub>2</sub>SiO<sub>4</sub> phosphor material for EPR and luminescence investigations. *International Journal of Materials Research*, 115(6), 438–445. <https://doi.org/10.1515/ijmr-2023-0222>
- Singh, V., Prasad, A., Deopa, N., Rao, A. S., Jung, S., Singh, N., Rao, J. L., & Lakshminarayana, G. (2021). Luminescence features of Mn<sup>2+</sup>-doped Zn<sub>2</sub>SiO<sub>4</sub>: A green color emitting phosphor for solid-state lighting. *Optik*, 225, 165715. <https://doi.org/10.1016/j.ijleo.2020.165715>
- Sivakumar, V., & Lakshmanan, A. (2014). Pyrolysis synthesis of Zn<sub>2</sub>SiO<sub>4</sub>:Mn<sup>2+</sup> phosphors – effect of fuel, flux and co-dopants. *Journal of Luminescence*, 145, 420–424. <https://doi.org/10.1016/j.jlumin.2013.08.016>
- Sivakumar, V., Lakshmanan, A., Sangeetha, L., Nandhagopal, J., Annadurai, G., Rani, R. S., & Saravanakumar, S. (2024). Effect of Flux and Co-doping on Photoluminescence Properties of Zn<sub>2</sub>SiO<sub>4</sub>:Eu<sup>3+</sup> Red Phosphors for Blue LED Excitable White LED Applications. *Journal of Fluorescence*. <https://doi.org/10.1007/s10895-024-04048-2>
- Sohn, K., Cho, B., & Park, H. D. (1999). Photoluminescence Behavior of Manganese-Doped Zinc Silicate Phosphors. *Journal of the American Ceramic Society*, 82(10), 2779–2784. <https://doi.org/10.1111/j.1151-2916.1999.tb02155.x>
- Song, K., Mohseni, M., & Taghipour, F. (2016). Application of ultraviolet light-emitting diodes (UV-LEDs) for water disinfection: A review. *Water Research*, 94, 341–349. <https://doi.org/10.1016/j.watres.2016.03.003>
- Synkiewicz-Musialska, B., Szwagierczak, D., Kulawik, J., Pałka, N., & Bajurko, P. R. (2020). Impact of additives and processing on microstructure and dielectric properties of willemite ceramics for LTCC terahertz applications. *Journal of the European Ceramic Society*, 40(2), 362–370. <https://doi.org/10.1016/j.jeurceramsoc.2019.10.005>
- Takesue, M., Hayashi, H., & Smith, R. L. (2009). Thermal and chemical methods for producing zinc silicate (willemite): A review. *Progress in Crystal Growth and Characterization of Materials*, 55(3–4), 98–124. <https://doi.org/10.1016/j.pcrysgrow.2009.09.001>
- Taylor, H. F. W. (1962). The dehydration of hemimorphite. *American Mineralogist*, 47, 932–944.
- Tripathi, S., Bose, R., Roy, A., Nair, S., & Ravishankar, N. (2015). Synthesis of Hollow Nanotubes of Zn<sub>2</sub>SiO<sub>4</sub> or SiO<sub>2</sub>: Mechanistic Understanding and Uranium Adsorption Behavior. *ACS Applied Materials & Interfaces*, 7(48), 26430–26436. <https://doi.org/10.1021/acsami.5b09805>
- United Nations Environment Programme (UNEP). (2013). Minamata convention on mercury. In *United Nations Environment Programme, Nairobi, Kenya*.
- Vařák, P., Nevindová, P., & Baborák, J. (2023). Er-doped zinc-silicate glass-ceramics with enhanced emission in the near-infrared region. *EPJ Web of Conferences*, 287, 05039. <https://doi.org/10.1051/epjconf/202328705039>
- Vien, L. T. T., Tu, N., Phuong, T. T., Tuan, N. T., Quang, N. V., Van Bui, H., Duong, A.-T., Trung, D. Q., & Huy, P. T. (2019). Facile synthesis of single phase  $\alpha$ -Zn<sub>2</sub>SiO<sub>4</sub>:Mn<sup>2+</sup> phosphor via high-energy planetary ball milling and post-annealing method. *Journal of Luminescence*, 215, 116612. <https://doi.org/10.1016/j.jlumin.2019.116612>

- Wahab, S. A. A., Matori, K. A., Zaid, M. H. M., Kechik, M. M. A., Effendy, N., & Khaidir, R. E. M. (2023). Blue emission: Optical properties of  $\text{Co}^{2+}$  doping towards  $\text{Zn}_2\text{SiO}_4$  glass-ceramics. *Optik*, 274, 170528. <https://doi.org/10.1016/j.ijleo.2023.170528>
- Wang, Q., Wang, Z., Qi, M., Zhao, H., Xin, X., Verma, A., Siritanon, T., Ramirez, A. P., Subramanian, M. A., & Jiang, P. (2024). Synthesis and Optical Properties Based on Ni-Doped  $\text{Zn}_2\text{SiO}_4$  Blue Pigments with High-NIR Reflectance. *ACS Sustainable Chemistry & Engineering*, 12(14), 5522–5532. <https://doi.org/10.1021/acssuschemeng.3c07982>
- Wu, Y., Yin, X., Zhang, Q., Wang, W., & Mu, X. (2014). The recycling of rare earths from waste tricolor phosphors in fluorescent lamps: A review of processes and technologies. *Resources, Conservation and Recycling*, 88, 21–31. <https://doi.org/10.1016/j.resconrec.2014.04.007>
- Yang, X., Chen, D., Liang, Y., Zhou, S., Xu, J., Liu, L., Lin, H., Xiong, Y., Cheng, Y., & Wang, Y. (2023). Energy focusing reinforced narrowband ultraviolet-B mechanoluminescence for bright-field stress visualization. *Journal of Materials Chemistry C*, 11(21), 6912–6919. <https://doi.org/10.1039/D3TC00722G>
- Yang, Y., Zhuang, Y., He, Y., Bai, B., & Wang, X. (2010). Fine tuning of the dimensionality of zinc silicate nanostructures and their application as highly efficient absorbents for toxic metal ions. *Nano Research*, 3(8), 581–593. <https://doi.org/10.1007/s12274-010-0019-3>
- Yan, S., Liang, Y., Chen, Y., Liu, J., Chen, D., & Pan, Z. (2021). Ultraviolet-C persistent luminescence from the  $\text{Lu}_2\text{SiO}_5:\text{Pr}^{3+}$  persistent phosphor for solar-blind optical tagging. *Dalton Transactions*, 50(24), 8457–8466. <https://doi.org/10.1039/D1DT00791B>
- Yao, W., Tian, Q., Liu, J., Wu, Z., Cui, S., Ding, J., Dai, Z., & Wu, W. (2016). Large-scale synthesis and screen printing of upconversion hexagonal-phase  $\text{NaYF}_4:\text{Yb}^{3+}, \text{Tm}^{3+}/\text{Er}^{3+}/\text{Eu}^{3+}$  plates for security applications. *Journal of Materials Chemistry C*, 4(26), 6327–6335. <https://doi.org/10.1039/C6TC01513A>
- Yi, X., Liu, H., Wang, Y., Chen, J., Chen, Z., Wang, Y., Yuan, X., & Zhu, K. (2024). Modulating trap properties by  $\text{Cr}^{3+}$ -doping in  $\text{Zn}_2\text{SiO}_4:\text{Mn}^{2+}$  nano phosphor for optical information storage. *Ceramics International*, 50(21), 43373–43382. <https://doi.org/10.1016/j.ceramint.2024.08.188>
- Yue, Z., Dong, M., Meng, S., & Li, L. (2009). Phase Characterization and Dielectric Properties of  $\text{Zn}_2\text{SiO}_4$  Ceramics Derived from a Sol-Gel Process. *Ferroelectrics*, 387(1), 184–188. <https://doi.org/10.1080/00150190902967030>
- Zhang, S., Liang, H., Liu, Y., Liu, Y., Hou, D., Zhang, G., & Shi, J. (2012). Intensive green emission of  $\text{ZnAl}_2\text{O}_4:\text{Mn}^{2+}$  under vacuum ultraviolet and low-voltage cathode ray excitation. *Optics Letters*, 37(13), 2511. <https://doi.org/10.1364/OL.37.002511>
- Zhang, Z., Zhou, S., Liao, Z., Jiang, J., Geng, H., Lv, Z., Liu, X., Qi, S., & Liu, S. (2025). AlGaN Polarized Ultrathin Tunneling Junction Deep Ultraviolet Light-Emitting Diodes. *Nano Letters*, 25(5), 1898–1906. <https://doi.org/10.1021/acs.nanolett.4c05443>
- Zhou, S., Liao, Z., Sun, K., Zhang, Z., Qian, Y., Liu, P., Du, P., Jiang, J., Lv, Z., & Qi, S. (2024). High-Power AlGaN-Based Ultrathin Tunneling Junction Deep Ultraviolet Light-Emitting Diodes. *Laser & Photonics Reviews*, 18(1). <https://doi.org/10.1002/lpor.202300464>

## Acknowledgements

As I complete this doctoral journey, I extend my sincere gratitude to all those who have supported me along the way.

I am deeply thankful to my supervisor, Dr. Rocío Estefanía Rojas-Hernandez, for her exceptional guidance and constant encouragement that have profoundly influenced both my research and scientific approach. Her passion and dedication have been a constant source of inspiration, pushing me to reach beyond what I thought possible. I also express my gratitude to my co-supervisor, Professor Irina Hussainova, for her exceptional support and mentorship throughout this process.

This research was made possible through the financial support of the Estonian Research Council under the PSG466 project. I also gratefully acknowledge the mobility funding provided by the European Union through the Dora Plus program and Erasmus+ Mobility Grant, which supported my research visits. I thank JECS Trust for funding a mobility stay project in 2023 (Contract 2023347). I am grateful to MAX IV Laboratory for providing beamtime on FinEstBeAMS beamline under Proposals 20230209 and 20240393.

My sincere appreciation goes to Dr. Jesús Lopez Sanchez, Dr. Fernando Rubio-Marcos, and Professor Jose F. Fernández for their valuable support and guidance during my research visit at the Institute of Ceramics and Glass in Spain. I am also grateful to Professor Thomas Jüstel for hosting me in his lab at Münster University in Germany, where our scientific discussions challenged and expanded my thinking in ways that continue to influence my research.

I wish to acknowledge the team at the Institute of Physics at Tartu University: Dr. Eduard Feldbach, Dr. Ivo Romet, and Dr. Vitali Nagirnyi for their expertise in luminescence characterization and significant contribution to this thesis. Special thanks to Dr. Kirill Chernenko for his assistance with the synchrotron experiments.

To my best friend and beamtime partner, Dr. Roman Ivanov, thank you for your collaboration and support throughout this journey. I also extend my thanks to Mr. Arash, Dr. Rahul, Dr. Mansoureh, Dr. Mohsen, Dr. Tatevik, Mrs. Sibel, Dr. Maksim Antonov, and my entire research group for their friendship and scientific insights.

The successful completion of this research was greatly facilitated by technical specialists whose expertise was essential. I extend my professional gratitude to Mr. Rainer Traksmaa for conducting the X-ray diffraction analyses and to Dr. Mart Viljus for performing scanning electron microscopy examinations. I also acknowledge Mr. Hans Vallner for his significant technical assistance throughout this research project.

Finally, my deepest appreciation goes to my family. To my beloved wife, Marwa, your patience, understanding, and support have been my foundation. To our precious child, Faya, your smile and innocent joy have been my greatest motivation, reminding me daily of what truly matters in life. To my mother, Najla, your love and belief in me have been my strength since childhood. And to my father Sebti, brother Sabri, and sisters Sabrine and Jinen, thank you for standing by me, encouraging me, and supporting me every step of the way. This achievement is as much yours as it is mine.

## Abstract

### Development of Rare-Earth-Free Zinc Silicate as a Novel Deep UV Emitter: Synthesis Strategies and Luminescent Properties

Deep ultraviolet light sources are essential for sterilization, phototherapy, and environmental purification applications. Current technologies rely primarily on mercury-based lamps, which pose significant environmental and health risks, or rare-earth based-phosphors, which face critical supply chain challenges. This situation has created an urgent need for sustainable alternatives that are both mercury-free and independent of rare earth elements. While previous research has explored various alternative materials, most approaches still depend on either toxic components or critical raw materials, limiting their long-term sustainability.

This thesis investigates undoped zinc silicate ( $\text{Zn}_2\text{SiO}_4$ ) as a novel solution for deep UV emission, representing the first comprehensive study of its intrinsic luminescence properties and synthesis-structure relationships. The choice of  $\text{Zn}_2\text{SiO}_4$  is strategically significant due to its composition of abundant, non-critical elements and its wide band gap of 5.5–6.2 eV, which theoretically enables deep UV emission.

Previous studies have focused primarily on  $\text{Zn}_2\text{SiO}_4$  as a host for rare earth dopants, with only limited investigation of its intrinsic emission capabilities, particularly in the deep UV range.

The research employed a systematic investigation using multiple scalable processing methods: conventional solid-state reaction, molten salt synthesis, sol-gel processing, screen-printing with molten salt flux for film fabrication, and spark plasma sintering for ceramic densification. The influence of precursor type, synthesis temperature, and processing route on phase formation and microstructure was elucidated through complementary analytical techniques, including X-ray diffraction, Raman spectroscopy, and electron microscopy.

Multi-technique luminescence characterization, employing X-ray-excited optical luminescence, cathodoluminescence, and synchrotron-excited photoluminescence at both room and cryogenic temperatures, revealed consistent intrinsic UV-B emission in the energy range of 4.37–4.45 eV (280–284 nm) across all material forms. Detailed mechanistic analysis established that this emission originates from host excitons interacting with  $[\text{ZnO}_4]^{6-}$  tetrahedral units, demonstrating the intrinsic nature of the luminescence without requiring extrinsic dopants.

Optimization of synthesis conditions, particularly using amorphous silica precursors and controlled thermal processing (1100–1200 °C), enabled enhanced phase formation kinetics, uniform microstructures, and increased luminescence intensity. The molten salt-assisted approach facilitated the formation of highly ordered rod-like  $\text{Zn}_2\text{SiO}_4$  morphologies at significantly reduced temperatures (700 °C), while sol-gel processing enabled the most resolved UV-B emission characteristics. Novel screen-printing with molten salt flux achieved direct growth of oriented films with exceptional (300) texturing (Lotgering factor up to 0.94), with optimal UV-B emission obtained using 1.5Zn stoichiometry processed at 1100 °C. Spark plasma sintering produced bulk ceramics with near-theoretical density (98%) and threefold enhancement in UV-B emission intensity compared to conventional sintering methods.

The established correlations between synthesis parameters, structural features, and emission properties demonstrate the potential of  $\text{Zn}_2\text{SiO}_4$  as a sustainable deep UV emitter, free from both rare-earth elements and mercury. These findings not only advance the understanding of wide band gap silicate luminescence mechanisms but also provide a framework for developing other rare-earth-free optical materials. The methodologies developed herein establish a foundation for environmentally sustainable UV technologies in sterilization, phototherapy, and environmental purification.

## Lühikokkuvõte

### Haruldaste muldmetallide vaba tsinksilikaadi kui uue süva-UV kiirguri arendus: sünteesistrateegiad ja luminescentsomadused

Süvaultraviolettkiirguse allikad on hädavajalikud steriliseerimisega, fototeraapiaga ja keskkonnapuhastusega seotud rakendustes. Kaasaegsed tehnoloogiad põhinevad peamiselt elavhõbeda baasil lampidel, mis kujutavad endast märkimisväärselt ohtu keskkonnale ja tervisele, või haruldaste muldmetallide põhistel luminofooridel, mis seisavad silmitsi kriitiliste tarneahelatega seotud probleemidega. See olukord on loonud tungiva vajaduse jätkusuutlike alternatiivide järele, mis oleksid nii elavhõbedavabad kui ka sõltumatud haruldastest muldmetallidest. Kuigi varasemate uurimuste raames on uuritud erinevaid alternatiivseid materjale, sõltub enamik lähenemisviise endiselt kas toksilistest komponentidest või kriitilistest toormaterjalidest, piirates seeläbi pikaajalist jätkusuutlikkust.

Käesolev doktoritöö uurib lisandivaba tsinksilikaat ( $\text{Zn}_2\text{SiO}_4$ ) kui potentsiaalselt uudset alternatiivi süva-UV kiirguse tekitamiseks, olles esimene põhjalik uuring selle materjali omakiirguslike luminescentsomaduste ja seoste kohta sünteesimeetodi ning struktuuri vahel.  $\text{Zn}_2\text{SiO}_4$  valik on strateegiliselt oluline tänu selle koostisele, mis koosneb laia levikuga, mitte-kriitilistest elementidest, ning selle laiale keelutsoonile 5.5–6.2 eV, mis teoreetiliselt võimaldab süva-UV kiirguse teket.

Varasemad piiratud uuringud on keskendunud peamiselt erinevate lisanditega (haruldaste muldmetallidega)  $\text{Zn}_2\text{SiO}_4$  luminescentsomaduste uurimisele, jättes seega omakiirguslikud luminescentsomadused suuresti tähelepanuta, eriti süva-UV piirkonnas.

Käesolevas uurimistöös kasutati süstemaatilist lähenemist, kasutades selleks mitmeid skaleeritavaid töötusmeetodeid: tavapärane tardfaasreaktsioon, sulasoolasüntees, sool-geel meetod, siiditrükk sulasoola-baasil rübustiga kilede valmistamiseks ning säde-plasma paagutus keraamika tihendamiseks. Lähteainete tüübi, sünteesimise temperatuuri ja töötlemisviisi mõju faasimoodustumisele ja mikrostruktuurile selgitati täiendavate analüütiliste meetodite abil, sealhulgas röntgendifraktsioonanalüüs, Raman-spektroskoopia ja elektronmikroskoopia.

Erinevad luminescentsi karakteriseerimise meetodid nagu röntgen- ja katoodluminescents ning sünkrotronkiirgusega ergastatud fotoluminescents nii toatemperatuuril aga ka krüogeensetel temperatuuridel, kinnitasid UV-B kiirguse eksisteerimist kõigis uuritud proovides energiahemikus 4.37–4.45 eV (280–284 nm). Üksikasjalik mehhanistlik analüüs kinnitas, et see kiirgus pärineb põhiaine eksitonide interaktsioonist  $[\text{ZnO}_4]^{6-}$  tetraeedriliste kompleksidega, kinnitades sellisel viisil lisandite vaba luminescentsi omakiirguslikku olemust.

Sünteesitingimuste optimeerimine, eelkõige amorfse ränidioksiidi ja kontrollitud termilise töötlemise (1100–1200 °C) kasutamine, võimaldas parandada faasi moodustumise kineetikat, mikrostruktuuri ning suurendada luminescentsi intensiivsust. Sulasoola meetodi rakendamine viis kõrge korrapärasusega niitjate  $\text{Zn}_2\text{SiO}_4$  niitkristallide moodustumiseni märkimisväärselt vähendatud temperatuuridel (700 °C). Samal ajal sool-geel töötlusmeetodi rakendamine võimaldas saavutada kõrge eristatavusega UV-B emissioonikarakteristikuid. Uudne siiditrüki meetod sulasoola baasil rübustit kasutades võimaldas saavutada erakordse (300) tekstuuriga orienteeritud kilesid (Lotgeringi tegur



kuni 0.94), kusjuures optimaalse UV-B kiirguse saamiseks kasutati 1.5Zn stöhiomeetriat töötlemistemperatuuri 1100 °C rakendades. Säte-plasma paagutus võimaldas saada peaaegu teoreetilise tihedusega (98%) keraamilise materjali saavutades, võrreldes tavapäraste paagutusmeetoditega, kolm korda intensiivsema UV-B kiirguse.

Kindlaks tehtud seosed sünteesiparameetrite, struktuursete omaduste ja kiirgusomaduste vahel näitavad  $Zn_2SiO_4$  potentsiaali jätkusuutliku süva-UV kiirgurina, mis on nii haruldastest muldmetallidest kui ka elavhõbedast vaba. Need tulemused mitte ainult ei paranda arusaama laia keelutsooniga silikaatide luminesentsi mehhanismidest, vaid loovad samuti raamistiku ka teiste haruldaste muldmetallide vabade optiliste materjalide arendamiseks. Käesoleva töö raames välja töötatud meetodikad loovad aluse keskkonnasäästlike UV-tehnoloogiatele arendamiseks steriliseerimise, fototeraapia ja keskkonnapuhastuse rakendustes.

## Appendix

### Publication I

**Necib, J.**, Hussainova, I., & Rojas-Hernandez, R.E. (2025). Effect of silica precursor on the synthesis of  $\text{Zn}_2\text{SiO}_4$ -based material. *Proceedings of the Estonian Academy of Sciences*, 74(2), 217–221. <https://doi.org/10.3176/proc.2025.2.24>.





Proceedings of the  
Estonian Academy of Sciences  
2025, 74, 2, 217–221

<https://doi.org/10.3176/proc.2025.2.24>

[www.eap.ee/proceedings](http://www.eap.ee/proceedings)  
Estonian Academy Publishers

## MATERIALS ENGINEERING

### RESEARCH ARTICLE

Received 15 January 2025  
Accepted 3 March 2025  
Available online 12 May 2025

#### Keywords:

Zn<sub>2</sub>SiO<sub>4</sub>, solid-state reactions,  
synthesis, silica, precursors

#### Corresponding author:

Jallouli Necib  
[jallouli.necib@taltech.ee](mailto:jallouli.necib@taltech.ee)

#### Citation:

Necib, J., Hussainova, I. and  
Rojas-Hernandez, R. E. 2025. Effect  
of silica precursor on the synthesis of  
Zn<sub>2</sub>SiO<sub>4</sub>-based material. *Proceedings  
of the Estonian Academy of Sciences*,  
74(2), 218–222.  
<https://doi.org/10.3176/proc.2025.2.24>

© 2025 Authors. This is an open  
access article distributed under the  
terms and conditions of the Creative  
Commons Attribution (CC BY) license  
(<http://creativecommons.org/licenses/by/4.0>).

# Effect of silica precursor on the synthesis of Zn<sub>2</sub>SiO<sub>4</sub>-based material

Jallouli Necib, Irina Hussainova and Rocío E. Rojas-Hernandez

Department of Mechanical and Industrial Engineering, Tallinn University of Technology,  
Ehitajate tee 5, 19180 Tallinn, Estonia

## ABSTRACT

The synthesis of zinc silicate (Zn<sub>2</sub>SiO<sub>4</sub>) powders via the solid-state method was studied using amorphous and crystalline silica precursors. This work explores the impact of reaction temperature (700–1300 °C) on phase evolution and microstructural changes. A comprehensive characterization was carried out using X-ray diffraction, Raman spectroscopy, and scanning electron microscopy. X-ray diffraction analysis revealed a progression from unreacted precursors at lower temperatures to a mixed-phase composition (α-Zn<sub>2</sub>SiO<sub>4</sub> and β-Zn<sub>2</sub>SiO<sub>4</sub>) at intermediate temperatures, ultimately resulting in a single-phase α-Zn<sub>2</sub>SiO<sub>4</sub> at 1300 °C. Notably, Raman spectroscopy detected the presence of the metastable β-Zn<sub>2</sub>SiO<sub>4</sub> phase. Morphological analysis using scanning electron microscopy demonstrated the important role of precursor type and reaction conditions on particle characteristics: crystalline silica yielded larger, more uniform particles, while amorphous silica promoted the formation of spherical Zn<sub>2</sub>SiO<sub>4</sub> particles with an average diameter of approximately 1 μm. These findings are of significant interest for tailoring the properties of Zn<sub>2</sub>SiO<sub>4</sub> ceramics to be used for advanced applications in optoelectronics and luminescence technologies.

## 1. Introduction

Zinc silicate (Zn<sub>2</sub>SiO<sub>4</sub>) has gained significant attention owing to its outstanding luminescence properties, which make it an indispensable material for diverse applications such as phototherapy, dosimetry, and optoelectronic devices [1,2]. The material exists in five polymorphic forms: I (α), II (β), III, IV, and V, with the β-phase being metastable and transforming into the thermodynamically stable α-phase at elevated temperatures. The functional properties of Zn<sub>2</sub>SiO<sub>4</sub> are highly dependent on its crystalline structure and morphology, which are significantly influenced by the synthesis method and processing conditions [3]. Notably, Mn<sup>2+</sup>-doped α-Zn<sub>2</sub>SiO<sub>4</sub> exhibits green emission, whereas Mn<sup>2+</sup>-doped β-Zn<sub>2</sub>SiO<sub>4</sub> produces yellow emission [2]. This tunable emission behavior between the α and β phases highlights the potential for tailoring luminescent properties through crystal structure control.

Solid-state synthesis is widely employed for the production of Zn<sub>2</sub>SiO<sub>4</sub> due to its simplicity, cost-effectiveness, and scalability [4]. This method involves high-temperature reactions between precursor oxides such as zinc oxide (ZnO) and silica (SiO<sub>2</sub>). However, achieving high phase purity, controlled morphology, and optimal particle size necessitates careful consideration of precursor characteristics and reaction parameters. SiO<sub>2</sub>, a critical reactant in Zn<sub>2</sub>SiO<sub>4</sub> synthesis, exists in various forms, including amorphous and crystalline phases. These forms exhibit distinct reactivity and thermal behavior, which can profoundly influence phase formation, particle morphology, and ultimate functional properties.

This study systematically investigates the influence of silica precursor type (amorphous and crystalline) on the synthesis of Zn<sub>2</sub>SiO<sub>4</sub> powders via the solid-state method. The work focuses on understanding the effects of reaction temperature (700–1300 °C) on phase evolution, as well as the morphology and particle size distribution. The complementary analysis of X-ray diffraction (XRD) and Raman spectra, particularly in identifying metastable phases, offers valuable insights into the mechanisms of reactions. The main objectives of this work were to elucidate the role of precursor type in the formation of Zn<sub>2</sub>SiO<sub>4</sub> phases, including the metastable β-phase, and to provide recommendations for optimizing synthesis conditions to adapt the properties of Zn<sub>2</sub>SiO<sub>4</sub> to specific technological applications.

## 2. Experimental section

### 2.1. Materials and synthesis

ZnO (Symrise GmbH, 99.5%), amorphous silica (Thermo Fisher Scientific, 99.9%), and crystalline silica with quartz polymorph (Alfa Aesar, 99.5%) were used to synthesize  $\text{Zn}_2\text{SiO}_4$  powders via the solid-state method. The average particle sizes of the precursors were as follows: ZnO  $\sim 400$  nm, amorphous  $\text{SiO}_2 \sim 500$  nm, and crystalline  $\text{SiO}_2 \sim 1.21$   $\mu\text{m}$ . Stoichiometric amounts of ZnO and  $\text{SiO}_2$  powders were initially mixed using an agate mortar and pestle to ensure initial homogeneity. Subsequently, the mixture was further homogenized by planetary ball milling (Model YKM-1) at 250 rpm for 8 hours using yttria-stabilized zirconia (YSZ) balls and zirconia jars under dry conditions. After ball milling, the homogenized powder mixtures were heat-treated in air at temperatures ranging from 700 to 1300 °C for 2 hours.

### 2.2. Characterization

Phase identification was performed using XRD on a Rigaku SmartLab SE system with Cu K $\alpha$  radiation in Bragg-Brentano geometry ( $2\theta$  range: 10–80°). Raman spectroscopy employed a Horiba LabRAM HR800 with a 532 nm Nd:YAG laser for excitation. Morphological and microstructural analyses were conducted using a Zeiss ULTRA-55 field-emission scanning electron microscope (SEM).

## 3. Results and discussion

### 3.1. Phase evolution

Figure 1a,b shows the X-ray diffraction patterns of the samples synthesized at 700, 900, 1100, and 1300 °C using crystalline and amorphous silica precursors, respectively.

At 700 °C, both samples exhibit ZnO characteristic peaks observed at  $2\theta = 31.77^\circ, 34.43^\circ, 36.24^\circ, 47.52^\circ, 56.60^\circ, 62.85^\circ, 67.96^\circ$ , and  $69.07^\circ$ , corresponding to the reflection planes (100), (002), (101), (102), (110), (103), (112), and (201), respectively, and correlated with the standard JCPDS card No. 36-1451. The material synthesized using crystalline silica, hereinafter referred to as the crystalline-based sample, also shows  $\text{SiO}_2$  XRD peaks (JCPDS No. 33-1161) due to the crystalline nature of this precursor. In both materials no  $\text{Zn}_2\text{SiO}_4$  formation was detected at this temperature. At 900 °C, the material synthesized using amorphous silica, designated as the amorphous silica-derived sample, displayed  $\alpha\text{-Zn}_2\text{SiO}_4$  (JCPDS No. 37-1485) and  $\beta\text{-Zn}_2\text{SiO}_4$  (JCPDS No. 14-0653) phases, alongside residual ZnO and silica polymorphs (quartz, cristobalite, and tridymite). In contrast, the crystalline silica-based sample exhibited only low-intensity  $\alpha\text{-Zn}_2\text{SiO}_4$  peaks, with residual ZnO and quartz. The enhanced formation of  $\beta\text{-Zn}_2\text{SiO}_4$  in the amorphous silica-based sample can be attributed to the higher reactivity of amorphous silica, which facilitates the formation of metastable phases.

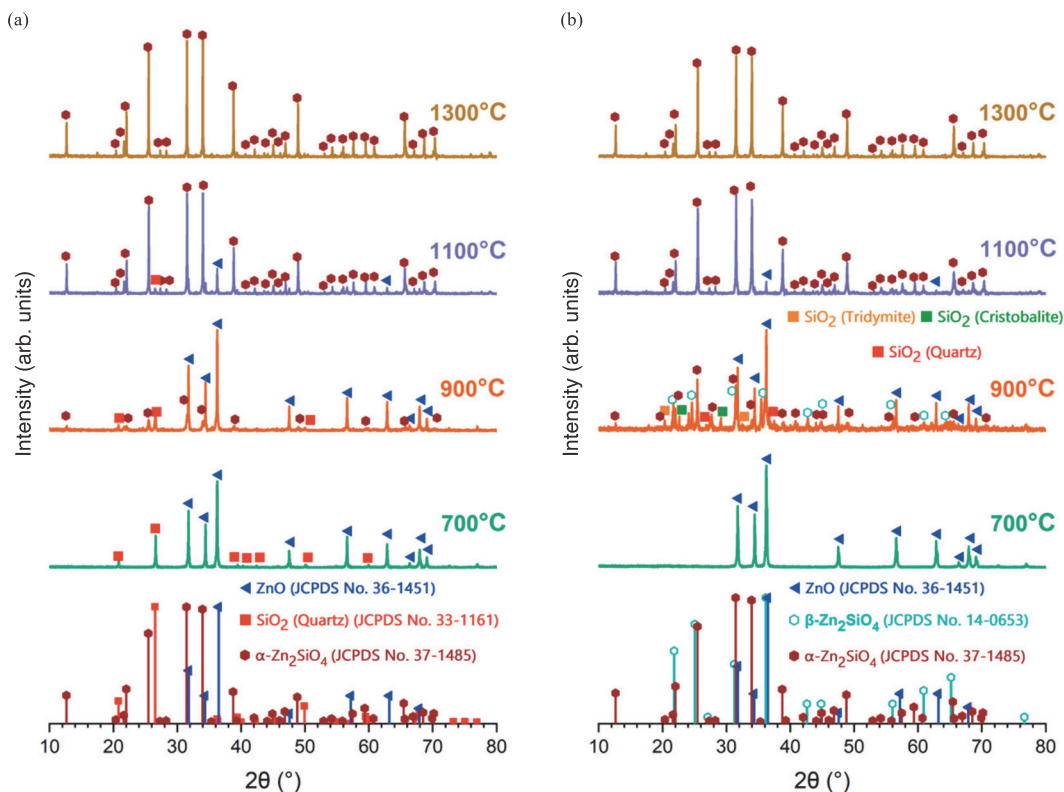


Fig. 1. XRD patterns of  $\text{Zn}_2\text{SiO}_4$  powders synthesized at 700, 900, 1100, and 1300 °C using (a) crystalline silica and (b) amorphous silica as precursors.

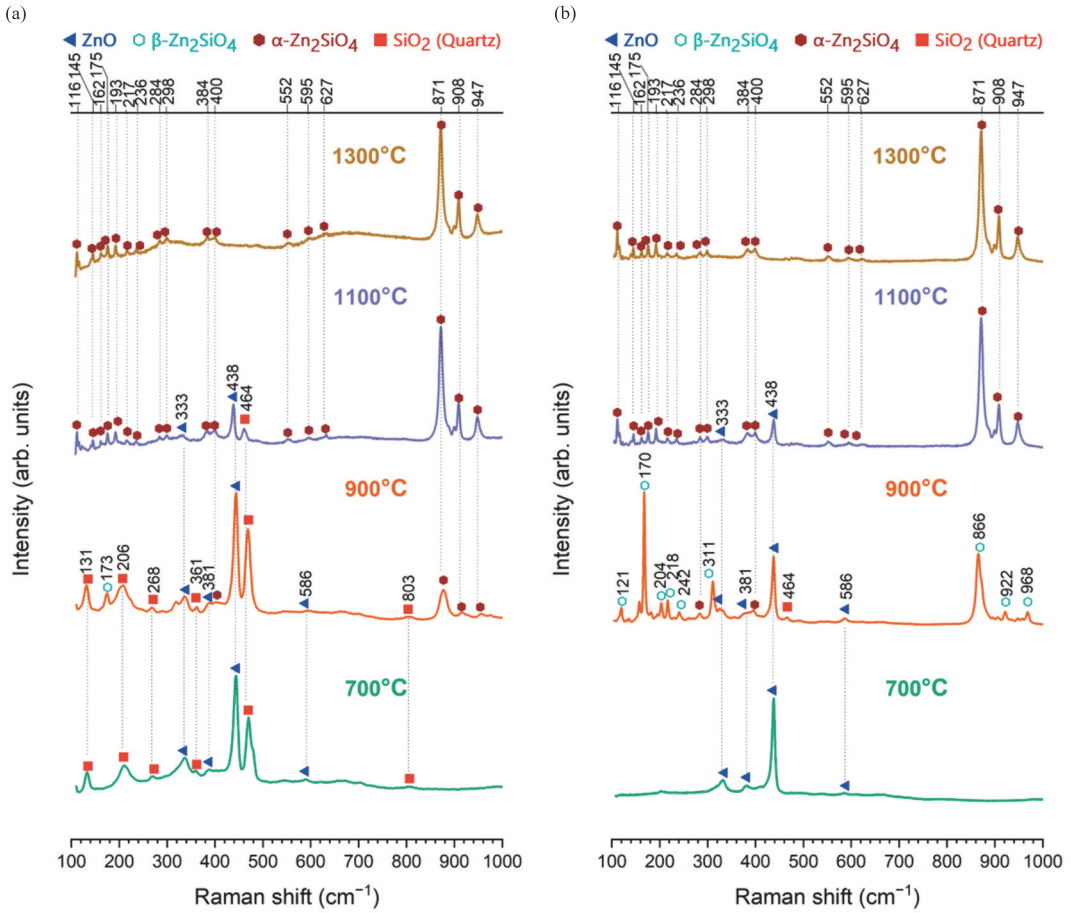


Fig. 2. Raman spectra of  $\text{Zn}_2\text{SiO}_4$  powders synthesized at 700, 900, 1100, and 1300 °C using (a) crystalline silica and (b) amorphous silica as precursors.

The transformation of amorphous silica to tridymite and cristobalite at 900 °C may further promote the formation of metastable  $\beta\text{-Zn}_2\text{SiO}_4$ , as this phase is derived from a distorted tridymite- or cristobalite-like framework, where zinc atoms partially replace silicon in the lattice, while additional zinc ions occupy interstitial positions [5]. This observation suggests that utilizing amorphous silica as the silica source for solid-state synthesis with ZnO may enhance the formation of  $\beta\text{-Zn}_2\text{SiO}_4$  compared with the direct use of quartz. Stabilizing the metastable  $\beta\text{-Zn}_2\text{SiO}_4$  phase could further enhance the functional versatility of the synthesized materials, enabling applications that leverage its unique properties.

At 1100 °C,  $\alpha\text{-Zn}_2\text{SiO}_4$  became the dominant phase in both samples. However, residual ZnO and quartz persisted in the crystalline silica-based sample, while the amorphous silica-based sample showed ZnO as a minor phase. Upon elevating the crystallization temperature to 1300 °C, a single-phase rhombohedral  $\alpha\text{-Zn}_2\text{SiO}_4$  structure developed in the samples from both precursor types, indicating the completion of the phase transformation.

Raman spectroscopy corroborated the phase evolution observed during the XRD analysis and provided additional structural insights (Fig. 2a,b).

For the crystalline silica-based sample, the Raman spectrum at 700 °C revealed prominent peaks at 333, 381, 438, and 586  $\text{cm}^{-1}$ , corresponding to the  $E_1^{\text{high}} - E_2^{\text{low}}$ ,  $A_1(\text{TO})$ ,  $E_2^{\text{high}}$ , and  $E_1(\text{LO})$  vibrational modes of ZnO, respectively [6]. Six Raman modes associated with quartz were also observed at 131, 206, 268, 361, 464, and 803  $\text{cm}^{-1}$ , assigned to the  $E(\text{TO} + \text{LO})$ ,  $A_1$ ,  $E(\text{TO} + \text{LO})$ ,  $A_1$ ,  $A_1$ , and  $E(\text{LO})$  modes, respectively [7]. In contrast, only ZnO Raman modes were detected in the sample prepared with amorphous silica at this temperature.

At 900 °C, Raman analysis of the crystalline silica-based sample revealed the presence of both  $\alpha\text{-Zn}_2\text{SiO}_4$  peaks and a low-intensity peak at 173  $\text{cm}^{-1}$ , associated with  $\beta\text{-Zn}_2\text{SiO}_4$  [8]. This observation, not detectable by XRD, demonstrates the higher sensitivity of Raman spectroscopy in detecting even small amounts of the metastable  $\beta$ -phase, highlighting its complementarity to XRD in phase analysis.

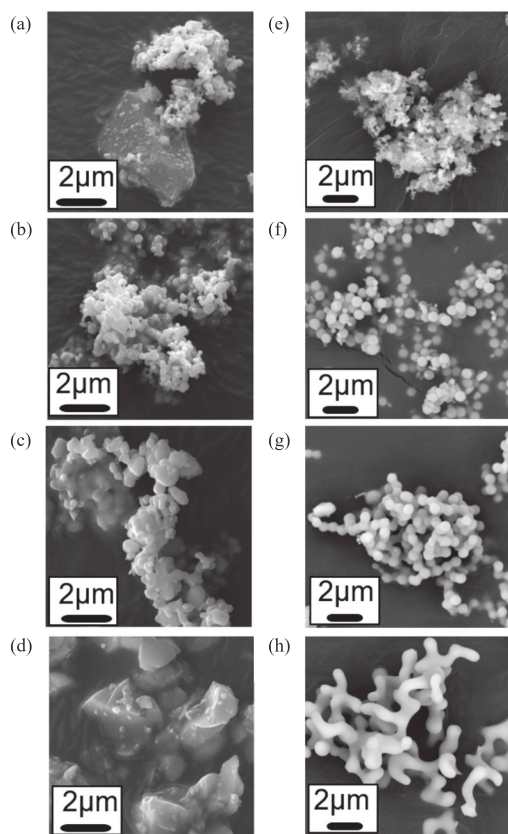


Fig. 3. SEM micrographs of  $\text{Zn}_2\text{SiO}_4$  powders synthesized at 700, 900, 1100, and 1300 °C using (a–d) crystalline silica and (e–h) amorphous silica as precursors.

For the amorphous silica-based sample, additional peaks appeared at 900 °C, including a weak peak at  $464\text{ cm}^{-1}$  attributed to residual quartz. Raman bands at 121, 170, 204, 218, 242, 311, 866, 922, and  $968\text{ cm}^{-1}$  were assigned to  $\beta\text{-Zn}_2\text{SiO}_4$  [8], while a low-intensity peak at  $284\text{ cm}^{-1}$  was attributed to  $\alpha\text{-Zn}_2\text{SiO}_4$ .

At 1100 °C, Raman peaks associated with ZnO diminished significantly for both samples using the two precursor types, reflecting the progression of the reaction between ZnO and silica to form  $\text{Zn}_2\text{SiO}_4$ . Above 1100 °C, the spectra were dominated by prominent peaks at 116, 145, 162, 175, 193, 217, 236, 284, 298, 384, 400, 552, 595, 627, 871, 908, and  $947\text{ cm}^{-1}$ , attributed to  $\alpha\text{-Zn}_2\text{SiO}_4$  [8]. These modes correspond to vibrations of the  $[\text{SiO}_4]^{4-}$  and  $[\text{ZnO}_4]^{6-}$  tetrahedra in the  $\alpha\text{-Zn}_2\text{SiO}_4$  structure. Notably, the intense band at  $872\text{ cm}^{-1}$  is associated with symmetric Si–O stretching ( $\nu_1(\text{A})$ ) vibrations, while the peaks at 908 and  $947\text{ cm}^{-1}$  are attributed to asymmetric stretching vibrations ( $\nu_3(\text{F}_2)$ ) [9]. At 1300 °C, only  $\alpha\text{-Zn}_2\text{SiO}_4$  peaks were observed in both precursor types, confirming the complete transformation.

The XRD and Raman analyses indicate the presence of multiple polymorphs of zinc silicate that coexist in the material synthesized at 900 and 1100 °C, underscoring the com-

plex composition and structural variation obtained by this route. The stabilization of the metastable  $\beta\text{-Zn}_2\text{SiO}_4$  phase sheds light on its potential applications in various fields.

### 3.2. Morphological analysis

The SEM analysis (Fig. 3) elucidates the influence of precursor selection and synthesis temperature on the morphology of  $\text{Zn}_2\text{SiO}_4$  powders.

For crystalline silica-based samples (Fig. 3a–d), notable morphological evolution was observed with increasing synthesis temperature. At 700 °C, distinct particle types were evident: smaller, whiter ZnO particles and larger, irregularly shaped  $\text{SiO}_2$  particles, which were attributed to the quartz present in the precursor mixture. As the temperature increased to 900 °C and 1100 °C, the emergence of smaller, spherical  $\text{Zn}_2\text{SiO}_4$  particles alongside the larger irregular particles was observed. At 1300 °C, particle growth and coalescence resulted in a more uniform particle size distribution.

In contrast, amorphous silica-based samples (Fig. 3e–h) exhibited a different morphological evolution. At 700 °C, smaller ZnO particles were observed alongside spherical  $\text{SiO}_2$  particles. At 900 °C, the ZnO particles were more uniformly distributed around the  $\text{SiO}_2$  particles, facilitating surface reactions and the formation of small zinc silicate particles [10]. These particles subsequently grew and coalesced to form spherical  $\text{Zn}_2\text{SiO}_4$  structures. At 1100 °C, the particles exhibited increased size and uniformity, with an average diameter of approximately  $1\text{ }\mu\text{m}$ , which is relatively small for particles synthesized via the solid-state method. At 1300 °C, significant sintering occurred, leading to the formation of interconnected particles with evident necking between them.

The findings highlight the importance of the nature, initial reactivity, and particle size of the silica precursor in tailoring the morphology and structural properties of the zinc silicate material. These findings contribute to our understanding of the underlying mechanisms governing  $\text{Zn}_2\text{SiO}_4$  synthesis.

## 4. Conclusions

This work studied the influence of silica precursor type and synthesis temperature on the phase evolution and morphological characteristics of  $\text{Zn}_2\text{SiO}_4$  powders produced via the solid-state method. A combined approach employing XRD, Raman spectroscopy, and SEM analyses was utilized to comprehensively characterize the synthesized powders. XRD analysis revealed a temperature-dependent phase evolution. At the lower temperature of 700 °C, unreacted precursors were observed. With an increase in temperature to 900 °C, a mixed-phase composition comprising  $\alpha\text{-Zn}_2\text{SiO}_4$  and  $\beta\text{-Zn}_2\text{SiO}_4$  emerged. Raman spectroscopy detected the presence of the metastable  $\beta\text{-Zn}_2\text{SiO}_4$  phase, complementing the XRD analysis. At 1300 °C, the single-phase  $\alpha\text{-Zn}_2\text{SiO}_4$  was developed for both precursor types. Morphological SEM analysis revealed distinct particle characteristics influenced by the type of silica precursor. Crystalline silica yielded larger particles, while amorphous silica facilitated the synthesis of smaller, spherical  $\text{Zn}_2\text{SiO}_4$  particles with an average diameter of approximately  $1\text{ }\mu\text{m}$  at 1100 °C.



These findings underscore the critical role of precursor selection and reaction conditions in tailoring the phase composition, particle size, and morphology of  $\text{Zn}_2\text{SiO}_4$  powders, which are crucial parameters for their performance in various applications, such as luminescent materials and advanced technologies.

#### Data availability statement

All research data are contained within the article and can be shared upon request from the authors.

#### Acknowledgments

The financial support from the Estonian Research Council, through grants PSG-466 (Rocío E. Rojas-Hernandez) and PRG-643 (Irina Hussainova), is gratefully acknowledged. The publication costs of this article were partially covered by the Estonian Academy of Sciences.

#### References

1. Karazhanov, S. Zh., Ravindran, P., Fjellvåg, H. and Svensson, B. G. Electronic structure and optical properties of  $\text{ZnSiO}_3$  and  $\text{Zn}_2\text{SiO}_4$ . *J. Appl. Phys.*, 2009, **106**(12), 123701. <https://doi.org/10.1063/1.3268445>
2. Afandi, M. M., Byeon, S., Kang, T., Kang, H. and Kim, J. Bright yellow luminescence from  $\text{Mn}^{2+}$ -doped metastable zinc silicate nanophosphor with facile preparation and its practical application. *Nanomaterials*, 2024, **14**(17), 1395. <https://doi.org/10.3390/nano14171395>
3. Xie, X., Chen, J., Song, Y., Zhou, X., Zheng, K., Zhang, X. et al.  $\text{Zn}_2\text{SiO}_4$ :  $\text{Eu}^{3+}$  micro-structures: controlled morphologies and luminescence properties. *J. Lumin.*, 2017, **187**, 564–572. <https://doi.org/10.1016/j.jlumin.2017.04.003>
4. Singh, S., Singh, D., Siwach, P., Gupta, I. and Kumar, P. Synthesis strategies for rare earth activated inorganic phosphors: a mini review. *Appl. Res.*, 2025, **4**(1). <https://doi.org/10.1002/appl.202400190>
5. Taylor, H. F. W. The dehydration of hemimorphite. *Am. Mineral.*, 1962, **47**(7–8), 932–944.
6. Cuscó, R., Alarcón-Lladó, E., Ibáñez, J., Artús, L., Jiménez, J., Wang, B. et al. Temperature dependence of Raman scattering in  $\text{ZnO}$ . *Phys. Rev. B*, 2007, **75**(16), 165202. <https://doi.org/10.1103/PhysRevB.75.165202>
7. Scott, J. F. and Porto, S. P. S. Longitudinal and transverse optical lattice vibrations in quartz. *Phys. Rev.*, 1967, **161**(3), 903–910. <https://doi.org/10.1103/PhysRev.161.903>
8. Loiko, P., Dymshits, O., Volokitina, A., Alekseeva, I., Shemchuk, D., Tsenter, M. et al. Structural transformations and optical properties of glass-ceramics based on  $\text{ZnO}$ ,  $\beta$ - and  $\alpha$ - $\text{Zn}_2\text{SiO}_4$  nanocrystals and doped with  $\text{Er}_2\text{O}_3$  and  $\text{Yb}_2\text{O}_3$ ; Part I. The role of heat-treatment. *J. Lumin.*, 2018, **202**, 47–56. <https://doi.org/10.1016/j.jlumin.2018.05.010>
9. Czaja, M., Lisiecki, R., Juroszek, R. and Krzykowski, T. Luminescence properties of tetrahedral coordinated  $\text{Mn}^{2+}$ ; genthelvite and willemite examples. *Minerals*, 2021, **11**(11), 1215. <https://doi.org/10.3390/min11111215>
10. Milde, M., Dembski, S., Osvet, A., Batentschuk, M., Winnacker, A. and SEXTL, G. Polymer-assisted sol–gel process for the preparation of photostimulable core/shell structured  $\text{SiO}_2/\text{Zn}_2\text{SiO}_4\text{:Mn}^{2+}$  particles. *Mater. Chem. Phys.*, 2014, **148**(3), 1055–1063. <https://doi.org/10.1016/j.matchemphys.2014.09.017>

## Ränidioksiidi eelkäija mõju $\text{Zn}_2\text{SiO}_4$ -põhise materjali sünteesile

Jallouli Necib, Irina Hussainova ja Rocío E. Rojas-Hernandez

Tahkefaasilise meetodi abil uuriti tsinksilikaadi ( $\text{Zn}_2\text{SiO}_4$ ) pulbrite sünteesi, kasutades amorfseid ja kristalseid ränidioksiidi eelkäijaid. Töö keskendus reaktsioonitemperatuuri (700–1300 °C) mõjule faasimuutustele ja mikrostruktuurilistele muutustele. Läbiviidud põhjalik analüüs hõlmas röntgendifraktsiooni, Ramani spektroskoopiat ja skaneerivat elektronmikroskoopiat. Röntgendifraktsioonanalüüs näitas, et madalamatel temperatuuridel esinesid reageerimata eelkäijad, keskmistel temperatuuridel tekkis segafaasiline koostis ( $\alpha$ - $\text{Zn}_2\text{SiO}_4$  ja  $\beta$ - $\text{Zn}_2\text{SiO}_4$ ) ning 1300 °C juures moodustus ühefaasiline  $\alpha$ - $\text{Zn}_2\text{SiO}_4$ . Ramani spektroskoopia tuvastas meta-stabiilse  $\beta$ - $\text{Zn}_2\text{SiO}_4$  faasi olemasolu. Skaneeriva elektronmikroskoopia abil tehtud morfoloogiline analüüs näitas, et eelkäijate tüüp ja reaktsioonitingimused mängivad olulist rolli osakeste omaduste kujunemisel: kristalne ränidioksiid andis suuremad ja ühtlasemad osakesed, samas kui amorfne ränidioksiid soodustas ligikaudu 1 µm läbimõõduga sfääriliste  $\text{Zn}_2\text{SiO}_4$  osakeste moodustumist. Tulemused on olulised  $\text{Zn}_2\text{SiO}_4$ -põhise keraamika omaduste kohandamiseks, et seda saaks kasutada kõrgtehnoloogilistes rakendustes optoelektronikas ja luminescentstehnoloogiates.





**Publication II**

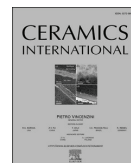
**Necib, J.**, Feldbach, E., Romet, I., Nagirnyi, V., Hussainova, I., Jüstel, T., & Rojas-Hernandez, R.E. (2025). Elucidating reaction mechanism by molten salt of potential rare-earth-free  $\text{Zn}_2\text{SiO}_4$  UV-B emitter: Insights into morphology and emission features. *Ceramics International*, In Press. <https://doi.org/10.1016/j.ceramint.2025.05.212>.





Contents lists available at ScienceDirect

Ceramics International

journal homepage: [www.elsevier.com/locate/ceramint](http://www.elsevier.com/locate/ceramint)

# Elucidating reaction mechanism by molten salt of potential rare-earth-free $\text{Zn}_2\text{SiO}_4$ UV-B emitter: Insights into morphology and emission features

Jallouli Necib<sup>a</sup>, Eduard Feldbach<sup>b</sup>, Ivo Romet<sup>b</sup>, Vitali Nagirnyi<sup>b</sup>, Irina Hussainova<sup>a</sup>, Thomas Jüstel<sup>c</sup>, Rocío E. Rojas-Hernandez<sup>a,d,\*</sup>

<sup>a</sup> Department of Mechanical and Industrial Engineering, Tallinn University of Technology, Ehitajate 5, 19180, Tallinn, Estonia

<sup>b</sup> Institute of Physics, University of Tartu, W. Ostwald Str 1, 50411, Tartu, Estonia

<sup>c</sup> FH Münster University of Applied Sciences, Department of Chemical Engineering, Stegerwaldstr. 39, D-48565, Steinfurt, Germany

<sup>d</sup> Electroceramic Department, Instituto de Cerámica y Vidrio, CSIC, Kelsen 5, 28049, Madrid, Spain

## ARTICLE INFO

Handling Editor: Dr P. Vincenzini

### Keywords:

Rare-earth-free luminescent materials  
 $\text{Zn}_2\text{SiO}_4$   
 Molten salt synthesis  
 X-ray-excited optical luminescence  
 Cathodoluminescence  
 Synchrotron radiation  
 UV-B emission

## ABSTRACT

This study presents a novel approach to the synthesis of rare-earth-free zinc silicate  $\text{Zn}_2\text{SiO}_4$  (Willemitte) powders by the molten salt method using crystalline and amorphous silica as precursors, which allows the formation of both  $\alpha$ - and  $\beta$ -polymorphs of  $\text{Zn}_2\text{SiO}_4$  at temperatures as low as 700 °C. Highly reactive amorphous silica stabilizes the  $\beta$ - $\text{Zn}_2\text{SiO}_4$  phase more effectively as compared to crystalline silica. Structural analysis reveals enhanced crystallinity and phase purity in amorphous silica-based samples. Morphological characterization demonstrates that both precursors facilitate the formation of rod-shaped structures at temperatures of 700–900 °C; however, at elevated temperatures (1100–1300 °C), these structures disappear in samples based on crystalline silica, whereas they are retained in amorphous silica-based samples. The growth mechanism of  $\text{Zn}_2\text{SiO}_4$  rods is found to be affected by ZnO precursors that are serving as nucleation sites, and the molten salt environment that promotes atomic diffusion. Furthermore, the produced structures were tested as a potential UV-B rare-earth-free  $\text{Zn}_2\text{SiO}_4$  emitter, and displayed the ability of the material to emit across a broad spectral range. At room temperature, a prominent green emission at 2.38 eV (521 nm), attributed to  $\text{Mn}^{2+}$  impurities, is observed, while low-temperature measurements reveal intense UV-B emission, particularly in amorphous silica-based samples. These findings highlight the potential of the molten salt method to produce high-quality  $\text{Zn}_2\text{SiO}_4$  materials with tailored optical properties offering a sustainable and scalable alternative to rare-earth-based phosphors for applications in medical imaging, scintillators, and radiation detection.

## 1. Introduction

Ultraviolet B (UV-B) radiation (280–315 nm) has attracted considerable attention because of its diverse applications in cosmetics, medicine, agriculture, and microbial inactivation. Studies have demonstrated that UV-B emitters can modulate inflammatory responses in skin diseases [1,2], enhance vitamin D synthesis [3], maintain bone health [3,4], and prevent osteoporosis [5]. In particular, narrowband UV-B is widely employed to treat various skin diseases and disorders, such as vitiligo, psoriasis, dermatitis, erythropoietic protoporphyria, pityriasis rosea, and uremic pruritus [6–12]. Beyond medical applications, UV-B emitting materials are promising for disinfection or even sterilization [13], as eco-friendly alternatives to hazardous agricultural chemicals and pesticides [14], and for bright-field stress sensing [15].

The development of UV-B phosphors has predominantly relied on rare-earth (RE) elements, including cerium [13], praseodymium [16], and gadolinium [17–19]. However, reliance on RE elements presents challenges, such as limited availability, high costs, and environmental concerns associated with their extraction and recycling [20–23]. These challenges have motivated the search for rare-earth-free phosphors as sustainable alternatives.

Wide band gap materials such as  $\text{K}_2\text{ZrSi}_2\text{O}_7$  [24],  $\text{ZnGa}_2\text{O}_4$  [25], and  $\text{ZnAl}_2\text{O}_4$  [26,27] have emerged as promising candidates for rare-earth-free UV emitters.

Zinc ortho-silicate ( $\text{Zn}_2\text{SiO}_4$ ), with a band gap of 5.5–6.2 eV [28–31], has also been extensively studied, primarily as a host matrix for RE and transition metal dopants. However, the potential of undoped  $\text{Zn}_2\text{SiO}_4$  as a UV-B emitter remains largely unexplored. In our previous work, we

\* Corresponding author. Department of Mechanical and Industrial Engineering, Tallinn University of Technology, Ehitajate 5, 19180, Tallinn, Estonia.

E-mail addresses: [rocio.rojas@taltech.ee](mailto:rocio.rojas@taltech.ee), [rociorojas@icv.csic.es](mailto:rociorojas@icv.csic.es) (R.E. Rojas-Hernandez).

<https://doi.org/10.1016/j.ceramint.2025.05.212>

Received 17 March 2025; Received in revised form 5 May 2025; Accepted 13 May 2025

Available online 13 May 2025

0272-8842/© 2025 Elsevier Ltd and Techna Group S.r.l. All rights are reserved, including those for text and data mining, AI training, and similar technologies.

demonstrated that undoped  $\text{Zn}_2\text{SiO}_4$  powders synthesized via the sol-gel method exhibit strong UV-B emission [32], underscoring their potential as a rare-earth-free alternative for UV-B-emitting applications.

Conventionally,  $\text{Zn}_2\text{SiO}_4$  is synthesized using high-temperature solid-state reactions [33,34], where  $\text{ZnO}$  and  $\text{SiO}_2$  react to form zinc silicate. However, these approaches require prolonged processing times, elevated temperatures, and significant energy consumption, often resulting in non-uniform microstructures that limit practical applications.

The molten salt method offers a promising alternative for  $\text{Zn}_2\text{SiO}_4$  synthesis, enabling synthesis at lower temperatures with shorter processing times, uniform particle growth, and precise morphological control [35]. Its simplicity, scalability, and cost-effectiveness make it an attractive option for large-scale phosphor production [35]. Despite the advantages of low-cost investments and fabrication, the molten salt method has been scarcely applied to  $\text{Zn}_2\text{SiO}_4$  synthesis. To date, only two studies have employed this technique: one investigating Mn-doped  $\text{Zn}_2\text{SiO}_4$  [36] and the other exploring the production of  $\text{Zn}_2\text{SiO}_4$  nanowires [37]. The present work particularly focuses on the molten salt synthesis of rare-earth-free  $\text{Zn}_2\text{SiO}_4$  powders using amorphous silica and crystalline silica as silicon sources to evaluate the influence of their reactivity and thermal behavior on phase formation, particle morphology, and luminescent properties. By systematically examining the effects of synthesis temperature and precursor type, this work demonstrates the molten salt method as a practical and adaptable technique for producing  $\text{Zn}_2\text{SiO}_4$ . These results contribute to the advancement of rare-earth-free UV-B-emitting materials that are safer and more environmentally sustainable.

## 2. Experimental section

### 2.1. Synthesis

Rare-earth-free  $\text{Zn}_2\text{SiO}_4$  powders were synthesized using the molten salt method with two distinct silicon sources: crystalline silica with the quartz polymorph (Alfa Aesar, 99.5 %,  $d_{50} \approx 1.21 \mu\text{m}$ ) and amorphous silica (Thermo Fisher Scientific, 99.9 %,  $d_{50} \approx 500 \text{ nm}$ ).  $\text{ZnO}$  (Symrise GmbH, 99.5 %,  $d_{50} \approx 400 \text{ nm}$ ) was used as the zinc source. The molten salt medium consisted of a eutectic mixture of  $\text{NaCl}$  (VWR, 99.5 %) and  $\text{KCl}$  (VWR, 99.5 %) in a 0.5:0.5 M ratio, with a salt to  $\text{Zn}_2\text{SiO}_4$  molar ratio of 3:1.

Stoichiometric amounts of  $\text{ZnO}$  and  $\text{SiO}_2$  (crystalline or amorphous) were combined with the molten salt medium and initially mixed using an agate mortar and pestle. The mixture was further homogenized via planetary ball milling (Model YKM-1) at 250 rpm for 8 h under dry conditions using yttria stabilized zirconia (YSZ) balls and zirconia jars. The homogenized mixtures were heat-treated in air at temperatures ranging from 700 to 1300 °C for 2 h. After cooling, the products were manually ground and sieved through a 37  $\mu\text{m}$  nylon sieve.

The samples prepared with crystalline silica are referred to as crystalline silica-based samples, while those prepared with amorphous silica are referred to as amorphous silica-based samples.

### 2.2. Characterization

#### 2.2.1. Structural, chemical analysis and microstructure characterization

X-ray diffraction (XRD) analysis was conducted to investigate the phase composition of the synthesized powders. The examination was performed at room temperature using a Rigaku SmartLab SE instrument equipped with a D/teX Ultra 250 1D detector. The measurements were performed in a Bragg-Brentano arrangement using  $\text{Cu K}\alpha$  radiation and a  $2\theta$  range of 10–80°. The average crystallite size ( $D$ ) was determined using Williamson-Hall analysis [38]:

$$\beta \cos \theta = \frac{k \lambda}{D} + 4 \varepsilon \sin \theta \quad (1)$$

where  $\lambda$  is the wavelength of the  $\text{Cu-K}\alpha$  radiation (1.54060 Å),  $k$  is the form factor (0.9),  $\beta$  is the peak broadening after instrumental correction (in radians),  $\theta$  is the Bragg diffraction angle, and  $\varepsilon$  represents the lattice strain. The crystallite size was extracted from the y-intercept of the  $\beta \cos \theta$  versus  $4 \sin \theta$  plot.

To investigate the presence of trace impurities, inductively coupled plasma-optical emission spectrometry (ICP-OES) analysis was performed using an IRIS ADVANTAGE Thermo Jarrel Ash from Thermo Fisher Scientific.

Raman spectroscopy measurements were carried out using a Horiba LabRAM HR800 Micro-Raman system with a 532 nm Nd-YAG laser as the excitation source. The morphological and microstructural features were analyzed using field-emission scanning electron microscopy (FE-SEM; Zeiss ULTRA-55).

#### 2.2.2. Thermoanalysis

A PerkinElmer DSC-7 calorimeter was used to conduct thermogravimetric (TG) and differential scanning calorimetry (DSC) studies. The analyses were performed in air, with the temperature increasing from room temperature to 1200 °C at a rate of 10 °C min<sup>-1</sup>.

#### 2.2.3. Luminescence measurements

Luminescence characterization of RE-free  $\text{Zn}_2\text{SiO}_4$  powders was performed using X-ray, electron beam, and synchrotron radiation excitations. X-ray-excited optical luminescence (XEOL) measurements were carried out using an Edinburgh instruments FLS980 spectrometer equipped with a Hamamatsu R298P photomultiplier. X-rays were generated using a Neptune 5200 X-ray tube (Oxford Instruments) operating at voltages ranging from 10 to 50 kV. Cathodoluminescence (CL) analysis was performed using an electron beam with an energy of 10 keV. The low-temperature measurements were performed using an ARS closed-cycle helium cryostat. The comprehensive details of the experimental setup have been published elsewhere [39]. Synchrotron radiation experiments in the 4.5–11 eV energy range were conducted at the FinEstBeAMS beamline, MAX IV Lab, Lund, Sweden [40,41]. To minimize the effects of higher-order incident light on the luminescence excitation spectra,  $\text{MgF}_2$  or fused silica filters were selected based on the specific excitation energy range under study. An Andor Shamrock SR-303i spectrometer equipped with a Hamamatsu H8259-01 photon-counting head was used to detect luminescence. The excitation spectra were normalized to the incident photon flux, which was measured using an energy-calibrated AXUV100G photodiode. The emission spectra were transformed into energy space using the Jacobian transformation procedure.

## 3. Results and discussion

### 3.1. Phase formation and structural analysis

The phase composition of the synthesized powders via the molten salt method was investigated using XRD and Raman spectroscopy. Fig. 1a and b present the XRD patterns of  $\text{Zn}_2\text{SiO}_4$  powders synthesized at temperatures ranging from 700 to 1300 °C using crystalline and amorphous silica as precursors, respectively. At 700 °C, the XRD patterns revealed the coexistence of the  $\alpha\text{-Zn}_2\text{SiO}_4$  (JCPDS No. 37–1485) and  $\beta\text{-Zn}_2\text{SiO}_4$  (JCPDS No. 14–0653) phases, with a higher contribution of  $\beta\text{-Zn}_2\text{SiO}_4$  in an amorphous silica-based sample compared to a crystalline silica-based sample. Additionally, another XRD reflections were observed and attributed to starting raw precursors such as  $\text{ZnO}$ ,  $\text{SiO}_2$ ,  $\text{NaCl}$ , and  $\text{KCl}$ . In a crystalline silica-based sample, the main XRD peaks of  $\text{NaCl}$  ( $2\theta = 31.49^\circ$ ),  $\text{KCl}$  ( $2\theta = 28.58^\circ$ ), and  $\text{ZnO}$  ( $2\theta = 36.25^\circ$ ) exhibited comparable intensities, suggesting similar concentrations of these phases. Low-intensity peaks corresponding to quartz were observed as well. In contrast, an amorphous silica-based sample showed a distinct XRD pattern, where the  $\text{ZnO}$  peak was less prominent. The

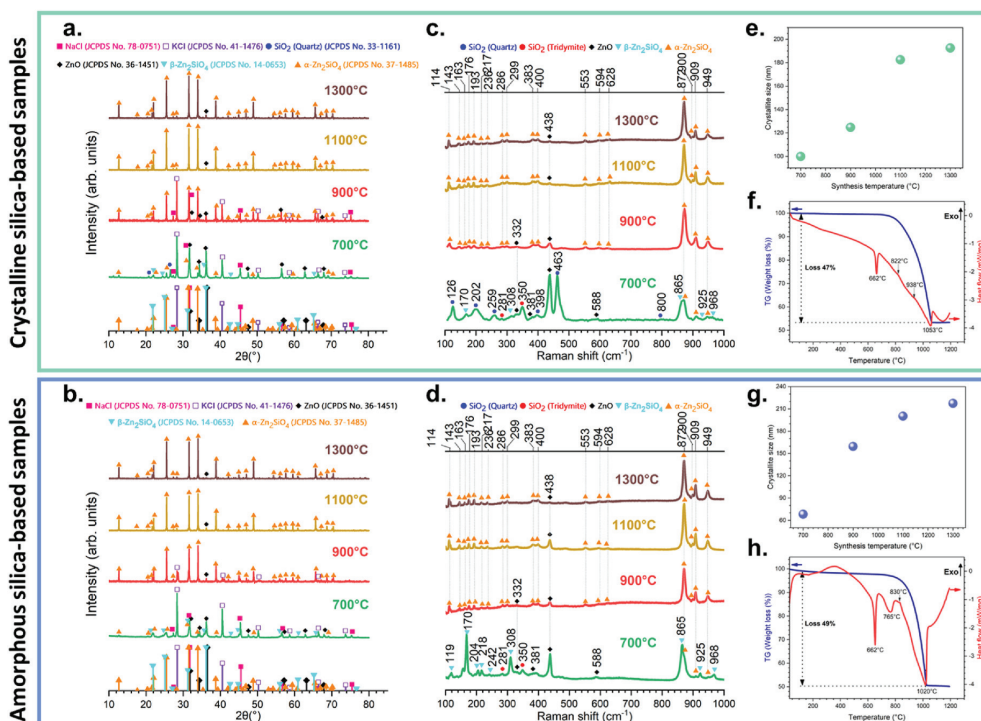


Fig. 1. Structural evolution of  $\text{Zn}_2\text{SiO}_4$  powders synthesized at temperatures ranging from 700 to 1300 °C using crystalline silica (a, c, e, f) and amorphous silica (b, d, g, h) as precursors: XRD data (a, b), Raman spectra (c, d), Crystallite size of  $\alpha\text{-Zn}_2\text{SiO}_4$  (e, g) and thermal analysis (TG: blue; DSC: red) (f, h). (For interpretation of the references to colour in this figure legend, the reader is referred to the Web version of this article.)

formation of the  $\text{Zn}_2\text{SiO}_4$  phases at 700 °C demonstrates that the molten salt flux facilitates precursor diffusion and reaction through reactant interfaces, enabling zinc silicate formation at lower temperatures compared to the conventional solid-state method [42]. The eutectic mixture of NaCl and KCl acts as a liquid medium, improving mass transport, increasing ZnO-SiO<sub>2</sub> contact, and promoting diffusion-driven reactions.

At 900 °C,  $\alpha\text{-Zn}_2\text{SiO}_4$  became the dominant phase in both precursor systems. In crystalline silica-based samples, residual ZnO, NaCl, and KCl peaks were still detectable. In contrast, amorphous silica-based samples exhibited minimal residual ZnO, with significantly reduced intensities of NaCl and KCl peaks. These observations highlight the enhanced reactivity of amorphous silica, attributed to its disordered structure and higher surface energy, which promotes more efficient consumption of ZnO and a greater degree of  $\text{Zn}_2\text{SiO}_4$  formation, i.e. less energy is needed to promote the reaction between ZnO and SiO<sub>2</sub>, showing how crucial is the nature of the precursor when the reaction assisted by the molten salt is kinetically more favourable.

At temperatures above 1100 °C, only ZnO persisted as a secondary phase, with its concentration decreasing further at 1300 °C for amorphous silica-based samples. Interestingly, crystalline silica-based samples exhibited a slight increase in ZnO concentration at 1300 °C. This discrepancy can be explained by the different reactivity and thermal behaviour of silica precursors. Crystalline silica undergoes phase transitions (quartz to cristobalite) at high temperatures, which reduce its reactivity and availability for further reaction with ZnO, resulting in a higher residual ZnO concentration at 1300 °C.

To quantify the phase composition, Rietveld refinement of the XRD patterns was performed for samples synthesized at 1100 and 1300 °C (see Supporting Information S1). For crystalline silica-based samples,

the phase fractions were 97.49 %  $\alpha\text{-Zn}_2\text{SiO}_4$  and 2.51 % ZnO at 1100 °C, and 94.53 %  $\alpha\text{-Zn}_2\text{SiO}_4$  and 5.47 % ZnO at 1300 °C. In contrast, amorphous silica-based samples exhibited phase fractions of 96.1 %  $\alpha\text{-Zn}_2\text{SiO}_4$  and 3.9 % ZnO at 1100 °C, and 98.71 %  $\alpha\text{-Zn}_2\text{SiO}_4$  and 1.29 % ZnO at 1300 °C. These results confirm that amorphous silica promotes a higher conversion rate to  $\text{Zn}_2\text{SiO}_4$ , consistent with its higher reactivity and the observed reduction in residual ZnO at elevated temperatures. The slight increase in ZnO concentration in crystalline silica-based samples at 1300 °C can be attributed to the reduced reactivity of crystalline silica.

The crystallite size of  $\alpha\text{-Zn}_2\text{SiO}_4$  in the synthesized powders, determined using Williamson-Hall analysis to account for both size and strain effects, exhibited a clear increase with temperature, as shown in Fig. 1e and g. For crystalline silica-based samples, the crystallite sizes were 99.87, 124.84, 182.49, and 192.59 nm for the samples synthesized at 700, 900, 1100, and 1300 °C, respectively. In comparison, amorphous silica-based samples yielded crystallite sizes of 68.31, 159.42, 200.21, and 217.47 nm for the same synthesis temperatures. At 700 °C, the amorphous silica-based sample favoured the formation of  $\beta\text{-Zn}_2\text{SiO}_4$ , resulting in smaller crystallite sizes compared to the crystalline silica-based sample, where the contribution of  $\alpha\text{-Zn}_2\text{SiO}_4$  was higher. At higher temperatures (900–1300 °C), the higher reactivity of amorphous silica promoted more complete crystallization of  $\alpha\text{-Zn}_2\text{SiO}_4$ , leading to larger crystallite sizes. The increase in crystallite size with temperature is consistent with enhanced crystallinity and grain growth, typical of high-temperature solid-state reactions by pressureless synthesis.

To complement the XRD analysis, Raman spectroscopy was employed to investigate the vibrational modes and structural characteristics of the synthesized powders. Fig. 1b and f present the Raman spectra of zinc silicate materials synthesized via the molten salt method,

using crystalline and amorphous silica, respectively. In the crystalline silica-based sample at 700 °C, the Raman spectrum primarily displayed characteristic peaks related to Raman modes of the starting precursor materials, ZnO and SiO<sub>2</sub>. Four Raman modes attributed to ZnO were identified at 332, 381, 438, and 588 cm<sup>-1</sup>, corresponding to the  $E_2^{high}$  –  $E_2^{low}$ ,  $A_1(TO)$ ,  $E_2^{high}$ , and  $E_1(LO)$  vibrational modes, respectively [43]. Additionally, six Raman modes associated with SiO<sub>2</sub> of the quartz polymorph were observed at 126, 202, 259, 398, 463, and 800 cm<sup>-1</sup> assigned to the  $E(TO + LO)$ ,  $A_1$ ,  $E(TO + LO)$ ,  $A_1$ ,  $E(TO)$ , and  $E(LO)$  modes, respectively [44]. Raman modes for the tridymite polymorph of SiO<sub>2</sub> appeared at 281 and 350 cm<sup>-1</sup> [45]. Peaks related to  $\alpha$ -Zn<sub>2</sub>SiO<sub>4</sub> and  $\beta$ -Zn<sub>2</sub>SiO<sub>4</sub> were also detected, confirming the XRD results. In the amorphous silica-based sample, the Raman spectrum exhibited peaks corresponding to ZnO and tridymite, as well as peaks attributed to  $\alpha$ -Zn<sub>2</sub>SiO<sub>4</sub> and  $\beta$ -Zn<sub>2</sub>SiO<sub>4</sub>. The  $\beta$ -Zn<sub>2</sub>SiO<sub>4</sub> polymorph was a dominant phase, with the characteristic peaks at 119, 170, 204, 218, 242, 308, 865, 925, and 968 cm<sup>-1</sup> [46]. The lower intensity of tridymite peaks in this sample compared to the crystalline silica-based sample suggests a more efficient conversion of amorphous silica to tridymite, which subsequently reacts with ZnO to form  $\beta$ -Zn<sub>2</sub>SiO<sub>4</sub>. This behaviour is consistent with the higher reactivity of amorphous silica, which facilitates faster phase transformation under molten salt conditions. The structural origin of  $\beta$ -Zn<sub>2</sub>SiO<sub>4</sub>, which resembles a distorted tridymite or cristobalite framework where silicon atoms are partially replaced by zinc atoms and additional zinc ions occupy interstitial sites [47], further supports this interpretation. These findings demonstrate that amorphous silica is more effective in promoting the formation of  $\beta$ -Zn<sub>2</sub>SiO<sub>4</sub> under molten salt synthesis conditions, making it a preferable precursor for applications requiring this metastable phase. Furthermore, stabilizing the  $\beta$ -Zn<sub>2</sub>SiO<sub>4</sub> phase could expand the functionality of the synthesized materials, making them suitable for applications that benefit from its distinctive characteristics.

Above 900 °C, the spectra were dominated by prominent peaks at 114, 143, 163, 176, 193, 217, 236, 286, 299, 383, 400, 553, 594, 628, 872, 900, 909, and 949 cm<sup>-1</sup>, attributed to  $\alpha$ -Zn<sub>2</sub>SiO<sub>4</sub> [46]. These modes correspond to the vibrations of the [SiO<sub>4</sub>]<sup>4-</sup> and [ZnO<sub>4</sub>]<sup>6-</sup> tetrahedra in the  $\alpha$ -Zn<sub>2</sub>SiO<sub>4</sub> structure. The most intense bands are attributed to the SiO<sub>4</sub> tetrahedra, notably the prominent peak at 872 cm<sup>-1</sup> corresponding to the symmetric Si-O stretching  $\nu_1(A)$  vibration [48]. Additionally, the peaks observed at 900, 909, and 949 cm<sup>-1</sup> are associated with the triply degenerate asymmetric stretching vibrations  $\nu_3(F_2)$  [48]. The Raman modes at 383 and 400 cm<sup>-1</sup> were assigned to the symmetric  $\nu_2(E)$  bending vibrations of the O-Si-O groups [48]. These vibrational assignments were consistent with those of previous studies on similar silicate materials [49–52]. The presence of a peak at 553 cm<sup>-1</sup> and bands in the 594–628 cm<sup>-1</sup> range may be indicative of stretching vibrations from the ZnO<sub>4</sub> tetrahedra [48], although further investigation is required to confirm this interpretation. Low-frequency Raman peaks below 300 cm<sup>-1</sup> are attributed to lattice vibrations [53]. Although Raman peaks corresponding to ZnO were still present at 900 °C, their intensities diminished at higher temperatures, indicating an ongoing reaction between ZnO and silica to form Zn<sub>2</sub>SiO<sub>4</sub>. To further investigate the structural properties, the full width at half maximum (FWHM) of the main Raman peak of  $\alpha$ -Zn<sub>2</sub>SiO<sub>4</sub> at 872 cm<sup>-1</sup> was analyzed (see Supporting Information S2). The FWHM values were 11.06, 8.45, and 8.41 cm<sup>-1</sup> for crystalline silica-based samples synthesized at 900, 1100, and 1300 °C, respectively. For amorphous silica-based samples, the corresponding values were 8.26, 8.18, and 8.14 cm<sup>-1</sup>. The values of FWHM calculated agree with the ones estimated for this type of forsterite structure shown by different authors [54]. The decrease in FWHM with increasing temperature reflects improved crystallinity, consistent with the XRD and crystallite size analysis. These results further support the higher reactivity of amorphous silica, which promotes more complete crystallization and phase formation compared to crystalline silica.

The combined XRD and Raman analyses demonstrate that the molten

salt method enables the formation of Zn<sub>2</sub>SiO<sub>4</sub> at relatively low temperatures, with amorphous silica promoting higher reactivity and the formation of the metastable  $\beta$ -Zn<sub>2</sub>SiO<sub>4</sub> phase. The decrease in FWHM values and increase in crystallite size with temperature confirm the improved crystallinity, highlighting the potential of this method for producing high-quality Zn<sub>2</sub>SiO<sub>4</sub> materials.

### 3.2. Thermal analysis

To investigate the thermal behaviour of the molten salt together with the zinc oxide and silica precursors, TG and DSC analyses were conducted on the ZnO + SiO<sub>2</sub> + (NaCl and KCl) mixture, as shown in Fig. 1f (crystalline silica-based samples) and Fig. 1h (amorphous silica-based samples). The TG curves revealed a significant mass reduction of 47 % and 49 % between 25 °C and 1050 °C for crystalline and amorphous silica-based samples, respectively, primarily due to the evaporation of the NaCl-KCl eutectic mixture. The higher mass reduction in the amorphous silica-based sample further confirms its enhanced reactivity compared to crystalline silica, consistent with XRD and Raman results. Above 1050 °C, the weight loss rate decreased, indicating near-complete salt evaporation.

The DSC curves showed a sharp endothermic peak at approximately 662 °C, corresponding to the melting of the NaCl-KCl eutectic mixture [55]. This melting event facilitates the diffusion-driven reaction between ZnO and SiO<sub>2</sub>, consistent with the onset of Zn<sub>2</sub>SiO<sub>4</sub> formation at 700 °C observed in XRD and Raman analyses. In the amorphous silica-based samples, an additional endothermic peak at 763 °C is attributed to the crystallization of the  $\beta$ -Zn<sub>2</sub>SiO<sub>4</sub> phase, aligning with the preferential formation of  $\beta$ -Zn<sub>2</sub>SiO<sub>4</sub> in amorphous silica.

Another endothermic peak at 822 °C (crystalline silica-based samples) and 830 °C (amorphous silica-based samples) corresponds to the formation of the  $\alpha$ -Zn<sub>2</sub>SiO<sub>4</sub> phase, consistent with its dominance XRD and Raman results for the samples synthesized at 900 °C. A peak at 938 °C likely reflects the vaporization of residual NaCl and KCl particles not fully incorporated into the eutectic mixture [56]. Finally, a complete weight loss occurred at 1020 °C (amorphous silica-based samples) and 1053 °C (crystalline silica-based samples), consistent with the thermal decomposition of molten salts [55].

To conclude, taking into account the thermal analysis carried out in the mixture of eutectic salt, silica and ZnO, the liquid media foster the reaction at lower temperatures, which is reflected in the presence of the endothermic peaks at 700 and 763 °C. The chemical reactivity is higher by using amorphous silica that implies the formation of  $\beta$ -Zn<sub>2</sub>SiO<sub>4</sub>, probably because silicon tetrahedra of amorphous silica are able to move easier than in the crystalline form.

### 3.3. Microstructural and morphological characterization

SEM analysis (Fig. 2) was employed to investigate the influence of precursor selection and synthesis temperature on the morphology of Zn<sub>2</sub>SiO<sub>4</sub> powders.

At 700 °C, the powders consisted of irregularly shaped particles with the initial emergence of rod-like structures, which became more pronounced at 900 °C. Statistical analysis using ImageJ software revealed specific size distributions: for crystalline silica-based samples, the rods measured 1.52–10 µm in length and 0.37–1.31 µm in diameter. In contrast, amorphous silica-based samples exhibited smaller rods, with lengths ranging from 0.72 to 8.33 µm and diameters from 0.31 to 0.91 µm. At elevated temperatures (1100 and 1300 °C), crystalline silica-based samples displayed increased particle agglomeration, leading to the disappearance of rod-like structures. Conversely, amorphous silica-based samples retained these structures, highlighting the critical role of the silica precursor in determining the final morphology. While rod-shaped Zn<sub>2</sub>SiO<sub>4</sub> particles are commonly associated with wet-chemical synthesis methods [57], their formation in molten salt synthesis is less understood. In wet-chemical processes, rod growth typically occurs



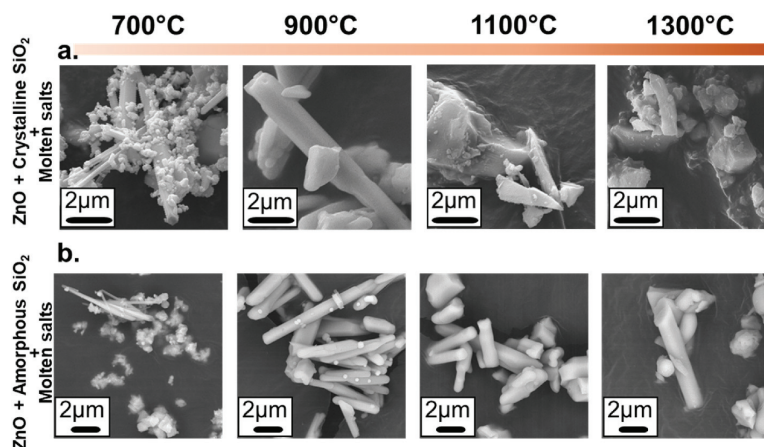


Fig. 2. SEM micrographs of  $\text{Zn}_2\text{SiO}_4$  powders synthesized at 700, 900, 1100, and 1300 °C using (a) crystalline silica and (b) amorphous silica as precursors.

through mechanisms such as oriented attachment or Ostwald ripening, where smaller particles dissolve and redeposit onto larger structures. In contrast, the molten salt environment appears to facilitate a seed-growth mechanism, with ZnO precursors serving as nucleation sites for the formation of  $\text{Zn}_2\text{SiO}_4$  rods [57].

To further investigate this phenomenon, both ZnO powder and amorphous  $\text{SiO}_2$  powder were separately mixed with a eutectic KCl-NaCl mixture and heat-treated at 900 °C. This approach allowed for a detailed examination of the individual roles of ZnO and  $\text{SiO}_2$  in the synthesis process.

Morphological examination of the starting materials revealed distinct characteristics. The amorphous silica particles shown in Fig. 3a displayed uniform spherical features, while the crystalline silica particles presented in Fig. 3b exhibited irregular morphology. The as-received ZnO particles (Fig. 3c) underwent significant morphological changes, upon heat treatment with the eutectic salt mixture, evolving into well-defined rod-like structure, as shown in Fig. 3e. This transformation highlights the ability of ZnO to act as a structural template, guiding the growth of  $\text{Zn}_2\text{SiO}_4$  rods. Conversely, the heat-treated amorphous  $\text{SiO}_2$  particles shown in Fig. 3d revealed the increase in size, forming interconnected networks rather than distinct rod-like shapes. This difference in behaviour underscores the critical role of ZnO in directing the morphology of the final product. The molten salt

eutectic mixture played a pivotal role in facilitating these transformations. By enhancing atomic diffusion at the ZnO- $\text{SiO}_2$  interface, the molten salt environment enabled the efficient transport of reactants, promoting the growth of rod-like  $\text{Zn}_2\text{SiO}_4$  structures. A schematic representation of the proposed mechanism is provided in Fig. 3f, which offers a clear visualization of the process.

These findings underscore the importance of precursor reactivity and particle size in tailoring the morphology of  $\text{Zn}_2\text{SiO}_4$ . Amorphous silica, with its higher reactivity and disordered structure, facilitates the retention of rod-like structures even at elevated temperatures. In contrast, crystalline silica leads to increased agglomeration and the loss of such morphological features. This study provides valuable insights into the mechanisms governing  $\text{Zn}_2\text{SiO}_4$  synthesis and demonstrates the potential of the molten salt method for controlling the morphology of zinc silicate materials.

Having established the structural and morphological characteristics of the synthesized  $\text{Zn}_2\text{SiO}_4$  powders, we now turn to their luminescent properties, which were investigated using a combination of spectroscopic techniques under varying excitation sources.

#### 3.4. Luminescence studies

Luminescence studies were conducted using three complementary

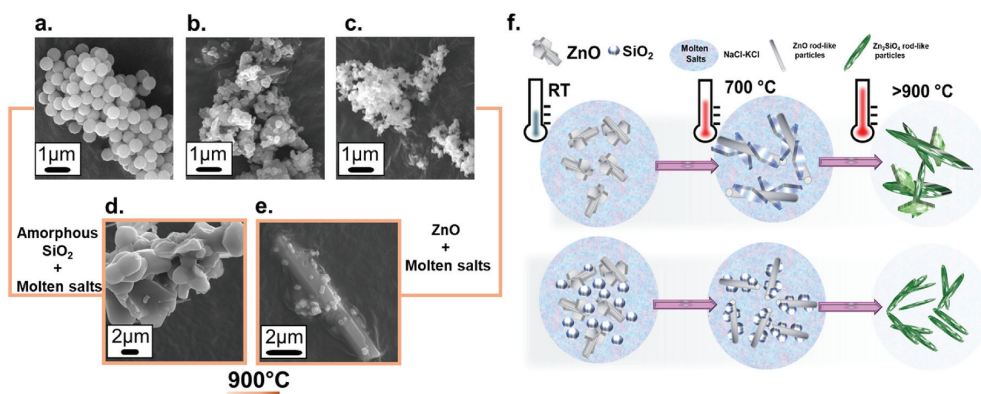


Fig. 3. SEM micrographs of as-received powders: (a) amorphous silica, (b) crystalline silica, and (c) ZnO; and after heat treatment at 900 °C with a KCl-NaCl eutectic mixture: (d) amorphous silica and (e) ZnO. (f) Schematic of  $\text{Zn}_2\text{SiO}_4$  rod-like particle formation via molten salt synthesis.



techniques: X-ray-excited optical luminescence at room temperature, cathodoluminescence at both RT and 6 K, and photoluminescence under synchrotron radiation excitation at 6 K. These approaches were chosen to comprehensively characterize the emission properties of the  $\text{Zn}_2\text{SiO}_4$  materials, spanning a wide range of excitation energies and temperature conditions. The molten salt synthesis method played a pivotal role in tailoring the luminescent properties by enhancing precursor reactivity, promoting defect formation, and enabling the formation of  $\text{Zn}_2\text{SiO}_4$  phase at lower temperatures compared to conventional solid-state method.

XEOL, in particular, is a powerful spectroscopic technique for studying materials that convert absorbed X-ray energy into light in the optical region (UV to NIR) [58,59]. XEOL offers unique advantages over conventional UV/visible excitation methods, particularly for materials with complex compositions or multiple dopants, as it provides insights into both surface and bulk luminescent properties [60]. This technique has been effectively used to study silicate-based nanoscale scintillators, which exhibit strong luminescence under X-ray excitation, making them suitable for such applications as X-ray-induced photodynamic therapy [61]. In this study, XEOL was employed to investigate the luminescent properties of  $\text{Zn}_2\text{SiO}_4$  materials at room temperature, as shown in Fig. 4a and b. A prominent green emission band at 2.38 eV (521 nm) was observed and attributed to  $\text{Mn}^{2+}$  transitions [62]. Although Mn was not intentionally added during synthesis, analysis by ICP-OES enabled the detection of Mn with concentrations less than 0.01 wt%. This low concentration demonstrates that the incorporation of Mn cation into  $\text{Zn}_2\text{SiO}_4$  lattice is highly effective. It is well established that  $\text{Mn}^{2+}$  substitutes  $\text{Zn}^{2+}$  in tetrahedral sites and acts as luminescence center with high quantum efficiency [62,63], explaining the observation of the characteristic green emission even at such minimal impurities' levels. This observation aligns with the extreme sensitivity of luminescence

techniques to Mn, and even small impurities can be detected. This green emission enhances the functional versatility of the synthesized materials. Furthermore, it aligns with previous studies on silicate-based materials, which have consistently demonstrated strong XEOL activity in the visible range, particularly within the green spectral region [63]. The observation of this green emission even at 700 °C highlights the effectiveness of the molten salt method in facilitating enhanced precursor reactivity and  $\text{Zn}_2\text{SiO}_4$  phase formation at lower temperatures, which is not typically achievable with conventional solid-state synthesis. The intensity of this emission band increased with synthesis temperature in crystalline silica-based samples, reflecting enhanced crystallinity (Fig. 4c). Amorphous silica-based samples exhibited more intense green emission, with the sample synthesized at 1100 °C showing the highest intensity (Fig. 4c). At lower synthesis temperatures (700 °C), a weak emission band at 3.13 eV (396 nm) was observed, attributed to the free exciton transition or near-band-edge (NBE) emission of ZnO [64, 65]. As the temperature increased, additional emission bands emerged in crystalline silica-based samples including a band at 2.74 eV (452 nm) attributed to zinc-related defects ( $\text{Zn}_i \rightarrow V_{\text{Zn}}$  transitions) [66–68], a band at 2.98 eV (416 nm) linked to a radiative transition between the  $\text{Zn}_i$  level and valence band [69], and a band at 3.04 eV (408 nm) associated with silica-related defects [70–72]. A key finding of this study is the observation of UV-B emission bands at 3.93 eV (315 nm) and 4.36 eV (284 nm) at higher synthesis temperatures (1100–1300 °C), particularly in crystalline silica-based samples. As has been stated in the previous work [32], there is an absorption band at 370 nm (3.35 eV) that it is noticeably suppressed when mainly  $\text{Zn}_2\text{SiO}_4$  phase is predominant in the material. This can cause emission reabsorption that may be responsible for the distortion of the recorded emission spectra and a dip observed in these at 3.35 eV (370 nm).

To the best of our knowledge, this is the first report of UV-B emissions

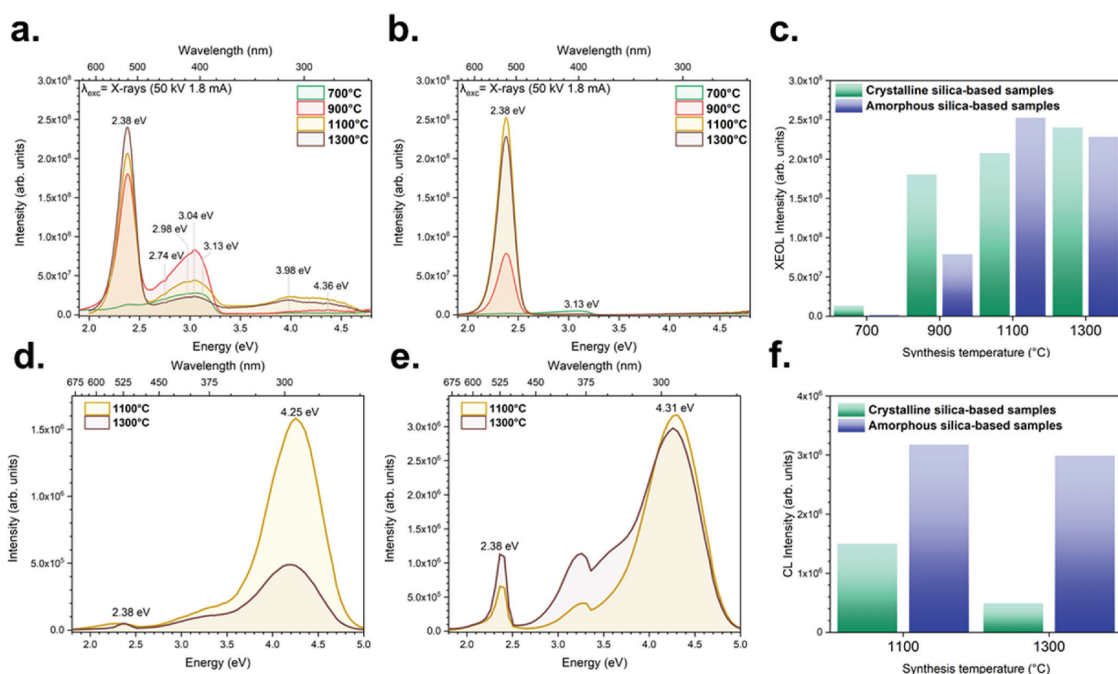


Fig. 4. Room-temperature XEOL spectra of  $\text{Zn}_2\text{SiO}_4$  powders synthesized at 700, 900, 1100, and 1300 °C using (a) crystalline silica and (b) amorphous silica. (c) XEOL intensity of green emission as a function of synthesis temperature. CL spectra of  $\text{Zn}_2\text{SiO}_4$  powders synthesized at 1100 and 1300 °C using (d) crystalline silica and (e) amorphous silica, recorded at 6 K. (f) CL intensity of UV-B emission as a function of synthesis temperature. (For interpretation of the references to colour in this figure legend, the reader is referred to the Web version of this article.)

in  $\text{Zn}_2\text{SiO}_4$  systems synthesized via the molten salt method, demonstrating the ability of the material to emit across a broad spectral range, from UV to visible. These UV-B emissions will be explored in detail in subsequent sections. The observed luminescent properties, combined with the stability of the material and efficient energy conversion under X-ray excitation, highlight the potential of  $\text{Zn}_2\text{SiO}_4$  for applications in medical imaging, scintillators, and radiation detectors, where deep-penetrating radiation and high luminescence efficiency are essential [61].

The luminescent properties of the materials were further investigated through CL characterization at both RT & 6 K, with a focus on samples synthesized at 1100 and 1300 °C. At room temperature (see Supporting Information S3), amorphous silica-based samples exhibited a dominant green emission at 2.38 eV (521 nm), while their crystalline silica-based counterparts displayed weaker Mn-associated luminescence. Both systems showed a broad emission band spanning 2.5–5 eV, which overlaps with the UV-B spectral region, making it challenging to clearly resolve the UV-B emission at room temperature. To address this, low-temperature measurements were employed based on the prior findings for  $\text{Zn}_2\text{SiO}_4$  powders synthesized via the sol-gel method, which demonstrated that UV-B emissions are significantly enhanced at cryogenic temperatures [32]. These conditions allowed for a more detailed analysis of the emission behaviour under electron beam excitation.

The CL emission spectra recorded at 6 K for the materials synthesized at 1100 and 1300 °C are shown in Fig. 4d and e. At this temperature, a significant enhancement in the intensity of the UV-B emission bands was observed, particularly in samples prepared using amorphous silica. The samples synthesized at 1100 °C exhibited the highest UV-B emission intensity for both precursor types, with the amorphous silica-based sample showing approximately double the intensity of the crystalline silica-based sample (Fig. 4f). However, for the samples synthesized at

1300 °C, the UV-B emission intensity decreased by two-thirds in the crystalline silica-based sample, while only a slight reduction was observed in the amorphous silica-based sample (Fig. 4f). This trend aligns with the structural and phase composition analysis, which demonstrated the higher reactivity of amorphous silica and its ability to promote more complete  $\text{Zn}_2\text{SiO}_4$  formation, as evidenced by the reduced residual ZnO content at elevated temperatures. The observed behaviour suggests that an optimal concentration of the secondary ZnO phase plays a critical role in enhancing or suppressing the UV-B emission.

The UV-B emission, centred at 4.25 eV (292 nm) in crystalline silica-based samples and slightly blue-shifted to 4.31 eV (288 nm) in amorphous silica-based samples, is attributed to perturbed crystal lattice governed by local defects [32]. This emission is relatively rare in  $\text{Zn}_2\text{SiO}_4$ , with limited reports in zinc silicate films and nanocables [73–76]. A broad band in the region of 2.7–3.8 eV, which is reabsorption-distorted in our samples, has been attributed to  $\text{Zn}^{2+}$  ions in [77].

These results reveal the strong interdependence of phase composition, microstructure, and luminescent properties, highlighting how precursor selection and synthesis temperature critically influence the optical behaviour of  $\text{Zn}_2\text{SiO}_4$  materials.

To further elucidate the electronic transitions and defect-related emissions in the  $\text{Zn}_2\text{SiO}_4$  materials, photoluminescence studies were conducted under synchrotron radiation excitation at 6 K at the FinEst-BeAMS beamline. Given that the CL studies indicated that samples synthesized at 1100 °C exhibited the highest emission intensity, we focused our synchrotron radiation investigations on these samples. These measurements provided additional insights into the UV-B emission bands and their dependence on synthesis conditions, complementing the findings from XEOL and CL studies.

The 2D excitation-emission maps in Fig. 5a (crystalline silica-based

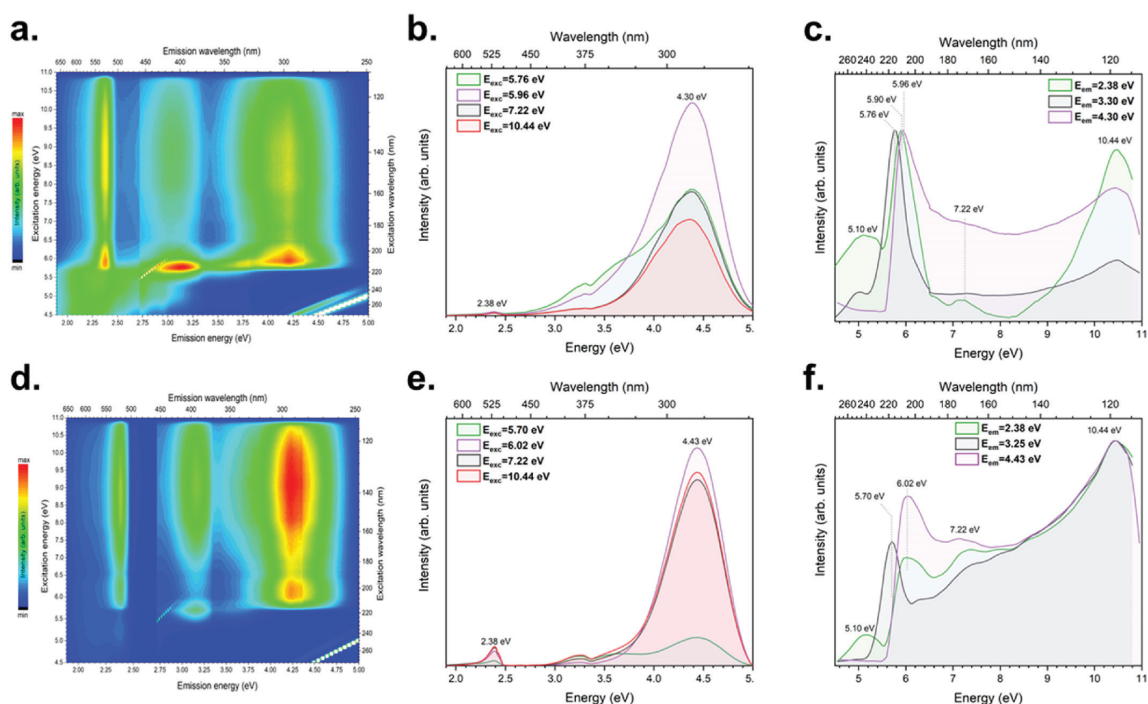


Fig. 5. (a, d) 2D excitation-emission maps, (b, e) emission spectra, and (c, f) normalized excitation spectra at 6 K of  $\text{Zn}_2\text{SiO}_4$  powders synthesized at 1100 °C using (a–c) crystalline silica and (d–f) amorphous silica upon synchrotron-ray excitation.

sample) and Fig. 5d (amorphous silica-based sample) illustrate the luminescence intensity as a function of excitation energy at 6 K, with a colour gradient indicating the normalized intensity (red for the highest intensity and blue for the lowest). Diagonal lines at the bottom of the images represent the excitation light and its second-order diffraction passing through the secondary monochromator. Analysis of the contour plots revealed three distinct emission bands: a green emission peak at 2.38 eV (521 nm), a second band spanning 2.85–3.40 eV, and a deep UV band extending from 3.45 to 4.80 eV. The deep UV emission was the most intense, particularly in amorphous silica-based samples, with excitation energies ranging from 5.60 to 10.80 eV, further corroborating the enhanced luminescent properties of these materials.

For a more detailed analysis, the spectra were extracted from the contour plots and corrected for the spectral sensitivity of the detection system. Notably, the raw data presented in the maps exhibit a slight shift compared to the corrected spectra. Fig. 5b and e display the emission spectra of the crystalline and amorphous silica-based samples, respectively, under specific excitation energies. In crystalline silica-based sample, the spectra were recorded at excitation energies of 5.76, 5.96, 7.22, and 10.44 eV, while for amorphous silica-based sample, the excitation energies were 5.70, 6.02, 7.22, and 10.44 eV. The emission spectra revealed distinct bands in both sample types. A weak green emission centred at 2.38 eV (521 nm) was observed, attributed to  $\text{Mn}^{2+}$  impurities, consistent with the XEOL and CL results. The most prominent feature was a broad UV-B emission band, centred at 4.30 eV (288 nm) for crystalline silica-based sample, which reached maximum intensity under 5.96 eV excitation. In contrast, the amorphous silica-based sample exhibited a slightly blue-shifted UV-B emission peaking at 4.43 eV (280 nm) under 6.02 eV excitation.

To gain deeper insight into the origin of the observed emission bands, the excitation spectra were recorded at 6 K, as illustrated in Fig. 5c and f. The excitation spectrum for the green emission in the crystalline silica-based sample exhibits distinct bands at 5.10 eV (243 nm) and 5.90 eV (210 nm), along with a shoulder at 7.22 eV (172 nm) and a prominent band at 10.44 eV (118 nm). In the amorphous silica-based sample, the second band shifts to 6.02 eV (206 nm), while the other features remain consistent. The 5.10 eV (243 nm) peak is attributed to the direct excitation of  $\text{Mn}^{2+}$  ions within the  $\text{Zn}_2\text{SiO}_4$  crystal lattice [78,79].

The excitation spectrum of the UV-B emission reveals an onset at approximately 5.96 eV (208 nm) for the crystalline silica-based sample and 6.02 eV (206 nm) for the amorphous silica-based sample, aligning with the estimated band gap of  $\text{Zn}_2\text{SiO}_4$  single crystals derived from partial densities of states (PDOS) calculations [80]. This suggests that the UV-B emission originates from intrinsic electronic transitions within the  $\text{Zn}_2\text{SiO}_4$  material, likely due to self-trapped excitons or excitons perturbed by lattice defects, such as oxygen vacancies [32]. Additional experiments, such as electron paramagnetic resonance (EPR) studies, could provide further insights into the nature of these defects.

First-principles calculations reported in the literature for the electronic band structure of  $\text{Zn}_2\text{SiO}_4$  provided further insights into the excitation mechanisms. The spectral features around 7.22 eV (172 nm) are associated with excitation of the  $[\text{SiO}_4]^{4-}$  cluster [79,81,82], while the 10.44 eV (118 nm) peak corresponds to excitation of the  $[\text{ZnO}_4]^{6-}$  cluster [79,81–83]. In the amorphous silica-based sample, the 10.44 eV (118 nm) band is particularly prominent, indicating a stronger contribution from the  $[\text{ZnO}_4]^{6-}$  cluster. For the emission around 3.3 eV (376 nm), the maximum excitation energy shifts to 5.76 eV (215 nm) in the crystalline silica-based sample, whereas a band at 5.70 eV (218 nm) is detected in the amorphous silica-based sample.

These findings highlight the intricate relationship between intrinsic electronic transitions, defect-related processes, and the luminescent properties of  $\text{Zn}_2\text{SiO}_4$ . The enhanced UV-B emission in amorphous silica-based samples demonstrates the potential of the molten salt method to tailor optical properties, paving the way for further exploration of  $\text{Zn}_2\text{SiO}_4$  in advanced applications.

#### 4. Conclusions

In this study, the rare-earth-free  $\text{Zn}_2\text{SiO}_4$  powders were processed by the molten salt method to tune the microstructural, structural and optical properties of  $\text{Zn}_2\text{SiO}_4$ . Both amorphous and crystalline silica precursors enabled the formation of  $\alpha$ - and  $\beta$ - $\text{Zn}_2\text{SiO}_4$  polymorphs at the relatively low temperature of 700 °C. Amorphous silica demonstrated the superior reactivity and promoted stabilization of the  $\beta$ - $\text{Zn}_2\text{SiO}_4$  phase more effectively as compared to crystalline silica. Mechanism of the growth of the rod-shaped crystals was proposed to follow the known “template mechanism”. Structural and morphological analyses evidenced that amorphous silica promoted higher phase purity, enhanced crystallinity, and the retention of rod-like structures at elevated temperatures, while crystalline silica leads to increased agglomeration and reduced reactivity. Luminescence studies have demonstrated the material’s ability to emit across a broad spectral range. At room temperature, XEOL measurements identified a prominent green emission attributed to  $\text{Mn}^{2+}$  impurities, with intensity increasing as a function of synthesis temperature. Low-temperature CL and PL studies revealed an intense UV-B emission, particularly in amorphous silica-based samples, arising from intrinsic electronic transitions or defect-related processes. Furthermore,  $\text{Zn}_2\text{SiO}_4$  microstructural and structural modifications allow to tune the UV-B emission in terms of intensity. The coexistence of  $\alpha$ - and  $\beta$ - $\text{Zn}_2\text{SiO}_4$  polymorphs along with the dual emission of the material in the green and UV-B regions highlights its potential for multifunctional applications. The molten salt method proved to be a versatile and scalable approach, offering shorter processing time and simplified equipment demands for the synthesis of silicate-based phosphor materials. This work provides valuable insights into the synthesis mechanism and optimization of  $\text{Zn}_2\text{SiO}_4$  materials for advanced applications in medical imaging, scintillators, and radiation detection, paving the way for further exploration of rare-earth-free luminescent materials.

#### CRediT authorship contribution statement

**Jallouli Necib:** Writing – review & editing, Writing – original draft, Visualization, Validation, Methodology, Investigation, Formal analysis, Conceptualization. **Eduard Feldbach:** Writing – review & editing, Validation, Methodology. **Ivo Romet:** Writing – review & editing, Validation, Methodology. **Iviti Nagirnyi:** Writing – review & editing, Validation, Investigation. **Irina Hussainova:** Writing – review & editing, Supervision, Investigation, Funding acquisition. **Thomas Jüstel:** Writing – review & editing, Supervision, Investigation. **Rocío E. Rojas-Hernandez:** Writing – review & editing, Writing – original draft, Visualization, Validation, Supervision, Resources, Methodology, Investigation, Formal analysis, Data curation, Conceptualization.

#### Declaration of competing interest

The authors declare that they have no known competing financial interests or personal relationships that could have appeared to influence the work reported in this paper.

#### Acknowledgments

The financial support from the Estonian Research Council (grants PSG-466 (R. E. Rojas-Hernandez), PRG-643 (I. Hussainova), PRG2733 (V. Nagirnyi)) is gratefully acknowledged. Researchers from the University of Tartu, Estonia were supported also by the ERDF funding’s in Estonia granted to the Centre of Excellence TK141 “Advanced materials and high-technology devices for sustainable energetics, sensorics and nanoelectronics (HiTechDevices)” (grant no. TK141 2014–2020.4.01.15-0011). We acknowledge MAX IV Laboratory for time on Beamline FinEstBeAMS under Proposal 20230209. Research conducted at MAX IV, a Swedish national user facility, is supported by the Swedish Research Council under contract 2018–07152, the Swedish

Governmental Agency for Innovation Systems under contract 2018–04969, and Formas under contract 2019–02496.

## Appendix A. Supplementary data

Supplementary data to this article can be found online at <https://doi.org/10.1016/j.ceramint.2025.05.212>.

## References

- [1] T. Tanaka, N. Sasaki, A. Krisnanda, M. Shinohara, H.Z. Amin, S. Horibe, K. Ito, M. Iwaya, A. Fukunaga, K.I. Hirata, Y. Rikitake, Novel UV-B phototherapy with a light-emitting diode device prevents atherosclerosis by augmenting regulatory t-cell responses in mice, *J. Am. Heart Assoc.* 13 (2024) e031639, <https://doi.org/10.1161/JAHA.123.031639>.
- [2] J. Ye, H. Huang, G. Luo, L. Yin, B. Li, S. Chen, H. Li, Y. Yang, Y. Yang, NB-UVB irradiation attenuates inflammatory response in psoriasis, *Dermatol. Ther.* 33 (2020) e13626, <https://doi.org/10.1111/dth.13626>.
- [3] W. Liu, Y. Wang, H. Qiu, D. Chen, S. Wu, Q. Ji, B. Chang, Y. Li, H. Zhao, Y. Tan, Y. Gu, Long-term ultraviolet B irradiation at 297 nm with light-emitting diode improves bone health via vitamin D regulation, *Biomed. Opt. Express* 15 (2024) 4081–4100, <https://doi.org/10.1364/BOE.520348>.
- [4] R. Guo, Y. Du, S. Zhang, H. Liu, Y. Fu, The effects of ultraviolet supplementation to the artificial lighting on rats' bone metabolism, bone mineral density, and skin, *J. Photochem. Photobiol. B Biol.* 188 (2018) 12–18, <https://doi.org/10.1016/j.jphotobiol.2018.08.020>.
- [5] S. Ochial, Y. Nishida, Y. Higuchi, D. Morita, K. Makida, T. Seki, K. Ikuta, S. Imagama, Short-range UV-LED irradiation in postmenopausal osteoporosis using ovariectomized mice, *Sci. Rep.* 11 (2021) 7875, <https://doi.org/10.1038/s41598-021-86730-0>.
- [6] R.P. Sonekar, S.K. Omanwar, S.V. Moharil, S.M. Dhopte, P.L. Muthal, V. K. Kondawar, Combustion synthesis of narrow UVB emitting rare earth borate phosphors, *Opt. Mater.* 30 (2007) 622–625, <https://doi.org/10.1016/j.optmat.2007.02.016>.
- [7] A. Bishnoi, D. Parsad, Phototherapy for vitiligo: a narrative review on the clinical and molecular aspects, and recent literature, *Photodermatol. Photoimmunol. Photomed.* 40 (2024) e12968, <https://doi.org/10.1111/phpp.12968>.
- [8] G. Gaitanis, L. Feldmeyer, R. Wolf, Acquired reactive perforating dermatosis within poikiloderma of civatte elicited by narrow-band UVB therapy for psoriasis, *JEADV Clin. Pract.* (2024) 1–4, <https://doi.org/10.1002/jvc2.567>.
- [9] E. Tung-Hahn, H.N. Gray, J. Schneider, L. Moy, R. Moy, Adjunctive treatment of atopic dermatitis with novel at-home handheld narrow-band UVB phototherapy, *Arch. Dermatol. Res.* 316 (2024), <https://doi.org/10.1007/s00403-024-03271-y>.
- [10] S. Tintle, A. Alikhan, M.E. Horner, J.L. Hand, D.M.R. Davis, Cutaneous porphyrias part II: treatment strategies, *Int. J. Dermatol.* 53 (2014) 3–24, <https://doi.org/10.1111/ijd.12016>.
- [11] N. Dąbrowska, P. Węgrzyn, K. Węgrzyn, G. Laskowski, A. Salińska, M. Wasilewski, J. Skwara, A. Góra, M. Nowicki, D. Barański, Pityriasis rosea: a distinct entity or viral exanthem? *Dermatol. Rev. Przegl. Dermatol.* 111 (2024) 198–208, <https://doi.org/10.5114/dr.2024.143025>.
- [12] G.B. Soares, G. Yosipovitch, Pruritus: an approach to diagnosis and management for the inpatient dermatologist, *Curr. Dermatol. Rep.* 12 (2023) 125–135, <https://doi.org/10.1007/s13671-023-00392-x>.
- [13] X. Lin, C. Li, S. Xu, J. Wang, H. Yang, Y. Qu, Q. Chen, Z. Li, M. Su, G. Liu, H. Liu, Smart windows based on ultraviolet-B persistent luminescence phosphors for bacterial inhibition and food preservation, *Food Chem.* 448 (2024) 139142, <https://doi.org/10.1016/j.foodchem.2024.139142>.
- [14] R. Hidalgo-Sanz, M.A. Del-Castillo-Alonso, S. Sanz, C. Olarte, J. Martínez-Abaigar, E. Núñez-Olivera, The two mycological sides of Ultraviolet-B radiation: harmless for mushroom mycelia, harmful for mycopathogenic mould spores, *Agriculture* 14 (2024) 681, <https://doi.org/10.3390/agriculture14050681>.
- [15] X. Yang, D. Chen, Y. Liang, S. Zhou, J. Xu, L. Liu, H. Lin, Y. Xiong, Y. Cheng, Y. Wang, Energy focusing reinforced narrowband ultraviolet-B mechanoluminescence for bright-field stress visualization, *J. Mater. Chem. C* 11 (2023) 6912–6919, <https://doi.org/10.1039/D3TC00722G>.
- [16] S. Yan, Y. Liang, J. Liu, D. Chen, S. Miao, J. Bi, K. Sun, Development of ultraviolet-B long-lived persistent phosphors in Pr<sup>3+</sup>-doped garnets, *J. Mater. Chem. C* 9 (2021) 14730–14739, <https://doi.org/10.1039/D1TC03819B>.
- [17] V. Singh, J.K. Lee, M. Seshadri, A.A. Bhat, S. Watanabe, T.K.G. Rao, Photoluminescence and EPR spectroscopic studies on narrowband ultraviolet-B (NB-UVB) emitting trivalent gadolinium-doped CaAl<sub>2</sub>O<sub>7</sub> material for phototherapy lamps, *Ceram. Int.* 50 (2024) 4632–4639, <https://doi.org/10.1016/j.ceramint.2023.11.207>.
- [18] Y. Kikuchi, S. Matsuyama, S. Kawamura, F. Fujishiro, M. Miwa, S. Toyama, Experimental investigation on UV light output of YPO<sub>4</sub>:Gd particles for ion beam induced fluorescence microscopy, *Nucl. Instrum. Methods Phys. Res. B* 557 (2024) 165518, <https://doi.org/10.1016/j.nimb.2024.165518>.
- [19] W. Zhao, L. Li, T. Li, J. Qiu, Y. Yang, UV-B-persistent luminescence of CaF<sub>2</sub>:Gd<sup>3+</sup> for radiation labeling and tracing, *Adv. Opt. Mater.* 12 (2024), <https://doi.org/10.1002/adom.202401320>.
- [20] P. Wang, Y.Y. Yang, O. Heidrich, L.Y. Chen, L.H. Chen, T. Fishman, W.Q. Chen, Regional rare-earth element supply and demand balanced with circular economy strategies, *Nat. Geosci.* 17 (2024) 94–102, <https://doi.org/10.1038/s41561-023-01350-9>.
- [21] M. Danouche, A. Bounaga, A. Oulkhir, R. Boulif, Y. Zeroual, R. Benhida, K. Lyamlouli, Advances in bio/chemical approaches for sustainable recycling and recovery of rare earth elements from secondary resources, *Sci. Total Environ.* 912 (2024) 168811, <https://doi.org/10.1016/j.scytot.2024.07.022>.
- [22] H. Diao, H. Yang, T. Tan, G. Ren, M. You, L. Wu, M. Yang, Y. Bai, S. Xia, S. Song, M. Quintana, Navigating the rare earth elements landscape: challenges, innovations, and sustainability, *Miner. Eng.* 216 (2024) 108889, <https://doi.org/10.1016/j.mineng.2024.108889>.
- [23] A. Barros, N. Ledos, R. Valleix, J. Cathalan, G. Chadeyron, P.A. Bouit, M. Hissler, D. Boyer, High-performance rare-earth-free fluorophores: toward white LEDs, *ACS Appl. Opt. Mater.* 2 (2024) 834–841, <https://doi.org/10.1021/acsaoam.4c00102>.
- [24] R. Gerdes, D. Ensling, M. Haase, T. Jüstel, UV C luminescence of a modified zirconium silicate framework upon cathode ray and VUV excitation, *J. Lumin.* 198 (2018) 410–417, <https://doi.org/10.1016/j.jlumin.2018.02.071>.
- [25] S. Karmakar, I.H. Emu, M.A. Halim, P.K. Sarkar, M. Sultana, A. Tasnim, M. A. Hamid, I.F. Shiam, R. Droopad, A. Haque, Growth optimization, optical, and dielectric properties of heteroepitaxially grown ultrawide-bandgap ZnGa<sub>2</sub>O<sub>4</sub> (111) thin film, *J. Appl. Phys.* 135 (2024) 115702, <https://doi.org/10.1063/5.0190906>.
- [26] R.E. Rojas-Hernandez, F. Rubio-Marcos, I. Romet, A. Del Campo, G. Gorni, I. Hussainova, J.F. Fernandez, V. Nagirnyi, Deep-ultraviolet emitter: rare-earth-free ZnAl<sub>2</sub>O<sub>4</sub> nanofibers via a simple wet chemical route, *Inorg. Chem.* 61 (2022) 11886–11896, <https://doi.org/10.1021/acs.inorgchem.2c01646>.
- [27] R.E. Rojas-Hernandez, F. Rubio-Marcos, I. Romet, E. Feldbach, M. Buryi, D. John, R. Ivanov, I. Hussainova, J.F. Fernandez, V. Nagirnyi, On the potential of transparent rare-earth-free ZnAl<sub>2</sub>O<sub>4</sub> ceramics targeted at the UV-C to UV-B emission, *Appl. Mater. Today* 38 (2024) 102230, <https://doi.org/10.1016/j.apmt.2024.102230>.
- [28] P.V. Ramakrishna, D.B.R.K. Murthy, D.L. Sastry, K. Samatha, Synthesis, structural and luminescence properties of Mn doped ZnO/Zn<sub>2</sub>SiO<sub>4</sub> composite microphosphor, *Spectrochim. Acta* 129 (2014) 274–279, <https://doi.org/10.1016/j.saa.2014.03.081>.
- [29] S. Tripathi, R. Bose, A. Roy, S. Nair, N. Ravishankar, Synthesis of hollow nanotubes of Zn<sub>2</sub>SiO<sub>4</sub> or SiO<sub>2</sub>: mechanistic understanding and uranium adsorption behavior, *ACS Appl. Mater. Interfaces* 7 (2015) 26430–26436, <https://doi.org/10.1021/acsami.5b09805>.
- [30] G. Essalah, G. Kadim, A. Jabar, R. Masrouf, M. Ellouze, H. Guermazi, S. Guermazi, Structural, optical, photoluminescence properties and Ab initio calculations of new Zn<sub>2</sub>SiO<sub>4</sub>/ZnO composite for white light emitting diodes, *Ceram. Int.* 46 (2020) 12656–12664, <https://doi.org/10.1016/j.ceramint.2020.02.031>.
- [31] S. Zh. Karazhanov, P. Ravindran, H. Fjellvåg, B.G. Svensson, Electronic structure and optical properties of Zn<sub>2</sub>SiO<sub>3</sub> and Zn<sub>2</sub>SiO<sub>4</sub>, *J. Appl. Phys.* 106 (2009) 123701, <https://doi.org/10.1063/1.3268445>.
- [32] J. Necib, E. Feldbach, I. Romet, V. Nagirnyi, I. Hussainova, R.E. Rojas-Hernandez, Investigation of deep UV emission of rare-earth-free Zn<sub>2</sub>SiO<sub>4</sub> micropowders: the correlation of structural and luminescence properties, *J. Lumin.* 280 (2025) 121070, <https://doi.org/10.1016/j.jlumin.2025.121070>.
- [33] L.T.T. Vien, N. Tu, T.T. Phuong, N.T. Tuan, N.V. Quang, H. Van Bui, A.T. Duong, D. Q. Trung, P.T. Huy, Facile synthesis of single phase α-Zn<sub>2</sub>SiO<sub>4</sub>:Mn<sup>2+</sup> phosphor via high-energy planetary ball milling and post-annealing method, *J. Lumin.* 215 (2019) 116612, <https://doi.org/10.1016/j.jlumin.2019.116612>.
- [34] A. Majumdar, D. Ganguli, Solid state synthesis of willemite, Zn<sub>2</sub>SiO<sub>4</sub>: role of precursors, *Trans. Indian Ceram. Soc.* 50 (1991) 93–97, <https://doi.org/10.1080/0371750X.1991.10804499>.
- [35] Y. Fan, Y. Cao, M. Li, S. Xu, Y. Yang, X. Zhang, J. Zhang, B. Chen, Molten salt synthesized Tb<sup>3+</sup>, Pr<sup>3+</sup> or Dy<sup>3+</sup> single doped CaTa<sub>2</sub>O<sub>11</sub> with persistent luminescence, *Phys. Chem. Chem. Phys.* 26 (2024) 28971–28979, <https://doi.org/10.1039/D4CP03989K>.
- [36] G. Hu, W. Li, G. He, J. Wang, Y. Zhao, Y. Zhang, B. Yao, Molten salt synthesis of Zn<sub>1-x</sub>Mn<sub>x</sub>SiO<sub>4</sub> luminescent materials in NaCl–ZnCl<sub>2</sub> eutectic salt, *Ceram. Int.* 42 (2016) 7852–7856, <https://doi.org/10.1016/j.ceramint.2016.01.037>.
- [37] H. Chen, G. Wang, L. Zhao, X. He, C. Huang, W. Li, W. Fang, X. Du, Mesoporous biologically-controlled 3D architectures assembling with Zn<sub>2</sub>SiO<sub>4</sub> textured nanowires by biogenic-templated incorporating molten-salt method, *Microporous Mesoporous Mater.* 243 (2017) 331–338, <https://doi.org/10.1016/j.micromeso.2017.02.017>.
- [38] V.D. Mote, Y.P. Purushotham, B.N. Dole, Williamson-hall analysis in estimation of lattice strain in nanometer-sized ZnO particles, *J. Theor. Appl. Phys.* 6 (2012) 1–8, <https://doi.org/10.1186/2251-7235-6-6>.
- [39] E. Feldbach, E. Toldsepp, M. Kirm, A. Lushchik, K. Mizohata, J. Räisänen, Radiation resistance diagnostics of wide-gap optical materials, *Opt. Mater.* 55 (2016) 164–167, <https://doi.org/10.1016/j.optmat.2016.03.008>.
- [40] V. Pankratov, R. Pärna, M. Kirm, V. Nagirnyi, E. Nömmiste, S. Omelkov, S. Vielhauer, et al., Progress in development of a new luminescence setup at the FinEstBeAMS beamline of the MAX IV laboratory, *Radiat. Meas.* 121 (2019) 91–98, <https://doi.org/10.1016/j.radmeas.2018.12.011>.
- [41] R. Pärna, R. Sankari, E. Kukk, E. Nömmiste, M. Valden, M. Lastusaari, K. Kooser, et al., FinEstBeAMS-A wide-range Finnish-Estonian beamline for materials science at the 1.5 GeV storage ring at the MAX IV laboratory, *Nucl. Instrum. Methods Phys. Res.* 859 (2017) 83–89, <https://doi.org/10.1016/j.nima.2017.04.002>.
- [42] J. Guojian, X. Jiayue, S. Hui, Z. Yan, X. Linhe, Z. Hanrui, L. Wenlan, Fabrication and properties of zinc silicate phosphors through solid state reaction, *Adv. Mater. Res.* 160–162 (2011) 594–598, <https://doi.org/10.4028/www.scientific.net/AMR.160-162.594>.



- [43] R. Cuscó, E. Alarcón-Lladó, J. Ibáñez, L. Artús, J. Jiménez, B. Wang, M.J. Callahan, Temperature dependence of Raman scattering in ZnO, *Phys. Rev. B* 75 (2007) 165202, <https://doi.org/10.1103/PhysRevB.75.165202>.
- [44] J.F. Scott, S.P. Porto, Longitudinal and transverse optical lattice vibrations in quartz, *Phys. Rev.* 161 (1967) 903–908, <https://doi.org/10.1103/PhysRev.161.903>.
- [45] P. Bruhns, R.X. Fischer, Crystallization of cristobalite and tridymite in the presence of vanadium, *Eur. J. Mineral* 12 (2000) 615–624, <https://doi.org/10.1127/0935-1221/2000/0012-0615>.
- [46] P. Loiko, O. Dymshits, A. Volokitina, I. Alekseeva, D. Shemchuk, M. Tsentser, A. Bachina, A. Khusetov, E. Vilejshikova, P. Petrov, A. Baranov, A. Zhilin, Structural transformations and optical properties of glass-ceramics based on ZnO,  $\beta$ - and  $\alpha$ -Zn<sub>2</sub>SiO<sub>4</sub> nanocrystals and doped with Er<sub>2</sub>O<sub>3</sub> and Yb<sub>2</sub>O<sub>3</sub>: part I. The role of heat-treatment, *J. Lumin.* 202 (2018) 47–56, <https://doi.org/10.1016/j.jlumin.2018.05.010>.
- [47] H.F.W. Taylor, The dehydration of hemimorphite, *Am. Mineral.* 47 (1962) 932–944.
- [48] M. Czaja, R. Lisiecki, R. Juroszek, T. Krzykowski, Luminescence properties of tetrahedral coordinated Mn<sup>2+</sup>: genthelvite and willemite examples, *Minerals* 11 (2021) 1215, <https://doi.org/10.3390/min11111215>.
- [49] A.K. Yadav, P. Singh, A review of the structures of oxide glasses by Raman spectroscopy, *RSC Adv.* 5 (2015) 67583–67609, <https://doi.org/10.1039/C5RA13043C>.
- [50] E. Faulques, E. Fritsch, M. Ostroumov, Spectroscopy of natural silica-rich glasses, *J. Mineral. Petrol. Sci.* 96 (2001) 120–128, <https://doi.org/10.2465/jmps.96.120>.
- [51] J. Song, K. Song, J. Wei, H. Lin, J. Xu, J. Wu, W. Su, Microstructure characteristics and microwave dielectric properties of calcium apatite ceramics as microwave substrates, *J. Alloys Compd.* 731 (2018) 264–270, <https://doi.org/10.1016/j.jallcom.2017.10.028>.
- [52] J. Rouquette, I. Kantor, C.A. McCommon, V. Dmitriev, L.S. Dubrovinsky, High-pressure studies of (Mg<sub>0.9</sub>Fe<sub>0.1</sub>)<sub>2</sub>SiO<sub>4</sub> olivine using Raman spectroscopy, X-ray diffraction, and Mössbauer spectroscopy, *Inorg. Chem.* 47 (2008) 2668–2673, <https://doi.org/10.1021/ic701983w>.
- [53] B.C. Babu, G.G. Wang, B. Yan, Q. Yang, A.P. Baker, Effects of Cr<sup>3+</sup> addition on the structure and optical properties of  $\alpha$ -Zn<sub>2</sub>SiO<sub>4</sub> synthesized by sol-gel method, *Ceram. Int.* 44 (2018) 938–946, <https://doi.org/10.1016/j.ceramint.2017.10.026>.
- [54] H.W. Nesbitt, G.M. Bancroft, G.S. Henderson, Temperature dependence of Raman shifts and line widths for Q<sup>0</sup> and Q<sup>2</sup> crystals of silicates, phosphates, and sulfates, *Am. Mineral.* 103 (2018) 966–976, <https://doi.org/10.2138/am-2018-6314>.
- [55] R.E. Rojas-Hernandez, F. Rubio-Marcos, R.H. Gonçalves, M.A. Rodriguez, E. Veron, M. Allix, C. Bessada, J.F. Fernandez, Original synthetic route to obtain a SrAl<sub>2</sub>O<sub>4</sub> phosphor by the molten salt method: insights into the reaction mechanism and enhancement of the persistent luminescence, *Inorg. Chem.* 20 (2015) 9896–9907, <https://doi.org/10.1021/acs.inorgchem.5b01656>.
- [56] P. Wasserscheid, Volatile times for ionic liquids, *Nature* 439 (2006) 797, <https://doi.org/10.1038/439797a>.
- [57] H.H. Nersisyan, H.I. Won, J.W. Yoon, C.W. Won, Highly crystalline rod-shaped Zn<sub>2</sub>SiO<sub>4</sub>: Mn<sup>2+</sup> phosphor particles prepared in frontal exothermic waves, *J. Electrochem. Soc.* 159 (2012) B406, <https://doi.org/10.1149/2.091204jes>.
- [58] X. Guo, M. Bettinelli, F. Piccinelli, S. Ruggieri, Z. Wang, T.K. Sham, X-ray excited optical luminescence from lanthanide ions in double phosphate and double silicate crystalline hosts, *J. Lumin.* 269 (2024) 120455, <https://doi.org/10.1016/j.jlumin.2024.120455>.
- [59] T.K. Sham, D.T. Jiang, I. Coulthard, J.W. Lorimer, X.H. Feng, K.H. Tan, S.P. Frigo, R.A. Rosenberg, D.C. Houghton, B. Bryskiewicz, Origin of luminescence from porous silicon deduced by synchrotron-light-induced optical luminescence, *Nature* 363 (1993) 331–334, <https://doi.org/10.1038/363331a0>.
- [60] H. Ji, Z. Huang, Z. Xia, M.S. Molokeev, V.V. Atuchin, M. Fang, S. Huang, New yellow-emitting whitlockite-type structure Sr<sub>1.75</sub>Ca<sub>1.25</sub>(PO<sub>4</sub>)<sub>2</sub>:Eu<sup>2+</sup> phosphor for near-UV pumped white light-emitting devices, *Inorg. Chem.* 53 (2014) 5129–5135, <https://doi.org/10.1021/ic500230v>.
- [61] W. Sun, T. Shi, L. Luo, X. Chen, P. Lv, Y. Lv, Y. Zhuang, J. Zhu, G. Liu, X. Chen, H. Chen, Monodisperse and uniform mesoporous silicate nanosensitizers achieve low-dose X-ray-induced deep-penetrating photodynamic therapy, *Adv. Mater.* 31 (2019) 1808024, <https://doi.org/10.1002/adma.201808024>.
- [62] N. Rakov, F. Matias, Y. Xing, G.S. Maciel, Mn<sup>2+</sup> doped Zn<sub>2</sub>SiO<sub>4</sub> phosphors: a threefold-mode sensing approach for optical thermometry in the visible region at 525 nm, *Opt. Mater.* X 24 (2024) 100359, <https://doi.org/10.1016/j.omx.2024.100359>.
- [63] X. Jiang, X. Gao, L. Li, P. Zhou, S. Wang, T. Liu, J. Zhou, H. Zhang, K. Huang, Y. Li, M. Wang, Enhancement of light and X-ray charging in persistent luminescence nanoparticle scintillators Zn<sub>2</sub>SiO<sub>4</sub>: Mn<sup>2+</sup>, Yb<sup>3+</sup>, Li<sup>+</sup>, *ACS Appl. Mater. Interfaces* 17 (2023) 21228–21238, <https://doi.org/10.1021/acsaami.3c00664>.
- [64] B.K. Meyer, H. Alves, D.M. Hofmann, W. Kriegseis, D. Forster, F. Bertram, J. Christen, Bound exciton and donor-acceptor pair recombinations in ZnO, *Phys. Status Solidi B* 241 (2004) 231–260, <https://doi.org/10.1002/psb.200301962>.
- [65] C. Baratto, E. Comini, M. Ferroni, G. Faglia, G. Sberveglieri, Plasma-induced enhancement of UV photoluminescence in ZnO nanowires, *CrystEngComm* 15 (2013) 7981–7986, <https://doi.org/10.1039/C3CE41055B>.
- [66] C.H. Ahn, Y.Y. Kim, D.C. Kim, S.K. Mohanta, H.K. Cho, A comparative analysis of deep level emission in ZnO layers deposited by various methods, *J. Appl. Phys.* 105 (2009) 013502, <https://doi.org/10.1063/1.3054175>.
- [67] S.H. Jeong, B.S. Kim, B.T. Lee, Photoluminescence dependence of ZnO films grown on Si (100) by radio-frequency magnetron sputtering on the growth ambient, *Appl. Phys. Lett.* 82 (2003) 2625–2627, <https://doi.org/10.1063/1.1569665>.
- [68] P.S. Xu, Y.M. Sun, C.S. Shi, F.Q. Xu, H.B. Pan, The electronic structure and spectral properties of ZnO and its defects, *Nucl. Instrum. Methods Phys. Res. B* 199 (2003) 286–290, [https://doi.org/10.1016/S0168-583X\(02\)01425-8](https://doi.org/10.1016/S0168-583X(02)01425-8).
- [69] N. Kaur, Y. Lee, D.Y. Kim, S. Lee, Optical bandgap tuning in nanocrystalline ZnO: y films via forming defect-induced localized bands, *Mater. Des.* 148 (2018) 30–38, <https://doi.org/10.1016/j.matdes.2018.03.042>.
- [70] L.N. Skuja, A.N. Trukhin, Comment on “Luminescence of fused silica: observation of the O<sub>2</sub>-emission band”, *Phys. Rev. B* 39 (1989) 3909, <https://doi.org/10.1103/PhysRevB.39.3909>.
- [71] M. Kohketsu, K. Awazu, H. Kawazoe, M. Yamane, Photoluminescence centers in VAD SiO<sub>2</sub> glasses sintered under reducing or oxidizing atmospheres, *Jpn. J. Appl. Phys.* 28 (1989) 615, <https://doi.org/10.1143/JJAP.28.615>.
- [72] H. Nishikawa, T. Shirokawa, R. Nakamura, Y. Ohki, K. Nagasawa, Y. Hama, Photoluminescence from defect centers in high-purity silica glasses observed under 7.9-eV excitation, *Phys. Rev. B* 45 (1992) 586, <https://doi.org/10.1103/PhysRevB.45.586>.
- [73] C. Li, Y. Bando, B. Dierre, T. Sekiguchi, Y. Huang, J. Lin, D. Golberg, Effect of size-dependent thermal instability on synthesis of Zn<sub>2</sub>SiO<sub>4</sub>:SiO<sub>2</sub> core-shell nanotube arrays and their cathodoluminescence properties, *Nanoscale Res. Lett.* 5 (2010) 773–780, <https://doi.org/10.1007/s11671-010-9556-7>.
- [74] T. Furukawa, S. Kanamori, M. Fukuta, Y. Nawa, H. Kominami, Y. Nakanishi, A. Sugita, W. Inami, Y. Kawata, Fabrication of bright and thin Zn<sub>2</sub>SiO<sub>4</sub> luminescent film for electron beam excitation-assisted optical microscope, *Opt. Express* 23 (2015) 18630–18637, <https://doi.org/10.1364/OE.23.018630>.
- [75] X. Feng, X. Yuan, T. Sekiguchi, W. Lin, J. Kang, Aligned Zn–Zn<sub>2</sub>SiO<sub>4</sub> core-shell nanocables with homogeneously intense ultraviolet emission at 300 nm, *J. Phys. Chem. B* 109 (2005) 15786–15790, <https://doi.org/10.1021/jp0514980>.
- [76] B. Dierre, X. Yuan, T. Sekiguchi, Low-energy cathodoluminescence microscopy for the characterization of nanostructures, *Sci. Technol. Adv. Mater.* 11 (2010) 043001, <https://doi.org/10.1088/1468-6996/11/4/043001>.
- [77] D. Ehrh, H.T. Vu, A. Herrmann, G. Völksch, Luminescent ZnO-Al<sub>2</sub>O<sub>3</sub>-SiO<sub>2</sub> glasses and glass ceramics, *Adv. Mater. Res.* 39–40 (2008) 231–236, <https://doi.org/10.4028/www.scientific.net/AMR.39-40.231>.
- [78] K.A. Petrovykh, V.S. Kortov, N.V. Gaponenko, A.A. Rempel', M.V. Rudenko, L. S. Khoroshko, S.S. Voznesenskii, A.A. Sergeev, V.A. Pustovarov, Photoluminescence of the nanosized xerogel Zn<sub>2</sub>SiO<sub>4</sub>: Mn<sup>2+</sup> in pores of anodic alumina, *Phys. Solid State* 58 (2016) 2062–2067, <https://doi.org/10.1134/S1063783416100280>.
- [79] V.S. Kortov, K.A. Sergeeva, V.A. Pustovarov, A.A. Rempel, Photoluminescence of nanostructured Zn<sub>2</sub>SiO<sub>4</sub>: Mn<sup>2+</sup> ceramics under UV and VUV excitation, *J. Surf. Invest. X-Ray, Synchrotron Neutron Tech.* 11 (2017) 727–731, <https://doi.org/10.1134/S1027451017040097>.
- [80] H.J. Chang, H.D. Park, K.S. Sohn, J.D. Lee, Electronic structure of Zn<sub>2</sub>SiO<sub>4</sub> and Zn<sub>2</sub>SiO<sub>4</sub>: mn, *J. Kor. Phys. Soc.* 34 (1999) 545–548.
- [81] Y. Hao, Y. Wang, Luminescent properties of Zn<sub>2</sub>SiO<sub>4</sub>: Mn<sup>2+</sup> phosphor under UV, VUV and CR excitation, *J. Lumin.* 122 (2007) 1006–1008, <https://doi.org/10.1016/j.jlumin.2006.01.352>.
- [82] K.C. Mishra, K.H. Johnson, B.G. DeBoer, J.K. Berkowitz, J. Olsen, E.A. Dale, First principles investigation of electronic structure and associated properties of zinc orthosilicate phosphors, *J. Lumin.* 47 (1991) 197–206, [https://doi.org/10.1016/0022-2313\(91\)90012-K](https://doi.org/10.1016/0022-2313(91)90012-K).
- [83] S. Zhang, H. Liang, Y. Liu, Y. Liu, D. Hou, G. Zhang, J. Shi, Intensive green emission of ZnAl<sub>2</sub>O<sub>4</sub>: Mn<sup>2+</sup> under vacuum ultraviolet and low-voltage cathode ray excitation, *Opt. Lett.* 37 (2012) 2511–2513, <https://doi.org/10.1364/OL.37.002511>.

### **Publication III**

**Necib, J.**, Feldbach, E., Romet, I., Nagirnyi, V., Hussainova, I., & Rojas-Hernandez, R. E. (2025). Investigation of deep UV emission of rare-earth-free  $\text{Zn}_2\text{SiO}_4$  micropowders: the correlation of structural and luminescence properties. *Journal of Luminescence*, 280, 121070. <https://doi.org/10.1016/j.jlumin.2025.121070>.





Contents lists available at ScienceDirect

Journal of Luminescence

journal homepage: [www.elsevier.com/locate/jlumin](http://www.elsevier.com/locate/jlumin)

# Investigation of deep UV emission of rare-earth-free $\text{Zn}_2\text{SiO}_4$ micropowders: The correlation of structural and luminescence properties

Jallouli Necib<sup>a</sup>, Eduard Feldbach<sup>b</sup>, Ivo Romet<sup>b</sup>, Vitali Nagirnyi<sup>b</sup>, Irina Hussainova<sup>a</sup>,  
Rocío E. Rojas-Hernandez<sup>a,c,\*</sup>

<sup>a</sup> Department of Mechanical and Industrial Engineering, Tallinn University of Technology, Ehitajate 5, 19180, Tallinn, Estonia

<sup>b</sup> Institute of Physics, University of Tartu, W. Ostwald Str 1, 50411, Tartu, Estonia

<sup>c</sup> Electroceramic Department, Instituto de Cerámica y Vidrio, CSIC, Kelsen 5, 28049, Madrid, Spain

## ARTICLE INFO

### Keywords:

Rare-earth-free phosphors  
 $\text{Zn}_2\text{SiO}_4$   
Cathodoluminescence  
UV-B emission  
Synchrotron radiation

## ABSTRACT

Extensive research has been devoted in recent decades to the development of deep ultraviolet emitters, which are utilized in various fields of human activity from medicine to agriculture. Currently, the developed deep ultraviolet radiation sources, based mainly on mercury and excimer lamps, have relatively low efficiency, disadvantages related to harmful effects on human health and the environment, or utilize rare-earth elements with limited availability. Herein, rare-earth-free zinc silicate ( $\text{Zn}_2\text{SiO}_4$ ) powders, showing a remarkable ultraviolet emission centered at 4.31 eV (287 nm), were synthesized by the sol-gel method and studied as a promising alternative for eco-friendly deep ultraviolet emitters. *In-situ* high-temperature X-ray diffraction analysis and Raman spectroscopy revealed a phase transformation in the material:  $\beta\text{-Zn}_2\text{SiO}_4$  is stabilized at 750–850 °C, and  $\alpha\text{-Zn}_2\text{SiO}_4$  is formed at 950 °C. Cathodoluminescence studies at room temperature and 6 K showed that the material synthesized at 1200 °C exhibits the highest ultraviolet emission intensity. Luminescence spectroscopy under excitation by synchrotron radiation near the onset of the fundamental absorption of the material and at higher energies provide strong reasoning to attribute the discovered ultraviolet emission to a perturbed crystal lattice governed by local defects. These findings not only provide new insights related to the luminescence mechanism but also make a breakthrough in developing a rare-earth-free ceramic material, highlighting the great potential for novel ultraviolet light emitting diodes.

## 1. Introduction

Ultraviolet (UV) light emitters, particularly in the UV-B (280–315 nm), and UV-C (100–280 nm) regions, have recently gained immense importance due to their variety of applications in various fields including, but not limited to, photolithography, sterilization, medical treatments, and material curing [1–6]. Existing UV radiation sources, such as excimer and mercury vapor lamps, face problems related to emission efficiency and the presence of harmful components. Consequently, the demand for new mercury-free UV light sources offering sustainable solutions has increased dramatically worldwide.

Particular attention has recently been directed toward UV-C-emitting phosphors which have demonstrated their potential in neutralizing the severe acute respiratory syndrome (SARS-CoV-2) and disinfecting various environments [7]. Also, the adjacent UV-B emitters, offer other promising opportunities. For example, focused UV-B sources

optimized for 310 nm are successfully used in cancer immunotherapy, dermatitis treatment, and enhanced plant growth stimulated with phytochemicals [8–10]. The UV-B irradiation at 294 nm can prevent plant diseases and help synthesizing a vital vitamin D3 in a human body [8].

Additionally, the use of UV-B emitting phosphors can replace toxic chemicals and pesticides in the agricultural sector. Recently, significant efforts have been devoted to the synthesis and characterization of UV-B emitting phosphors [11]. A number of studies have been focused on UV-B emitting phosphors utilizing rare-earth elements, specifically  $\text{Gd}^{3+}$  ions, doped in various materials, such as  $\text{LaAl}_{11}\text{O}_{18}:\text{Gd}$  [11],  $\text{CaAl}_4\text{O}_7:\text{Gd}$  [12],  $\text{CaF}_2:\text{Gd}$  [13] and  $\text{YPO}_4:\text{Gd}$  [14].

However, reliance on rare-earth (RE) elements presents significant challenges due to their limited availability, high cost, and environmental concerns. To address these challenges, rare-earth-free wide band-gap materials have emerged as alternatives. For example,  $\text{ZnAl}_2\text{O}_4$  spinel with the bandgap of about 7 eV [15,16] has recently

\* Corresponding author. Department of Mechanical and Industrial Engineering, Tallinn University of Technology, Ehitajate 5, 19180, Tallinn, Estonia.  
E-mail address: [rocio.rojas@taltech.ee](mailto:rocio.rojas@taltech.ee) (R.E. Rojas-Hernandez).

<https://doi.org/10.1016/j.jlumin.2025.121070>

Received 25 November 2024; Received in revised form 18 December 2024; Accepted 6 January 2025

Available online 28 January 2025

0022-2313/© 2025 Elsevier B.V. All rights are reserved, including those for text and data mining, AI training, and similar technologies.



demonstrated the possibility of UV-C to UV-B emission [17,18]. Furthermore,  $\text{ZnGa}_2\text{O}_4$ , characterized by a band gap of approximately 5 eV, has shown a promise for the deep-UV optoelectronic devices [19].

Considering these inspiring findings, an effective approach for UV-B emission might benefit from zinc silicate ( $\text{Zn}_2\text{SiO}_4$ ), which is known for its wide band gap estimated to 5.5–6.26 eV [20–23]. This material has been employed in various applications, including used in UV detectors, gas sensors, toxic ion adsorption from water, and optoelectronic devices [24–29] due to its unique electrical and luminescent properties.  $\text{Zn}_2\text{SiO}_4$  is also commonly utilized as a host for rare earth and transition metal dopant ions, which emit ultraviolet, visible, or infrared light, depending on the type of ion incorporated. Such dopants include  $\text{Eu}^{3+}$ ,  $\text{Er}^{3+}$ ,  $\text{Mn}^{2+}$ ,  $\text{Co}^{2+}$ ,  $\text{Sm}^{3+}$ ,  $\text{Dy}^{3+}$ ,  $\text{Nd}^{3+}$ ,  $\text{Tm}^{3+}$ ,  $\text{Tb}^{3+}$ ,  $\text{Li}^+$ ,  $\text{Pr}^{3+}$ , and  $\text{Gd}^{3+}$  [24,26,29–40].

Despite the extensive research on doped  $\text{Zn}_2\text{SiO}_4$ , the studies of undoped  $\text{Zn}_2\text{SiO}_4$  remain limited, and a comprehensive understanding of its emission mechanism has yet to be attained.

Zinc silicate is a polymorph and can occur in five phases: I ( $\alpha$ , willemite), II ( $\beta$ ), III, IV, and V. The  $\beta$ -phase is metastable, and at high temperatures transforms into the  $\alpha$ -phase, which is the most commonly used crystalline form.

Traditionally, willemite is synthesized through high-temperature solid-state methods [41,42]. However, these procedures demand elevated temperatures, energy, and extended processing times, often yielding irregular microstructures. In recent years, new methods for the synthesis of  $\text{Zn}_2\text{SiO}_4$  have emerged, including the hydrothermal approach [43], gel combustion method [44], spray pyrolysis technique [45], combustion synthesis method [32,46,47], and sol-gel method [40,48].

Among these, sol-gel synthesis stands out for its numerous advantages, including the achievement of favorable morphology and cost-effectiveness of the synthesis route [49].

This paper presents a comprehensive study of the powdered RE-free  $\text{Zn}_2\text{SiO}_4$  synthesized using the sol-gel method at different temperatures. Importantly, our study is the first to report deep UV emission in rare-earth-free  $\text{Zn}_2\text{SiO}_4$  powders. Although the current research does not provide ready-made materials for a UVB-delivering device, it effectively advances the concept by mapping the scientific fundamentals of the representative system. The main goal of this work was to gain a deeper understanding of the emission mechanism of willemite by investigating its structural and luminescent properties, as well as to assess its potential for deep UV emission. The presented proof-of-concept phenomena are of great importance for the next step in the development of new, safer and more environmentally friendly luminophores.

## 2. Experimental section

### 2.1. Synthesis

Zinc silicate powders were synthesized using the sol-gel method. Zinc nitrate hexahydrate ( $\text{Zn}(\text{NO}_3)_2 \cdot 6\text{H}_2\text{O}$ ) (Lachner, 99 %) and tetraethyl orthosilicate (TEOS) (VWR 99 %) served as zinc and silicon precursors, respectively. The following steps were executed. The partial hydrolysis of TEOS in ethanol and distilled water was performed at the beginning, followed by dissolving zinc nitrates in the pre-hydrolyzed TEOS solution with a Zn:Si molar ratio of 2:1. After magnetic stirring at room temperature (RT) until complete dissolution of the components, the temperature of the solution was increased to 60 °C to enhance hydrolysis and polycondensation. As a catalyst, nitric acid was added and the solution was stirred for an hour, then dried at 85 °C for 24 h yielding a densified powder. The obtained xerogel was heat-treated in air at temperature ranging from 600 to 1300 °C for 2 h dwell time with a heating rate of 5 °C min<sup>-1</sup>. After cooling, powders were manually ground and sieved using a 63  $\mu\text{m}$  nylon sieve.

### 2.2. Characterization

The thermogravimetric (TGA) and Differential Scanning Calorimetry (DSC) analyses were conducted using a PerkinElmer DSC-7 calorimeter under an air atmosphere, with a heating rate of 10 °C min<sup>-1</sup> from room temperature up to 1200 °C.

The structure and phase composition of the powders synthesized were analyzed via X-ray diffraction (Rigaku SmartLab SE) using a D/teX Ultra 250 1D detector at RT. *In-situ* high-temperature X-ray diffraction (HT-XRD) was performed using a Rigaku SmartLab SE diffractometer equipped with an HTK1200N Anton Paar oven chamber. Samples were heated to 1150 °C at a rate of 10 °C min<sup>-1</sup>, the X-ray diffractograms being recorded in the 2 $\theta$  range 10–70° with a step of 0.01°.

The Raman spectroscopy was performed by a Horiba LabRAM HR800 Micro-Raman system with a Nd-YAG laser (wavelength 532 nm) for excitation. Morphological features and microstructure examination was carried out using a field emission scanning electron microscope FE-SEM Zeiss ULTRA-55.

The average crystallite size, denoted as D, was determined using Scherrer's formula [50]:

$$D = \frac{k \lambda}{\beta \cos \theta} \quad (1)$$

where, k is a form factor (0.9),  $\lambda$  is the wavelength of the Cu  $\text{K}\alpha$  radiation (1.54060 Å),  $\beta$  is peak broadening after instrumental correction (in radians), and  $\theta$  is the Bragg diffraction angle.

UV–VIS absorption spectra were recorded at room temperature using the diffuse reflectance geometry on an Analytik-Jena Specord 200 plus spectrometer equipped with an integrating sphere.

Luminescence characteristics of the synthesized materials were explored under electron beam excitation, and under synchrotron radiation excitation. Cathodoluminescence (CL) analysis was conducted using an electron beam with energy of 10 keV. An ARS closed cycle helium cryostat enabled low-temperature measurements. The comprehensive details describing the experimental setup have been published elsewhere [51]. Additionally, synchrotron radiation studies in the 4.5–11 eV energy range were conducted at the FinEstBeAMS beamline, MAX IV Lab, Sweden, and fully described elsewhere [52,53]. Depending on the specific excitation energy region under study, either  $\text{MgF}_2$  or fused silica filters were employed to reduce the impact of higher-order incident light on the luminescence excitation spectra. Luminescence was detected using the Andor Shamrock SR-303i spectrometer equipped with a Hamamatsu H8259-01 photon counting head. The measured excitation spectra were normalized to the incident photon flux recorded with an energy-calibrated AXUV100G photodiode. All emission spectra were corrected for the spectral response of the detection system and an appropriate Jacobian transformation was applied to transfer the photoluminescence spectra into the energy space.

## 3. Results and discussion

### 3.1. Thermal analysis and phase evolution

To gain a clear vision on the thermal evolution of zinc silicate system, TGA and DSC curves of the  $\text{Zn}_2\text{SiO}_4$  dried gel were acquired (Fig. 1a). The TG analysis highlights a substantial (48 %) reduction in mass between 25 and 600 °C. This weight loss is attributed to the removal of hydration water and subsequent decomposition of nitrate and  $\text{Si}(\text{OH})_4$  components [54]. However, weight loss becomes less conspicuous when temperatures exceed 800 °C.

The DSC curve exhibits three distinctive endothermic peaks at approximately 133, 220, and 302 °C, respectively, accompanied by an exothermic peak around 785 °C. The initial endothermic peak at 133 °C (labeled as “1” in Fig. 1a) signifies the dehydration process of  $\text{Zn}(\text{NO}_3)_2 \cdot 6\text{H}_2\text{O}$  and hydrated silica.

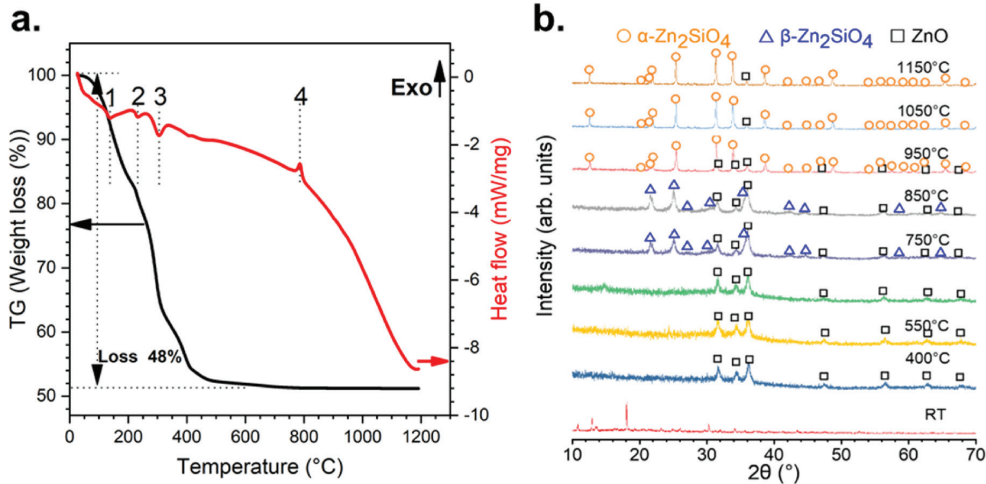


Fig. 1. (a) TGA (black line) and DSC curve (red line) analysis of dried gel of zinc silicate at RT and up to 1200 °C: The points labeled 1, 2, 3 indicate the temperatures at which characteristic endothermic or exothermic peaks appear. (b) Evolution of *in-situ* XRD collected upon heating from 25 to 1150 °C at a rate of 10 °C min<sup>-1</sup>. (For interpretation of the references to color in this figure legend, the reader is referred to the Web version of this article.)

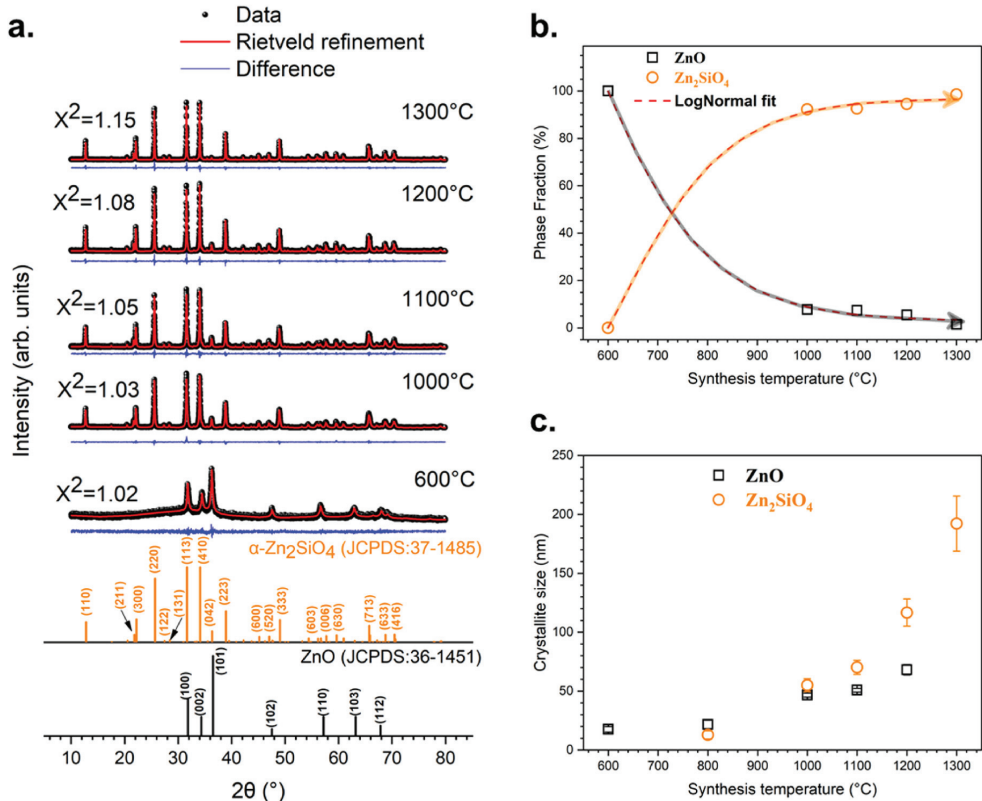


Fig. 2. (a) Rietveld refinement, and (b) Zn<sub>2</sub>SiO<sub>4</sub> and ZnO phase fraction of the samples synthesized at 600, 1000, 1100, 1200 and 1300 °C, respectively. (c) Crystallite size of the powders synthesized as a function of the synthesis temperature.

Subsequently, the peak at 220 °C (labeled as “2”) corresponds to the decomposition of organic constituents. The third endothermic peak, occurring at approximately 302 °C (labeled as “3”), is associated with the decomposition of nitrate radicals NO<sub>3</sub>. The observed exothermic peak at 785 °C (labeled as “4”) is likely attributed to the phase formation of Zn<sub>2</sub>SiO<sub>4</sub>.

The results of *in-situ* HT-XRD analysis of the reaction process are depicted in Fig. 1b, and illustrate the phase evolution for the Zn (NO<sub>3</sub>)<sub>2</sub>·6H<sub>2</sub>O + TEOS system as the temperature increases from RT to 1150 °C.

Phase compositions were identified with the aid of the Powder Diffraction File (PDF) cards from the Joint Committee on Powder Diffraction Standards. As anticipated, the RT X-ray diffractogram displayed distinctive peaks corresponding to the precursor materials. The characteristic diffraction peaks of the ZnO polymorph emerged upon heating to 400, 550, and 650 °C. These peaks match the standard ZnO XRD patterns (JCPDS No. 36–1451). Additionally, a weak halo was observed within the 2θ range of approximately 20–40°, indicating the presence of an amorphous silica phase. However, no evidence of Zn<sub>2</sub>SiO<sub>4</sub> phase was apparent at these temperatures. Upon further raising the temperature to 750 and 850 °C, the metastable β-Zn<sub>2</sub>SiO<sub>4</sub> phase was successfully stabilized alongside the ZnO phase. This aligns with the exothermic peak observed at 785 °C in the DSC curve. At 950 °C, the α-Zn<sub>2</sub>SiO<sub>4</sub> phase became dominant, the minor peaks were attributed to ZnO. This trend persisted at 1050 and 1150 °C, with intensity reduction in the peaks corresponding to the ZnO phase. To validate these observations, ex-situ XRD analysis was conducted on the samples that were heat-treated at six temperatures (600, 800, 1000, 1100, 1200, and 1300 °C) for 2 h in air, as detailed in Supporting Information S1a. Rietveld refinement was performed for all prepared ex-situ synthesized samples, except for the sample heat-treated at 800 °C with the β-Zn<sub>2</sub>SiO<sub>4</sub> phase due to its unknown space group. The results are illustrated in Fig. 2a and summarized in Table 1.

The diffractogram acquired at 600 °C exhibited the well-defined peaks, which are indicative of the formation of ZnO with the wurtzite structure. Furthermore, it shows a faint halo associated with the amorphous silica phase. An increase in the calcination temperature up to 800 °C (as confirmed by ex-situ XRD analysis in Supporting Information S1a), results in the coexistence of both ZnO and the β-Zn<sub>2</sub>SiO<sub>4</sub> phases. The β-Zn<sub>2</sub>SiO<sub>4</sub> phase was identified based on the standard pattern of β-Zn<sub>2</sub>SiO<sub>4</sub> (JCPDS card No. 014–0653) within the orthorhombic system that is characterized by cell parameters a = 8.400 Å, b = 32.200 Å, and c = 5.100 Å. As the space group was unspecified, the structure of β-Zn<sub>2</sub>SiO<sub>4</sub> remained largely unexplored. Notably, Taylor [55] conducted a study on the conversion of hemimorphite (Zn<sub>4</sub>Si<sub>2</sub>O<sub>7</sub>(OH)<sub>2</sub>·H<sub>2</sub>O) to β-Zn<sub>2</sub>SiO<sub>4</sub> and proposed its structural relationship with tridymite and cristobalite. This hypothesis implies that Zn<sup>2+</sup> ions are more likely to be in octahedral coordination in contrast to tetrahedral coordination, potentially explaining the lower stability of β-Zn<sub>2</sub>SiO<sub>4</sub> compared to α-Zn<sub>2</sub>SiO<sub>4</sub>, where all Zn<sup>2+</sup> ions are tetrahedrally coordinated. Upon reaching 1000 °C, the relative intensity of ZnO compared to Zn<sub>2</sub>SiO<sub>4</sub> substantially decreased. The peaks associated with the (100) and (002) planes of ZnO at 31.82 and 34.33° were overshadowed by the prominent peaks of willemite (113) and (410) at 31.65 and 34.12°, respectively.

Nonetheless, the peak corresponding to the (101) plane of ZnO at 36.49° remained detectable, albeit with very low intensity. At this stage, all diffraction peaks have been indexed to the standard pattern of α-Zn<sub>2</sub>SiO<sub>4</sub> willemite (Rhombohedral structure, JCPDS card No. 37–1485, space group R-3, unit cell parameters: a = b = 13.938 Å, c = 9.310 Å) [56], except a small amount of unreacted ZnO. Rietveld refinement revealed ZnO phase fractions of 7.74, 7.38, 5.40, and 1.43 % for temperatures of 1000, 1100, 1200, and 1300 °C, respectively, as depicted in Fig. 2b.

The enlarged XRD data of the (220) plane of willemite at ~25.55° for the samples synthesized at 1000, 1100, 1200, and 1300 °C (Supporting Information S1b) showed a slight shift toward higher diffraction angles with increasing temperature. This shift suggests minor lattice contraction, which is consistent with the lattice parameters obtained from Rietveld refinement (Table 1). Additionally, the narrowing and sharpening of peaks with increasing temperature indicate improved crystallinity. Crystallite size analysis using the Scherrer equation further supported this observation.

The calculated average crystallite size values D of the powders as function of the temperature are presented in Fig. 2c. The crystallite size increases with an increase of heating temperature. Specifically, for ZnO, the size expands from 17.58 nm at 600 °C to 68.08 nm at 1200 °C, while for α-Zn<sub>2</sub>SiO<sub>4</sub>, it grows from 55.02 nm at 1000 °C to 192.18 nm at 1300 °C. This phenomenon can be attributed to the temperature-induced enhancement of ion diffusion leading to a high growth rate of crystals (see also [57]).

3.2. Structural analysis by Raman spectroscopy and morphological characterization

Fig. 3a displays the Raman spectra of the powders heat-treated for 2 h at temperatures ranging from 600 to 1300 °C. At 600 °C, three Raman peaks were observed: 438 cm<sup>-1</sup> (assigned to the E<sub>2</sub><sup>high</sup> mode) and 387 cm<sup>-1</sup> (A<sub>1</sub>(TO) mode), characteristic of the first-order Raman scattering modes, as well as the peak around 332 cm<sup>-1</sup> (E<sub>2</sub><sup>high</sup> – E<sub>2</sub><sup>low</sup> mode) indicates the second-order Raman scattering involving the acoustic phonon modes [58]. The intense peak at 438 cm<sup>-1</sup> represents the vibration of oxygen atom in ZnO lattice. Conversely, the broader and less intense peak at 332 cm<sup>-1</sup> is attributed to the second-order Raman scattering by zone boundary phonons indicating disruptions in the crystal lattice caused by the vibrations of oxygen atoms and the zinc sub-lattice [59]. Additionally, the Raman spectrum displays broad bands spanning approximately 400–500 cm<sup>-1</sup> and 600–850 cm<sup>-1</sup>, which are likely originating from the presence of an amorphous silica phase. These bands gradually decrease in intensity with increasing temperature, suggesting a progressive reduction in the amount of silica phase. Furthermore, the Raman modes associated with the ZnO phase are present in the material up to 1100 °C and their intensity decreases at higher temperatures, indicating the ongoing reaction between ZnO and silica, leading to the formation of willemite. This transformation well correlated with the findings obtained from the XRD analysis.

For the sample heat-treated at 800 °C, the Raman spectrum of the sample reveals multiple peaks at 167, 204, 215, 310, 865, 922, and 965 cm<sup>-1</sup>, which indicates the crystallization process of β-Zn<sub>2</sub>SiO<sub>4</sub> [60]. The peaks around 167, 204, 215, and 310 cm<sup>-1</sup>, attributed to β-Zn<sub>2</sub>SiO<sub>4</sub>,

**Table 1**  
Refined structural parameters of the materials synthesized at 600, 1000, 1100, 1200 and 1300 °C in air atmosphere.

T (°C)	a (Å)		c (Å)		V (Å <sup>3</sup> )		χ <sup>2</sup>
	α-Zn <sub>2</sub> SiO <sub>4</sub>	ZnO	α-Zn <sub>2</sub> SiO <sub>4</sub>	ZnO	α-Zn <sub>2</sub> SiO <sub>4</sub>	ZnO	
600	–	3.24767 (0.00044)	–	5.20351 (0.00073)	–	47.530 (0.011)	1.02
1000	13.93544 (0.00035)	3.25136 (0.00021)	9.30824 (0.00024)	5.20470 (0.00055)	1565.451 (0.068)	47.649 (0.007)	1.03
1100	13.93422 (0.00045)	3.25169 (0.00027)	9.30769 (0.00031)	5.20384 (0.00068)	1565.085 (0.088)	47.651 (0.008)	1.05
1200	13.93299 (0.00029)	3.25132 (0.00027)	9.30748 (0.00020)	5.20481 (0.00070)	1564.774 (0.057)	47.649 (0.008)	1.08
1300	13.93290 (0.00021)	3.25268 (0.00027)	9.30732 (0.00015)	5.20228 (0.00066)	1564.726 (0.042)	47.666 (0.008)	1.15

(a, c) Lattice parameters, (V) unit cell volume and (χ<sup>2</sup>) goodness of fit.

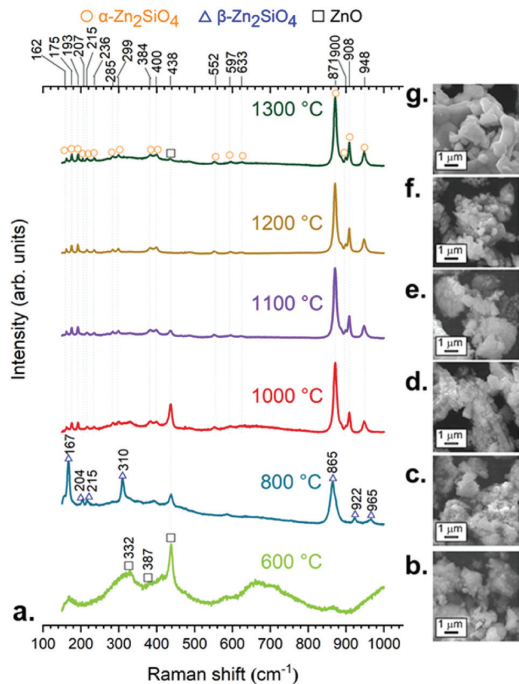


Fig. 3. (a) Structural analysis by Raman spectroscopy: Raman modes in the spectra of materials synthesized at 600, 800, 1000, 1100, 1200 and 1300 °C; (b–g) SEM micrographs of powders synthesized at a temperature range 600–1300 °C.

have been reported in a limited number of studies, yet their exact assignment being still unknown [60,61]. The highly intense Raman band at 865 cm<sup>-1</sup> corresponds to the  $\nu_1$  vibrational modes of the [SiO<sub>4</sub>] unit within  $\beta$ -Zn<sub>2</sub>SiO<sub>4</sub> [62]. The analysis clearly shows that with an increase in synthesis temperature above 1000 °C, the Raman vibrations related to the  $\beta$ -Zn<sub>2</sub>SiO<sub>4</sub> polymorph disappear, revealing the transformation of the metastable  $\beta$ -phase into the  $\alpha$ -phase. Above 1000 °C, the Raman modes assigned to willemite polymorph appear at 175, 193, 384, 553, 871, 900, 908, and 948 cm<sup>-1</sup>, whereas the peak at 871 cm<sup>-1</sup> is most intensive (Table 2, see also [63]). The peaks ranging from 150 to 300 cm<sup>-1</sup> are associated with the lattice vibrations of  $\alpha$ -Zn<sub>2</sub>SiO<sub>4</sub>, while the regions between 300 and 700 cm<sup>-1</sup> and 800–1000 cm<sup>-1</sup> correspond to the bending and stretching vibrations of the SiO<sub>4</sub> group, respectively

Table 2  
Raman active modes of crystalline phases obtained in comparison with literature data.

ZnO			$\alpha$ -Zn <sub>2</sub> SiO <sub>4</sub>			$\beta$ -Zn <sub>2</sub> SiO <sub>4</sub>	
This Work	Ref	Assignment [58]	This Work	Ref	Assignment [69]	This Work	Ref [61]
332	333[61]	E <sub>2</sub> <sup>high</sup> – E <sub>2</sub> <sup>low</sup>	215	215 [61]	E <sub>g</sub> <sup>2</sup>	167	169
387	387[70]	A <sub>1</sub> (TO)	236	236 [61]	E <sub>g</sub> <sup>2</sup>	204	205
438	438[61]	E <sub>2</sub> <sup>high</sup>	285	285 [61]	E <sub>g</sub> <sup>2</sup>	215	215
–	–	–	299	300 [61]	–	285	284
–	–	–	384	385 [61]	A <sub>g</sub>	310	311
–	–	–	400	400 [61]	–	400	397
–	–	–	552	553 [63]	E <sub>g</sub> <sup>2</sup>	–	–
–	–	–	597	594 [63]	A <sub>g</sub>	–	–
–	–	–	633	625 [63]	A <sub>g</sub>	–	–
–	–	–	871	873 [63]	A <sub>g</sub>	865	865
–	–	–	908	911 [63]	A <sub>g</sub>	922	922
–	–	–	948	952 [63]	A <sub>g</sub>	965	967

[63]. Furthermore, the Raman peaks centered at 871, 900, 908 and 948 cm<sup>-1</sup> originate from the surface of siloxane group [64]. Taking into account the studies on other silicates structures, the strongest peak at about 870 cm<sup>-1</sup> can be assigned to the symmetric stretching mode of the SiO<sub>4</sub> tetrahedron, while the weak modes above 900 cm<sup>-1</sup> are attributed to the asymmetric mode  $\nu_3$  [65–68].

Complementary, local structural information can be obtained by analyzing the ratio of the intensity of the peak at 900 to that of 871 cm<sup>-1</sup> and the Full Width Half Maximum (FWHM) of the peak at 900 cm<sup>-1</sup> as a function of the synthesis temperature, as detailed in the Supporting Information S2&S3. The analysis revealed a consistent increasing trend in the intensity ratio with increasing synthesis temperature: from 0.047 for the sample heat-treated at 1000 °C to 0.063 at 1100 °C. Remarkably, the sample synthesized at 1200 °C exhibited the highest ratio of 0.079, which then decreased to 0.078 at 1300 °C. In addition, the peak at 900 cm<sup>-1</sup> is slightly broader for the material synthesized at 1300 °C in comparison with 1200 °C suggesting a tendency to increased disorder at this temperature. These results highlight the strong influence of heating temperature on the level of disorder observed in zinc silicate samples.

Surface morphology and microstructure of Zn<sub>2</sub>SiO<sub>4</sub> powders were examined by SEM, as depicted in Fig. 3b–g. An increase in the heating temperature leads to noticeable changes in both particle size and morphology. At lower heating temperatures (600–800 °C), the particles exhibit small spherical shapes with relatively smooth surfaces, alongside some aggregation. The presence of agglomerated, shapeless nanosized particles suggests an amorphous nature, which is indicated by the halo in the diffractogram (Fig. 2a) and confirmed by the broad Raman modes observed in the sample heat-treated at 600 °C.

With higher heating temperatures, pronounced sintering occurs, as evidenced by the development of necking and connections between adjacent particles. This is reflected in the observation of a smoother surface and reduced particle aggregation (Fig. 3f). As the calcination temperature increases, the surface energy also increases, promoting the sintering of smaller particles and the formation of larger particles (Fig. 3g) [71–73].

3.3. Absorbance characterization

The effect of heating temperature on the optical properties of the synthesized materials was studied by UV–VIS absorption spectroscopy. Fig. 4 depicts the absorption spectra of the samples heat-treated at various temperatures from 600 to 1300 °C. Materials heat-treated at 600 and 800 °C exhibit a distinctive absorption band around 370 nm, which is characteristic for ZnO synthesized at relatively low temperatures. This band is blue-shifted with respect to the absorption band of bulk ZnO appearing at 380 nm [74,75]. This blue shift is commonly associated with the presence of nanoscale ZnO particles. The absorption band at 370 nm can be assigned to an excitonic absorption. In principle, a



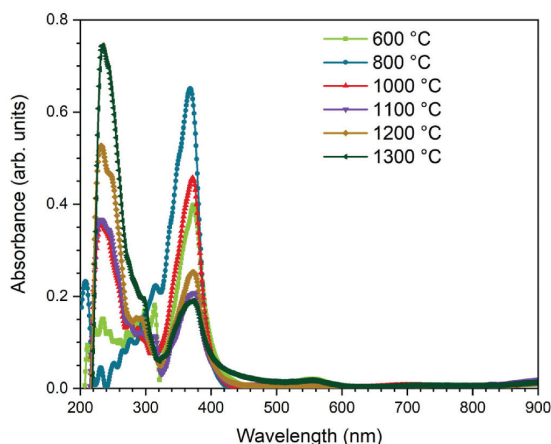


Fig. 4. UV-VIS absorption spectra of material synthesized at 600, 800, 1000, 1100, 1200 and 1300 °C, respectively.

quantum confinement effect and hence a blue shift is expected, but the average particle sizes of the ZnO synthesized here are larger than the Bohr exciton diameter for ZnO. (i.e., 6.48 nm) [76–79]. Therefore, the blue shift can be assigned to the local stress in the submicron particles [80]. Notably, this absorption band persisted in all samples, reaching its intensity maximum for the material synthesized at 800 °C, which can be correlated with the improved crystalline quality of the ZnO phase, as confirmed by X-ray diffraction and Raman analysis.

The intensity of the 370 nm UV absorption band is suppressed for the samples treated at temperatures above 800 °C, while a prominent absorption band peaking at approximately 232 nm emerges between 220 and 320 nm for temperatures above 1000 °C. This absorption feature is associated with the onset of the fundamental absorption of  $\text{Zn}_2\text{SiO}_4$  [81–83]. As the synthesis temperature increases, the  $\text{Zn}_2\text{SiO}_4$  phase of a higher crystallinity predominates, which is supported by the findings of the Rietveld refinement analysis and is correlated by a notable rise in absorption in the region of 220–320 nm.

The band gap energy ( $E_g$ ) of  $\alpha\text{-Zn}_2\text{SiO}_4$  was estimated from the absorption data via Tauc plot (Supporting Information S4). The calculated  $E_g$  values are 5.61, 5.64, 5.67, and 5.62 eV for the  $\alpha\text{-Zn}_2\text{SiO}_4$  phase

synthesized at 1000, 1100, 1200, and 1300 °C, respectively. These values are similar to those reported in Refs. [84,85].

### 3.4. Luminescence properties

To evaluate the potential of zinc silicate as a UV-B emitter and clarify the origin of the material emission, the processes of UV generation in the synthesized powders were investigated under an electron beam and synchrotron radiation excitation.

The cathodoluminescence spectra of the synthesized powders, recorded at RT and 6 K, are shown in Fig. 5.

The CL spectrum recorded at RT for the material synthesized at 600 °C reveals a weak emission band at 3.20 eV (387 nm), most probably attributed to the free exciton transition or near-band-edge emission (NBE) of ZnO [86,87]. As the synthesis temperature increases, a noticeable shift in the position of the UV peak from 3.20 (387 nm) to 3.07 eV (403 nm) is observed. The shift is accompanied by a significant enhancement in peak intensity due to increased crystallinity, as confirmed by X-ray diffraction and Raman analysis. Although the ZnO concentration becomes lower with increasing synthesis temperature, the crystallite size becomes larger, and the presence of ZnO is reliably registered by the CL method (see also [88]). The observed redshift in the UV peak position within the cathodoluminescence emission spectra may be attributed to morphological changes in ZnO [80].

With increasing heat treatment temperature above 1000 °C, the powders synthesized are mainly formed by a  $\text{Zn}_2\text{SiO}_4$  polymorph, exhibiting a broad emission band spanning approximately from 2.70 (459 nm) to 5 eV (248 nm). The Gaussian fit of the emission spectra (Supporting Information S5) reveals multiple components peaking at 3.07 (403 nm) and 3.58 eV (346 nm), and in the deep UV range where the emissions intensify with higher synthesis temperatures. For the sample synthesized at 1000 °C, the peaks are observed at 4.04 eV (307 nm) and 4.41 eV (281 nm), while the synthesis at 1200 °C causes the shift of emission peaks to 4.10 eV (302 nm) and 4.47 eV (277 nm), respectively. Synthesis at 1300 °C causes the appearance of a more intense peak at 4.13 eV (300 nm) alongside a lower intensity peak at 4.55 eV (272 nm).

Deep UV emission has relatively rarely been reported for  $\text{Zn}_2\text{SiO}_4$ , and only a limited number of studies focusing on zinc silicate films and nanocables have examined this emission [89–92]. The emission has been assigned to radiative recombination in the  $\text{Zn}_2\text{SiO}_4$  phase [90] or/and an indirect emission originating from  $\text{Zn}_2\text{SiO}_4$  [89]. The present study marks the first report of deep UV emission in zinc silicate in the form of powders. The reasons for these deep UV luminescence features

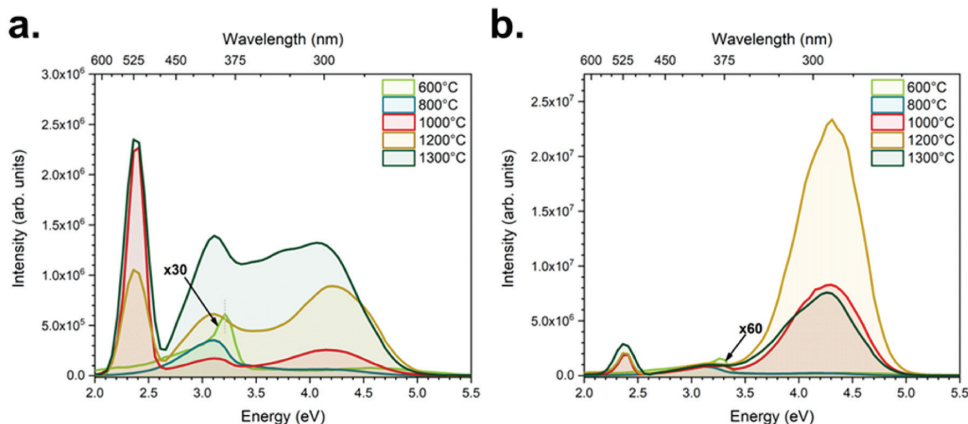


Fig. 5. CL spectra at RT (a) and 6 K (b) of the powders synthesized at 600, 800, 1000, 1200 and 1300 °C. The spectrum for the sample synthesized at 600 °C is multiplied by a factor of 30 at RT and 60 at 6 K.

found in the synthesized micropowders cannot be established with complete certainty; however, they can be attributed to a perturbed crystal lattice governed by local defects. An in-depth analysis is needed to establish the relationship between the features observed in the emission spectra.

An emission peak observed at around 3.07 eV (403 nm) is present in the spectra of all powders synthesized at temperatures above 1000 °C and is attributed to ZnO. According to XRD analysis using the Rietveld refinement, the quantities of ZnO are 7.74, 5.40, and 1.43 % for the samples synthesized at 1100, 1200, and 1300 °C, respectively. Although the percentage of ZnO is insignificant, the emission is most likely caused by the increased crystallinity of ZnO. The results indicate that the emission can be observed when excited by an electron beam, regardless of the ZnO concentration, as long as crystallinity prevails.

The samples heat-treated at 1000 °C and above displayed also a green emission band centered at 2.38 eV (521 nm), resembling the emission observed in Mn-doped  $\alpha$ -Zn<sub>2</sub>SiO<sub>4</sub> [93]. This emission is associated with the  $^4T_1(4G) \rightarrow ^6A_1(6S)$  transition in Mn<sup>2+</sup>, a well-known spectral feature of Mn-doped zinc silicates. Although Mn ions were not deliberately introduced during the synthesis, trace amounts of them could have been present in the starting materials.

Additionally, the luminescent properties of the material were studied at 6 K (Fig. 5b). At this temperature, the deep UV emission exhibited enhanced intensity as compared to RT. The sample synthesized at 1200 °C demonstrated the most pronounced UV-B emission. In contrast, the zinc silicate material synthesized at 1300 °C did not show similar enhancement in the UV-B emission at 6 K, whereas its intensity was lower than that observed in the sample synthesized at 1200 °C. This observation is consistent with the Raman analysis results, which indicate less disorder in the material synthesized at 1200 °C. Consequently, the most intense deep UV emission is presumably associated with a defect center in the more ordered  $\alpha$ -Zn<sub>2</sub>SiO<sub>4</sub> phase. The quenching of UV-B emission of the powders synthesized at temperatures above 1300 °C can be explained by the removal or passivation of the corresponding defect center. Moreover, a green emission band peaking at 2.38 eV (521 nm) was observed in these samples at room temperature, although with lower intensity. Similar trends are observed for the UV emission bands at 3.20 (387 nm) and 3.67 eV (338 nm).

To understand the origin of the emission peaks revealed by CL, photoluminescence studies were carried out at the FinEstBeAMS beamline using a selective excitation by VUV photons.

The low-temperature CL studies of the prepared materials pointed to the highest emission intensity in the Zn<sub>2</sub>SiO<sub>4</sub> sample synthesized at 1200 °C. Therefore, the studies under excitation by synchrotron radiation were focused on this material. Fig. 6 exhibits the 2D excitation-emission maps plotting in a color scale the luminescence intensity as a function of the excitation energy at RT and 6 K. The color gradient scale represents the luminescence intensity, with red for high value (highest

normalized intensity), while blue pixels represent the lowest relative intensities (dark blue for no emission). The diagonal lines on the bottom of the image represent the excitation light and its second order passing through the secondary monochromator. At RT, the main emission areas are located around 2.38 (521 nm) and 2.98 eV (416 nm) under 5.7 eV (218 nm) excitation. At 6 K, the mapping reveals that the predominant luminescence area is located around 3.90–4.50 eV.

A detailed analysis of the contour diagrams showed that four distinct emission bands could be distinguished in the sample at room temperature. A prominent green emission peak was observed at 2.38 eV (521 nm), while a UV emission band was present in the 2.60–3.27 eV range centered at 2.98 eV (416 nm). Another UV emission band was detected in the 3.43–3.62 eV range, peaking at 3.54 eV (350 nm). Furthermore, a deep UV emission band spanned from 3.90 to 4.50 eV. The green emission band attained its maximum intensity when excited within the narrow energy range 5.60–5.90 eV, whereas the other emission bands achieved their peak intensities under excitation between 5.60 and 6.30 eV.

Interestingly, the deep UV emission becomes more prominent at 6 K. This behavior is also observed in CL experiments. The green emission and the UV emission bands near 3 eV were retained, although with a lower intensity.

Emission and excitation spectra were extracted from the contour plots to analyze the specific emission and excitation wavelengths. The obtained spectra were corrected for spectral sensitivity of the registration channel, which explains a small shift in comparison with the raw data presented in the 2D excitation-emission map. It must be clarified that these corrections entail the drop of the 9 eV excitation peak maxima as is shown Fig. 8b in comparison to the results in the contour plots in Fig. 6b. In an attempt to clarify the origin of the observed emission bands, the emission spectra were analyzed under excitation in the region of the band gap edge energy between 5.70 (218 nm) and 7.20 eV (172 nm) and in the fundamental absorption region of zinc silicate at 10.42 eV (119 nm). The emission spectra under excitation at 5.7 eV (218 nm), 6.02 eV (206 nm), 7.2 eV (172 nm), and 10.42 eV (119 nm) are presented in Fig. 7a at RT and Fig. 7b at 6 K.

Across all RT spectra, distinct emission bands are consistently observed. The predominant green emission exhibits the highest intensity under the 5.7 eV (218 nm) excitation. Additionally, a broad emission band spans the 2.6 (477 nm) to 5.2 eV (238 nm) range. After Jacobian transformation and Gaussian fit, as detailed in Supporting Information S6, multiple peaks emerge within this range. A weak UV emission around 3.11 eV (399 nm) is attributed to the free exciton transition of ZnO. Another UV peak at 3.54 eV (350 nm) is commonly reported in sol-gel silica and is attributed to non-bridging oxygen hole centers (NBOHC), a type of point defect that readily forms in silica during heating [94]. This band becomes more pronounced under 7.2 eV (172 nm) excitation. In the deep UV range, two components are observed at

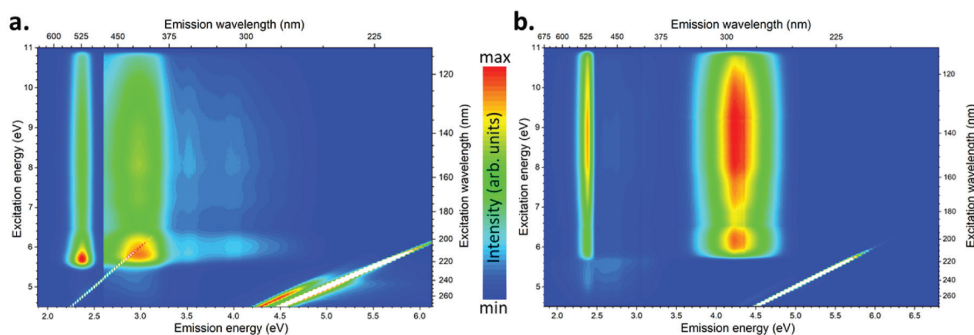
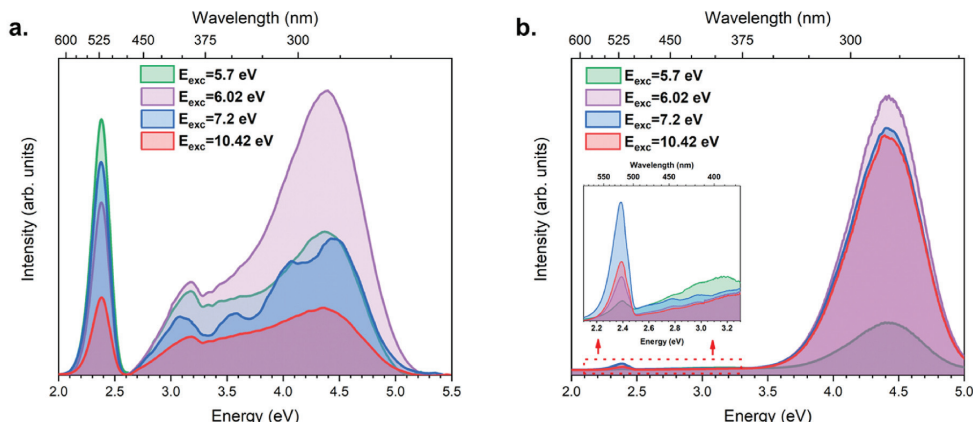
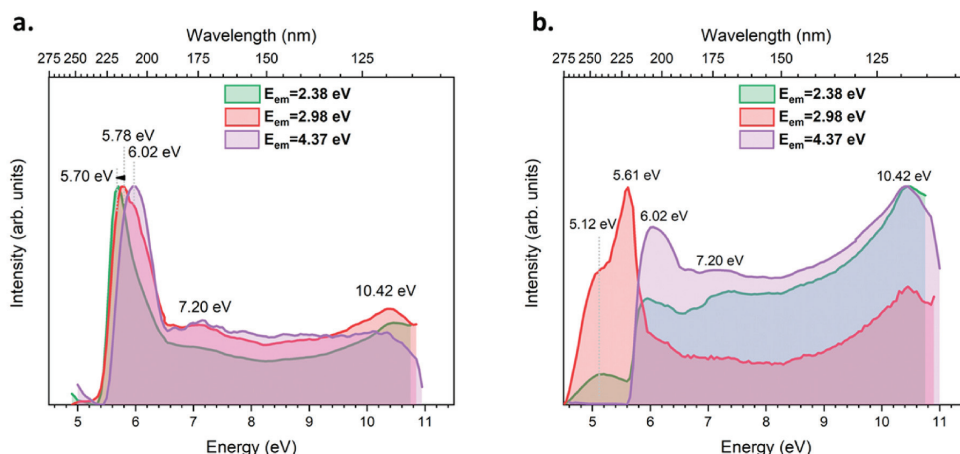


Fig. 6. 2D excitation-emission maps at (a) RT and (b) 6 K of the powders synthesized at 1200 °C.



**Fig. 7.** Emission spectra at (a) RT and (b) 6 K under synchrotron-ray excitation for the samples synthesized at 1200 °C, with excitation energies of 5.7 eV (green), 6.02 eV (purple), 7.2 eV (blue), and 10.42 eV (red). (For interpretation of the references to color in this figure legend, the reader is referred to the Web version of this article.)



**Fig. 8.** Normalized excitation spectra at (a) RT and (b) 6 K of the material synthesized at 1200 °C upon synchrotron-ray excitation, for emission energies of 2.38 eV (green), 2.98 eV (red), and 4.37 eV (purple). (For interpretation of the references to color in this figure legend, the reader is referred to the Web version of this article.)

4.04 (307 nm) and 4.48 eV (277 nm), with maximum intensity under 6.02 eV (206 nm) excitation. These deep UV emissions become more prominent at 6 K, a behavior also noted in CL experiments. At this low temperature, the manganese impurity emission and the excitonic emission associated with ZnO persist, though with much lower intensity compared to the dominant deep UV bands, which shift to 4.25 (292 nm) and 4.50 eV (275 nm).

To enhance the understanding of the observed emission bands, the measurements of excitation spectra were analyzed at both RT and 6 K, as illustrated in Fig. 8a and b. These spectra were monitored for the emission photon energies 4.37 eV (284 nm), 2.98 eV (416 nm), and 2.38 eV (521 nm).

In the excitation spectra corresponding to the Zn<sub>2</sub>SiO<sub>4</sub> green emission at 2.38 eV (521 nm), observed at RT, in addition to the low-energy absorption band at 4.7 eV (263 nm) (not shown here; see Ref. [95]) a significant excitation peak appears at 5.70 eV (218 nm). This excitation band located near the fundamental absorption edge of the material is likely to be related to the host material exciton trapped near Mn<sup>2+</sup>

impurity cation and transferring its energy to the impurity luminescence center. The maximum of the excitation spectrum of the 2.98 eV (416 nm) emission is observed at 5.78 eV (214 nm).

The excitation spectrum of UV-B emission centered at 4.37 eV (284 nm) showed an onset around 6 eV that corresponds to the band gap of the material estimated for a Zn<sub>2</sub>SiO<sub>4</sub> single crystal by the partial densities of states (PDOS) [93]. Since several emissions demonstrate maximum intensity near the bandgap energies (Fig. 8), it can be assumed that they are caused by host excitons either self-trapped or perturbed by defects of various types. However, other mechanisms might also contribute to the observed emissions. Further experiments, such as time-resolved photoluminescence, could provide a deeper understanding of these emissions and help reveal the nature of the luminescence centers. Additionally, EPR studies like those conducted for the ZnAl<sub>2</sub>O<sub>4</sub> compound [18], may clarify the role of defects in the luminescence behavior. Both approaches will be pursued in our future work to achieve a more complete understanding of the emission mechanisms in Zn<sub>2</sub>SiO<sub>4</sub>.

At low temperatures (6 K), the excitation spectrum of the emission at 2.38 eV (521 nm) demonstrates peaks located at 5.12 (242 nm), 6.02 eV (206 nm) in the near-edge energy region, as well as some structures at 7.20 (172 nm) and 10.42 eV (119 nm) situated in the fundamental absorption region of the material. The peak at 5.12 eV (242 nm) is likely associated with the intrinsic transition in  $\text{Mn}^{2+}$  ions distributed in the  $\text{Zn}_2\text{SiO}_4$  crystal lattice [95,96]. The shift of the higher-energy peak from 5.7 eV (218 nm) at RT to 6.02 eV (206 nm) at 6 K reflects the behavior common for other extrinsic emission and can be ascribed to the low temperature shift of the fundamental absorption edge. This shift is less noticeable in the excitation spectrum for the UV-B emission at 4.37 eV (284 nm), which allows one to relate this emission to self-trapped excitons or excitons slightly perturbed by lattice defects, e.g. oxygen vacancy. Based on first-principle calculations of the electronic band structure of the material, the spectral feature located around 7.20 eV (172 nm) might be attributed to the excitation of the  $[\text{SiO}_4]^{4-}$  cluster [95,97,98], while the peak at 10.42 eV (119 nm) is likely to be associated with the excitation of the  $[\text{ZnO}_4]^{6-}$  cluster [95,97–99].

Detailed excitation spectra analysis at low temperatures provided key insights into the emission mechanisms of  $\text{Zn}_2\text{SiO}_4$  powders, clarifying the structural factors that contribute to deep UV emission. This investigation aligns with the primary objective of this work: to enhance the understanding of the emission properties of willemite and evaluate its potential as a deep UV emitter. In summary, this work explored the sol-gel synthesis route to develop UV-B emitter powders and demonstrated that synthesis temperature has a significant effect on the crystallinity and phase composition of the powders, allowing tuning of emission intensity.

The luminescence studies consistently exhibit the enhancement on the emission for the powder synthesized at 1200 °C. The use of a feasible and not laborious synthesis shows the potential of this route to obtain UV-B emitter powders based on  $\text{Zn}_2\text{SiO}_4$  material without the incorporation of dopants such as transition metal ions or rare earths.

#### 4. Conclusions

The rare-earth-free  $\text{Zn}_2\text{SiO}_4$  powders synthesized by the sol-gel method showed distinctive UV-B emission. Here, we report on the cathodoluminescence and synchrotron radiation-induced luminescence studies of deep UV emission in zinc silicate powders for the first time. The results of the study underscore the potential of the  $\text{Zn}_2\text{SiO}_4$  powders as deep UV emitters.

Through a comprehensive investigation, which included thermal analyses, XRD, Raman spectroscopy, and microstructural examination, valuable insights into the phase evolution and crystal structures over a wide range of synthesis temperatures were acquired.

Thermal analysis indicated the formation of ZnO at lower temperatures (400–650 °C), the appearance of metastable  $\beta$ - $\text{Zn}_2\text{SiO}_4$  at approximately 750 °C, and the stabilization of  $\alpha$ - $\text{Zn}_2\text{SiO}_4$  above 950 °C. Increasing the synthesis temperature results in a noticeable transition from compact irregularly shaped particles to larger spherical particles.

The material synthesized at 1200 °C demonstrated the strongest UV-B radiation, indicating a significant contribution of the perturbed crystal lattice by local defects under these synthesis conditions. The excitation spectra revealed complex energy transfer mechanisms, including excitonic processes and direct excitation of impurity centers. The onset of the excitation spectrum of the main UV-B emission of  $\text{Zn}_2\text{SiO}_4$  is at 6.02 eV (206 nm), which is in a good agreement with the band-gap value, and supports the assignments of this emission to self-trapped excitons or excitons influenced by lattice defects, such as oxygen vacancies. Nonetheless, further studies are required to fully understand the emission mechanisms.

Additionally, green narrow emission band centered at 2.38 eV (521 nm) is noticeably observed at RT; this emission is attributed to an intrinsic transition in  $\text{Mn}^{2+}$  ions distributed in the  $\text{Zn}_2\text{SiO}_4$  crystal lattice.

As mentioned, the Mn cations were not deliberately introduced during the synthesis. However, the presence of both emissions increases the versatility of the synthesized materials for practical applications. Our work marks a significant breakthrough in the development of environmentally friendly, rare-earth-free UV-B emitting zinc silicate powders which offer promising material for practical technological fields, whereby deep UV light is eagerly demanded, such as next-generation UV-B emitting devices for disinfection and sterilization.

#### CRediT authorship contribution statement

**Jallouli Necib:** Writing – review & editing, Writing – original draft, Validation, Methodology, Investigation, Formal analysis, Conceptualization. **Eduard Feldbach:** Writing – review & editing, Formal analysis. **Ivo Romet:** Writing – review & editing, Investigation. **Vitali Nagirnyi:** Writing – review & editing, Writing – original draft, Validation, Methodology, Investigation. **Irina Hussainova:** Writing – review & editing, Validation, Investigation. **Rocio E. Rojas-Hernandez:** Writing – review & editing, Writing – original draft, Visualization, Validation, Supervision, Software, Resources, Project administration, Methodology, Investigation, Funding acquisition, Formal analysis, Data curation, Conceptualization.

#### Declaration of competing interest

The authors declare that they have no known competing financial interests or personal relationships that could have appeared to influence the work reported in this paper.

#### Acknowledgments

The financial support from the Estonian Research Council (grants PSG-466 (R. E. Rojas-Hernandez), PRG-643 (I. Hussainova), PRG629 (V. Nagirnyi)) is gratefully acknowledged. Researchers from the University of Tartu, Estonia were supported also by the ERDF funding's in Estonia granted to the Centre of Excellence TK141 “Advanced materials and high-technology devices for sustainable energetics, sensorics and nanoelectronics (HiTechDevices)” (grant no. TK141 2014–2020.4.01.15-0011). We acknowledge MAX IV Laboratory for time on Beamline FinEstBeAMS under Proposal 20230209. Research conducted at MAX IV, a Swedish national user facility, is supported by the Swedish Research Council under contract 2018–07152, the Swedish Governmental Agency for Innovation Systems under contract 2018–04969, and Formas under contract 2019–02496.

#### Appendix A. Supplementary data

Supplementary data to this article can be found online at <https://doi.org/10.1016/j.jlumin.2025.121070>.

#### Data availability

Data will be made available on request.

#### References

- [1] Huang, C., Ouyang, D., Chen, B.E., Keshta, Advanced lithography materials: from fundamentals to applications, *Adv. Colloid Interface Sci.* 329 (2024) 103197, <https://doi.org/10.1016/j.cis.2024.103197>.
- [2] L. Liu, S. Peng, Y. Guo, Y. Lin, X. Sun, L. Song, J. Shi, Y. Zhang, Designing X-ray-excited UVC persistent luminescent material via band gap engineering and its application to anti-counterfeiting and information encryption, *ACS Appl. Mater. Interfaces* 14 (2022) 41215–41224, <https://doi.org/10.1021/acsami.2c12407>.
- [3] Y. Kebbi, A.I. Muhammad, A.S. Sant'Ana, L. do Prado-Silva, D. Liu, T. Ding, Recent advances on the application of UV-LED technology for microbial inactivation: progress and mechanism, *Compr. Rev. Food Saf.* 19 (2020) 3501–3527, <https://doi.org/10.1111/1541-4337.12645>.



- [4] H. Singh, S.K. Bhardwaj, M. Khatri, K.H. Kim, N. Bhardwaj, UVC radiation for food safety: an emerging technology for the microbial disinfection of food products, *Chem. Eng. J.* 417 (2021) 128084, <https://doi.org/10.1016/j.cej.2020.128084>.
- [5] V. Goulden, T.C. Ling, P. Babakinejad, R. Dawe, E. Eadie, H. Fassihi, A. Pityan, et al., British association of Dermatologists and British photodermatology group guidelines for narrowband ultraviolet B phototherapy 2022, *Br. J. Dermatol.* 187 (2022) 295–308, <https://doi.org/10.1111/bjd.21669>.
- [6] B. Jiang, X. Shi, T. Zhang, Y. Huang, Recent advances in UV/thermal curing silicone polymers, *Chem. Eng. J.* 435 (2022) 134843, <https://doi.org/10.1016/j.cej.2022.134843>.
- [7] A. Gidari, S. Sabbatini, S. Bastianelli, S. Pierucci, C. Busti, D. Bartolini, A. M. Stabile, et al., SARS-CoV-2 survival on surfaces and the effect of UV-C light, *Viruses* 13 (2021) 408, <https://doi.org/10.3390/v13030408>.
- [8] M.A. Khan, N. Maeda, M. Jo, Y. Akamatsu, R. Tanabe, Y. Yamada, H. Hirayama, 13 mW operation of a 295–310 nm AlGaIn UV-B LED with a p-AlGaIn transparent contact layer for real world applications, *J. Mater. Chem. C* 7 (2019) 143–152, <https://doi.org/10.1039/C8TC03825B>.
- [9] T.R. Kwon, S.E. Lee, J.H. Kim, Y.N. Jang, S.Y. Kim, S.K. Mun, C.W. Kim, J. Na, B. J. Kim, 310 nm UV-LEDs attenuate imiquimod-induced psoriasis-like skin lesions in C57BL/6 mice and inhibit IL-22-induced STAT3 expression in HaCaT cells, *Photochem. Photobiol. Sci.* 19 (2020) 1009–1021, <https://doi.org/10.1039/c9pp00444krsc.li/pss>.
- [10] A. Takada, K. Matsushita, S. Horioka, Y. Furuichi, Y. Sumi, Bactericidal effects of 310 nm ultraviolet light-emitting diode irradiation on oral bacteria, *BMC Oral Health* 17 (2017) 1–10, <https://doi.org/10.1186/s12903-017-0382-5>.
- [11] V. Singh, N. Singh, M.S. Pathak, S. Watanabe, T.G. Rao, P.K. Singh, V. Dubey, UV emission from  $Gd^{3+}$  ions in  $LaAlO_3$  phosphors, *Optik* 157 (2018) 1391–1396, <https://doi.org/10.1016/j.jlco.2017.12.034>.
- [12] V. Singh, J.K. Lee, M. Seshadri, A.A. Bhat, S. Watanabe, T.K.G. Rao, Photoluminescence and EPR spectroscopic studies on narrowband ultraviolet-B (NB-UVB) emitting trivalent gadolinium-doped  $CaAl_2O_4$  material for phototherapy lamps, *Ceram. Int.* 50 (2024) 4632–4639, <https://doi.org/10.1016/j.ceramint.2023.11.207>.
- [13] W. Zhao, L. Li, T. Li, J. Qiu, Y. Yang, UVB persistent luminescence of  $CaF_2:Gd^{3+}$  for radiation labeling and tracing, *Adv. Opt. Mater.* 12 (2024), <https://doi.org/10.1002/adom.202401320>.
- [14] Y. Kikuchi, S. Matsuyama, S. Kawamura, F. Fujishiro, M. Miwa, S. Toyama, Experimental investigation on UV light output of  $YPO_4:Gd$  particles for ion beam induced fluorescence microscopy, *Nucl. Instrum. Methods Phys. Res. B* 557 (2024) 165518, <https://doi.org/10.1016/j.nimb.2024.165518>.
- [15] H. Kominami, T. Iguchi, Y. Nakanishi, K. Hara, Ultra-violet emission of aluminates phosphors prepared by solid phase synthesis, *J. Adv. Res.* 2 (2011) 21109, 021109.
- [16] T. Ishinaga, T. Iguchi, H. Kominami, K. Hara, M. Kitaura, A. Ohnishi, Luminescent property and mechanism of  $ZnAl_2O_4$  ultraviolet emitting phosphor, *Phys. Status Solidi C* 12 (2015) 797–800, <https://doi.org/10.1002/pssc.201400317>.
- [17] R.E. Rojas-Hernandez, F. Rubio-Marcos, I. Romet, A. del Campo, G. Gorni, I. Hussainova, J.F. Fernandez, V. Nagirnyi, Deep-ultraviolet emitter: rare-earth-free  $ZnAl_2O_4$  nanofibers via a simple wet chemical route, *Inorg. Chem.* 61 (2022) 11886–11896, <https://doi.org/10.1021/acs.inorgchem.2c01646>.
- [18] R.E. Rojas-Hernandez, F. Rubio-Marcos, I. Romet, E. Feldbach, M. Buryi, D. John, R. Ivanov, I. Hussainova, J.F. Fernandez, V. Nagirnyi, On the potential of Transparent Rare-Earth-Free  $ZnAl_2O_4$  Ceramics targeted at the UV-C to UV-B emission, *Appl. Mater. Today* 38 (2024) 102230, <https://doi.org/10.1016/j.apmt.2024.102230>.
- [19] S. Karmakar, I.H. Emu, M.A. Halim, P.K. Sarkar, M. Sultana, A. Tasnim, M. A. Hamid, I.F. Shiam, R. Droopad, A. Haque, Growth optimization, optical, and dielectric properties of heteroepitaxially grown ultrawide-bandgap  $ZnGa_2O_4$  (111) thin film, *J. Appl. Phys.* 135 (2024), <https://doi.org/10.1063/5.0190906>.
- [20] P.V. Ramakrishna, D.B.R.K. Murthy, D.L. Sastry, K. Samatha, Synthesis, structural and luminescence properties of Mn doped  $ZnO/ZnSiO_4$  composite microphosphor, *Spectrochim. Acta Mol. Biomol. Spectrosc.* 129 (2014) 274–279, <https://doi.org/10.1016/j.saa.2014.03.081>.
- [21] S. Tripathi, R. Bose, A. Roy, S. Nair, N. Ravishanker, Synthesis of hollow nanotubes of  $Zn_2SiO_4$  or  $SiO_2$ : mechanistic understanding and uranium adsorption behavior, *ACS Appl. Mater. Interfaces* 7 (2015) 26430–26436, <https://doi.org/10.1021/acsami.5b09805>.
- [22] G. Essalah, K. Kadim, A. Jabar, R. Masrouf, M. Ellouze, H. Guermazi, S. Guermazi, Structural, optical, photoluminescence properties and Ab initio calculations of new  $Zn_2SiO_4/ZnO$  composite for white light emitting diodes, *Ceram. Int.* 46 (2020) 12656–12664, <https://doi.org/10.1016/j.ceramint.2020.02.031>.
- [23] S.Zh Karazhanov, P. Ravindran, H. Fjellvåg, B.G. Svensson, Electronic structure and optical properties of  $ZnSiO_3$  and  $Zn_2SiO_4$ , *J. Appl. Phys.* 106 (2009), <https://doi.org/10.1063/1.3268445>.
- [24] C.H. Hsu, C.E. Liu, L.Y. Lai, M.T. Kuo, J.R. He, H.P. Lin, Synthesis of mesoporous  $Eu^{3+}$  doped zinc/silicate phosphors for highly selective and sensitive detection of sulfide ions, *ACS Omega* 8 (2023) 44229–44237, <https://doi.org/10.1021/acsomega.3c06823>.
- [25] D.K. Bhatti, R. Verma, S. Rani, D. Agarwal, S. Mehra, A.K. Gangwar, B.K. Gupta, N. Singh, A.K. Srivastava, Synthesis and characterization of highly crystalline Bi-functional Mn-doped  $Zn_2SiO_4$  nanostructures by low-cost sol-gel process, *Nanomaterials* 13 (2023) 538, <https://doi.org/10.3390/nano13030538>.
- [26] R.B. Basavaraj, H. Nagabhushana, B. Daruka Prasad, S.C. Sharma, S.C. Prashantha, B.M. Nagabhushana, A single host white light emitting  $Zn_2SiO_4:Re^{3+}$  (Eu, Dy, Sm) phosphor for LED applications, *Optik* 126 (2015) 1745–1756, <https://doi.org/10.1016/j.jlco.2014.07.149>.
- [27] P. Dai, Z. Xu, X. Yu, Y. Wang, L. Zhang, G. Li, Z. Sun, X. Liu, M. Wu, Mesoporous hollow  $Zn_2SiO_4:Mn^{2+}$  nanospheres: the study of photoluminescence and adsorption properties, *Mater. Res. Bull.* 61 (2015) 76–82, <https://doi.org/10.1016/j.materresbull.2014.10.002>.
- [28] Y. Yang, Y. Zhuang, Y. He, B. Bai, X. Wang, Fine tuning of the dimensionality of zinc silicate nanostructures and their application as highly efficient absorbers for toxic metal ions, *Nano Res.* 3 (2010) 581–593, <https://doi.org/10.1007/s12274-010-0019-3>.
- [29] N. Effendy, S.H.A. Aziz, H.M. Kamari, K.A. Matori, M.H.M. Zaid, Enhanced green photoluminescence of erbium doped  $Zn_2SiO_4$  glass-ceramics as phosphor in optoelectronic devices, *J. Alloys Compd.* 783 (2019) 441–447, <https://doi.org/10.1016/j.jallcom.2018.12.362>.
- [30] V. Sivakumar, A. Lakshmanan, L. Sangeetha, J. Nandhagopal, G. Annadurai, R. S. Rani, S. Saravanakumar, Effect of flux and Co-doping on photoluminescence properties of  $Zn_2SiO_4:Eu^{3+}$  red phosphors for blue LED excitable white LED applications, *J. Fluoresc.* (2024), <https://doi.org/10.1007/s10895-024-04048-2>.
- [31] P. Vařák, P. Nevindová, J. Baborák, Er-doped zinc-silicate glass-ceramics with enhanced emission in the near-infrared region, *EPJ Web Conf.* 287 (2023) 05039, <https://doi.org/10.1051/epjconf/202328705039>.
- [32] N. Rakov, F. Matias, Y. Xing, G.S. Maciel,  $Mn^{2+}$  doped  $Zn_2SiO_4$  phosphors: a threefold-mode sensing approach for optical thermometry in the visible region at 525 nm, *Opt. Mater. X* 24 (2024) 100359, <https://doi.org/10.1016/j.omx.2024.100359>.
- [33] S.A.A. Wahab, K.A. Matori, M.H.M. Zaid, M.M.A. Kechik, N. Effendy, R.E. M. Khaidir, Blue emission: optical properties of  $Co^{2+}$  doping towards  $Zn_2SiO_4$  glass-ceramics, *Optik* 274 (2023) 170528, <https://doi.org/10.1016/j.jlco.2023.170528>.
- [34] Z.G. Portakal-Uçar, T. Dogan, S. Akça, Ü.H. Kaynar, M. Topaksu, Effect of  $Sm^{3+}$  and  $Mn^{2+}$  incorporation on the structure and luminescence characteristics of  $Zn_2SiO_4$  phosphor, *Radiat. Phys. Chem.* 181 (2021) 109329, <https://doi.org/10.1016/j.radphyschem.2020.109329>.
- [35] P. Mbule, D. Mlotswa, B. Mothudi, M. Dhlamini, Photoluminescence and thermoluminescence analysis of  $Zn_2SiO_4:Dy^{3+}$  nanophosphor, *J. Lumin.* 235 (2021) 118060, <https://doi.org/10.1016/j.jlumin.2021.118060>.
- [36] M. Bhardwaj, S. Rai, A. Gaur, Structural and morphological characterizations of ex-situ sol-gel derived luminescent  $Nd^{3+}$ - $Yb^{3+}$  ion co-doped zinc-silicate dense glass-ceramic, *J. Non-Cryst. Solids* 619 (2023) 122552, <https://doi.org/10.1016/j.jnoncrysol.2023.122552>.
- [37] A.Z.K. Azman, K.A. Matori, S.H. Ab Aziz, M.H.M. Zaid, S.A.A. Wahab, R.E. M. Khaidir, Comprehensive study on structural and optical properties of  $Tm_2O_3$  doped zinc silicate based glass-ceramics, *J. Mater. Sci. Mater. Electron.* 29 (2018) 19861–19866, <https://doi.org/10.1007/s10854-018-0115-9>.
- [38] S. Jacob, B.M. Nagabhushana, Chikkahanumantharayappa, Tb and Li doped Zinc Silicate green nanophosphors synthesized by solution combustion method, *Nano-Struct. Nano-Objects* 19 (2019) 100363, <https://doi.org/10.1016/j.nano.2019.100363>.
- [39] T. Jiang, W. Yang, W. Deng, Z. Yu, W. Wen, Improvement of microstructure and dielectric properties of  $La_{1-x}Si_{3-x}O_{8-x}$  ceramics by doping with rare earth elements (La, Pr, Nd, Sm), *J. Alloys Compd.* 1010 (2025) 177679, <https://doi.org/10.1016/j.jallcom.2024.177679>.
- [40] V. Singh, K. Bhatia, A.S. Rao, J.B. Joo, Trivalent Gd incorporated  $Zn_2SiO_4$  phosphor material for EPR and luminescence investigations, *Int. J. Mater. Res.* 115 (2024) 438–445, <https://doi.org/10.1515/ijmr-2023-0222>.
- [41] L.T.T. Vien, N. Tu, T.T. Phuong, N.T. Tuan, N.V. Quang, H. Van Bui, A.-T. Duong, D.Q. Trung, P.T. Huy, Facile synthesis of single phase  $\alpha$ - $Zn_2SiO_4:Mn^{2+}$  phosphor via high-energy planetary ball milling and post-annealing method, *J. Lumin.* 215 (2019) 116612, <https://doi.org/10.1016/j.jlumin.2019.116612>.
- [42] A. Majumdar, D. Ganguli, Solid state synthesis of willemite,  $Zn_2SiO_4$ : role of precursors, *Trans. Indian Ceram. Soc.* 50 (1991) 93–97, <https://doi.org/10.1080/0371750X.1991.10804499>.
- [43] P. Diana, S. Sebastian, D. Sivaganesan, M.A. Manthrammel, A. Kumar, M. Shkir, Hydrothermal synthesis of cerium-doped  $Zn_2SiO_4$  phosphor for futuristic lighting applications, *J. Solid State Chem.* 329 (2024) 124441, <https://doi.org/10.1016/j.jssc.2023.124441>.
- [44] Z.G. Portakal-Uçar, M. Oglakci, M. Yüksel, M. Ayvaci, N. Can, Structural and luminescence characterization of  $Ce^{3+}$  and  $Mn^{2+}$  co-activated zinc silicate nanocrystal obtained by gel combustion synthesis, *Mater. Res. Bull.* 133 (2021) 111025, <https://doi.org/10.1016/j.materresbull.2020.111025>.
- [45] V. Sivakumar, A. Lakshmanan, Pyrolysis synthesis of  $Zn_2SiO_4:Mn^{2+}$  phosphors – effect of fuel, flux and co-dopants, *J. Lumin.* 145 (2014) 420–424, <https://doi.org/10.1016/j.jlumin.2013.08.016>.
- [46] V.B. Bhatkar, S.K. Omanwar, S.V. Moharil, Combustion synthesis of the  $Zn_2SiO_4$ : Mn phosphor, *Phys. Stat. Sol.* 191 (2002) 272–276, [https://doi.org/10.1002/1521-396X\(200205\)191:1<272::AID-PSSA272>3.0.CO;2-R](https://doi.org/10.1002/1521-396X(200205)191:1<272::AID-PSSA272>3.0.CO;2-R).
- [47] X. Yi, H. Liu, Y. Wang, J. Chen, Z. Chen, Y. Wang, X. Yuan, K. Zhu, Modulating trap properties by  $Cr^{3+}$ -doping in  $Zn_2SiO_4:Mn^{2+}$  nano phosphor for optical information storage, *Ceram. Int.* 50 (2024) 43373–43382, <https://doi.org/10.1016/j.ceramint.2024.08.188>.
- [48] V. Singh, A. Prasad, N. Deopa, A.S. Rao, S. Jung, N. Singh, J.L. Rao, G. Lakshminarayana, Luminescence features of  $Mn^{2+}$ -doped  $Zn_2SiO_4$ : a green color emitting phosphor for solid-state lighting, *Optik* 225 (2021) 165715, <https://doi.org/10.1016/j.jlco.2020.165715>.
- [49] D. Bokov, A. Turki Jalil, S. Chupradit, W. Sukatan, M. Javed Ansari, I.H. Shewael, G.H. Valiev, E. Kianfar, Nanomaterial by sol-gel method: synthesis and application, *Adv. Mater. Sci. Eng.* 2021 (2021), <https://doi.org/10.1155/2021/5102014>.

- [50] V. Mote, Y. Purushotham, B. Dole, Williamson-Hall analysis in estimation of lattice strain in nanometer-sized ZnO particles, *J. Theor. Appl. Phys.* 6 (2012) 6, <https://doi.org/10.1186/2251-7235-6-6>.
- [51] E. Feldbach, E. Toldsepp, M. Kirm, A. Lushchik, K. Mizohata, J. Räisänen, Radiation resistance diagnostics of wide-gap optical materials, *Opt. Mater.* 55 (2016) 164–167, <https://doi.org/10.1016/j.optmat.2016.03.008>.
- [52] R. Pärna, R. Sankari, E. Kuk, E. Nömmiste, M. Valden, M. Lastusaari, K. Kooser, K. Kokko, M. Hirsimäki, S. Urpeläinen, P. Turunen, A. Kivimäki, V. Pankratov, L. Reisberg, F. Hennies, H. Tarawneh, R. Nyholm, M. Huttula, FinEstBeAMS – a wide-range Finnish-Estonian beamline for materials science at the 1.5 GeV storage ring at the MAX IV laboratory, *Nucl. Instrum. Methods Phys. Res.* 859 (2017) 83–89, <https://doi.org/10.1016/j.nima.2017.04.002>.
- [53] V. Pankratov, R. Pärna, M. Kirm, V. Nagirnyi, E. Nömmiste, S. Omelkov, S. Vielhauer, K. Chernenko, L. Reisberg, P. Turunen, A. Kivimäki, E. Kuk, M. Valden, M. Huttula, Progress in development of a new luminescence setup at the FinEstBeAMS beamline of the MAX IV laboratory, *Radiat. Meas.* 121 (2019) 91–98, <https://doi.org/10.1016/j.radmeas.2018.12.011>.
- [54] B. Li, Y. Yuan, S. Zhang, H. Jiang, Microstructure and microwave dielectric properties of  $(\text{Zn}_{1-x}\text{Mg}_x)\text{SiO}_4$  ceramics, *Bull. Mater. Sci.* 34 (2011) 921–925, <https://doi.org/10.1007/s12034-011-0215-0>.
- [55] H.F.W. Taylor, The dehydration of hemimorphite, *Am. Mineral.* 47 (1962) 932–944.
- [56] M. Masjedi-Arani, M. Salavati-Niasari, A simple sonochemical approach for synthesis and characterization of  $\text{Zn}_2\text{SiO}_4$  nanostructures, *Ultrason. Sonochem.* 29 (2016) 226–235, <https://doi.org/10.1016/j.ultrasonch.2015.09.020>.
- [57] A.R. Molla, A. Tarafder, B. Karmakar, Synthesis and properties of glasses in the  $\text{K}_2\text{O}-\text{SiO}_2-\text{Bi}_2\text{O}_3-\text{TiO}_2$  system and bismuth titanate ( $\text{Bi}_4\text{Ti}_3\text{O}_{12}$ ) nano glass-ceramics thereof, *J. Mater. Sci.* 46 (2011) 2967–2976, <https://doi.org/10.1007/s10853-010-5173-1>.
- [58] R. Cuscó, E. Alarcón-Lladó, J. Ibáñez, L. Artús, J. Jiménez, B. Wang, M.J. Callahan, Temperature dependence of Raman scattering in ZnO, *Phys. Rev. B* 75 (2007) 165202, <https://doi.org/10.1103/PhysRevB.75.165202>.
- [59] F. Ahmed, S. Kumar, N. Arshi, R. Prakash, Growth and characterization of ZnO nanorods by microwave-assisted route: green chemistry approach, *Adv. Mater. Lett.* 2 (2011) 183–187, <https://doi.org/10.5185/amlett.2011.1213>.
- [60] P. Loiko, O.S. Dymshits, V.V. Vitkin, N.A. Skoptsov, A.A. Zhilin, D.V. Shemchuk, M. Ya Tsentser, K. Bogdanov, A.M. Malyarevich, I.V. Glazunov, X. Mateos, K. V. Yumashev, Saturable absorber: transparent glass-ceramics based on a mixture of  $\text{Co}^{2+}$ - $\text{Zn}_2\text{SiO}_4$  and  $\text{Co}^{2+}$ - $\text{ZnO}$  nanocrystals, *Appl. Opt.* 55 (2016) 5505, <https://doi.org/10.1364/AO.55.005505>.
- [61] P. Loiko, O. Dymshits, A. Volokitina, I. Alekseeva, D. Shemchuk, M. Tsentser, A. Bachina, A. Khubetsov, E. Vilejshnikova, P. Petrov, A. Baranov, A. Zhilin, Structural transformations and optical properties of glass-ceramics based on ZnO,  $\beta$ - and  $\alpha$ - $\text{Zn}_2\text{SiO}_4$  nanocrystals and doped with  $\text{Er}_2\text{O}_3$  and  $\text{Yb}_2\text{O}_3$ : Part I. The role of heat-treatment, *J. Lumin.* 202 (2018) 47–56, <https://doi.org/10.1016/j.jlumin.2018.05.010>.
- [62] C. Lin, J. Wang, X. Zhao, E. Zhu, N. Long, C. Rüssel, Competitive crystallization of  $\beta$ - $\text{Zn}_2\text{SiO}_4$  and ZnO in an aluminosilicate glass, *Ceram. Int.* 44 (2018) 7209–7213, <https://doi.org/10.1016/j.ceramint.2018.01.168>.
- [63] C.C. Lin, P. Shen, Sol-gel synthesis of zinc orthosilicate, *J. Non-Cryst. Solids* 171 (1994) 281–289, [https://doi.org/10.1016/0022-3093\(94\)90197-X](https://doi.org/10.1016/0022-3093(94)90197-X).
- [64] B. Chandra Babu, S. Buddhudu, Analysis of structural and electrical properties of  $\text{Ni}^{2+}$ :  $\text{Zn}_2\text{SiO}_4$  ceramic powders by sol-gel method, *J. Sol. Gel Sci. Technol.* 70 (2014) 405–415, <https://doi.org/10.1007/s10971-014-3296-6>.
- [65] J. Song, K. Song, J. Wei, H. Lin, J. Xu, J. Wu, W. Su, Microstructure characteristics and microwave dielectric properties of calcium apatite ceramics as microwave substrates, *J. Alloys Compd.* 731 (2018) 264–270, <https://doi.org/10.1016/j.jallcom.2017.10.028>.
- [66] J. Rouquette, I. Kantor, C.A. McCommon, V. Dmitriev, L.S. Dubrovinsky, High-pressure studies of  $(\text{Mg}_{0.9}\text{Fe}_{0.1})_2\text{SiO}_4$  olivine using Raman spectroscopy, X-ray diffraction, and Mössbauer spectroscopy, *Inorg. Chem.* 47 (2008) 2668–2673, <https://doi.org/10.1021/ci701983v>.
- [67] A.K. Yadav, P. Singh, A review of the structures of oxide glasses by Raman spectroscopy, *RSC Adv.* 5 (2015) 67583–67609, <https://doi.org/10.1039/C5RA13043C>.
- [68] E. Faulques, E. Fritsch, M. Ostroumov, Spectroscopy of natural silica-rich glasses, *J. Mineral. Petrol. Sci.* 96 (2001) 120–128, <https://doi.org/10.2465/jmps.96.120>.
- [69] N.S. Bekturganov, M.R. Bissengaliyeva, D.B. Gogol, Calculation of vibrational spectra and thermodynamic functions of a natural zinc silicate – willemite, *Eurasian Chem. Technol. J.* 15 (2013) 227, <https://doi.org/10.18321/ecjt226>.
- [70] T.C. Damen, S.P.S. Porto, B. Tell, Raman effect in zinc oxide, *Phys. Rev.* 142 (1966) 570–574, <https://doi.org/10.1103/PhysRev.142.570>.
- [71] G. Brazilius, R. Stankeviciute, A. Zalga, Sol-gel derived europium doped  $\text{CaMoO}_4$ :  $\text{Eu}^{3+}$  with complex microstructural and optical properties, *Mater. Sci.* 20 (2014), <https://doi.org/10.5755/joi.ms.20.1.4797>.
- [72] N.A.S. Omar, Y.W. Fen, K.A. Matori, S.H.A. Aziz, Z.N. Alassan, N.F. Samsudin, Development and characterization studies of  $\text{Eu}^{3+}$ -doped  $\text{Zn}_2\text{SiO}_4$  phosphors with waste silicate sources, *Procedia Chem.* 19 (2016) 21–29, <https://doi.org/10.1016/j.proche.2016.03.006>.
- [73] M. Hashem, E. Saion, N.M. Al-Hada, H.M. Kamari, A.H. Shaari, Z.A. Talib, S. B. Paiman, M.A. Kamarudeen, Fabrication and characterization of semiconductor nickel oxide (NiO) nanoparticles manufactured using a facile thermal treatment, *Results Phys.* 6 (2016) 1024–1030, <https://doi.org/10.1016/j.rinp.2016.11.031>.
- [74] V. Prasad, C. D'Souza, D. Yadav, A.J. Shaikh, N. Vigneshwaran, Spectroscopic characterization of zinc oxide nanorods synthesized by solid-state reaction, *Spectrochim. Acta Mol. Biomol. Spectrosc.* 65 (2006) 173–178, <https://doi.org/10.1016/j.saa.2005.10.001>.
- [75] K. Sowri Babu, A. Ramachandra Reddy, Ch Sujatha, K. Venugopal Reddy, A. N. Mallika, Synthesis and optical characterization of porous ZnO, *J. Adv. Ceram.* 2 (2013) 260–265, <https://doi.org/10.1007/s40145-013-0069-6>.
- [76] R.E. Dietz, J.J. Hopfield, D.G. Thomas, Excitons and the absorption edge of ZnO, *J. Appl. Phys.* 32 (1961) 2282–2286, <https://doi.org/10.1063/1.1777060>.
- [77] A.A. Mosquera, D. Horwat, A. Rashkovskiy, A. Kovalev, P. Miska, D. Wainstein, J. M. Albella, J.L. Endrino, Exciton and core-level electron confinement effects in transparent ZnO thin films, *Sci. Rep.* 3 (2013) 1714, <https://doi.org/10.1038/srep01714>.
- [78] B.L. Caetano, C.V. Santilli, F. Meneau, V. Brioso, S.H. Pulcinelli, In situ and simultaneous UV–vis/SAXS and UV–vis/XAFS time-resolved monitoring of ZnO quantum dots formation and growth, *J. Phys. Chem. C* 115 (2011) 4404–4412, <https://doi.org/10.1021/jp109585t>.
- [79] B. Kisan, P. Alagarsamy, Room temperature ferromagnetism in finite sized ZnO nanoparticles, *Phys. B Condens. Matter* 448 (2014) 115–119, <https://doi.org/10.1016/j.physb.2014.02.040>.
- [80] Z. Yang, Z. Ye, Z. Xu, B. Zhao, Effect of the morphology on the optical properties of ZnO nanostructures, *Physica E Low Dimens. Syst. Nanostruct.* 42 (2009) 116–119, <https://doi.org/10.1016/j.physe.2009.09.010>.
- [81] K. Pratibha, Chitralekha, H. Kaur, S. Shankar, S. Gaurav, Y. Dwivedi, Influence of annealing temperature on structural, optical and electrical properties of zinc silicate ( $\text{Zn}_2\text{SiO}_4$ ) nanophosphors, *Phys. B Condens. Matter* 658 (2023) 414836, <https://doi.org/10.1016/j.physb.2023.414836>.
- [82] E.A.G. Engku Ali, K.A. Matori, E. Saion, S.H.A. Aziz, M.H.M. Zaid, I.M. Alibe, Effect of sintering temperatures on structural and optical properties of ZnO-  $\text{Zn}_2\text{SiO}_4$  composite prepared by using amorphous  $\text{SiO}_2$  nanoparticles, *J. Aust. Ceram.* 55 (2019) 115–122, <https://doi.org/10.1007/s41779-018-0217-0>.
- [83] P. Sharma, H.S. Bhatti, Laser induced down conversion optical characterizations of synthesized  $\text{Zn}_2\text{Mn}_x\text{SiO}_4$  ( $0.5 \leq x \leq 5\text{mol}\%$ ) nanophosphors, *J. Alloys Compd.* 473 (2009) 483–489, <https://doi.org/10.1016/j.jallcom.2008.06.034>.
- [84] P. Diana, S. Sebastian, D. Sivaganesan, C.S.A. Raj, S.S. Kumar Jacob, T. H. AlAbdulaal, M. Shkir, Unveiling the luminescence of  $\alpha$ - $\text{Zn}_2\text{SiO}_4$  phosphor: profound influence of sintering temperatures, *Radiat. Phys. Chem.* 212 (2023) 111156, <https://doi.org/10.1016/j.radphyschem.2023.111156>.
- [85] M.N. Bessadok, D. Ananias, A. Bouri, C. Bouzidi, C. Barthou, L. El Mir, Effect of doping element on non-contact luminescence thermometry properties of nanocomposite  $\text{SiO}_2/\text{ZnSiO}_4\text{:X}$  ( $\text{X}=\text{Mn}, \text{V}, \text{Ca}$ ), *J. Lumin.* 269 (2024) 120480, <https://doi.org/10.1016/j.jlumin.2024.120480>.
- [86] B.K. Meyer, H. Alves, D.M. Hofmann, W. Kriegseis, D. Forster, F. Bertram, J. Christen, et al., Bound exciton and donor-acceptor pair recombinations in ZnO, *Phys. Status Solidi B* 241 (2) (2004) 231–260, <https://doi.org/10.1002/pssb.200301962>.
- [87] C. Baratto, E. Comini, M. Ferroni, G. Faglia, G. Sberveglieri, Plasma-induced enhancement of UV photoluminescence in ZnO nanowires, *CrystEngComm* 15 (39) (2013) 7981–7986, <https://doi.org/10.1039/C3CE41055B>.
- [88] N. Palladino, M. Ocelli, G. Wallez, Y. Coquinot, Q. Lemasson, L. Pichon, S. Stankic, et al., An analytical survey of zinc white historical and modern artists' materials, *Heritage Sci.* 12 (1) (2024) 47, <https://doi.org/10.1186/s40494-023-01082-4>.
- [89] T. Furukawa, S. Kanamori, M. Fukuta, Y. Nawa, H. Kominami, Y. Nakanishi, A. Sugita, W. Inami, Y. Kawata, Fabrication of bright and thin  $\text{Zn}_2\text{SiO}_4$  luminescent film for electron beam excitation-assisted optical microscope, *Opt Express* 23 (14) (2015) 18630–18637, <https://doi.org/10.1364/OE.23.018630>.
- [90] C. Li, Y. Bando, B. Dierre, T. Sekiguchi, Y. Huang, J. Lin, D. Golberg, Effect of size-dependent thermal instability on synthesis of  $\text{Zn}_2\text{SiO}_4\text{:SiO}_x$  core-shell nanotube arrays and their cathodoluminescence properties, *Nanoscale Res. Lett.* 5 (2010) 773–780, <https://doi.org/10.1007/s11671-010-9556-7>.
- [91] B. Dierre, X. Yuan, T. Sekiguchi, Low-energy cathodoluminescence microscopy for the characterization of nanostructures, *Sci. Technol. Adv. Mater.* 11 (2010) 4, <https://doi.org/10.1088/1468-6996/11/4/043001>.
- [92] X. Feng, X. Yuan, T. Sekiguchi, W. Lin, J. Kang, Aligned Zn-  $\text{Zn}_2\text{SiO}_4$  Core- shell nanocables with homogeneously intense ultraviolet emission at 300 nm, *J. Phys. Chem. B* 109 (33) (2005) 15786–15790, <https://doi.org/10.1021/jp0514980>.
- [93] H.J. Chang, H.D. Park, K.S. Sohn, J.D. Lee, Electronic structure of  $\text{Zn}_2\text{SiO}_4$  and  $\text{Zn}_2\text{SiO}_4\text{:Mn}$ , *J. Kor. Phys. Soc.* 34 (6) (1999) 545–548.
- [94] H. He, Y. Wang, Y. Zou, Photoluminescence property of ZnO- $\text{SiO}_2$  composites synthesized by sol-gel method, *J. Phys. D Appl. Phys.* 36 (2003) 2972–2975, <https://doi.org/10.1088/0022-3727/36/23/017>.
- [95] V.S. Kortov, K.A. Sergeeva, V.A. Pustovarov, A.A. Rempel, Photoluminescence of nanostructured  $\text{Zn}_2\text{SiO}_4\text{:Mn}^{2+}$  ceramics under UV and VUV excitation, *J. Surf. Invest.: X-Ray, Synchrotron Neutron Tech.* 11 (2017) 727–731, <https://doi.org/10.1134/S1027451017040097>.
- [96] K.A. Petrovskiy, V.S. Kortov, N.V. Gaponenko, A.A. Rempel, M.V. Rudenko, L. S. Khoroshko, S.S. Voznesenskii, A.A. Sergeev, V.A. Pustovarov, Photoluminescence of the nanosized xerogel  $\text{Zn}_2\text{SiO}_4\text{:Mn}^{2+}$  in pores of anodic alumina, *Phys. Solid State* 58 (2016) 2062–2067, <https://doi.org/10.1134/S1063783416100280>.

- [97] Y. Hao, Y. Wang, Luminescent properties of  $\text{Zn}_2\text{SiO}_4\text{:Mn}^{2+}$  phosphor under UV, VUV and CR excitation, *J. Lumin.* 122 (2007) 1006–1008, <https://doi.org/10.1016/j.jlumin.2006.01.352>.
- [98] K.C. Mishra, K.H. Johnson, B.G. DeBoer, J.K. Berkowitz, J. Olsen, E.A. Dale, First principles investigation of electronic structure and associated properties of zinc orthosilicate phosphors, *J. Lumin.* 47 (5) (1991) 197–206, [https://doi.org/10.1016/0022-2313\(91\)90012-K](https://doi.org/10.1016/0022-2313(91)90012-K).
- [99] S. Zhang, H. Liang, Y. Liu, Y. Liu, D. Hou, G. Zhang, J. Shi, Intensive green emission of  $\text{ZnAl}_2\text{O}_4\text{:Mn}^{2+}$  under vacuum ultraviolet and low-voltage cathode ray excitation, *Opt. Lett.* 37 (13) (2012) 2511–2513, <https://doi.org/10.1364/OL.37.002511>.

## List of Publications Not Included in This Thesis

- IV. **Necib, J.**, López-Sánchez, J., Rubio-Marcos, F., Serrano, A., Navarro, E., Peña, Á., Mnasri, T., Mourad, S., Rojas-Hernandez, R.E., Carmona, N., & Marín, P. (2022). A feasible pathway to stabilize monoclinic and tetragonal phase coexistence in barium titanate-based ceramics. *Journal of Materials Chemistry C*, 10(46), 17743-17756.
- V. Gouadria, H., Mnasri, T., Jamale, A.P., Sánchez, J.L., **Necib, J.**, Marín, P., Carmona, N., & Smari, M. (2023). Spectroscopic properties, conduction processes and the Summerfield scaling of barium titanate ceramics based on Bi and Fe. *Inorganic Chemistry Communications*, 157, 111417.
- VI. Rojas-Hernandez, R.E., Rubio-Marcos, F., **Necib, J.**, Danilson, M., Fernandez, J.F., & Hussainova, I. (2023). Cost-effective screen printing approach for Ce/Nd-doped  $\text{ZnAl}_2\text{O}_4$  films: tuning crystallinity induced by the substrate. *Physical Chemistry Chemical Physics*, 25(23), 15829-15838.
- VII. Gouadria, H., Smari, M., Mnasri, T., **Necib, J.**, Sánchez, J.L., Marín, P., Jamale, A.P., & Younes, R.B. (2023). Implementing a sol-gel route to adjust the structural and dielectric characteristics of Bi and Fe co-doped  $\text{BaTiO}_3$  ceramics. *Inorganic Chemistry Communications*, 147, 110241.



# Curriculum vitae

## Personal data

Name: Jallouli Necib  
Date of birth: 08.07.1989  
Place of birth: Mdilla, Tunisia  
Citizenship: Tunisia

## Contact data

E-mail: Jallouli.necib@taltech.ee; jalloulnecib@gmail.com

## Education

2021–2025 Tallinn University of Technology – PhD  
2017–2020 Innovative Materials and Energy Management,  
Faculty of Sciences of Gafsa, Tunisia – MSC  
2009–2012 Fundamental Physics, Faculty of Sciences of Gafsa,  
Tunisia –BSC  
2005–2009 High school – Ibn Rached, Gafsa, Tunisia

## Language competence

Arabic Native  
English Fluent  
French Fluent  
Spanish Basic

## Professional employment

01.05.2024–... Junior Research, Tallinn University of Technology,  
School of Engineering, Department of Mechanical  
and Industrial Engineering  
01.09.2023–30.04.2024 Engineer, Tallinn University of Technology, School of  
Engineering, Department of Mechanical and  
Industrial Engineering

## Project

PSG466 “Enhanced and wavelength-tunable luminescence in nanostructured phosphor films (EWALUNFILMS) (01.09.2020–30.04.2026)”, Rocío Estefania Rojas Hernandez, Tallinn University of Technology, School of Engineering, Department of Mechanical and Industrial Engineering

## Research visits

01.04.2019–30.06.2019 Applied Magnetism Institute, Madrid, Spain  
15.09.2019–15.10.2019 Applied Magnetism Institute, Madrid, Spain  
01.09.2020–23.12.2020 Applied Magnetism Institute, Madrid, Spain  
01.03.2021–31.05.2021 Applied Magnetism Institute, Madrid, Spain.  
23.03.2022–02.04.2022 Institute of Ceramics and Glass, Madrid, Spain  
14.04.2022–19.04.2022 European Synchrotron Radiation Facility, Grenoble,  
France  
17.04.2023–26.04.2023 Institute of Ceramics and Glass, Madrid, Spain  
13.07.2023–27.07.2023 Institute of Ceramics and Glass, Madrid, Spain  
13.12.2023–20.12.2023 MAX IV Laboratory, Lund, Sweden  
01.04.2024–31.05.2024 Münster University of Applied Sciences, Münster,  
Germany  
11.02.2025–17.02.2025 MAX IV Laboratory, Lund, Sweden

## **Conferences**

2020	4th Young Researchers in Magnetism, within the joint meeting of the Spanish Club of Magnetism and the Spanish Chapter of the IEEE Magnetics Society, Bilbao, Spain, 19 November 2020
2022	Conference of Ceramics in Europe, Krakow, Poland, 10-14 July, 2022
2023	Modern Materials and Manufacturing (MMM2023) conference, Tallinn, Estonia, 2-4 May 2023
2023	Graduate School of Functional Materials and Technologies: (GSFMT) Scientific Conference, Tartu, Estonia, 23-24 May, 2023
2023	XVIIIth Conference of the European Ceramic Society, Lyon, France, 2-6 July 2023
2024	6th International Conference RARE EARTH MATERIALS Advances in Synthesis, Studies and Application, Vilnius, Lithuania, 20-23 October, 2024
2025	Modern Materials and Manufacturing (MMM2025) conference, Tallinn, Estonia, 6-8 May 2025

## **Honors and Awards**

2025	<b>Best Paper Award</b> Modern Materials and Manufacturing (MMM2025) conference, Tallinn, Estonia
------	--

## Elulookirjeldus

### Isikuandmed

Nimi:	Jallouli Necib
Sünniaeg:	08.07.1989
Sünnikoht:	Mdilla, Tuneesia
Kodakondsus:	Tuneesia

### Kontaktandmed

E-post:	Jallouli.necib@taltech.ee; jalloulnecib@gmail.com
---------	---

### Hariduskäik

2021–2025	Tallinna Tehnikaülikool – PhD
2017–2020	Innovatiivsed materjalid ja energiamajandus, Faculty of Science, Gafsa, Tuneesia – MSC
2009–2012	Fundamentaalfüüsika, Faculty of Science, Gafsa, Tuneesia – BSC
2005–2009	Keskharidus – Ibn Rached, Gafsa, Tuneesia

### Keelteoskus

Araabia keel	Emakeel
Inglise keel	Kõrgtase
Prantsuse keel	Kõrgtase
Hispaania keele	Algtase

### Teenistuskäik

01.05.2024–...	Nooremteadur, Tallinna Tehnikaülikool, Inseneriteaduskond, Mehaanika ja tööstustehnika instituut
01.09.2023–30.04.2024	Insener, Tallinna Tehnikaülikool, Inseneriteaduskond, Mehaanika ja tööstustehnika instituut

### Projektid

PSG466 “Suurendatud ning häälestatav luminestsents fosforipõhistes nanostruktuursetes kiledes (EWANUFILMS) (01.09.2020–30.04.2026)”, Rocío Estefania Rojas Hernandez, Tallinna Tehnikaülikool, Inseneriteaduskond, Mehaanika ja tööstustehnika instituut

### Välismaal teadustöö

01.04.2019–30.06.2019	Applied Magnetism Institute, Madrid, Spain
15.09.2019–15.10.2019	Applied Magnetism Institute, Madrid, Spain
01.09.2020–23.12.2020	Applied Magnetism Institute, Madrid, Spain
01.03.2021–31.05.2021	Applied Magnetism Institute, Madrid, Spain.
23.03.2022–02.04.2022	Institute of Ceramics and Glass, Madrid, Spain
14.04.2022–19.04.2022	European Synchrotron Radiation Facility, Grenoble, France
17.04.2023–26.04.2023	Institute of Ceramics and Glass, Madrid, Spain
13.07.2023–27.07.2023	Institute of Ceramics and Glass, Madrid, Spain
13.12.2023–20.12.2023	MAX IV Laboratory, Lund, Sweden
01.04.2024–31.05.2024	Münster University of Applied Sciences, Münster, Germany
11.02.2025–17.02.2025	MAX IV Laboratory, Lund, Sweden



**Konverentsid**

2020	4th Young Researchers in Magnetism, within the joint meeting of the Spanish Club of Magnetism and the Spanish Chapter of the IEEE Magnetics Society, Bilbao, Spain, 19 November 2020
2022	Conference of Ceramics in Europe, Krakow, Poland, 10-14 July, 2022
2023	Modern Materials and Manufacturing (MMM2023) conference, Tallinn, Estonia, 2-4 May 2023
2023	Graduate School of Functional Materials and Technologies: (GSFMT) Scientific Conference, Tartu, Estonia, 23-24 May, 2023
2023	XVIIIth Conference of the European Ceramic Society, Lyon, France, 2-6 July 2023
2024	6th International Conference RARE EARTH MATERIALS Advances in Synthesis, Studies and Application, Vilnius, Lithuania, 20-23 October, 2024
2025	Modern Materials and Manufacturing (MMM2025) conference, Tallinn, Estonia, 6-8 May 2025

**Autasud ja auhinnad**

2025

**Parima artikli auhind**

Modern Materials and Manufacturing (MMM2025) conference, Tallinn, Estonia

ISSN 2585-6901 (PDF)  
ISBN 978-9916-80-340-0 (PDF)